2016

The Design, Fabrication, and Validation of a Film Cooled Rotating Turbine Cascade with an Actively Cooled Shroud in a Closed Loop Wind Tunnel

Christopher Michael Drewes
Louisiana State University and Agricultural and Mechanical College

THE DESIGN, FABRICATION, AND VALIDATION OF A FILM COOLED ROTATING TURBINE CASCADE WITH AN ACTIVELY COOLED SHROUD IN A CLOSED LOOP WIND TUNNEL

A Thesis

Submitted to the Graduate Faculty of the
Louisiana State University and
Agricultural and Mechanical College
in partial fulfillment of the
requirements for the degree of
Master of Science

in

The Department of Mechanical and Industrial Engineering

by
Christopher M. Drewes
BSME, Louisiana State University, 2011
May 2016

Acknowledgements

First, I would like to thank my parents Mark and Robin Drewes whose love and support have allowed me to achieve all of my goals in life. I would like to thank Dr. Sumanta Acharya for his guidance over the course of this project and for my development as a graduate student. Special thanks to Chiyuki Nakamata of IHI Corporation, Tokyo, Japan, the project sponsor, whose involvement was critical in the wind tunnel design. I would like to sincerely thank Benjamin Wayne Hood for his help in the design and fabrication of the closed loop wind tunnel and test section. A debt of gratitude is also owed to Carey Celestin for his help in debugging Matlab code. Throughout the design process, members of the TIER lab were there to offer advice and help in times of need especially J.W. Post, Onieluan Tamunobere, Louis Moreaux, Greg Kramer, and Del Segura. I would like to thank the members of my graduate committee, Dr. Kieth Gonthier and Dr. Shengmin Guo and finally David McIntyre of Airside Equipment Inc. Baton Rouge, Louisiana, for generously donating four electronically actuated air duct dampers.

Table of Contents

List of Tables

List of Figures

Abstract

To test shroud and blade cooling effectiveness, a closed loop, heated wind tunnel housing a film cooled rotating turbine cascade with prescribed blade and vane geometry surrounded by a fully cooled shroud with a leading edge gap were designed and assembled on Louisiana State University's campus. Heat transfer coefficients and film cooling effectiveness results were computed using a 1-D semi-infinite solid conduction analysis of material temperatures obtained with liquid crystal thermography. Proper analysis required a step change in air temperature; so a bypass loop provided mainstream air heating while maintaining the shroud and blades at ambient temperature. Also, analysis required hollow tip film cooled turbine blades constructed of low thermal conductivity material, resulting in fabrication by 3-D plastic printing.

An analytical stress model and finite element analysis validated plastic blade structural base design. Static-structural and dynamic fatigue loading analyses determined rotor shaft size. Heat transfer and pressure loss calculations verified the system's required blade and shroud cooling characteristics. Finally, velocity vector measurements at the nozzle guide vane leading edge and recorded pressures in a nozzle guide vane passageway upstream of the turbine cascade location validated incoming freestream flow properties for the design condition at which heat transfer measurements were recorded.

A total pressure loss analysis for varying rotor speed and blowing ratio was conducted with the development of total pressure contours downstream of the exit guide vanes to understand losses in the nozzle-rotor passage. Loss structures were found at the tip and root of the exit guide vane, attributed to the shed vortex and tip leakage

vortex developed from the rotor blade. Total pressure loss decreased as blowing ratio increased due to energy added to the mainstream flow through the film cooling air. Rotor speed was varied from 55 to 655 RPM. Total pressure losses were lowest at 55 RPM, increased with increasing rotor speed past the 355 RPM design speed, and decreased as rotor speed approached 655 RPM. These results could be attributed to the introduction or extraction of shaft work in the rotating system along with aerodynamic losses associated with changes from the incidence angle design.

Chapter 1: Introduction

The word Turbomachinery comes from the third declension Latin noun Turbo, Turbinis which is defined as a whirlwind or tornado. This is fitting due to the very fact that all turbomachines have a rotating set of blades that rotate or whirl as they interact with the fluid at hand. A turbomachine is a device that either converts fluid energy into rotational shaft work or it takes an input of shaft power and converts that to fluid power. Of those turbomachines that convert shaft power into fluid energy: fans, compressors, and pumps are the most common. These machines input energy into the fluid which increases the fluid velocity, thereby creating a rise in fluid total pressure. On the other hand, common turbomachines that convert fluid power into usable shaft power through fluid expansion include wind, hydraulic, or steam turbines.

Applications for turbomachines date back to the Romans who used paddle wheels to grind grain, but it wasn't until the late eighteenth century that John Barber patented a design using the thermodynamic gas turbine cycle. In the nineteenth century, George Brayton developed the modern gas turbine cycle which bears his name. The Brayton cycle consists of an adiabatic compression where work is imparted on the fluid followed by an isobaric heat addition usually in the form of combustion, followed by an adiabatic expansion where work is extracted from the fluid, and finally an isobaric heat rejection which is commonly completed by exhaust air being rejected to the environment. Although Brayton is credited with the thermodynamic cycle design, it wasn't until later that the first usable gas turbine that produced more power than it consumed was invented by AEgidius Elling. Even after the concept of the gas turbine was widely accepted, it was not until the invention of the turbojet engine by Sir Frank

Whittle which we know today as the modern gas turbine, that these machines became practical for multiple uses.

Modern gas turbines are used to power aircraft, marine vessels, and even military tanks because of their high power to weight ratio. Gas turbines are also extensively used for power generation. Louisiana State University has its own 20MW cogeneration gas turbine which provides auxiliary electricity and steam for the campus. Some of the largest gas turbines can output a power of more than 340MW. Depending on its use, modern gas turbines consist of three or four major components: compressor, combustor, turbine, and nozzle. Ambient air enters the compressor where energy, from the rotating shaft, is added to the air and the pressure increases before it reaches the combustor. Here, fuel is added to the airstream and burned to increase the temperature of the air while the pressure remains nearly constant. The resulting high enthalpy air is then expanded through the turbine. The turbine extracts energy from the flow and a portion of that power is used to run the compressor, and the remaining energy is either extracted through additional turbine stages, or it is used to create thrust via a nozzle as seen in Figure 1.

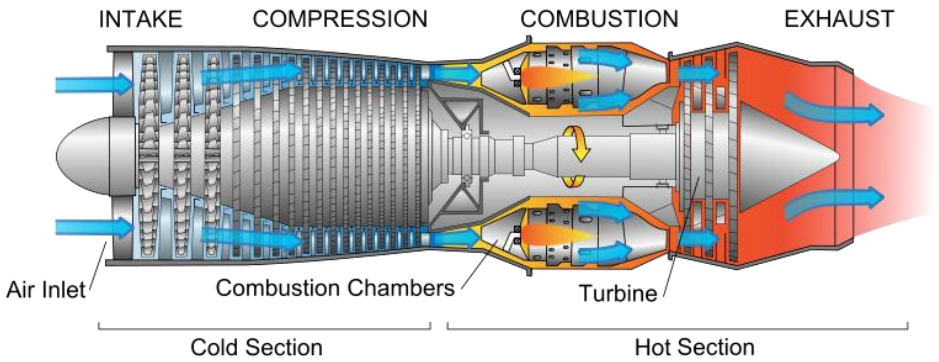

Figure 1 - Simplified Turbine Schematic (**http://bit.ly/1mMZ8Or**)

Another name for the gas turbine cycle is the Brayton Cycle which can be seen diagrammatically in Figure 2 and in pressure-volume space and temperature-entropy space in Figure 3. In stage 1-2 of the ideal Brayton Cycle, ambient air is taken into the compressor where it is isentropically compressed. In stage 2-3, fuel is added to the compressed air and is burned isobarically. The turbine stage, 3-4, consists of expanding the air through an isentropic process, and thus the cycle completes from stage 4 back to 1 with a constant pressure heat rejection. Through a First Law of Thermodynamics analysis, the thermal efficiency of the Ideal Brayton Cycle is detailed in the following equation [1].

$$\eta = 1 - \frac{T_1}{T_2} = 1 - \left(\frac{P_1}{P_2}\right)^{\frac{\gamma-1}{\gamma}} \qquad \text{[Eq. 1]}$$

As the pressure or temperature ratio of the compressor increases, the efficiency of the gas turbine increases. Thus, as the combustor exit temperature limits are increased, the efficiency will increase. The temperature ratio is limited, however, by the material limits of the combustor and turbine components.

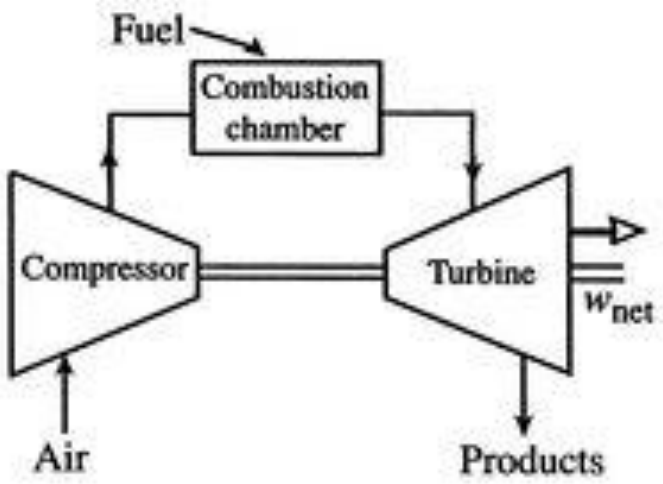

Figure 2 - Brayton Cycle (**http://bit.ly/1Ufp7ZX**)

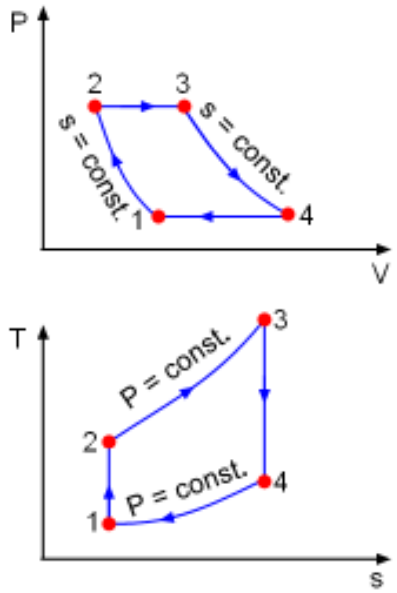

Figure 3 - Ideal Brayton Cycle (**http://bit.ly/22yJCXs**)

In propulsion based gas turbines, engine performance is generally characterized by the specific thrust and the thrust specific fuel consumption (TSFC). The specific thrust is the thrust per unit mass flow of air, and the TSFC is the mass flow rate of fuel divided by thrust. It is desired to maximize specific thrust and minimize TSFC. Both performance characterizations can be related to the temperature at the combustor exit, turbine inlet. They are generally related by the following:

$$Specific\ Thrust = \frac{\tau}{\dot{m}_a} \propto \sqrt{T_e} \qquad \text{[Eq. 2]}$$

$$TSFC = \frac{\dot{m}_f}{\tau} \propto 1/\sqrt{T_e} \qquad \text{[Eq. 3]}$$

where

$$\tau = thrust\ (N)$$
$$\dot{m}_a = mass\ flow\ rate\ of\ air\ (kg/s)$$
$$\dot{m}_f = mass\ flow\ rate\ of\ fuel\ (kg/s)$$
$$T_e = temperature\ at\ the\ combustor\ exit\ (K)$$

The gas turbine thrust performance can be improved by an increase in combustor exit temperature [2]. Performance in land-based power generation turbines is similar in that it is also desired to increase this temperature.

Increasing combustor exit temperature creates a problem because the first stage of the turbine is directly downstream of the combustor. By increasing the temperature, the turbine blades are exposed to temperatures as high as 3000 °F, which are well above the melting point of the typical nickel alloy blade materials. The first stage nozzle guide vanes and blades have to be actively cooled along with the end walls.

In order to avoid melting the turbine blades especially at the tip, where high thermal loading is seen, internal and external cooling strategies are applied. These cooling strategies take cooler air from the compressor and supply that air to the turbine blades and endwall both internally through coolant passages, and externally through pin holes and slots. This air creates a film barrier that separates the surfaces of the blade and end wall from the harsh, high temperatures of the main flow.

These cooling methods have been explored since the 1960s, and much research has been done in this field to improve turbine blade cooling. Many factors must be considered when designing such a cooling system. Some of these include: location, size, shape, number of holes, hole angle, and blowing ratio. The blowing ratio is the ratio of the product of the density and velocity of the main flow to the coolant flow and is defined below where subscripts *c* and ∞ represent coolant and free stream. The research is very beneficial since a slight increase in efficiency will allow for great savings in fuel costs over time along with added performance.

$$Blowing\ Ratio = m = \frac{\rho_c u_c}{\rho_\infty u_\infty} \qquad \text{[Eq. 4]}$$

where

$$\rho = density\ of\ air$$
$$u = velocity\ of\ air$$

With regard to increasing the efficiency of a gas turbine, aerodynamic losses also play an important role. While being able to maintain higher combustor temperatures is key to increasing power output, aerodynamic losses from bypassing coolant air and secondary flow losses can nullify efficiency increases from enthalpy gains. Generations of researchers have studied ways to reduce secondary flow structures through endwall contouring and film cooling strategies. Blade and vane passage boundary layer growth contributes to these secondary flows which increase the turbulence of the bulk fluid motion thereby reducing lift created via the pressure gradient from the pressure side to the suction side of the blade which can be extracted as work. This same pressure gradient causes the tip leakage vortex similar to the tip vortex seen on airplane wings. This vortex causes high heat transfer on the blade tip and shroud region in the tip gap of the turbine cascade. Various tip structures have been studied over the years to impede the growth and development of the tip leakage vortex. Some of these geometries include tip squealer cavities and more recently winglets. In the current study, a squealer tip geometry is used along with pressure side, tip, and shroud coolant injection to abate the heat transfer caused by the tip leakage vortex.

1.1 Outline of Thesis

A literature review of the research performed on shroud and tip cooling in both rotational and stationary cascades will be presented in the following section. This research delves into both experimental and computational analyses of gas turbine engines with film cooling, allowing one to gain a perspective and understanding of the flow structures and heat transfer mechanisms which drive turbine designers to create an effective cooling strategy to optimize blade performance. The third section describes

the design of the experimental apparatus to examine film cooling including major components and their design. All design calculations and decisions are provided as well as details of the current setup and instructions on how to operate the facility. The final portion of this report focuses on the results of aerodynamic testing of the rotating turbine facility offering a validation of the experiment's design.

Chapter 2 Literature Review

2.1 Introduction

The following is a summative assessment of various journal articles pertaining to heat transfer and fluid dynamics involving tip leakage flow on high pressure turbine blades. Various experimental techniques have been used to study the flow and subsequent heat transfer of turbine blade tips. Liquid crystal, infrared, and mass transfer are the most common experimental techniques. These techniques are used to better understand the interactions between the leakage flow and the film coolant flow as well as to validate computational fluid dynamic codes. Study of tip leakage flow and heat transfer is an important field in turbine blade design because it is at the tip where failure is most common. This is due to impediments in internal cooling at the tip and high temperature gas flow over the tip caused by the pressure gradient.

In today's high pressure turbines, failure most commonly occurs at the tip region. Due to increasing turbine inlet temperatures which improve thermal efficiency, the high pressure turbine is subject to high heat loads. The tip region is exposed to higher gas temperature through leakage flow which occurs due to a pressure differential across the blade thickness. The loss of life in the tip is due to these high temperatures, lack of adequate cooling, and rubbing on the outer casing or shroud. A tip gap is necessary to allow for thermal expansion, but this comes at a cost. It has been found that about one third of aerodynamic losses occur due to leakage flow at the tip. It has proven difficult to cool the tip region of the blade because internal cooling has been rendered ineffective by the leakage flow. In today's engines, film cooling holes are employed at the tip and on the pressure side near the tip to protect it from the adverse hot gas

leakage flow. Tip coolant holes are generally used at the sweet spot near the leading edge to reduce heat transfer coefficients [3]. Squealer rims are also used to help reduce the leakage flow by causing a pressure drop using a labyrinth seal [4]. Blowing ratio and tip gap clearance both have effects on the heat transfer and film cooling effectiveness of a particular coolant strategy. The squealer rim geometry has an effect as well. In recent years, additional studies covering the flow field and heat transfer at the tip have offered insight regarding techniques to increase cooling effectiveness and reduce aerodynamic losses. The following section discusses experimental techniques currently employed to obtain heat transfer information in gas turbine research. Section 2.3 explores various journal articles on studies involving different cooling strategies and their effect on heat transfer coefficients, film cooling effectiveness, and the flow field.

2.2 Experimental Techniques in Tip Heat Transfer Research

Various experimental techniques have been developed to study heat transfer associated with turbine rotor blades. The most prevalent techniques in literature are liquid crystal thermography, IR thermography, mass transfer thermography, and thin film heat flux gauge thermography. Each method has its unique advantages and disadvantages for each testing case, and a summary of the theory behind each method and its application will be discussed.

2.2.1 Liquid Crystal Thermography

Today, liquid crystal thermography is a time-tested measurement technique for heat transfer in research applications. Liquid crystal has been used in research since the early 70's and has evolved into a fast and efficient way to map heat transfer coefficients in aero-thermal research. Thermochromic liquid crystals (TLCs) reflect

different colors based on their temperature. “Liquid crystals are organic compounds derived from the esters of cholesterol” [3]. In order for the liquid crystals to change color at a particular temperature, their lattice structure changes and reflects only one wavelength of light, while the other wavelengths are transmitted. The first study to use liquid crystal thermography was performed by Vennemann and Butefisch in 1973 for a high speed heat transfer experiment. Since the dawn of liquid crystal thermography, continuing camera equipment and computer analysis improvements have aided in the speed at which tests can be performed and analyzed. In ’92-’93, Camci et al. used color processing software to separate the hue, saturation, and intensity of a given image. They found that the temperature was linearly related to the hue of the image, and thus were able to map out surface temperatures in two dimensions [3].

Ekkad and Han [3] describe their method for setting up and running a liquid crystal test. The equipment involved in their test is also involved in other similar tests pertaining to gas turbine research. In order to capture the color of the liquid crystal at a given time, an RGB color camera was used. A 24-bit frame grabber board was installed on the computer to capture the images that would be analyzed. Software was written to output the time of the appearance of a specific color band for each pixel which will be used to determine heat transfer coefficients and other important parameters. A test piece was painted black and subsequently, a thin layer of TLCs were painted over the surface. A calibration was conducted to relate the colors to specific temperatures and relate changes in hue to changes in temperature. Before the actual transient test begins, the background intensity of the color must be found. If the surface is evenly lit, the intensity can be recorded as a basis for determining color change. This initial

background intensity is important so that the image is clear and that the color change is not lost due to a saturation of white light or a deficiency in reflected light.

Different types of TLCs can be used for analysis involving heat transfer in gas turbines. Narrow band liquid crystal has a transition temperature of about 1°C which results in an uncertainty of around 0.1°C. This gives a relatively small uncertainty in heat transfer coefficients for a transient 1-D analysis. Wide band liquid crystal can be used for cases where a step change is not possible. This technique will give a temperature history over a longer period of time; and the transition temperature for this wide band liquid crystal is about 20°C,resulting in uncertainties in heat transfer coefficients of an order of magnitude higher than for narrow band [4].

The analysis for finding heat transfer coefficients on a surface given a step change in temperature of the mainstream air is demonstrated below. To find heat transfer coefficients, the 1-D semi-infinite assumption is used for this given experiment. Therefore, the test object must have a low thermal conductivity and diffusivity so that conduction can be approximated as flowing in only one direction normal from the surface. The surface thickness is another important aspect of the 1-D assumption. The thickness must be great enough so that heat will not be transferred from the surface through the testing object and into another convective fluid or conductive medium. The wall temperature at a particular time (t) is found using the liquid crystal coating and camera setup. The initial wall temperature and free stream air temperatures are also recorded. The 1-D transient conduction equation is as follows along with its boundary conditions:

$$k\frac{\partial^2 T}{\partial x^2} = \rho C_p \frac{\partial T}{\partial t} \quad \text{[Eq. 5]}$$

With the boundary conditions:

At $t = 0$, $T = Ti$

At $x = 0$, $-k\frac{\partial T}{\partial x} = h(T_w - T_m)$

As $x \to \infty$, $T = T_i$

Given the initial and boundary conditions seen above and the temperature history at the surface (x=0) that can be found through liquid crystal thermography, one can back out the heat transfer coefficients using the following equation.

$$\frac{T_w - T_i}{T_m - T_i} = 1 - \exp\left(\frac{h^2 \alpha t}{k^2}\right) erfc\left(\frac{h\sqrt{\alpha t}}{k}\right) \quad \text{[Eq. 6]}$$

The initial wall temperature (T_i) is recorded before the step change while the mainstream air temperature (T_m) is recorded continuously and can be assumed constant for the duration of the experiment. The values of material conductivity and diffusivity are also input as constants, allowing for determination of the heat transfer coefficients [3].

In order for the 1D semi-infinite assumption to be valid, the test piece must have a low thermal conductivity and diffusivity. In Kwak and Han's experiment [5], they used a machined aluminum blade as a base for their heat transfer test blade. The physical properties of aluminum helped to disperse the heat applied initially to the blade before the test was run. A polycarbonate shell was placed over the aluminum base to maintain conduction from the blade root to the tip allowing for the 1D assumption to be valid for their analysis. In this test the blade and coolant were heated to the same temperature while the main stream air was left at room temperature (about 20 degrees Celsius less). They performed the HTC analysis utilizing a backwards regression technique to plot their findings.

Most of the testing performed using liquid crystal thermography has been done in wind tunnels employing stationary cascades. In these stationary cascades, a given flow entrance and exit velocity and angle are maintained. In order to model the desired turbulence, a turbulence grid can be utilized. This grid is generally custom made to offer the correct amount of turbulence that would be seen in engine type flow conditions. In order to test the turbulence values, a hot wire anemometer probe is used at various locations along the inlet flow. These values are averaged to check that the turbulence coincides with the prescribed flow conditions. The grid can be altered by moving bars closer together or further apart to adjust for the prescribed turbulence. Many of these wind tunnels are outfitted with pressure taps throughout the test rig to ensure proper flow. Often, test blades are fitted with pressure taps at various points on the span to check the flow and heat transfer results. Wake conditions are sometimes prescribed where a wake generator is needed to simulate the nozzle guide vane wake. Generally, a spinning disk outfitted with wooden dowels is adequate to create wakes seen at the entrance of a blade cascade. In order to achieve the exit flow conditions, tailboards are used to direct the flow in the correct direction and to offer the correct pressure ratio [3].

2.2.2 Infrared Thermography

Infrared (IR) thermography is similar to liquid crystal thermography (LCT) in the analysis method. Most testing is performed in a similar way to LCT using a step change in temperature of the incoming free stream air and the equations provided above. The basis for IR thermography (IRT) is the same semi-infinite 1D assumption that LCT is based on. Given the temperature history of each pixel, one can back out the heat transfer coefficients. An advantage of IRT is that only one test is needed in order to find

heat transfer coefficients and film cooling effectiveness. The adiabatic wall temperature which is needed for the film cooling effectiveness can be extrapolated from the temperature data in a single given experiment. IR thermography can be used at just about any temperature ratio, whereas LCT can have a maximum temperature ratio of about 20° C. Disadvantages associated with IRT are the high cost of an IR camera and a window with ideal transmissive properties for a camera's particular wavelength [6].

In a blow down test performed by O'Dowd et al. [6] utilizing IRT, the free-stream temperature took 12 seconds to reach equilibrium resulting in a less than ideal temperature step change. To account for this, a heat flux history must be reconstructed for each blade tip location (i.e. every pixel of the captured IR temperature image). The following equation, relates the temperature history to the heat flux. In this equation, tau is the sampling rate, m is the number of samples taken, and n is an integration variable.

$$\dot{q}(t) = \left(\frac{2\sqrt{\rho c k}}{\sqrt{\pi \tau}}\right) \sum_{n=0}^{m} \left[(T_{n-1} + T_{n+1} - 2T_n)(m-n)^{1/2} \right] \text{ [Eq. 7]}$$

This heat flux reconstruction is a numerical approximation which gives a linear relationship between heat flux and wall temperature over the given time period. This is a finite difference technique as seen in the equation above. When plotted against each other, the adiabatic wall temperature can be extrapolated and the slope of the line is the heat transfer coefficient. This method is used for each pixel to give a contour of the heat transfer coefficients and film cooling effectiveness.

In a similar test run by O'Dowd et al. [6], an Impulse Response method is used. This method is similar to the finite difference heat flux reconstruction in that it uses the temperature history of the test specimen, but differs from the finite difference technique

in that it uses known pairs of exact solutions to obtain an impulse response filter to convert temperature into heat flux using Fast Fourier Transforms.

One can obtain heat transfer coefficients using a steady state method where the heat equation is used with a constant, easily measurable heat flux. In this method, a thin foil heater is used at the tip of a non-conductive blade to give a uniform heat flux. This heat flux is known for a given voltage, current and resistance. From this heat flux and subsequent wall temperate found after the system reached equilibrium, heat transfer coefficients can be found. A second test is needed to find the adiabatic wall temperature and thus the film cooling effectiveness of the blade. Disadvantages to this method are that conduction is incurred into the blade and is not constant for the total area of the blade.

A more detailed explanation of an IR test was given by Nasir et al. [7]. Their analysis is similar to that used in LCT in that the temperature is recorded at two separate times during the transient test to find the two unknowns – heat transfer coefficient (h) and the adiabatic wall temperature (Tf). He solves the following equations simultaneously so that superposition integration becomes unnecessary, thus, simplifying the analysis.

$$\frac{T_{w1}-T_i}{T_f-T_i} = 1 - \exp\left(\frac{h^2 \alpha t_1}{k^2}\right) erfc\left(\frac{h\sqrt{\alpha(t_1)}}{k}\right) \quad \text{[Eq. 8]}$$

$$\frac{T_{w2}-T_i}{T_f-T_i} = 1 - \exp\left(\frac{h^2 \alpha t_2}{k^2}\right) erfc\left(\frac{h\sqrt{\alpha(t_2)}}{k}\right) \quad \text{[Eq. 9]}$$

$$\eta = \frac{T_m-T_f}{T_m-T_c} \quad \text{[Eq. 10]}$$

In this particular experiment, the heat transfer blade is heated to a uniform temperature using a cartridge heater for 2 hours. The film coolant air is bypassed until the

experiment begins. The wall temperature is recorded using an IR camera and the mainstream and coolant temperatures are measured using thermocouples. The blade is cooled during the test so that the mainstream air is cooler than the blade and film coolant air.

2.2.3 Mass Transfer (Naphthalene Sublimation) Technique

The use of Napthalene sublimation has been well documented in heat transfer research. This technique offers advantages in that heat/mass transfer is due only to convection while both conduction and radiative heat transfer are ignored. The conduction and radiation effects skew the results of other tests and are not present in mass transfer analysis. Heat transfer can be described by mass transfer in relating the Nusselt and Schmidt numbers.

$$h_m = \frac{\dot{m}}{\rho_{v,w} - \rho_{v,\infty}} = \frac{\dot{m}}{\rho_{v,w}} \quad \text{[Eq. 11]}$$

Since $\rho_{v,\infty} = 0$

Where $\dot{m} = \rho_s \frac{\delta y}{\delta \tau}$

ρ_v is the vapor density of naphthalene and the mass removal rate is the density multiplied by the thickness lost over test duration time. This approach makes the mathematical analysis simple, but has drawbacks in that it is difficult to measure the amount of naphthalene removed. Also, when naphthalene is removed, the blade shape changes which could change the flow structures around the wall [8].

In a study presented by Srinivasan et al. [8], the tip gap changes at up to 4.6% of the nominal tip gap due to naphthalene sublimation and removal. In order to obtain accurate measurements of the thickness of naphthalene lost, a linear variable

differential transformer (LVDT) was used. Cho et al. [9] describe their method for finding the density of the naphthalene vapor in the following equation.

$$\rho_{v,w} = \frac{P_{naph}}{R_{naph} T_w} \quad \text{[Eq. 12]}$$

This equation uses the ideal gas law for the naphthalene vapor at the temperature that the test is run. Cho relates the Nusselt number to the Sherwood number using a correlation for turbulent flow.

The aforementioned heat transfer testing techniques were all considered in the design of the rotating turbine cascade. It was concluded that liquid crystal thermography would be the most feasible method to use, given the budget and design of the facility. In order to gain a better understanding of turbine blade tip heat transfer and cooling techniques, a study of previous research was done for comparison.

2.3 Turbine Blade Tip Heat Transfer (Uncooled Blade Tips)

Heat transfer results have been collected and summarized in the following section for various tip geometries without film cooling. The geometries considered were: flat tip, full squealer rim, cut-back squealer rim, pressure side squealer, SS squealer, camber line squealer, or a combination of these types.

2.3.1 Effects of Tip Geometry on Heat Transfer

Newton et al. [10], studied heat transfer on a flat tip turbine blade with and without cooling. For the no coolant case, a region of high heat transfer occurred on the tip in a line parallel to the pressure side of the blade. This region of high heat transfer was due to the leakage flow separating over the pressure side and reattaching on the tip. They also note that the heat transfer on the blade tip is higher than any other portion of the blade, including the stagnation region. Christophel et al. [11] observed a similar

line of high heat transfer near the pressure side of the blade, but they also found a region of lower heat transfer near the leading edge where the pressure gradient is lower, resulting in a lower tip leakage mass flow.

Kwak et al. [12] found that for a squealer rim along the camber line, heat transfer is highest near the suction side of the tip. The flow separates over the squealer and reattaches at the suction side creating a localized region of high heat transfer. Similarly, Azad et al. [13] observed a region near the suction side tip where heat transfer was highest, but also determined that the pressure side had lower overall heat transfer coefficients. However, Saxena and Ekkad [14] found a “bifurcation” in the heat transfer coefficients with a more even distribution on the pressure and suction side.

Azad et al. [13] found that the pressure side squealer caused the highest tip heat transfer coefficients of all the test cases. For the same tip geometry, Kwak et al. [12] found that the flow reattaches and forms a vortex near the leading edge of the blade at about 20% of the chord. The suction side squealer was found to have the lowest heat transfer coefficients for each tip gap clearance in each of the aforementioned studies. A small amount of flow circulates at the base of the suction side causing slightly higher heat transfer coefficients. With a full squealer tip, heat transfer coefficients are lower than that of the flat tip case. A portion near the leading edge, as seen on the pressure side squealer, has a region of high heat transfer coefficients. This is due to leakage flow becoming trapped and circulating within the cavity at this point. Similarly, for the full squealer case, higher heat transfer coefficients were found by Azad et al. at the trailing edge where the leakage flow is trapped and turbulence is increased. They determined

that a cutback squealer could mitigate this issue allowing the leakage flow to exit the tip cavity.

Another case studied was a combination of pressure side and camber line squealers. Both Kwak et al. [12] and Azad et al. [13] found that this case performed better than the flat plate, but still had hot spots caused by reattachment near the suction side and in the cavity between the two squealer rims. The final case studied was a combination of suction side and camber line squealers. This set-up performed like the suction side squealer, but had higher heat transfer coefficients in the cavity formed between the two squealer rims. All of the cases studied showed lower overall heat transfer than the flat blade tip, resulted in the movement of the region of high heat transfer coefficients from near the pressure side of the blade to another region, and displayed a slight increase in heat transfer coefficients as the tip gap increased.

In shroud testing, Kwak et al. [12] found that the heat transfer coefficients are much higher for the flat blade tip than for a tip with a squealer. For the flat tip, a place of high heat transfer coefficients is seen along the pressure side where leakage flow impinges on the shroud. This is caused by the higher flow rate of leakage air which flows over the flat tip with no obstruction to cause a pressure drop and impede the passage flow. The tip leakage vortex causes a region of high heat transfer coefficients near the suction side traveling downstream for all cases. This vortex becomes more and more prevalent as the tip gap is increased and causes high heat transfer in its path. All blade tip geometries tested revealed higher heat transfer coefficients as the tip gap is increased. Additional discussion of shroud heat transfer can be found in section 2.4.

2.3.2 Effects of Endwall Motion on Tip Heat Transfer

In order to study the effects of end wall motion on tip heat transfer, Srinivasan et al. [15] constructed a wind tunnel with a stationary cascade and a moving end wall. In order to achieve a moving end wall, they constructed a conveyor belt system to simulate the relative motion of the blades passing by the shroud or sheathing. In a similar study, Palafox et al. [16] took measurements in a wind tunnel with a stationary cascade of blades with spans of 1 meter and a conveyor belt moving endwall. These studies can be reasonably compared to a rotating rig as they mimic the relative motion of the rotating blades past the shroud surface.

Srinivasan et al. [15] define the engineering equivalent speed (EES) as the belt velocity divided by twice the mainstream flow. This EES is the basis for a correlation between the results with end wall motion and a stationary end wall. Palafox et al. [16] performed their experiments using the design velocity triangle speed for their endwall belt setup.

Both studies revealed an area toward the leading edge of the blade with relatively lower Sherwood and Nusselt numbers; this corresponds to the ‘sweet spot’ where the tip usually has lower heat transfer due to low-pressure gradients driving the tip flow in this region. Near the pressure side edge, separation and reattachment of the flow causes a narrow region of high mass/heat transfer. The reattachment vortex impinges on this region causing higher heat transfer due to the greater pressure differentials, and presumably, greater leakage velocities at these locations.

Srinivasan et al. [15] found, at the mid chord region, a reduction of 9% from the stationary case of heat/mass transfer for a small tip gap clearance of 0.6% of the chord

length. This reduction is most likely due to the leakage vortex moving closer to the suction side of the blade caused by the motion of the endwall. Similarly, Palafox et al. [16] found a reduction of 13.3% in overall nusselt number for a flat tip case run with a tip gap of 0.56% of the chord length and a moving endwall. Both higher Sherwood and Nusselt numbers were discovered on the trailing edge of the blade, seemingly due to the fact that the leakage vortex is extended down the blade due to the motion of the end wall. Through PIV velocity measurements, Palafox et al. determined that the separation bubble is reduced in size at the midchord of the blade tip and causes lower heat transfer coefficients near the pressure side of the blade.

For a larger tip gap clearance of 0.86%, Srinivasan et al. [15] found that nearly no decrease in heat/mass transfer was evident. They posit that this is most likely due to the fact that the flow is driven by pressure gradients and is less affected by viscous effects coming from the relative motion of the end wall running over the blade. However, Palafox et al. [16] found a reduction of overall Nusselt number to be 12.45% similar to the 0.56% tip gap case.

2.3.3 Transonic Turbine Blade Tip Heat Transfer

In this study, Zhang et al. [17] compare CFD results with experimental results using the Oxford High Speed Linear Cascade Research Facility. In this experimental setup, a blow down type facility provides high pressure air from a compressor which is pumped into an inlet settling plenum. Air is controlled with a valve which can adjust the Reynolds and Mach numbers independently. Once the air passes through the plenum, it flows through a 100 kW mesh heater where the air is abruptly heated to 25 degrees Celsius above the ambient temperature. This air then passes through a 5 blade

cascade. The center three blades are provisioned to allow adjustment of the tip gap clearances. The air is controlled by a PID controller which adjusts the control valve to keep the flow conditions constant for the duration of the 1D transient test. The heat transfer blades were fabricated using a 3D printer and made from a low thermal conductivity epoxy resin to keep the 1D semi-infinite assumption valid. IR thermography was used to obtain a temperature history of the test and Nusselt numbers were calculated to be compared to the CFD. A thermocouple was placed on the tip of the blade to allow for calibration of the IR camera through the Zinc-Selenide window. In addition, pressure measurements were taken at mid-span and at 95% of the span to find local Mach numbers and compare them to the computed results. The Rolls Royce HYDRA suite, used for the computational study, has a core of a “preconditioned Runge-Kutta solver of the discrete Euler or Reynolds-Averaged Navier Stokes equations. A Spalart-Allmaras turbulence model is implemented” [17]. The computational domain was one blade with a periodic boundary condition. ICEM software was used to import the physical geometry and apply the mesh given the tip gap. The results were proven to be grid-independent by the fact that values did not change as the grid was made denser. The experimental results show that as the tip gap is decreased, the Nusselt number also decreases due to the reduction in mass flow. As observed on most blade geometries, a region of high Nusselt numbers was seen on the leading edge of the blade. A hot spot forms on the trailing edge of the blade which has been well documented in literature as well. The Nusselt numbers predicted by the CFD were in good agreement with the experimental results. Both locally and over the entire blade, the magnitude and contour match up well. As can be seen in the CFD results and

reported by Zhang et al. [17], multiple heat strips are present on the blade tip due to shock wave reflections. In this region, the rapid acceleration and subsequent deceleration causes a high amount of heat transfer to occur locally. In the region of supersonic flow, heat flux is caused by enhanced turbulence production and dissipation rather than viscous shear effects.

Jackson et al. [18] found similar results when performing experiments in a transonic rotating test rig with engine representative Mach and Reynolds numbers. A rotating test rig was placed in the isentropic light piston tunnel offering isentropically compressed air for 200 ms. Heat transfer measurements were taken using thin film thermometers coupled to a slip ring on the shaft. A CFD analysis was also performed using a Reynolds-Averaged Navier Stokes (RANS) solver. Good agreement between the experimental results and the CFD were shown along the camberline and at a line 30% of the tip width offset. The study showed a region of high heat transfer near the pressure side edge corresponding to the reattachment of the separation bubble. The results also showed that heat transfer is higher in the subsonic zone of the blade tip as opposed to the sonic region. The author attributes the higher heat transfer in the sonic zone to an induction of turbulence in the lower Mach number region where the separation bubble exists.

Zhang et al. [17] determined that for all tip gaps, flow is subsonic at the leading edge, and flow becomes supersonic at 30-40% of the chord. The magnitude of the Mach number decreases as tip gap is decreased due to a reduction in mass flow rate of the leakage flow. The abrupt transition of supersonic flow is evidence of a shock wave within the tip gap region. These waves become less evident when the tip gap is

reduced to 0.5% of the chord length. Jackson et al. [18] also found that the Mach number decreased with a decreasing tip gap and thus the heat load increased with a decrease in tip gap clearance. They attribute this to the shear effects of the casing on the blade tip.

2.4 Turbine Blade Tip Heat Transfer (With Cooling)

In the previous section, it was shown that a full squealer rim offered lower tip heat transfer coefficients without film cooling when compared to partial squealer rims. Film cooling has been shown to inhibit heat transfer especially at the tip, and various studies explore its effects coupled with different squealer tip geometries.

2.4.1 Turbine Blade Tip Film Cooling

Testing performed by Nasir et al. [7] on a GE-E^3 blade was conducted in a stationary cascade to explore the effects of tip geometry coupled with film cooling. Two studies were conducted, one with a flat tip and the other with a recessed tip, similar to that of a full squealer rim. It was found that, for the flat tip, as the blowing ratio (BR) was increased from 1 to 2, heat transfer decreased in the tip region; however the heat transfer increased as the blowing ratio was increased from 2 to 3 due to lift off incurred in the coolant flow which reduced its effectiveness.

Newton et al. [10] performed experiments on a flat tip blade with and without coolant injection to compare their results. They found that introducing coolant inside the separation bubble caused a net heat flux reduction of 37%. This was more effective than the case of coolant introduction at the location of the bubble's reattachment. Interestingly, regions of increased heat transfer were found near the injection sites

where the local leakage flow velocity was increased, but a reduction in overall heat transfer was found.

In order to compare results to a baseline experiment, Kwak and Han [5] performed a no-coolant case. On the no cooling case for a flat tip blade, a region of low heat transfer coefficients is seen near the trailing edge. This is referred to as the sweet spot. In this region, there is little pressure differential to drive a leakage flow, resulting in minimal heat transfer. They posit that the wider cavity near the leading edge allows the hot leakage flow to reattach and enter the cavity, whereas the narrower passage near the trailing edge keeps the leakage flow from entering the cavity and it passes over the suction side.

Nasir et al. [7] attribute the high heat transfer coefficients seen on the pressure side from the middle to the trailing edge, to the pressure side entrance vortex which impinges flow on this region. In the case of coolant injection, a horseshoe vortex is created which drives the coolant flow from the pressure side of the leading edge to the suction side of the trailing edge. This horseshoe vortex was due to an acceleration in the flow caused by the coolant air blocking a portion of the leakage flow. For the recessed tip, a more even distribution of higher heat transfer coefficients is seen near the leading edge as opposed to the trailing edge. This effect is beneficial to turbine blade designers because the thicker portion of the leading edge can better handle the increased stresses caused by the higher heat load. For the recessed tip, a higher film cooling effectiveness is evidenced at a BR of 1 over most of the blade tip compared to that of the flat tip. Coolant air is trapped and mixes with the leakage flow in this region causing higher film cooling effectiveness. Similar to the flat tip case, a BR of 2 was

shown to offer the optimum film cooling effectiveness for the recessed blade tip with coverage over 50% of the tip

In a study performed by Acharya et al. [19], a highly loaded turbine blade with a cut-back squealer rim was analyzed. This study is significant in that it gives results for blade tip cooling in a stationary cascade for the same blade geometry studied in the rotating turbine cascade at the Tier Center described in this paper. Two blade coolant holes were located on the leading edge of the tip at a direction normal to the tip surface and 6 pressure side tip coolant holes were angled downstream to comprise the coolant strategy.

Similar to the study by Nasir et al. [7], lift off was seen at a BR of 2.9. At a BR of 1.0, film cooling effectiveness was found to be high adjacent to the holes and toward the trailing edge. For the given blade geometry, high heat transfer coefficients were found near the leading edge due to impingement of the leakage flow and the resulting leakage flow vortex. These same contours were also seen in the numerical simulation conducted. Low heat transfer was found near the pressure side moving down to the trailing edge which is most likely due to the fact that the leakage flow is separated in this region and does not reattach until closer to the suction side. At the trailing edge, the leakage flow does not reattach on the tip resulting in low heat transfer in this region. For a blowing ratio of 1.2, the lowest HTC's are seen. The highest HTC's on the contour map occur at the leading edge due to this impingement region. As the blowing ratio is increased to 4, lift-off of the coolant jet is seen and this detrimentally affects the HTC's at the leading edge where the tip leakage vortex becomes disturbed. In the study performed by Acharya et al. [19], lift off was seen at a BR of 2.9; and at a BR of 1.0, film

cooling effectiveness was found to be high adjacent to the holes and toward the trailing edge.

Film cooling effectiveness was also mapped in this study. The highest regions of film cooling effectiveness were seen adjacent to the tip coolant holes for a BR of 1.2. As the BR increased to 4 higher film cooling effectiveness values were found. This could be due to increased mixing between the coolant and leakage flows. Also, as the pressure side holes incurred increased flow rates, the coolant air would spill over into the squealer cavity causing mixing. This effect can be seen as the contour offers high film cooling effectiveness values along the chord.

Given that the turbine blade of interest at the Tier Center employs a cutback squealer rim, experiments conducted by Mhetras et al. [20] on a similar blade using pressure sensitive paint were of interest. The experimental set-up for this test rig uses pressure sensitive paint to obtain a correlation for film cooling effectiveness. “Pressure Sensitive Paint is a photo-luminescent material that emits light at an inversely proportional rate of the partial oxygen pressure” [20]. A CCD camera is used to measure the light intensity at each pixel and an intensity ratio can be formed from a datum at no flow conditions. In order to find film cooling effectiveness, air and nitrogen were used alternately as coolant and main flow. Nitrogen has a similar chemical makeup to air, but the nitrogen will lift the oxygen from the surface. Film cooling effectiveness can be found as a ratio of the concentration of oxygen in the air and coolant mixture to the concentration of nitrogen in the mainstream air. The author states that film cooling effectiveness is higher for the cutback squealer design than it is for a full squealer rim at all blowing ratios. At a BR of 1, increased coverage was seen near

the trailing edge of the tip due to the flow of coolant air escaping through the cutback region and accelerating in the narrow passage. The coolant jets all flow in the direction of the main stream air because the mainstream air has sufficient momentum to deflect the coolant. The two leading edge holes' coolant flows toward the suction side and pressure side rims. This could be due to the leakage flow separating and reattaching at the leading edge which has been documented in other papers.

Higher film cooling effectiveness can be seen at a BR of 1 than for higher BRs at the same depth of 4.6% of the blade span. This is due to the fact that the jet's momentum is low enough to allow it to spread out from the fan shaped compound angle holes. For all blowing ratios, film cooling effectiveness is low near the leading edge holes due to the higher pressure seen there. It can be observed that at a BR of 0.5, almost no coolant air is ejected through the leading edge holes and that air exits through the tip increasing effectiveness in the cavity.

For the cavity with 2.1% depth, similar film cooling effectiveness can be seen to that of the blade tip with 4.2% depth. A major difference is that the film cooling effectiveness is higher toward the leading edge, and the coolant jets at the leading edge follow the main stream flow path as opposed to being pushed outward by the leakage vortex. This is most likely due to the fact that the recirculation vortex cannot form due to the lower wall heights. A disadvantage of the shallower squealer cavity is that the recirculation vortex seems to be compressed and has a higher velocity which affects the trailing edge. This effect could be detrimental to a turbine blade where it would cause a high heat load on the trailing edge where the blade is thinner and more susceptible to failure.

Wang et al. [21] explored the mixing flow features through particle image velocimetry and computational fluid dynamics. This study's goal was to validate numerical techniques and offer insight into the mixing of coolant flow with the leakage flow over the tip of a turbine blade because this mixing significantly affects the cooling effectiveness.

This experiment was performed on a linear cascade with one test blade or two passages. The tunnel offers a periodic boundary condition in the pitch direction. A turbulence generator was placed 10cm upstream of the test section and had a 65% porosity. The blade was manufactured from stainless steel in a CNC mill and was placed on top of an adjustable platform into which coolant air was pumped through. The depth of the squealer rim was 2.5mm on the pressure side and 4.5mm on the suction site with a cutback portion on the trailing edge.

The tip leakage flow was studied using a two laser source PIV system. The particles infused had a diameter of 10 micrometers and had a density which closely coincided with the density of air. This two laser array offered measurements of the flow field in two dimensions which could define the flow or vortex field.

The CFD simulations were performed with CFX 11.0 and the "Navier-Stokes equations were solved using the finite volume method." A hybrid mesh was created with ICEM software with discretized regions at the tip grove and film cooling holes. The numerical calculations were given a periodic boundary condition to match the experimental set up.

To find the original leakage flow field, all of the coolant holes were plugged. The PIV system employed four laser sheets to obtain a velocity profile at those locations on

the suction side of the trailing edge of the blade. In order to compare the unsteady results of the PIV with the numerical results, the velocity measurements were taken several times and averaged. Preliminary findings had shown that the numerical and experimental results match identically in form, but not in magnitude. The tip leakage vortex on the suction side shows that the vortex extends from the tip and swirls down along the mainstream flow. This vortex gradually dissipates and moves away from the suction side.

A series of experiments performed to analyze the effect of film coolant introduction was performed and it was found that when coolant was added at the tip coolant holes, the region of high velocity near the leading edge was greatly reduced by a “blockage flow” caused by the tip coolant jets. In the case of pressure side cooling only, a region of low velocity appears at the pressure side just upstream of the blade. In the case of both pressure side and tip coolant, the total leakage flow was “strongly counterchecked.

In analyzing the mass flow rate of leakage flow and coolant air flow, the following was determined: a blowing ratio of 3 was found as the optimum case for impeding the leakage flow when all of the coolant holes were injecting coolant (both pressure side and suction side); when only the tip holes were opened, this configuration had a greater effect on impeding the leakage flow than the pressure side holes alone.

CFD was performed to analyze the effect of blowing ratio on the leakage flow and offer insight into the coolant coverage. It was found that for a blowing ratio of 1.0, the coolant from the tip covered the leading edge as well as the trailing edge. When the blowing ratio was increased to 3.0, the coolant air mixed directly with the leakage flow

offering little coverage. This has been presented in multiple open papers. The conclusion of these results show that for higher mass flow (higher blowing ratio), less leakage flow passes over the tip. But this comes at a cost to tip coolant coverage which protects the tip from hot gas flow.

Tamunobere and Acharya [22] performed a study in the Tier Center closed loop wind tunnel with a rotating turbine cascade. The turbine blade tip has two tip film cooling holes located near the leading edge of the tip and a set of pressure side coolant holes along the length of the cutback squealer and employs the same blade tip cooling strategy in the study performed by Acharya et al. [19]. Their study showed the effects of rotation on film cooling at the tip. A major difference between the stationary cascade and the rotating cascade is that the film cooling air migrates toward the suction side in the former rather than the pressure side in the latter. This migration of the coolant air is caused predominantly by the blade relative motion and is only marginally affected by centripetal and Coriolis forces. Similar to the results found by Acharya et al. [19] the overall film cooling effectiveness increased as the blowing ratio increased, while the heat transfer coefficients increased with increasing blowing ratio. At higher blowing ratios, the coolant can further penetrate the leakage flow and cover more of the tip, however the separation bubble formed at the leading edge also interacts with the coolant air causing locally higher heat transfer coefficients near the tip coolant holes.

2.4.2 Pressure Side Near-Tip Cooling

Kwak et al. [12] obtained heat transfer coefficients on the near tip pressure side of an uncooled blade. A region of high heat transfer coefficients are found near the trailing edge which is most likely caused by a boundary layer transition to turbulence.

This is present for all blade tip geometries tested. The results were inconclusive as to whether different tip geometries aided in lowering the heat transfer coefficients on the pressure side of the blade, though their magnitude was found to be nearly half of those on the tip region.

Pressure side near tip cooling was studied by Nasir et al. [7] and it was seen that film cooling effectiveness is minimal for both the flat blade and full squealer rim cases. Coolant jet streaks can be seen for a BR of 1 and are not present for a BR of 2 for the flat tip. When the BR is increased to 2, coolant flow lifts off and does not reattach on the tip. At a BR of 3, the flow lifts off, hits the shroud and reattaches to the suction side of the tip. In the recessed tip it does not appear that pressure side cooling is effective at all. This could be due to the fact that there is higher pressure in the squealer cavity, causing the coolant air to pass over the cavity and mix with the leakage flow.

For combination cooling on the flat tip with a BR of 1 or 2, the coolant jets become wider than for the single cases due to a higher bulk mass flow of coolant air; and a small amount of film cooling effectiveness is seen between the holes due to the pressure side coolant injection. For a BR of 3, high film cooling effectiveness is seen when the tip coolant jet lifts off of the surface, hits the shroud, and reattaches to the tip surface. This is seen in the combination case because the pressure side holes cause a blockage which allows the coolant holes to maintain increased momentum.

Christophel et al. [11] found that near-tip pressure side cooling holes created regions of higher convective heat transfer. The effects of both film cooling and tip gap were explored. At a smaller tip gap, cooling was found to be more effective overall.

Although regions of local high heat transfer coefficients occurred, the net heat flux reduction was found to be higher for the coolant case than for the no coolant case.

Acharya et al. [19] found low HTC's adjacent to the coolant holes and slightly downstream of their coolant paths. Near the holes, toward the trailing edge, high heat transfer coefficients were seen for all blowing ratios. This could be due to the free-stream flow becoming disturbed and impinging on the point around the coolant jet. These high HTC's increased in magnitude as the blowing ratio was increased. Film cooling effectiveness was found to be highest downstream of the coolant jet flow. This is due to the mixing of the free-stream and jet flow. At a blowing ratio of 1.1, the highest film cooling effectiveness was seen in the jet flow. As the blowing ratio was increased to 2.7, a reduction in film cooling effectiveness was found near the trailing edge holes which could be due to the coolant jet flow becoming detached. As the BR was increased, the film cooling effectiveness increased for the three holes nearer to the leading edge.

2.5 Shroud Heat transfer and Cooling

Multiple cooling strategies have been developed to sustain these high combustion temperatures, and, for the past few decades, film cooling has been extensively studied to develop more efficient ways of cooling turbine components including the shroud [23]. Various methods of cooling the shroud have been studied. Kanjirakkad et al. [24] investigated two passive film cooling concepts, platform cooling which involves direct coolant injection through radially aligned holes and rail cooling where coolant is injected through compound angle holes. Their results show that platform cooling was effective in cooling the turbine blade shroud while the rail cooling

concept was less effective. Michel et al. [25] studied the effect of full coverage film cooling using compound angle holes in a multi-perforated ring. Results were compared between axially oriented holes and swirl inducing holes. They found that in both cases, the film remained attached to the wall. The higher concentration seen in the swirling case showed that film cooling was greatly enhanced. In these cases and in most cases in open literature, the effects of rotation on the heat transfer behavior and coolant strategies were not taken into consideration.

The effects of rotation are important to understanding the heat transfer on the shroud. Multiple mechanisms affect the flow field near the shroud. Centrifugal forces act on the flow as it enters the rotor domain. These forces increase the radial component of the flow acceleration as the rotation speed increases. Changing the blade rotation speed results in different flow incidence angles. The incidence angle affects the flow profile in the rotor domain and it leads to the acceleration and impingement of the flow at different locations on the shroud surface [26]. The tip leakage flow pattern and distribution also influence the shroud heat transfer. High pressure gradients create a high temperature, high speed leakage flow from the pressure side to the suction side of the blade over the tip. Thus, both the tip and the shroud are subject to high thermal loadings and material failure. As the leakage flow passes through the tip gap over to the suction side of the blade, the tip leakage vortex is created. This tip leakage vortex interacts with secondary vortices created by the relative motion of the shroud causing additional pressure losses and potentially high heat transfer coefficients on the suction surface near the tip and shroud [5]. However, as the blade rotation speed increases, the shear layer on the shroud wall formed due to the sweeping action of the blades

becomes stronger. This shear layer impedes the advancement of the tip leakage flow. Thus, the tip leakage vortex decreases in strength as the blade rotation speed increases [27, 28], and the heat transfer distributions on the shroud surface are expected to change with rotation speed.

A few studies have considered the effect of rotation on the shroud heat transfer behavior. Of the studies available, Thorpe et al. [29] explored uncooled over-tip casing mean heat transfer in a transonic axial flow turbine facility. Their results show that the heat flux decreased in a linear manner in the axial direction of the flow along the shroud. This linear decrease is due to the reduction in enthalpy as the freestream air performs work on the turbine rotor. Small fluctuations in the heat flux were also observed in the circumferential direction of the shroud due to the vane-blade interactions resulting in periodic changes in static pressure. The heat transfer coefficient was found to be highest in the gap between the nozzle guide vanes and the leading edge of the rotor blades, followed by a linear decrease. In another study, Thorpe et al. [30] collected time resolved heat transfer data to gain a better understanding of the periodicity and unsteadiness of the flow field. Their results show that the highest heat transfer occurs over the blade tip due to the tip leakage flow, while there is a noticeably lower value of heat transfer in the rotor passageway. The shroud surface near the apex of the suction side of the blade tip experiences the highest heat transfer. This region of high heat transfer begins just upstream of the blade and falls off toward the trailing edge. When measuring the adiabatic wall temperature of the shroud, it was found that the maximum temperature measured on the shroud was within the tip gap region and this temperature

was higher than the stage inlet total temperature leading one to conclude that the rotor is performing work on the tip leakage flow.

Clearly, rotation is important in analyzing the mechanism of heat transfer on the shroud and the subsequent mechanisms to cool the shroud. An understanding of the effect of rotation is necessary in developing cooling strategies that will effectively protect the shroud. Thorpe et al. [29, 30], experimentally, and Rahman et al. [26], computationally, among others, have studied the heat transfer on the shroud with rotation.

Tamunobere et al. [31] studied the effects of rotation on shroud cooling with angled film cooling holes in the direction of rotation. It was found that as the blowing ratio increased, heat transfer coefficients decreased and the film cooling effectiveness increased. This defies the general trends of streamwise film cooling holes where lift off occurs at higher blowing ratios reducing the film cooling effectiveness. The angled holes, coupled with the rotating blades keep the film cooling jet attached; and the jet rolls into the adjacent jet keeping a more uniform film cooling coverage. It is also conjectured that the coolant air had a much lower level of turbulence than the near shroud region, thus reducing the heat transfer rates especially as the blowing ratio increased. Rotational speed was also explored and it was found that as the speed was reduced below the design speed, the critical region of high heat transfer migrated to the downstream portion of the shroud, while at rotational speeds above the design condition, the region of high heat transfer migrated toward the upstream section of the shroud. The lower rotational speed causes flow separation at the LE of the blade due to an increase in the relative incidence angle and the reattachment is pushed downstream

of the blades causing the higher heat transfer. At higher than design speeds, the incidence angle is negative and is flowing against the pressure gradient of the blade causing impingement and turbulence at the leading edge of the shroud. Hole spacing or pitch was also varied in this study and more complete cooling was seen as the hole pitch was reduced; however, pitch reduction comes at a higher manufacturing cost thereby requiring that an optimum cooling spacing be found.

Chapter 3: Facility Design, Fabrication, and Operation

3.1 Design Specifications

The goal of this project is to experimentally determine heat transfer coefficient (HTCs) and film cooling effectiveness (FCE) data for a film cooled high pressure turbine rotor blade tip and shroud under varying conditions of cooling and rotation. In order to test the film cooling strategy employed on the blade tip, pressure side tip, and shroud, a rotating turbine heat transfer facility has been designed and fabricated. The testing performed in the heat transfer wind tunnel offered scaled flow conditions to test the effectiveness of the film cooling design.

The design process began by analyzing the requirements, detailed in Table 1, showing the stator and rotor blade geometries, tip gap clearance, tip-hole geometry, and flow parameters for the on-design test condition.

Table 1 - Design Parameters

Axial Chord	Cax/Cax	1
Blade Pitch	t/Cax	1.03704
Throat Width	Wt/Cax	0.32099
Actual chord ratio	C/Cax	1.40988
Tip hole ratio	Dt/Cax	0.02469
Number of blades		64
Aspect ratio	H/Cax	1.8
Boss ratio	Hub/Tip	0.8
Rotation Number	Ro	0.003

3.1.1 Blade and Shroud Geometry

Three dimensional models of the blade and vane designs with the basic geometry are detailed in Figures 4 and 5 below. The blade tip has a squealer rim with coolant holes on the tip and pressure sides. The NGV and EGV profiles are two dimensional, while the rotor blade has a twisted 3D profile.

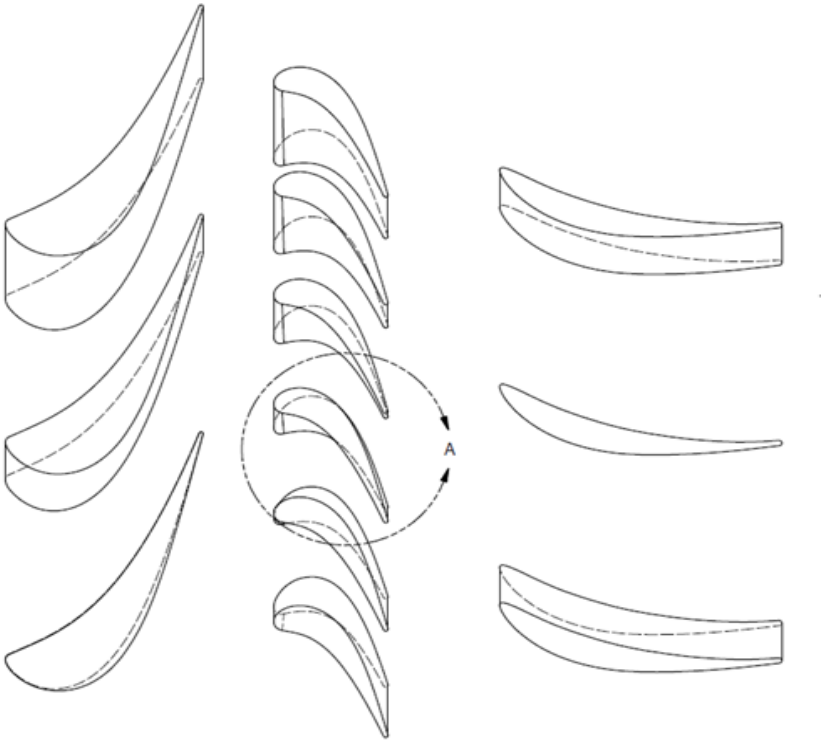

Figure 4 - Stator-Rotor-Stator Geometry

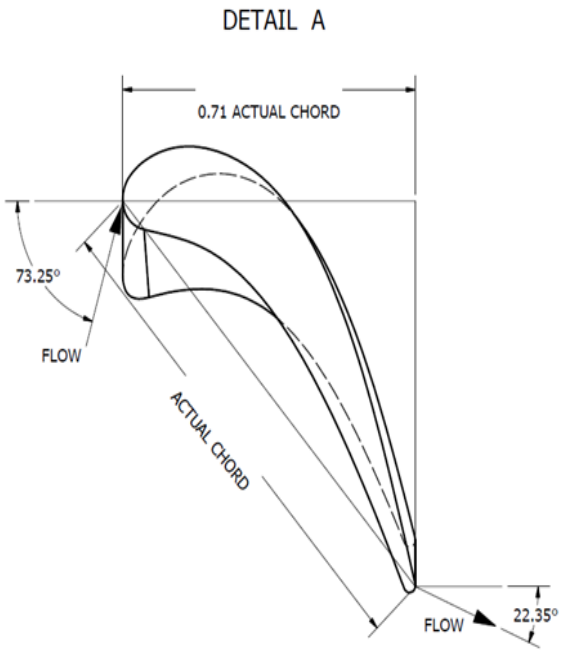

Figure 5 - Detail of the Rotor Geometry (in). (Squealer Tip Hidden for Clarity)

The physical geometry of the shroud cooling holes were detailed in Table 2 and illustrated in Figure 6. The shroud consists of 1696 total holes cut at a 45 degree angle

ejecting coolant in the direction of rotation. The shroud consists of five discreet rows of coolant holes with increasing pitch, or spacing as their axial distance increased from the leading edge of the shroud. A leading edge gap was also employed where a continuous cooling hole or gap was placed upstream of the LE of the rotor blade. A detailed design of the shroud can be seen later in this paper.

Table 2 - Proposed Shroud Coolant Hole Pitch Data

	Pitch (P/Dt)	Number of Holes	Position from LE (X/Dt)
F1	4.419	608	5
F2	5.597	480	10
F3	9.329	288	15
F4	11.994	224	20
F5	27.986	96	25

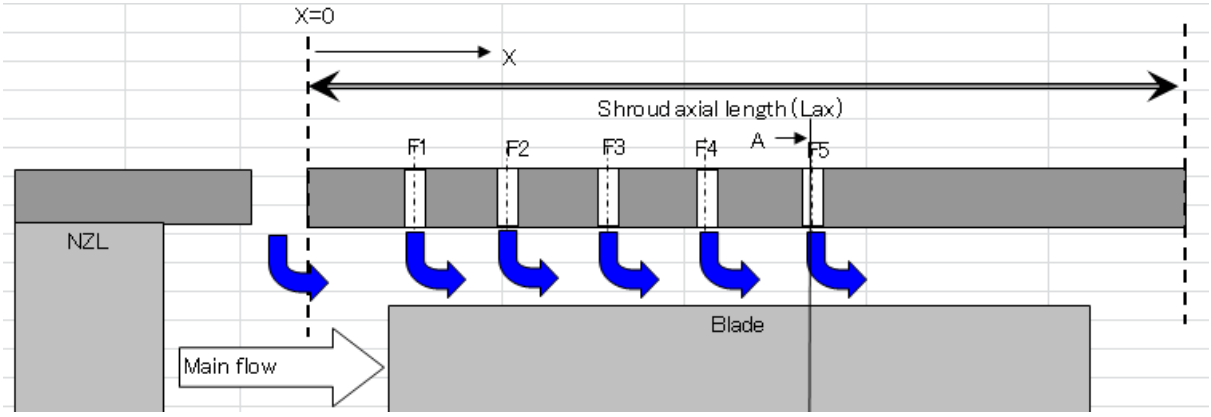

Figure 6 - Shroud Cooling Hole Location Diagram

3.1.2 Testing Technique Selection

Given the aforementioned geometry of the rotor and shroud, it was decided that the test rig and wind tunnel would have to be custom designed and off-the-shelf components would not be usable for the annulus of the one and a half stage system. Various concepts were explored in literature for the design of the wind tunnel that would enable the team to acquire accurate heat transfer results. Given the large design flow rate of air – on the order of 10,800 ft^3/min – a closed loop wind tunnel was determined

to be the best option and can be seen in Figure 7. An open loop wind tunnel would pull such a large amount of air from the facility that it was deemed unsafe and would also interfere with the building's HVAC system. A closed loop system was also necessary to properly heat the large volume flow rate of air.

Once a closed loop wind tunnel was selected, the method of testing would have to be finalized. In heat transfer research, it is typical to use one of two types of tests: steady-state or transient. In general, transient and steady-state testing differ in the way the test piece is heated. A transient test is performed by uniformly heating up the airflow to the test piece while steady-state testing involves applying a constant heat flux to the test piece. With both steady-state and transient testing, secondary factors must be considered which also include methods of visualization.

According to Ostanek et al. [32], steady-state test models are generally constructed of thermally conductive materials, such as copper or aluminum. The models are uniformly heated and insulated from ambient conditions until steady-state is reached on blade or endwall surfaces. Arranging foil heaters within the cooling channels by mounting the heaters onto the surfaces of the blades allows for application of a constant heat flux, with subsequent recording of the surface temperatures. Various measurement methodologies can be used to gain the heat transfer coefficients such as infrared (IR) imaging. Infrared imaging monitors the surface temperatures by use of an infrared camera, and this measurement technique requires IR access to the test piece either through an IR transmissive window or with the use of an IR borescope.

Given the rotating nature of the blades and their relatively small size, it was determined to be too difficult to manufacture miniaturized foil heaters that could offer a

constant heat flux for the steady-state system. A complex system of slip rings and heating elements would need to be applied to a rotating medium which would increase cost, complexity, manufacturing time, and maintenance time, adding to the manufacturing costs of having 64 3D twisted hollow blades machined from steel or aluminum. Therefore, it was decided that a transient test using the 1-D semi-infinite solid assumption with a convective boundary condition would be conducted in order to obtain HTCs and FCE data.

With the transient heat transfer analysis technique, an immediate heat addition to the airflow in the wind tunnel was necessary for the test. The amount of power needed for a screen heater or other instantaneous duct heating device would reach the order of 0.5 MW of power which was also unsafe and impractical to have supplied to the ERAD building.

In order to apply a step change in free-stream air temperature utilizing a manageable amount of power, a bypass system was created, allowing the mainstream air to reach a higher temperature gradually. Once the air in the bypass loop reached the desired temperature, an airflow damper was opened to allow the hot air to flow over the rotor facility, thereby providing the step change and initiating the heat transfer tests. Liquid crystal thermography was implemented to find the temperature history of the blade tip and shroud, and to extract the HTC and FCE from this data.

The purpose of this transient testing apparatus is to obtain the heat transfer coefficient and film cooling effectiveness data for both the blades and shroud using liquid crystal thermography. The experimental technique involves placing a thermographic liquid crystal coating rated for a particular temperature (Twall=35ºC) on

the surface to be tested. The surface changes to a green color when the surface matches the liquid crystal temperature. The surface is at a uniform initial temperature before sudden exposure to the heated mainstream air. Every pixel on the surface reaches the chosen wall temperature depending on the local heat transfer coefficient. Using an imaging system, a pixel by pixel analysis of the color change is used to calculate the heat transfer coefficient and film cooling effectiveness of the surface using the heat transfer equation shown below

$$T_w - T_{i1} = \sum_{j=1}^{N}[1 - \exp\left(\frac{h^2\alpha(t_1-\tau_j}{k^2}\right) erfc\left(\frac{h\sqrt{\alpha(t_1-\tau_j)}}{k}\right).[\eta T_{c1} + (1-\eta)(\Delta T_{m1})_j] \qquad \text{[Eq. 13]}$$

The heat transfer coefficient and film cooling effectiveness are both unkowns in the equation above. Since there are two unkowns, a two test method is used. For the second test, the coolant air is heated. Since there are now two sets of data and two unknowns, the heat transfer coefficient and film cooling effectiveness can be calculated simultaneously. Duhamel's integration is used to account for the variation of the temperature with time.

Multiple blowing ratios were tested to fully understand the film cooling effectiveness. Thus, the coolant flow rate must be controlled and measured along with the free-stream air. Tests have been completed on similar blades in a stationary cascade, but the effects of rotation such as the Coriolis forces needed to be taken into consideration. A variable frequency drive (VFD) was utilized to precisely control the rate of rotational speed to accurately capture these rotational effects. The VFD chosen had a dynamic braking capability in which it uses the motor windings to brake the motor in the event of overspeed, enabling tests to be run at speed below the design speed.

3.2 Wind Tunnel Detailed Design

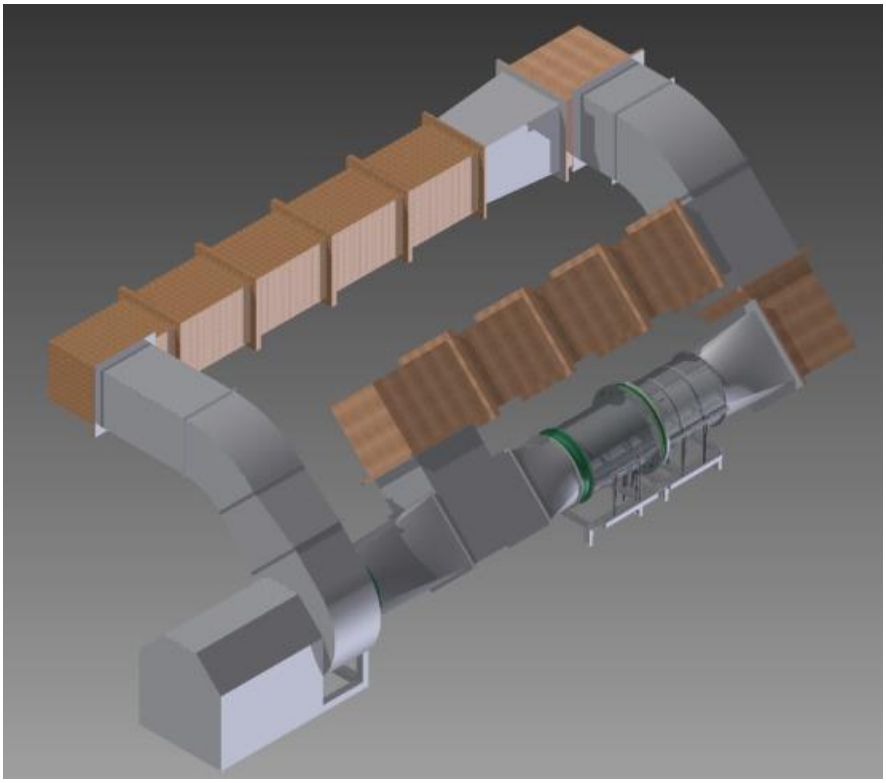

Figure 7 - Three Dimensional Rendering of the Wind Tunnel Facility

3.2.1 General Arrangement and Duct Design

The space constraints of the lab in room 115 ERAD on LSU's campus drove the envelope dimensions of the wind tunnel. As much space as possible was used to allow the flow to become fully developed upon entering the annular test section, thereby improving the aerodynamics for testing. An envelope of 34' x 15' x 11' (length x width x height), seen in Figure 8, was determined to be the useful area of the lab. Utilizing this entire envelope, installing and maintaining the wind tunnel would become cumbersome, so it was decided to hang the upstream straight portion from the ceiling in the room -- high enough for the operators to walk freely underneath. Threaded rod with a 3/8" nominal diameter and 2000 lb. concrete anchors were used to hang individual duct segments from the steel channel ceiling supports.

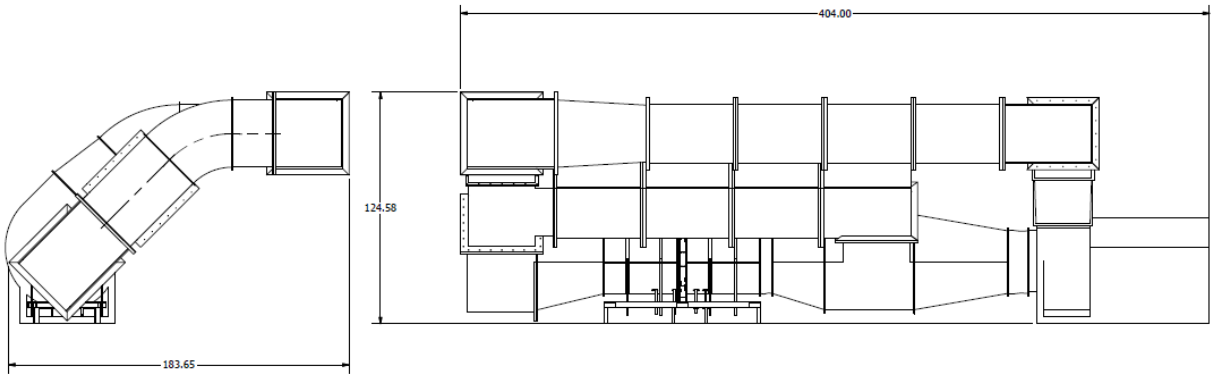

Figure 8 - Wind Tunnel Envelope (Units in Inches)

To keep cost as low as possible while providing the necessary air flow, the decision was made to fabricate as many pieces of duct as possible using ¾" plywood and 2x4 wood flanges – the detailed design can be found in the Figure 9. ¾" plywood and pine 2x4's provided the needed strength and rigidity for construction. Given the common size of 8'x4' sheets of plywood, 4' lengths of wood duct were fabricated using eight steel "L" brackets to tie the four segments of plywood sheeting together as detailed in Figure 9. Each 4' duct segment for the straight portion of the tunnel was 30.5" x 30.5" to maximize the use of each piece of plywood, providing a constant cross section to reduce pressure loss and thus reduce the required fan size. At each plywood-to-plywood seam, silicone sealant was used to reduce duct leakage which robs the tunnel of performance. After attaching the 2x4 flange to the plywood box with set screws, individual duct segments were connected by a series of 25 bolts placed through the adjoining flanges. Utilizing wood with its inherent flexible nature, aided in the overall facility installation by allowing for thermal growth in the sheet metal sections of contoured duct, and by offering relief from tolerance stack-up in the typical low dimensional tolerance construction of ductwork.

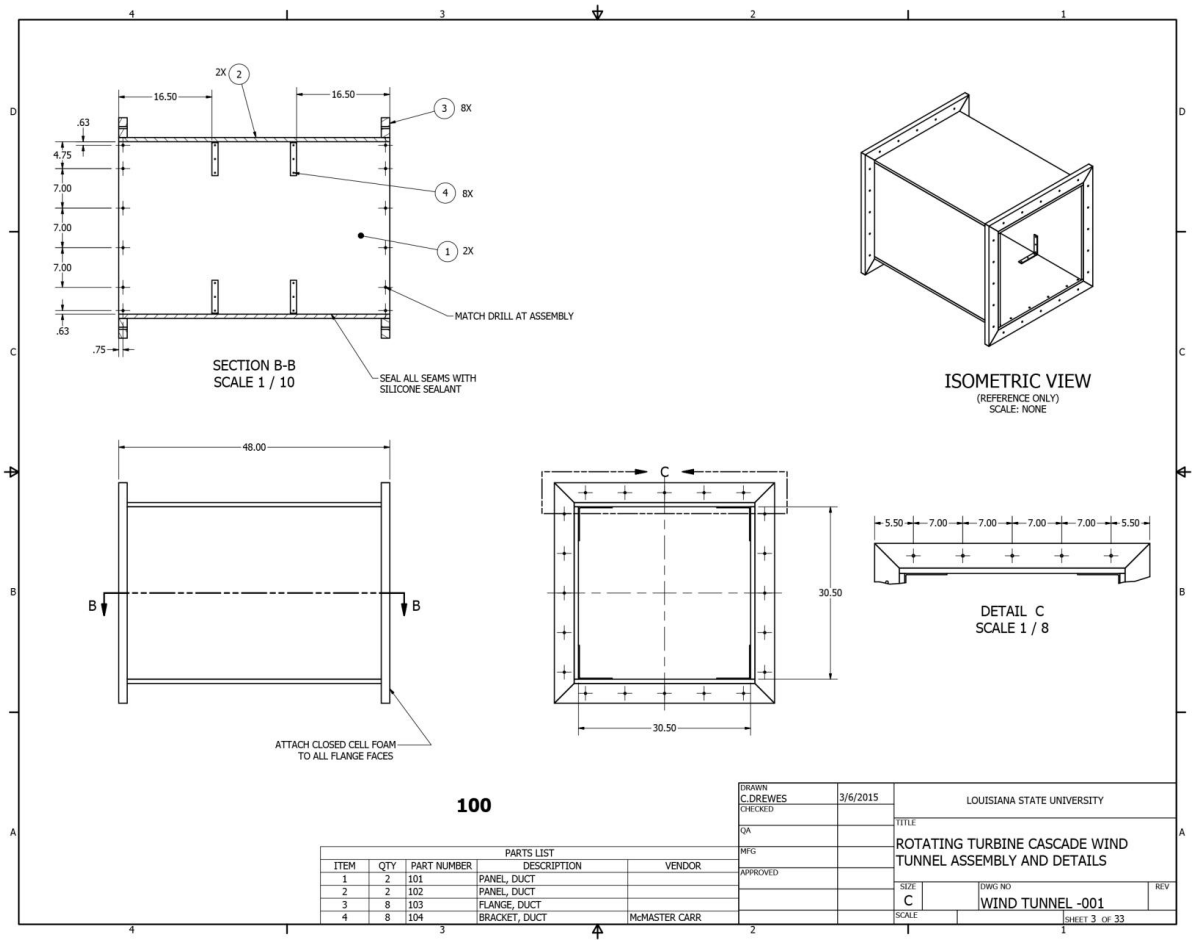

Figure 9 - Production Drawing of Straight Wood Duct

3.2.2 Bypass Air System Design

The wind tunnel is a closed-loop design which requires two separate flow paths. In bypass mode, air flows through the by-pass wooden duct allowing no airflow through the sheet metal test section, thus bypassing the test piece so that it can remain near room temperature while the mainstream air is heated to about 30ºC above the ambient. Bypass is accomplished by closing off the inlet and outlet dampers of the test section segment of the wind tunnel at the two respective junctions with the bypass section, while leaving the bypass dampers open and the airflow path is described by Figure 10. For testing, the bypass dampers are closed, while the test section dampers are opened

allowing the heated mainstream air to flow directly into the annular test section and is described by Figure 11

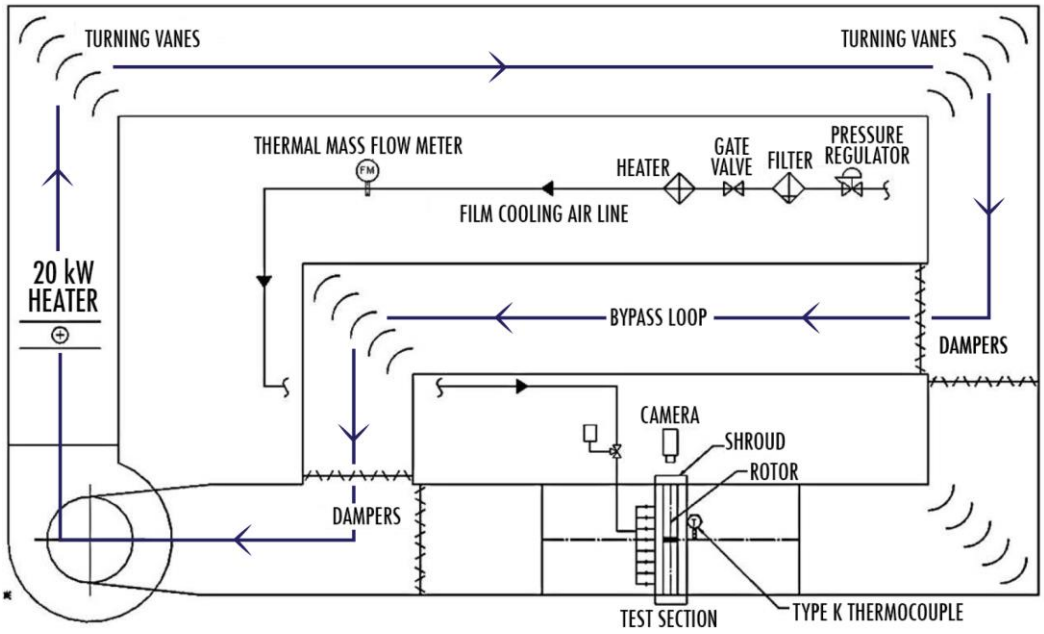

Figure 10 - Wind Tunnel in Bypass Mode

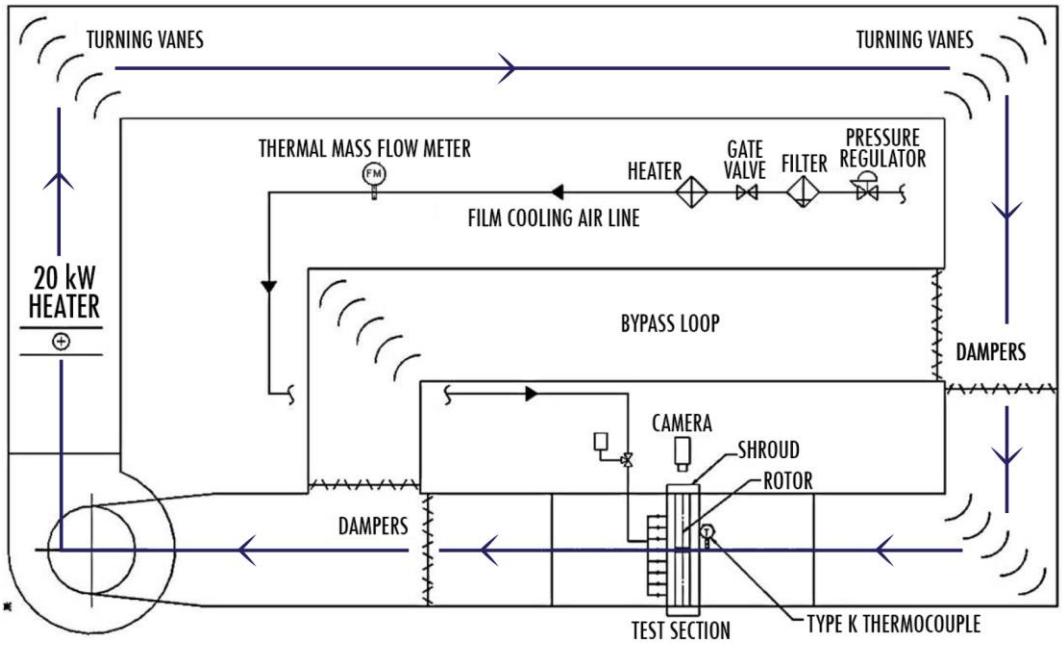

Figure 11 - Wind Tunnel in Test Mode

The four duct dampers used to control and divert the flow are opened and closed using 10 VDC switch-activated electronic actuators. Complete actuation takes

approximately 1.5 seconds selected to minimize the transient behaviors in the flow path. These dampers were donated by Airside Equipment, Baton Rouge, LA, and fit a standard duct size of 36” x 36”, thereby requiring a diffuser to be installed that increased the test section duct to the compatible size. The diffuser was located at the end of the straight length of duct and constructed with adequate length to minimize the included angle and reduce the pressure loss, thereby preventing separation due to the adverse pressure gradient caused by reducing the speed of the flow. Duct assembly, details, and installation drawings can be found in the appendix for further construction information.

Dampers were placed in duct pieces that resembled three-way flow valves. The dampers were all wired together such that a single switch would actuate the dampers in either a bypass mode or test mode configuration.

3.2.3 Corner Duct and Turning Vanes

Through a computational fluid dynamics study, it was quickly discovered in the design of the wind tunnel, that radiused turns would cause a majority of the flow to migrate to the outside of the duct, requiring far too much straight duct to redevelop the flow. Thus 90 degree turns were designed with turning vanes to reduce pressure drop and keep the flow as uniform as possible. Detailed drawing views can be seen in Figure 12. Turning vanes were found off-the-shelf with a cut-to-length rail and two dimensional vane profile. This reduced cost and made for an easier installation. The vanes and rails were assembled together and placed into the corner duct secction, then the rails were screwed into the duct wall to secure the assembly.

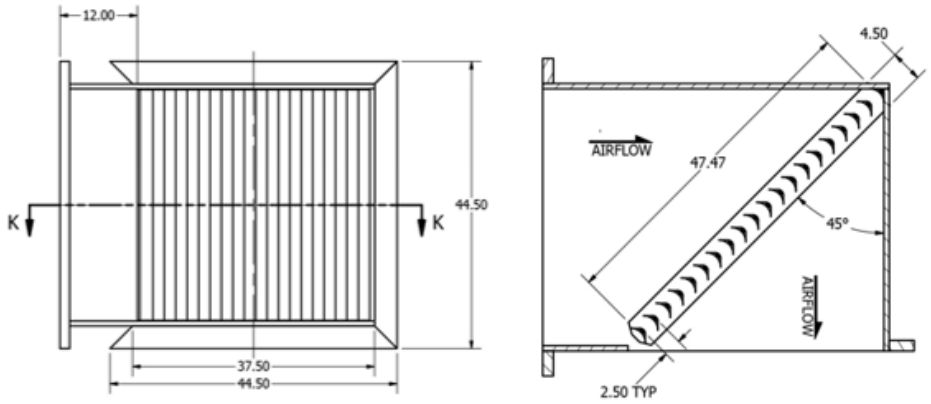

Figure 12 - Drawing Views of the Corner Duct Section

All of the wooden pieces of duct were fabricated in house by TIER Center students, and all of the sheetmetal portions were sub-contracted out to sheet metal shops around Baton Rouge, LA. Spiral Metals fabricated the transition shapes and curved radius duct for the test section seen in the installation and details drawing in the appendix. The sheet metal material chosen for the duct length was 16 Ga galvanized 1040 Steel and ¼" steel plate was cut as necessary to construct the flanges. These thicknesses were optimal for fabrication providing sufficient rigidity with common material in an easily obtainable mill run to reduce costs. The ¼" plate was laser cut to a tolerance of 0.010" to ensure bolt pattern consistency to allow for proper bolt allignment between adjoining sections of duct during installation.

3.2.4 Mainstream Air Heater Selection

A 20 kW duct heater was selected to heat the air in bypass mode prior to the test. In order to size the heater, a thermal resistance model was created to calculate the heat lost to the environment from the mainstream air. The log-mean temperature calculation for heat loss through a duct was used [33]. At the design conditions, a flow rate of 10,380 CFM was assumed with a total length of duct conservatively estimated to be 85'. An average velocity of 26.8 ft/s in the duct was selected, given the duct

dimensions. In order to simplify the calculations, only wood duct was assumed to be used for the entire system; although, a large portion of the duct was constructed from sheet metal. The negative effects of this assumption were mitigated by wrapping the sheet metal sections with an insulation blanket to avoid costly heat transfer to the outside environment. The thermal resistance of the insulation blanket far exceeded that of the wood duct, so it was deemed conservative to proceed with a total wood duct analytical model. A natural convection boundary condition was applied to the outside of the duct and a typical value for the heat transfer coefficient for stagnant air was assumed (h_o) and the convective heat transfer coefficient for the internal duct velocity was calculated using equations 15 and 16 and the results can be found in Figure 13.

$$\frac{T_\infty - T_{m,o}}{T_\infty - T_{m,i}} = \exp\left(-\frac{1}{\dot{m} C_p R_{tot}}\right) \quad \text{[Eq.14]}$$

$$Nu_D = \frac{\frac{f}{8}(Re_D - 1000)Pr}{1 + 12.7\left(\frac{f}{8}\right)^{\frac{1}{2}}(Pr^{\frac{2}{3}} - 1)} \quad \text{[Eq.15]}$$

$$Nu_D = \frac{hD}{K_f} \quad \text{[Eq.16]}$$

$$R_{wall,i} = \frac{1}{h_i A_{surf,i}} \qquad R_{wall,o} = \frac{1}{h_o A_{surf,o}} \qquad R_{wood} = \frac{t}{K_{wood} A_{surf}}$$

K_{wood} = 0.15 W/m-K

h_o= 15 W/m^2-K

h_i= 21.23 W/m^2-K

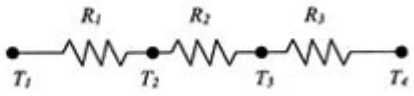

[Eq. 17, 18, 19]

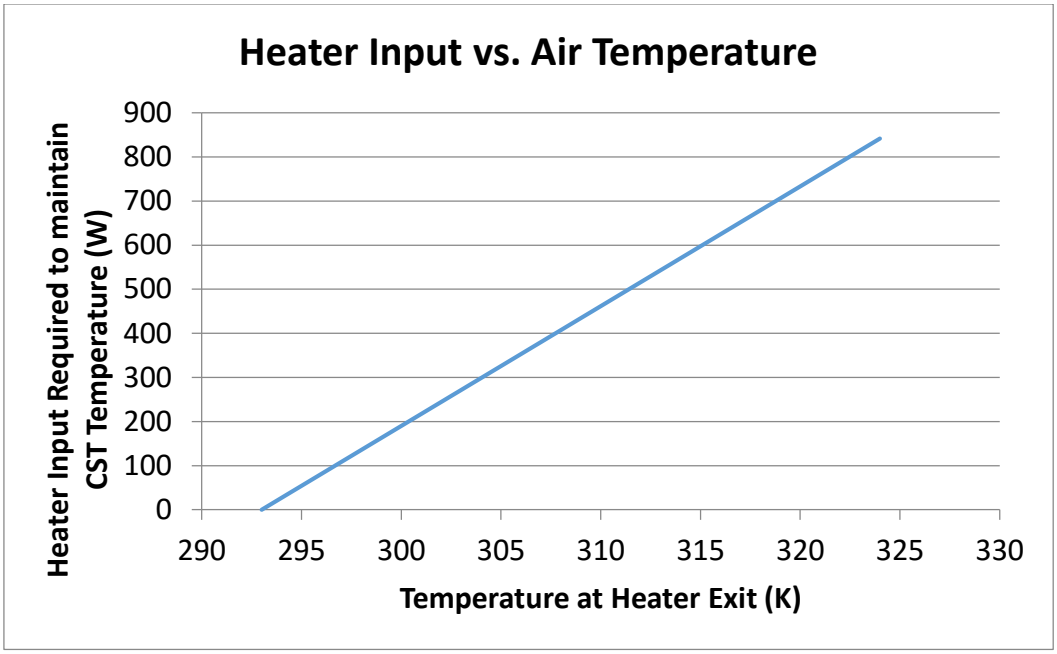

Figure 13 - Temperature Rise from Heater Input Based on Ambient of 293K

To provide the desired condition of heated air at 25ºC higher than the ambient air, modeling revealed that the tunnel would lose approximately 850 W. Considering the closed loop, a heater greater than 1kW would heat the air to the desired temperature based upon model calculations, however, the electrical and heat transfer efficiency must be taken into consideration. In addition, the wind tunnel will never truly be air tight and thus, ambient air will become entrained in the flow. When considering the wind tunnel in test mode, although the tests only run for approximately 30 seconds, it was deemed necessary to provide additional heating capacity to account for heat that would be lost through the uninsulated test section and to the blades in a higher velocity, more turbulent region of the tunnel. Again, utilizing off-the-shelf components to minimize cost, it was decided that a 20kW heater which was similar in price to a smaller HVAC duct heater would provide more than enough power to heat the air to the desired temperature. Another advantage of increased heating power was a reduction in time required to reach test conditions, allowing tests to be run more frequently and efficiently.

This heater was fitted with a remote bulb thermostat to control the air temperature and to shut off the heater after reaching the desired temperature. In addition to the internal over-temperature switch, the heater was coupled to the fan VFD so that it could not be operated unless the fan was running due to safety concerns of overheating the elements which could result in a fire.

3.2.5 Duct Pressure Loss Calculations and Fan Selection

Given that the duct design provided a sufficiently closed system, the selection of the fan could begin. Using the Moody Diagram for a given roughness of wood duct, with the Reynolds number of the flow based on the hydraulic diameter of the duct, pressure loss calculations were performed to size the fan accordingly. The modified Bernoulli's equation was used to find the head loss throughout the duct circuit and the results are found in Tables 3 and 4. The head loss can be described by the following equations:

$$\Delta P = \rho K \frac{V^2}{2} \quad \text{[Eq. 20]} \qquad\qquad \Delta P = \rho f \frac{L}{D} \frac{V^2}{2} \quad \text{[Eq. 21]}$$

where ρ is the fluid density, K is the pressure loss coefficient, f is the friction factor, L is the length of duct, and V is the fluid velocity. A system curve was created using this pressure loss analysis, seen in Figure 14, while the fan curve can be seen in Figure 15.

Table 3 - Pressure Loss Analysis Constants

Constants			
Duct Velocity	V_d	7	m/s
Test Section Velocity	V_d	24	m/s
Density	ρ	1.2	kg/m^3
Viscocity	μ	1.98E-05	kg/m-s
Friction Factor	*f*	0.016	
Mass Flow Rate	ṁ	5	kg/s

Table 4 - Pressure Loss Analysis Results

Head Losses	Velocity (m/s)	Equivalent Length (m)	Loss Coefficient	Pressure Loss (Pa)
Turning Vanes (3X)	7		0.16	14
Turns (45º Elbow) (2X)	7	16.0		15
Straight Duct	7	18.9		12
Test Section Annulus	24	1.22		46
Test Sect Inlet (Sharp Cont)	24		0.35	121
Test Sect exit (Sharp Expan)	24		0.45	156
Total				**364**

At the design conditions, the fan needs to develop 2 inWg at a mass flow rate of 5 kg/s. There was a large level of uncertainty in modeling the pressure drop across a rotating airfoil cascade that would be powered by an electric motor. The turbine would not be extracting energy from the air as it would under normal circumstances, so the losses would be due to momentum reduction in the airstream. No adequate model for these conditions existed, so a large margin for error was required. Also, a variable frequency drive was selected to operate the fan at any given speed over a defined range to dial in the flow rate and achieve the various experimental conditions. Furthermore, it was required to provide the capability of producing additional fan pressure and flow for other future uses of the wind tunnel and to allow for changes in support of production and installation which may inhibit the flow. As a result, a fan selection point was finalized at 20,000 CFM and 5 inWg nearly double that of the high pressure turbine rotor blade tip and shroud testing design point, but optimal for the potentially greater requirements of future testing and price. Finally, VFD fan control allows for operation of the forward airfoil blade fan scroll at reduced speeds to selectively dial in the airflow, moving the fan curve down the pressure axis to avoid

motor overheating and runaway that typically occurs in forward curved blade centrifugal fans. A photograph of the fan assembly can be seen in Figure 16.

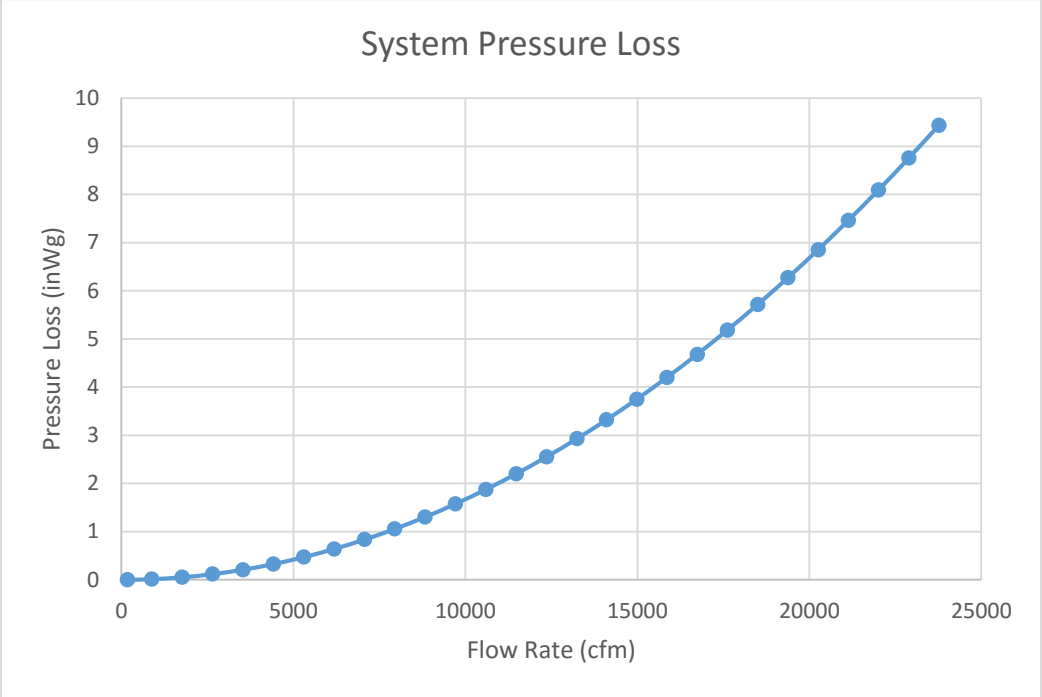

Figure 14 - Wind Tunnel System Curve

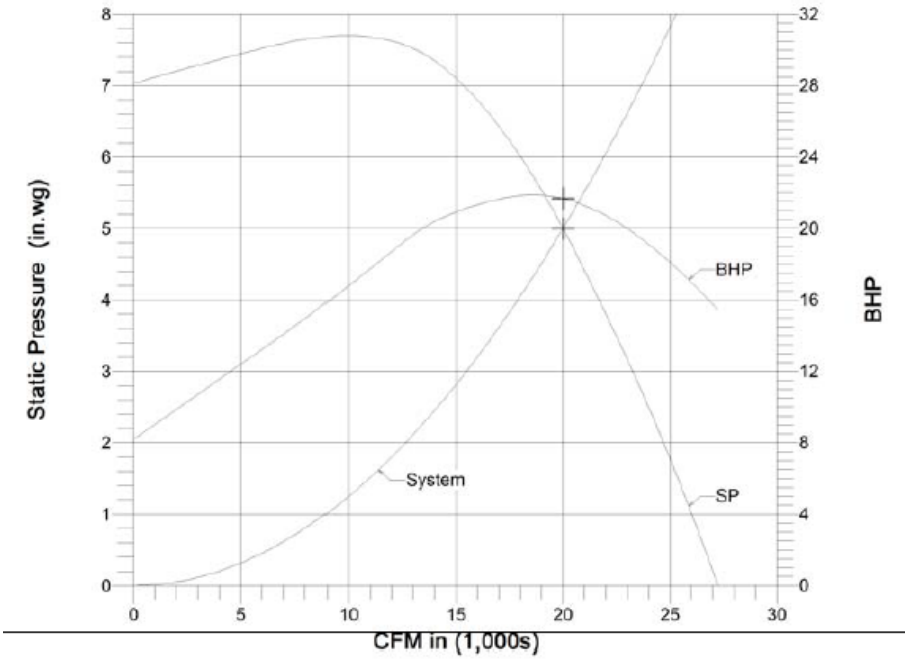

Figure 15 - Fan Performance Curve (Twin City Fan, Minneapolis, MN)

Figure 16 - Blower Installed

Given the space constraints in the Lab, vibration damping nitrile rubber pads were installed at each point where the fan contacts the concrete floor, match drilling the fan support base to install concrete anchors into the building foundation.

Two flexible bellows (See Figure 17) were also added to isolate the fan from the test section, to allow for any thermal expansion, and to allow for misalignment. One bellow is at the fan inlet, and the other is just downstream of the test section.

Figure 17 - Bellows Downstream of Test Section (left), Upstream of Fan (right)

3.3 Test Section Design

3.3.1 General Arrangement

A rotating test section has been designed and fabricated to obtain heat transfer coefficients and film cooling effectiveness contours on the shroud and tip of the rotor blades. All 64 turbine blades have a cut back squealer tip with tip and pressure side film cooling holes. The shroud is also film cooled with 1696 discreet film cooling holes and by a leading edge gap placed upstream of the leading edge of the rotor blade. Pressurized coolant air must be supplied to the rotating blades, thus coolant air is fed through a rotary union, which supplies the air to a hollow shaft. The shaft delivers this pressurized air to the hub assembly through four 3/8 inch diameter orifices, which connect to the rotor blades by way of 64 coolant holes drilled on the mounting plate that wraps around the outside edge of the hollow mounting disk of the hub and blade assembly. The mounting disk directly feeds the air to the rotor blades through an orifice in the base of each blade.

Power is delivered from the other end of the shaft by a rotor control motor. The motor shaft and rotor shaft are connected by a coupling, securing attachment. The rotor shaft is aligned by two flange-mounted ball bearings placed at the opposite sides of the hub and blade assembly. The bearings are connected to circular bearing supports, which not only align the bearing at the center of the annular section, but also add structural rigidity to the 16 gauge rolled sheet metal inner annular housing. In addition, there is a circular motor support that provides similar reinforcement. An exploded view of the assembly can be seen in the Figure 18.

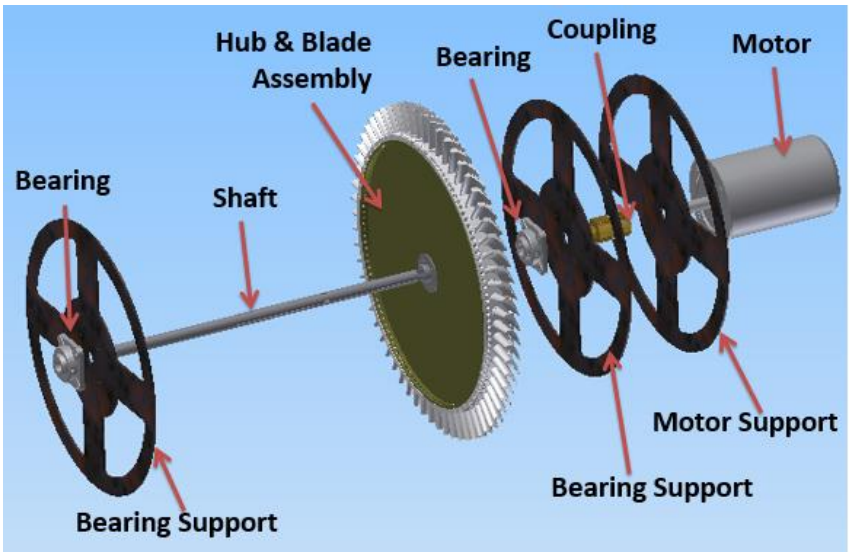

Figure 18 - Drive Train Exploded View

The test specification included the mainstream flow conditions, blade and vane geometry, and cooling flow parameters. With the test specifications in place, detailed design of the parts and assemblies could begin. The system was analyzed from the top down with ease of manufacturing being a priority given the low budget nature of the project. To begin, the shaft and motor would have to be sized to accommodate the supplied cooling air flow and the developed loading conditions. The drive train can be seen in the quarter section view of the test section, with the outer annulus hidden for clarity, in Figure 19.

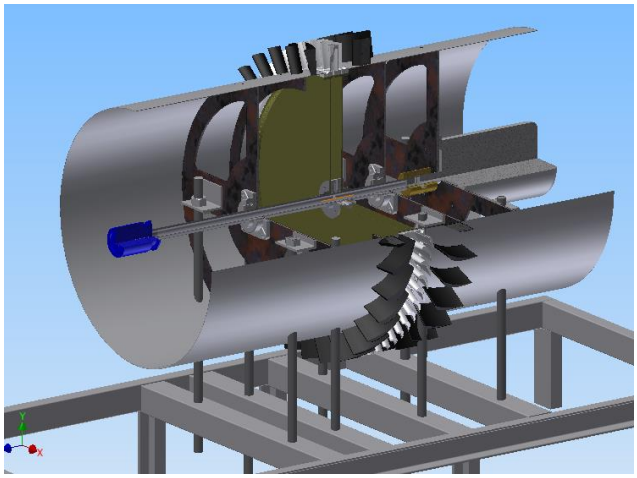
Figure 19 - Quarter Section View of the Test Section Drive Train

3.3.2 Motor Selection

In order to cut cost, a fuel pump motor previously used for other experiments was repurposed as the rotor power supply and control motor. This motor used for blade rotation is a Baldor (Fort Smith, AZ) 3 phase, 3 horsepower 230 VAC electric motor with maximum rated speed of 3400 RPM. It is controlled using a Baldor VFD purchased from Houston Armature Works in Baton Rouge, LA. The motor can be seen in Figure 20. In pumping configuration, the motor would be mounted vertically with tapped face holes to directly mate with the fuel pump. For shaft rotation required in this application, it is held in a horizontal configuration; therefore, a custom mount and support that matched the four motor face holes was fabricated from ¼" steel plate cut on a CNC waterjet table at Louisiana Cutting.

Figure 20 - Rotor Drive Electric Motor

3.3.3 Shaft Design

The drive shaft was designed to carry out two main functions for the hub assembly, delivering rotation and coolant air. Power is transmitted to the shaft from the

motor. This power is distributed to the hub assembly in the form of torque, which supplies rotation to the hub. From the opposite end of the shaft, coolant air is pumped into the shaft's hollow inner diameter, through which the air is transported to the hub to provide blade cooling. With space and flow constraints, direct drive was decided as the most effective method of power delivery to the shaft. A detailed section view can be found in Figure 21, labeling the key components.

The shaft was designed as a hollow tube with orifices on the outer surface near the middle of the shaft at the hub. This set-up allowed for the strength required as well as adequate hydraulic area to supply the coolant flow from the on-site compressor. The shaft design had a 1.25 inch outer diameter, a 0.87 inch inner diameter, and a length of 3 feet. Four equally spaced 3/8 inch diameter orifices are located where the hub assembly and shaft attach and are detailed in Figure 22. These orifices supply the coolant air to the hub. The hub connects to the shaft near the center of the shaft length by use of a square key. On either side of the hub, bearings with supports are located 6 inches away from the assembly in order to support the shaft assembly weight and withstand dynamic loading. One end of the shaft will connect to the rotary union, which will supply the coolant air from a stationary point to the rotating shaft, while the other end connects directly to the motor via a shaft coupling.

The maximum sustained pressure achieved by the compressors used to supply coolant air for this project is 150 psi. Adding a factor of safety and choosing from conventional dimensions for fitting the shaft with a rotary union, two options were chosen: a 0.25 or 0.5 inch diameter shaft through hole to match the available rotary union through hole.

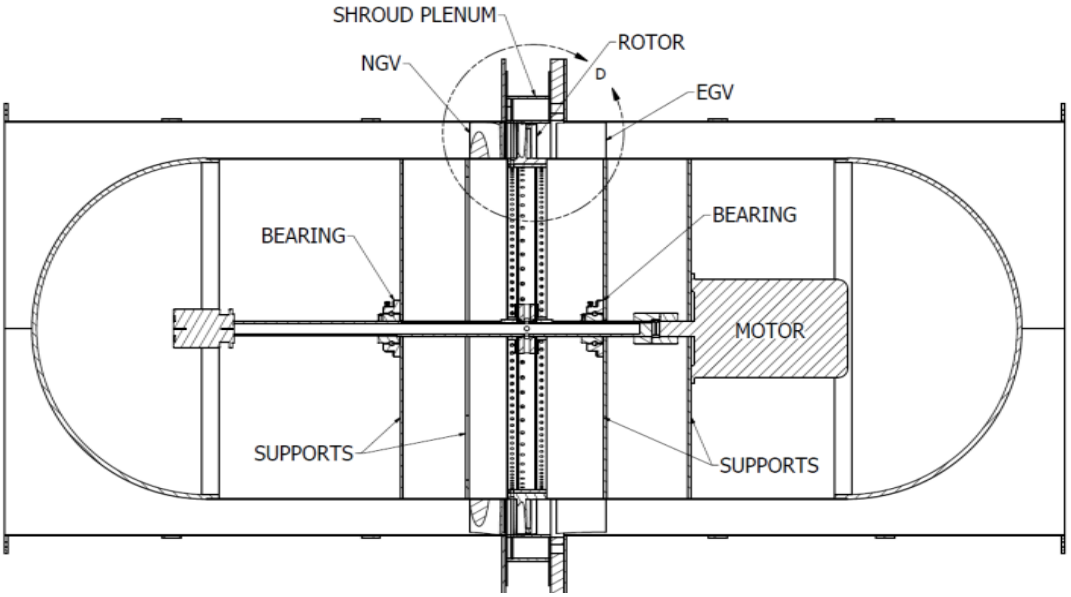

Figure 21 - Section View of the Test Section

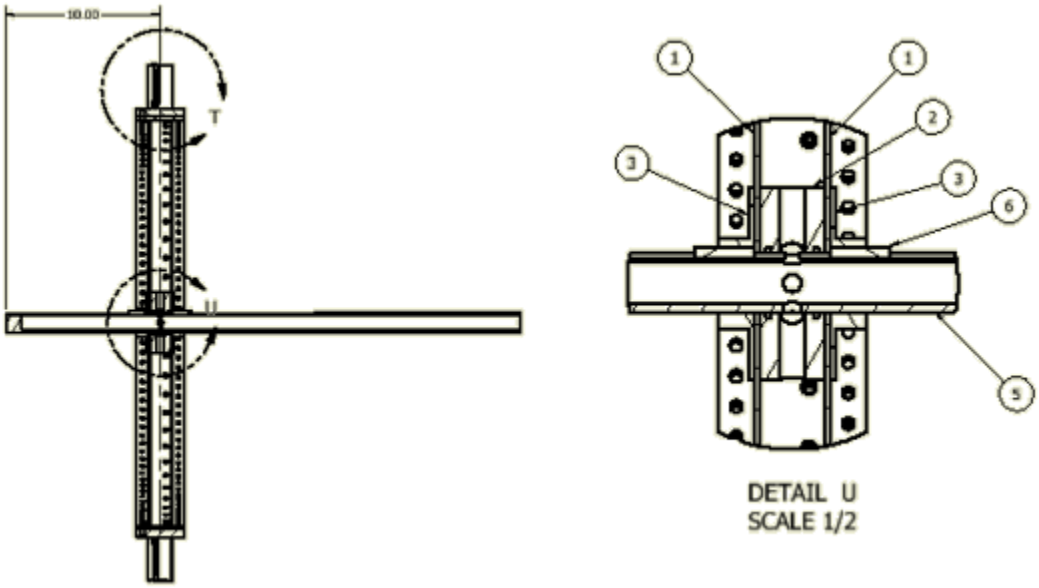

Figure 22 - Section View of Shaft-Rotor Assembly

A compressible flow analysis was performed to optimize the dimensions of the shaft's bored through-hole used to supply coolant air to the hub and blades. For the worst case scenario, flow would be choked in the shaft. Equation 22 describes the mass flow rate given a particular compressor pressure and pipe diameter assuming the flow is isentropic.

$$m_{flow} = 0.04 \frac{A^* p_o}{\sqrt{T_o}} \qquad \text{[Eq.22]}$$

A^* is assumed to be the area of the bored hole in the shaft, p_o is the compressor pressure, and T_o is the temperature of the incoming air. The units used are m^2, Pa, and K respectively. Figure 23 shows the comparative evaluation of a 0.25 in and 0.5 inch inner shaft diameter for mass flow rate versus variable compressor pressure for a maximum compressor performance point of 1377 SCFM at 157 psi. The specified design flow rate is 0.0423 kg/s (0.0933 lb/s); therefore, a shaft inner diameter of 0.25 inches would require a pressure at or slightly exceeding the 157 psi maximum rating for the selected test compressor, which would not allow for doubling the mass flow rate. As a result, testing various blowing ratios higher than the specified design condition would not be possible. From this information, the 0.5 inch inner diameter was chosen because blowing ratios as high as 5 can be achieved before reaching the maximum compressor pressure.

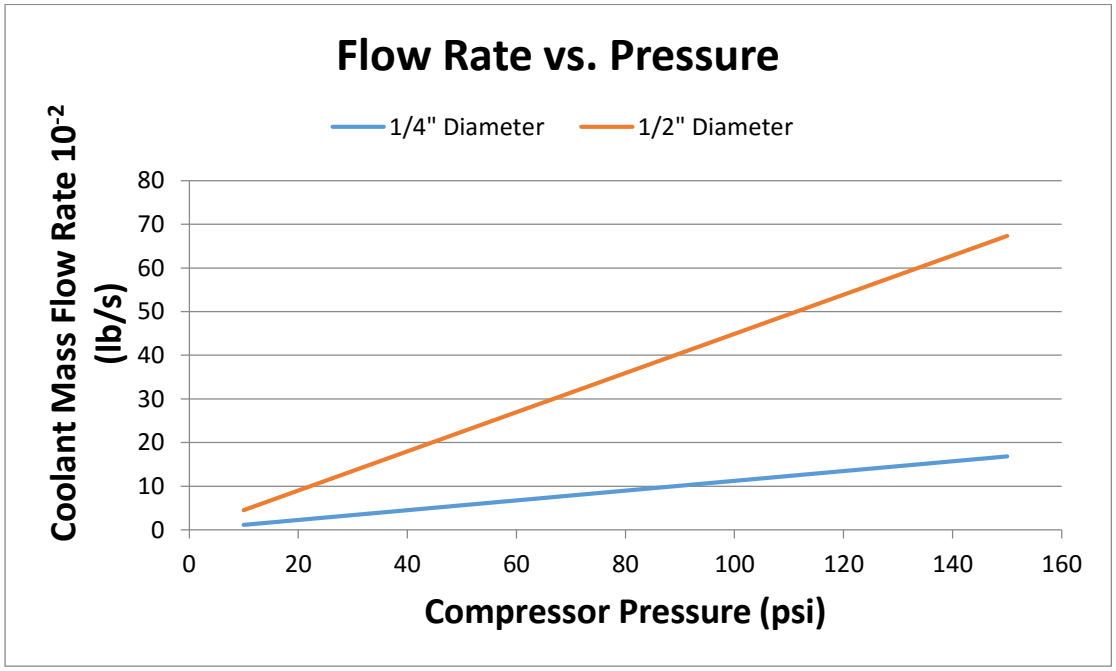

Figure 23 - Coolant Mass Flow Rate vs Compressor Pressure

Before finalizing the inner diameter, the dimension had to be assessed to ensure that the maximum test pressure would not exceed the maximum compressor pressure. As Figure 24 shows for the specified design flow of 0.0423 kg/s with a shaft inner diameter of 0.5 in, a corresponding pressure of approximately 20 psi develops, which is significantly under the compressor capacity, thereby allowing for viscous pressure loss through the supply coolant lines given a need for dryers, pressure regulators, heaters, and a gate valve. The viscous flow analysis can be found in the coolant line design section where it is shown that there is adequate pressure and flow delivered to the shaft for film cooling under the specified design coolant flow conditions and at double the specified flow conditions.

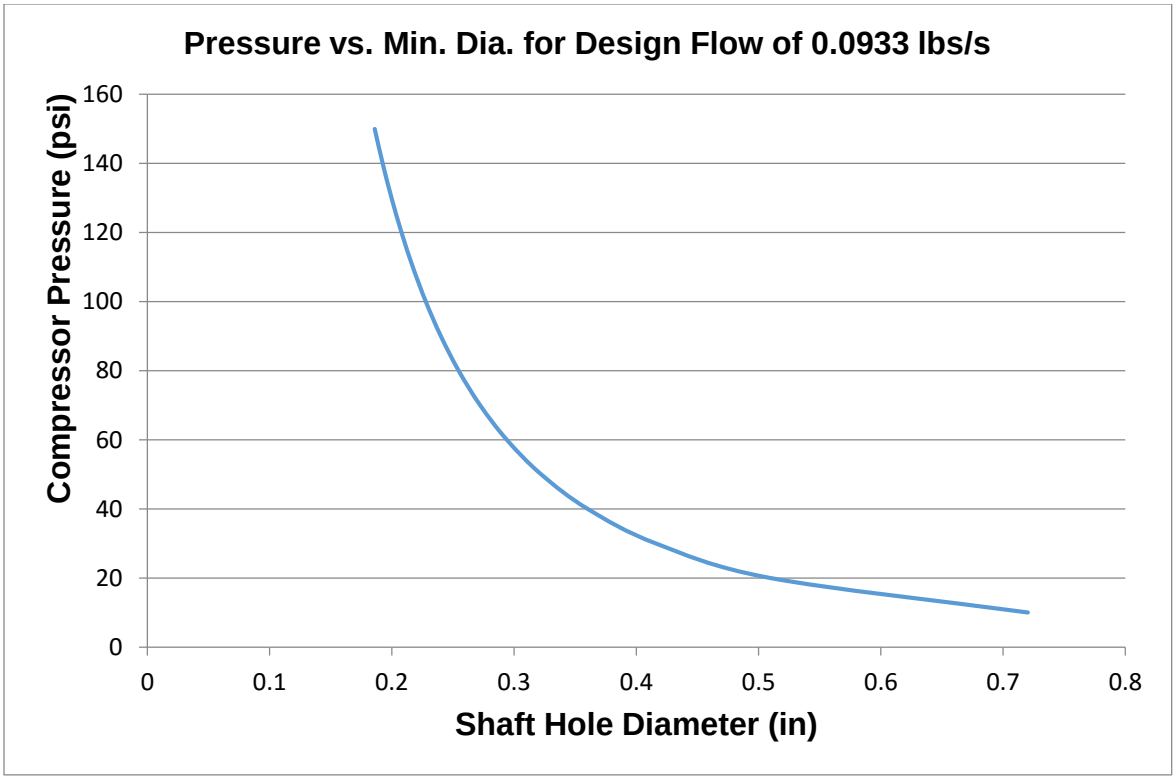

Figure 24 - Compressor Pressure vs. Shaft Inner Diameter

With dimensions set, a shaft static-structural analysis was performed with results shown in Table 5. Representing the shaft as a hollow tube with the previously set shaft

dimensions, the bearings were assumed to be pin supported holding the shaft up with the weight of the hub and blades bearing down on the shaft. The analysis only encompassed the section between the bearings, which is a length of 1 foot. With these assumptions, the maximum shaft deflection, moment, and shear can be seen in diagrams in Figure 25.

Table 5 - Static-Structural Analysis Results

Max Deflection	Max Moment	Max Shear
0.0021 in	300 lb-in	50 lbs

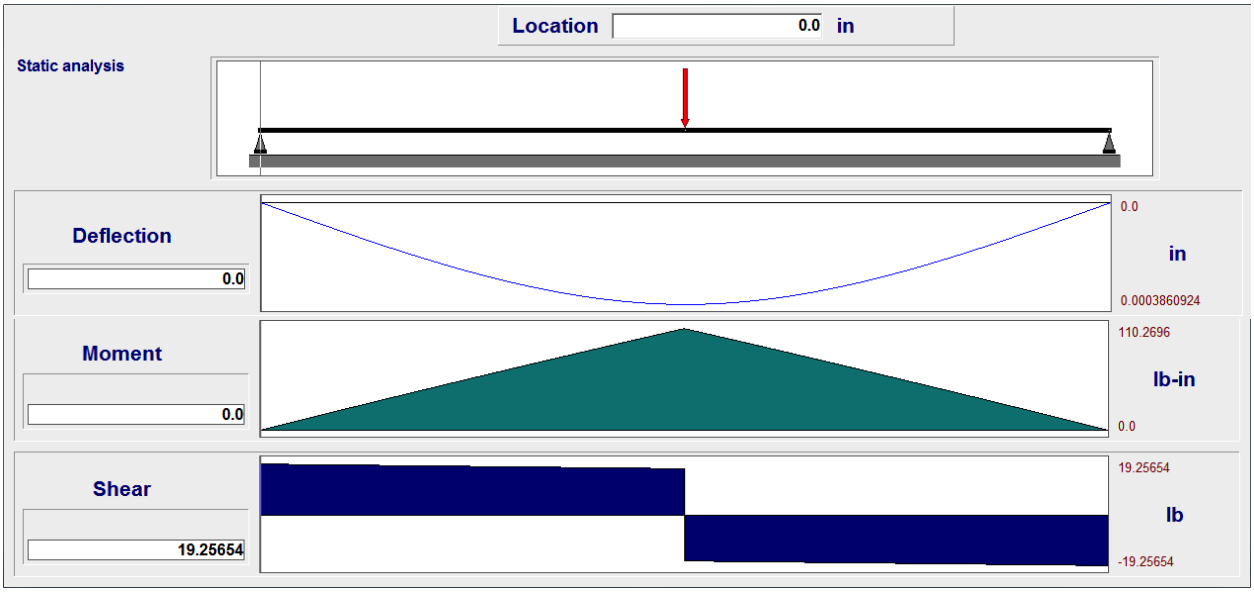

Figure 25 - Shaft Static-Structural Analysis (Beam 2-D Orand Systems)

From the structural analysis, critical locations and bending moment were defined to be utilized in calculations of maximum shaft stresses. The bending, torsion, and axial stresses are represented in both midrange and alternating components. The axial load was assumed to be minimal and was neglected. Stresses due to bending (σ) and torsion (τ) are generally calculated by Equations 23 24, 25, and 26, where M_a and M_m represent alternating and midrange moment, T_a and T_m represent alternating and

midrange torsion, K_f and K_{fs} are the fatigue stress concentration factors for bending and torsion respectively, I is the moment of inertia about the neutral axis, and c is the distance from the neutral axis to the outer edge of the shaft.

$$\sigma_a = K_f \frac{M_a c}{I} \qquad \text{[Eq. 23]} \qquad\qquad \sigma_m = K_f \frac{M_m c}{I} \qquad \text{[Eq. 24]}$$

$$\tau_a = K_{fs} \frac{T_a c}{J} \qquad \text{[Eq. 25]} \qquad\qquad \tau_m = K_{fs} \frac{T_m c}{J} \qquad \text{[Eq. 26]}$$

Assuming a shaft shape of a round bar or tube with a transverse round hole, the stress concentration factors were determined and bending and shear stress equations are reduced to Equations 27 and 28.

$$\sigma_a = \frac{M}{Z_{net}} \qquad \text{[Eq. 27]} \qquad\qquad \tau_a = \frac{TD}{2J_{net}} \qquad \text{[Eq. 28]}$$

Where Z_{net} is defined by Equation 29 and J_{net} is defined by Equation 30.

$$Z_{net} = \frac{\pi A}{32D}(D^4 - d^4) \qquad \text{[Eq. 29]} \qquad\qquad J_{net} = \frac{\pi A}{32}(D^4 - d^4) \qquad \text{[Eq. 30]}$$

A in Equations 21 and 22 are values listed in Table A-16 of *Shigley's Mechanical Engineering Design* [42]; D is the outside diameter of the tube (test section shaft); and d is the inside diameter of the tube (test section shaft). The shaft is assumed to have constant bending and torsion, the bending stress is completely reversed, and the torsion is steady. For these reasons, the midrange moment due to bending and the alternating moment due to torsion can be presumed to be zero.

Another value of importance was the fatigue factor of safety. A conservative approach to finding this value was using DE-Goodman Theory, which can be reduced to Equation 31 with the previously stated assumptions where n is the fatigue factor of safety, S_e is the endurance limit, and S_{ut} is the ultimate tensile strength.

$$\frac{1}{n}=\frac{16}{\pi D^3}\left\{\frac{1}{S_e}\left[4\left(K_f M_a\right)^2\right]^{1/2}+\frac{1}{S_{ut}}\left[3\left(K_{fs}T_m\right)^2\right]^{1/2}\right\} \qquad \text{[Eq. 31]}$$

Finally, to check for yielding, von Mises maximum stress is compared to the yield strength shown in Equation 32 where n_y is the yield strength factor of safety and S_y is the yield strength.

$$n_y=\frac{S_y}{\sigma'_{max}} \qquad \text{[Eq. 32]}$$

Here, the von Mises maximum stress is defined by Equation 33.

$$\sigma'_{max}=\left[\left(\sigma_m+\sigma_a\right)^2+3\left(\tau_m+\tau_a\right)^2\right]^{1/2} \qquad \text{[Eq. 33]}$$

Results of the stated calculations based on the yield stress of the Chrome-Moly (AISI 4130) for the specified shaft selection are shown in Table 6.

Table 6 - Mechanical Analysis Results

Fatigue Factor of Safety	Yield Factor of Safety
4.3	9.8

The shaft will encompass a square key, and since the outer diameter is 1.25 inches and the keyway was precut to a width of 0.25”, calculations were made on the key length, and it was determined that a length of 0.424 in (10.78 mm) is needed to resist crushing. This value was found using Equation 34 where F is the crushing force, t is the key thickness, and l is the key length.

$$\frac{S_y}{n}=\frac{F}{tl/2} \qquad \text{[Eq. 34]}$$

With shaft deflection calculated, the critical rotational speed (ω) for the shaft was then obtained. Critical speed was calculated to determine the point at which the shaft would

become unstable and deflections would increase without bound. Once the maximum deflection is calculated, the critical speed equation can be simplified to Equation 35, where y_{max} is the maximum deflection. Using this equation, the critical speed was calculated to be 424.3 rad/sec or 4052 RPM, which is well above the design speed of 1667 RPM.

$$\omega = \sqrt{\frac{g}{|y_{max}|}} \qquad \text{[Eq. 35]}$$

By setting the minimum shaft diameter, a ½ inch through-hole needed to be bored through the 1 ¾" outer diameter shaft along with four 3/8" diameter orifice holes at the hub connection to supply pressurized coolant air to the blades. The shaft, detailed in Figure 26, incorporated a unique design which involved threading a ½ inch NPT thread on the through-hole to mate to the rotary union. Meeting all analytical stress design requirements, AISI 4130 steel was the material selected for the shaft. In order to avoid the high cost of having the shaft custom manufactured, a tubular shaft with an outer diameter of 1 ¼ inches was purchased from Go-Kart Galaxy (Murchison, Texas). This tubular shaft came with a ¼ inch keyway already milled down the length of the shaft. This tubular shaft has a 0.19 inch wall thickness making the inner diameter 0.87 inch. In order for the rotary union, which has a ½ inch NPT male connection to mate with the purchased shaft, additional material was turned down to the 0.89 inch inner diameter and press fit inside at the end. This added material was tapped with ½ inch NPT threads to accept the male rotary union. On the opposite end of the shaft, a 0.89 inch brass plug was press fit into the shaft and was soldered into place to provide an airtight seal. The purchased shaft was 40 inches in length and subsequently cut down to

33 inches. The four 3/8 inch diameter orifice holes were drilled 10 inches from the drive side of the shaft where the hub mates to the shaft via a flange connector and ¼ inch keyway.

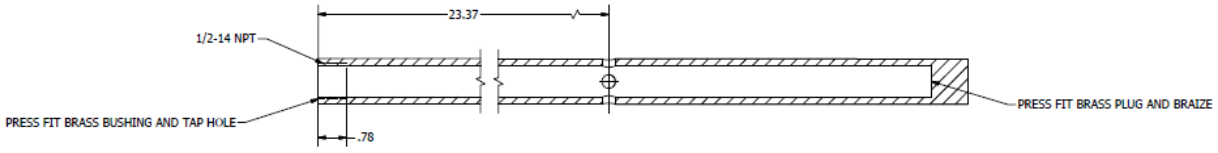

Figure 26 - Section View of Shaft

3.3.4 Bearing Selection

The shaft was designed with two bearings, one located on either side of the hub at a distance of 6 inches away from the hub assembly. Self-aligning ball bearings were selected for usage and are shown in Figure 27. Self-aligning ball bearings are characterized by the presence of two rows of balls and a common concave sphered raceway in the outer ring. This configuration makes the bearing insensitive to angular misalignments of the shaft relative to the housing, so shaft deflections or misalignment will not affect the bearings. Another positive factor of self-aligned bearings is a low friction coefficient compared to other rolling bearings. With a low friction factor, bearings are capable of running cooler at high speeds (SKF; Gothenburg, Sweden). Sealed bearings were selected for the test section design. Contact seals, made of oil and wear resistant acrylonitrile-butadiene rubber, protect each side of the balls. These types of bearings have an operating temperature range of -40^{o}C to 100^{o}C, which is sufficient for the test section.

Flanged mounted bearings were chosen for the test section and this mount made it possible to directly attach the bearings to the support disks. The housing material for the FYH bearing is Nickel-Plated cast iron, which offers corrosion resistance.

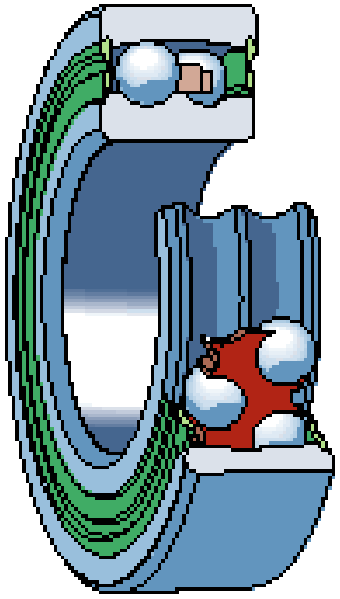

Figure 27 - Sealed Self-Aligning Ball Bearing (SKF; Gothenburg, Sweden)

The bearings are rated for a maximum shaft speed of 3700 RPM and a maximum load of 5770 lbs, which far exceeds the test design speed and load.

3.3.5 Hub Design

The hub assembly is the most critical component of the system. It provides a support structure for the rotor blades and allows for the passage of air from the shaft to each blade. A 3D rendered exploded view of the hub assembly is shown in Figure 28. It is made up of four components: hub flange (Figure 29), center spacer (Figure 29), two disks (Figure 30), and the mounting plate (Figure 30). The hub assembly was fabricated by Plant Machine Works in Baton Rouge, LA, one of the only machine shops in the area with a lathe large enough to accommodate a machined piece over two feet in diameter. 6061-T6 Aluminum was selected as the material for the hub. This material is known for its high strength, good workability, and high resistance to corrosion (asm.matweb.com). The T6 aluminum has better machinability than other 6061 aluminums due to its heat treatment. Another important parameter to consider is fatigue resistance. The hub will

experience varying shear stresses, which could cause fatigue over time. 6061-T6 Aluminum provides high hardness, fatigue strength, and shear strength making it an excellent choice for a hub that might experience wear and fatigue from the attached blades [36].

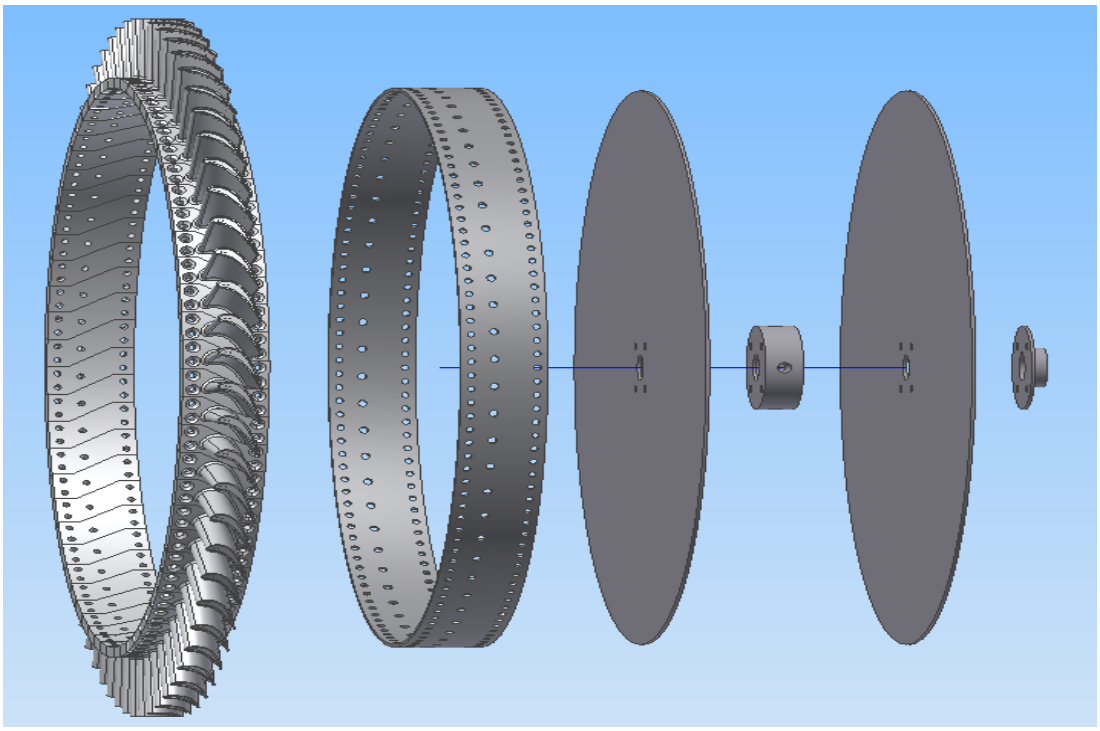

Figure 28 - Exploded View of Hub Assembly

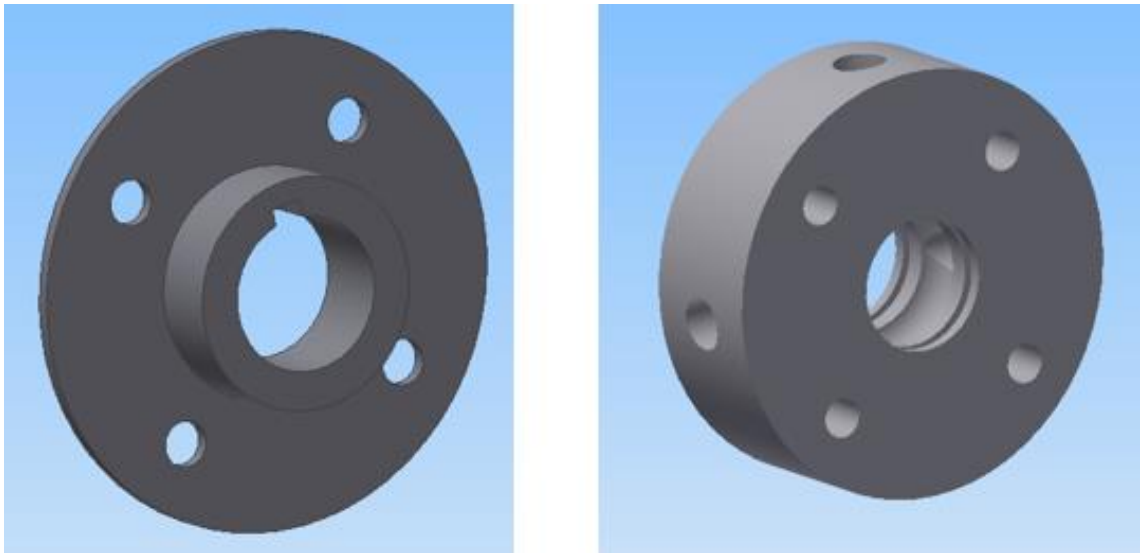

Figure 29 - Hub Flange (left) Hub Spacer (right)

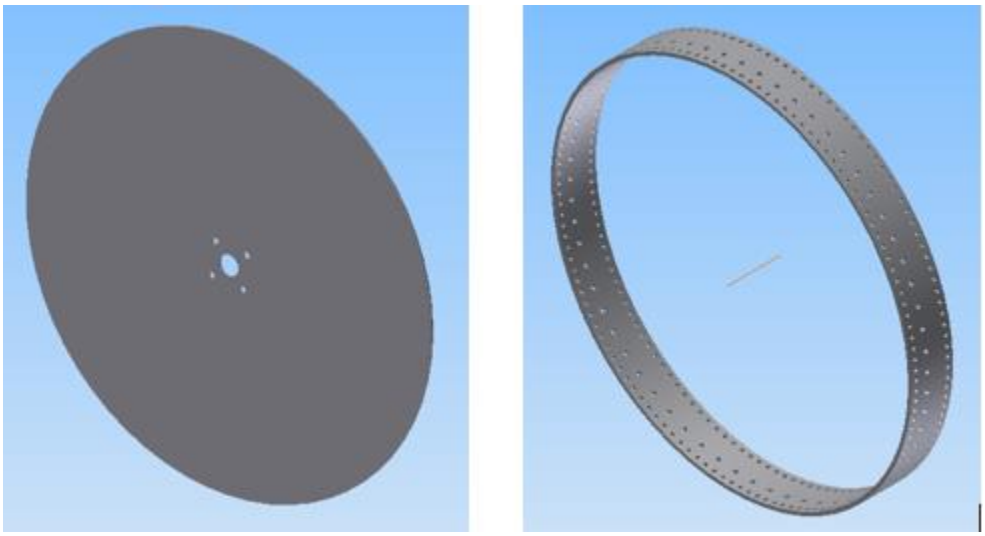

Figure 30 - Disk (left) Mounting Plate (right)

The hub flange was purchased from Go Kart Galaxy (Malakoff, TX). It is used to couple the shaft to the hub assembly. It is made for a 1 ¼ inch shaft with a square ¼ inch keyway. The hub flanges are located on either side of the hub disks seen in Figure 31.

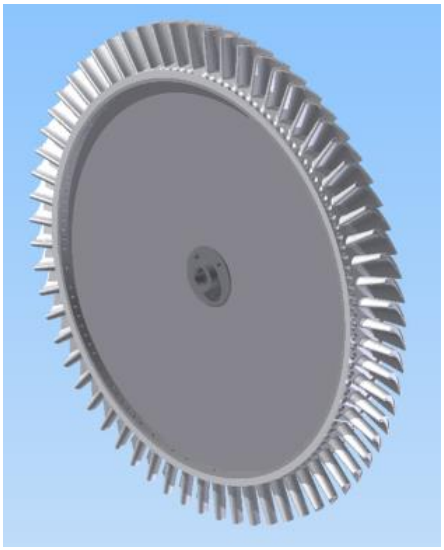

Figure 31 - Rotor-Hub Assembly

The flange has four bolt holes for attachment to the hub assembly. The center spacer is used to provide support between the two hub disks. It has four ½ inch equally spaced radial holes which align the four shaft orifices to allow air to flow from the shaft

to the plenum between the two disks. Two O-ring grooves were cut on either side of these holes to prevent air leakage. A lathe was used to form the circular block prior to drilling out the shaft hole and cutting the O-ring grooves. A drill press was used to cut the air flow holes and the bolt holes.

The two hub disks support the mounting plate and provide a plenum for the coolant air. They were cut from an eighth inch thick sheet of aluminum. Holes were drilled to match the shaft diameter and flange bolt pattern. One eighth inch aluminum sheet was selected due to its high strength-to-weight ratio. However, during fabrication, weld shrinkage and warping occurred at the heat affected zone of the TIG welded joint along the interface of the mounting plate. After collaborating with the manufacturer, it was decided to bolt in tapped gussets annularly around the plenum to strengthen and straighten the aluminum plates. The flange mating surface was face milled to give the required perpendicularity and avoid excessive vibration due to angular misalignment of the hub and rotor.

The main and most labor intensive component of the hub assembly is the mounting plate. The outer diameter (26.874±.004in.) is critical to keep the blades at the right height in relation to the surrounding shroud. After a thorough blade base design described in a following section, the mounting hub diameter was chosen to account for the added blade base material, thus keeping the design diameter true. Along the circumferential length of the plate, 64 equally spaced sets of five holes are required to match 64 blades. In each set, four outside holes, two holes along each outside plate edge, allow for a bolted connection to a blade while the inside hole provides a coolant air supply passage to the blade. A 3/8 inch thick sheet of aluminum was cut to length

and width. Then, it was rolled around and welded to the two hub disks. The entire assembly was then put on a lathe and turned down to the correct diameter. The holes were drilled on a large 5-axis CNC machine.

3.3.6 Rotary Union Selection

The rotary union, which can be seen in Figure 32, allows for a stationary air supply to mate with a rotating hollow shaft. For the rotating airfoil cascade, one supply of coolant air will be attached to the rotary union. Given the shaft and coolant air compressor design criteria, a supplier was found who could meet or exceed these criteria at a reasonable expense with a Deublin, part number 1205-000-003, rotary union. The rotary union is rated for 3000 RPM and 150 psi (1034 kPa), which is higher than the shaft design speed of 1667 RPM and matches the maximum operating pressure of the compressors on site. The rotary union was attached to the shaft via a threaded connection with ½ inch NPT threads, and Teflon tape was utilized to ensure a proper seal.

Figure 32 - Rotary Union (Deublin Waukegan, IL)

3.3.7 Coupling Selection

The selected shaft coupling was a Love-joy (Downers Grove, Illinois) L series jaw coupling with a Nitrile Butadiene rubber spider insert, which offers high vibration damping and allows for 1° of shaft misalignment. One of the coupling hubs fits the

existing 1 1/8 inch pump motor shaft and mates with it via a ¼ inch keyway and set-screw. On the opposing side of the spider insert, the other coupling hub mates with the 1 ¼ inch tubular shaft via a ¼ inch keyway and set-screw. In order to reduce costs, ¼ inch keys were purchased as standard items from McMaster-Carr. The coupling design is shown in Figure 33 ("L Type Standard Jaw Coupling"). This was the optimum coupling choice to dampen vibrations and offer ease of installation.

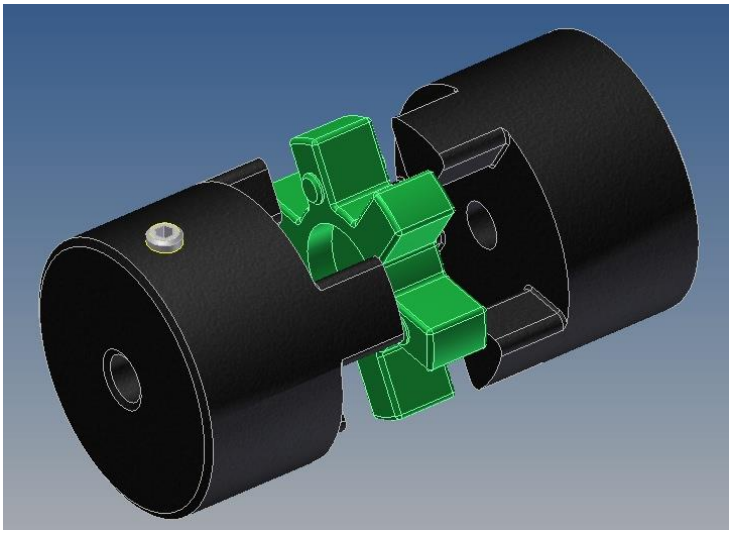

Figure 33 - Coupling Hub (Love-Joy Downers Grove, Illinois)

3.3.8 Rotor Blade Design

The rotor blades' geometry was specified by the project sponsor and delivered to the TIER Center in the form of a 3-D stereolithographic file. These high pressure turbine blades were designed with a full squealer rim blade tip with two discrete tip cooling holes as well as six pressure side cooling holes. The coolant strategy employed was a model of the tip coolant strategy being developed for the HPT of an aircraft engine. A blade material of low thermal conductivity must be used in order to analyze the heat transfer coefficient using a semi-infinite solid condition with convection at the surface. The wind tunnel will operate at a maximum of 30°C above the ambient for the

test. Given the complexities in manufacturing and material constraints, 3-D printing was the process selected for the build; and ABS plastic or equivalent was selected as the 3D printing medium of choice. ABS plastic's maximum working temperature is between 70 and 80°C, and the airfoil cascade will reach a maximum of 55°C. The blade geometry would have to be adjusted to account for strength and mounting provisions. Based upon a structural analysis of the blade and factoring ease of fabrication, it was decided to create a one piece blade with a base that could accept four ¼"-20 countersunk bolts. This base would have to be sized to offer the strength needed to avoid catastrophic blade failure and to keep the deflection under 10% of the tip gap.

The blades used for testing were manufactured using a 3-D printing process called selective laser sintering (SLS). These test blades have been built to the dimensions stated previously in this report, and a mounting base with a coolant air orifice has been added. The blades' axial chord length is 1.59 in with a pitch or blade spacing of 1.65 in, and the blade height or span length is 2.898 in. Given the three-dimensional shape of the blades and a requirement for the blades to have a low thermal conductivity, ABS plastic was the most optimal fabrication material. Options for CNC machining were ruled out due to high cost and the hollow nature of the blades. Typical turbine blades are cast and subsequently machined to a high tolerance. 3-D printing was the only option to create high quality, hollow, tip cooled turbine blades at a reasonable cost. These blades are directly mounted to the rotating hub by four bolts. This hub receives air from the hollow shaft and stores this air in a large plenum. The air is then distributed to the 64 blades via orifices on the hub rim. In order to hold the tight tip gap clearance to the shroud of 1.255mm with a tolerance of 0.1 mm, shims were cut

to match the root surface of the blade using a waterjet table and placed where necessary. Using a dial indicator to measure each blade off the centerline, the variation in blade heights was verified to be no greater than 0.1mm which is comparable to the design tolerances of an actual production turbine.

The blade base was designed using both classical strength calculations and finite element analysis to capture the three dimensional nature of the stress flow. In order to analyze the structural performance of the proposed rotor blade design, a simplified model was created. In this model, the base of the blade was assumed to be a trapezoidal beam of ½ inch thickness and a length of 2 inches. A concentrated load placed at the midspan of the beam was assumed to be the total centripetal force experienced by the mass of the blade at a radius of 354 mm (13.94 inches) rotating at a speed of 1800 RPM. The bending moment, shear force, and deflection were calculated using Beam 2D software (Beam 2D; Orand Systems Ontario, Canada). The maximum moment was found to be 35.35 lb-in, and the maximum shear force was found to be 70.7 lbs. The maximum tensile stress was calculated using Equation 36:

$$\sigma = \frac{Mc}{I} \qquad \text{[Eq. 36]}$$

where σ is the maximum tensile stress, M is the maximum moment, c is the maximum length from the centroid, and I is the moment of inertia. The moment of inertia was calculated to be 0.014 in^4, and the maximum length from the centroid was ¼ inch, resulting in a maximum tensile stress load of 631.7 psi. For an ultimate tensile strength of 4887 psi derived from a tensile test of ABS Plastic, the factor of safety was found to be 7.7. After calculating the shear stress given the shear area of the bolt holes to be 0.4 in^2, a factor of safety for shear failure was found to be 17. The blade deflection was

also analyzed in a similar way. The maximum deflection found by modeling the base as a beam was 0.0017 inches. The blade deflection involved modeling the blade as a beam of the same cross-sectional area as the prescribed blade geometry using Equation 37:

$$\partial = \frac{\mathrm{FL}}{\mathrm{AE}} \qquad \text{[Eq. 37]}$$

where ∂ is the deflection in the span direction, F is the applied force, A is the cross-sectional area of the beam, and E is the modulus of elasticity of the material used. The applied load was equal to the centripetal force experienced by the blade member which is equal to the mass of the blade multiplied by the rotational speed squared and the radius of rotation. The load applied was 37.6 lbs, the modulus of elasticity was assumed to be 236,000 psi, the cross-sectional area of the blade was 0.294 in^2, and the length was assumed to be the span of the blade, 2.9 in. The deflection found in the blade was 0.00157 in, thus making the total deflection of the blade and base 0.00327 in or 0.083 mm. This total deflection was 6.7% of the tip gap clearance of 1.255 mm. The blade design was concluded to be acceptable and the hub was designed to accommodate the calculated total blade deflection.

Given the 3-D nature of the blade and loading case, a concurrent FEA model was run to ensure a robust blade-base design. Using the boundary conditions mentioned in the classical study, the results can be seen below. A final mesh density of 94,109 elements was found to be optimal by increasing the number of elements until the converged solution held steady maximum stress and deflection values. A rotational velocity load of 1800 RPM was applied to the blade. The finite element model,

predicted radial deflection, and Von Mises stresses are shown in Figures 34, 35, and 36 respectively.

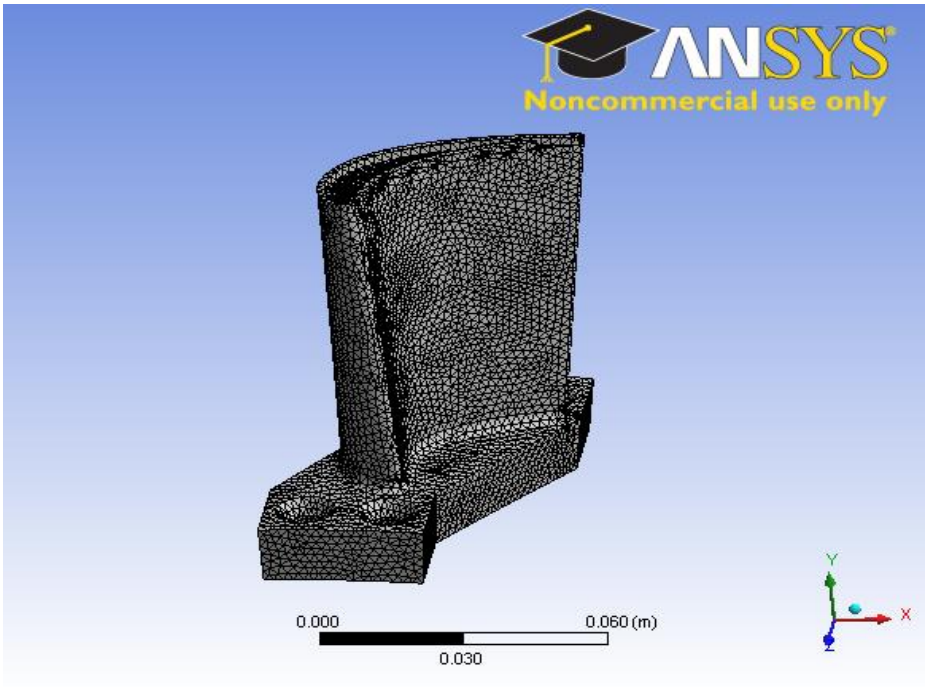

Figure 34 - Finite Element Model (FEM) with Tetrahedral Mesh Shown

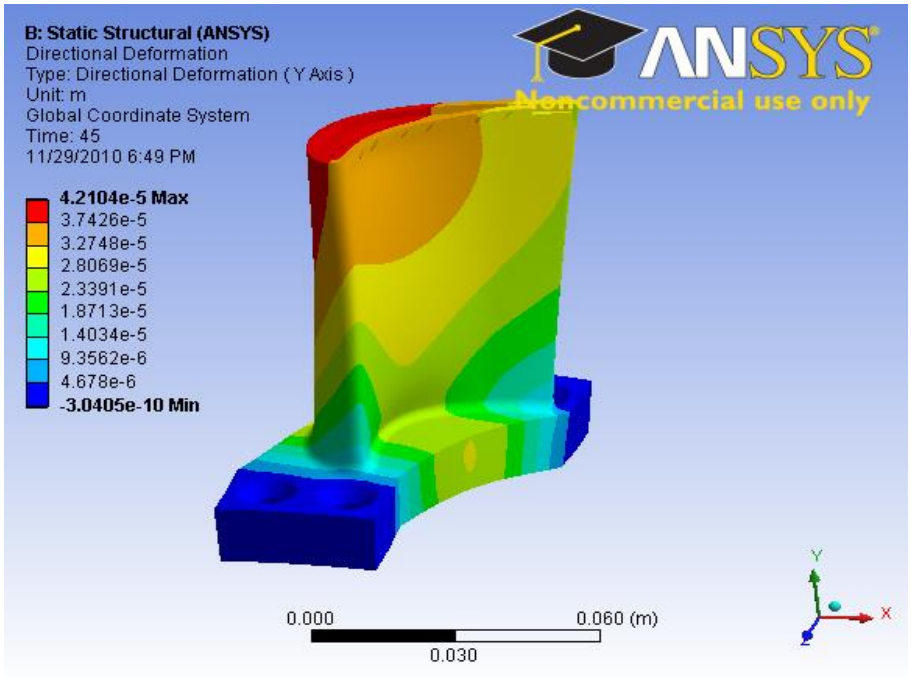

Figure 35 - Rotor Blade Radial Deflection (Units in Meters)

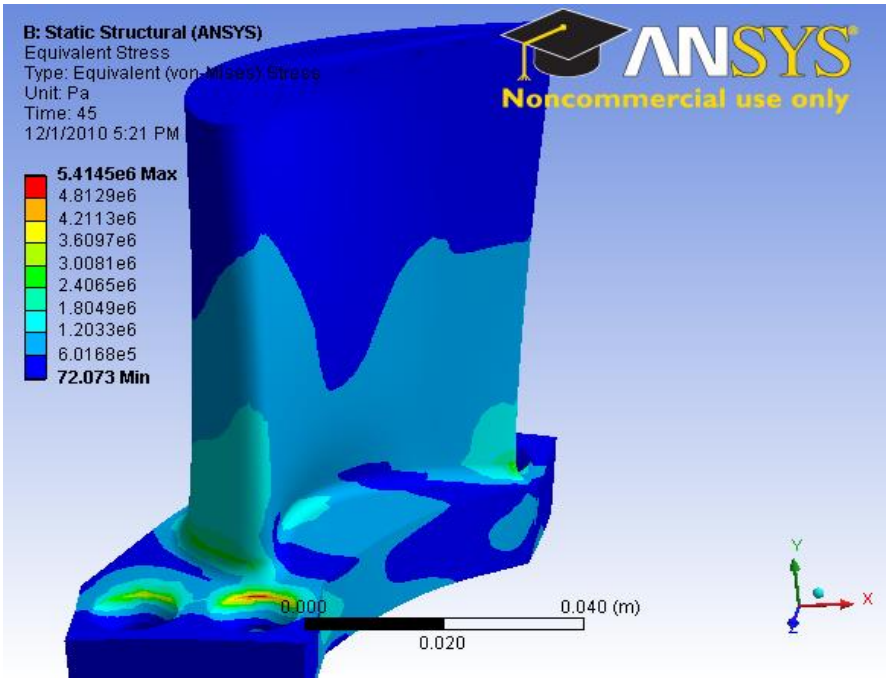

Figure 36 - Rotor Blade Von Mises Stress (Units in Pascals)

Given the material properties of ABS plastic, the maximum equivalent stress in the blade base near the fixed bolt hole determined by FEA was 5.4 Mpa or 783 psi which was on the same order of magnitude as the classical strength modeled beam maximum stress of 631.7 psi. Given an ultimate tensile strength of 4887 psi from the tensile test, a factor of safety from ultimate failure could be assumed to be 6.2. Every effort was made to increase the fillet size of the mating surface of the blade to the base to avoid stress concentrations which could result in a catastrophic blade loss. Another concern was deformation or stretching of the blade to a point where the squealer tip would rub on the shroud. The maximum elongation in the span-wise direction was found to be 0.042mm or 3.3% of the tip gap. This value was corroborated by the classical analysis and deemed acceptable, satisfying the design criteria to keep the tip growth under 10% of the tip gap for safe operation of the test rig.

After the structural analysis was performed on the blade geometry to ensure a proper design, the material properties of the 3-D printed blades needed to be validated to ease concerns that the printing process may cause the material to behave differently under load. Tensile testing was performed to analyze the material strength of the Vero Gray and Vero White polymers used in the rapid prototyping process. These polymers are very similar to ABS plastic, but have been modified to provide efficiency in a liquefying and curing process in the 3D printing apparatus. This process begins by spraying a 16-micrometer thin layer of a liquid polymer onto a building tray. Then, the polymer is instantly cured by laser sintering. In order for the build to take place, a gel like filler material is laid down as well, which is cleaned away by a jet of water. A tensile test specimen was drawn using Inventor Professional 11 and converted to a stereolithographic file type to be 3-D printed.

After printing, an ASTM D638 tensile test was performed on the test specimen by Ajay Kardak, and the final results can be seen in Figure 37 and Table 7. The yield strength of the Vero Gray polymer was found to be 4887.77 psi (33.7 MPa) while the modulus of elasticity was found to be 203 ksi (1398 MPa). The yield strength of the Vero White polymer was found to be 4250 psi (29.3 MPa) while the modulus of elasticity was found to be 187 ksi (1290 MPa). These material properties were found to be approximately 68% of those provided in the manufacturer's literature. Nevertheless, these strengths are well above the minimum strength requirements needed to avoid blade failure. All of the subsequent analyses used the tensile test results for the material properties to offer a higher degree of accuracy, especially in locations where

the material might behave anisotropically, and to provide a high degree of confidence in the design analysis.

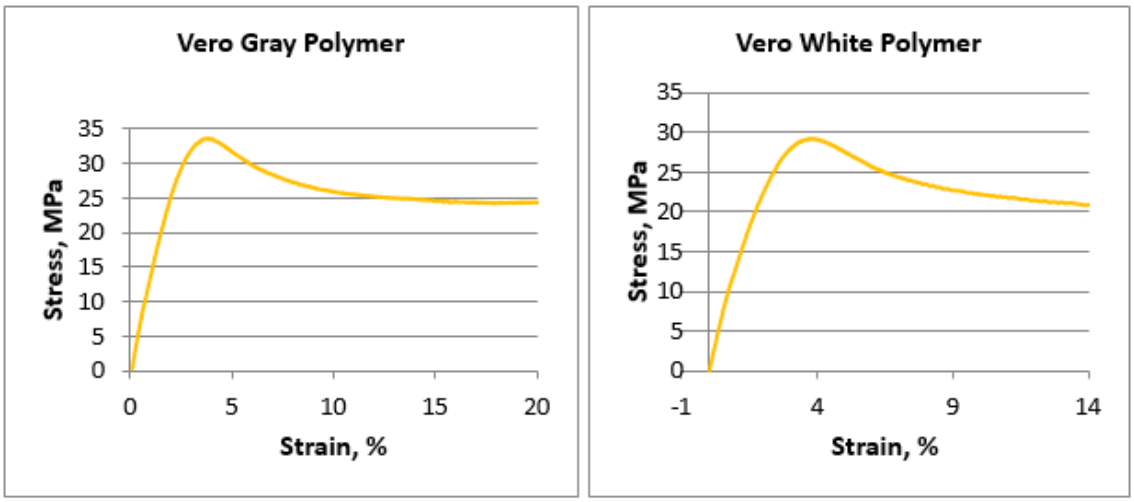

Figure 37 - Tensile Test Results

Table 7 - Tensile Test Results

Material	Yield Stress, MPa	Modulus, MPa	Stress at Offset, MPa
Vero Grey	33.7	1,398	26.2
Vero White	29.3	1,290	20.4

3.3.9 Stator Vane Design and Fabrication

The overall blade design includes two sets of stator blades located before and after the rotor blades. The nozzle guide vanes, NGV, are located directly upstream from the rotor blades while the exit guide vanes, EGV, are located directly downstream. The guide vanes turn the airflow for the rotor test blades; so once the free stream air comes into contact with the test blades, the airflow is at the correct angle for testing analysis.

The 3-D stator-rotor-stator layout includes 32 nozzle guide vanes, 64 rotor blades, and 32 exit guide vanes, encompassing 64 stator blades in total. The stator

blades are designed to be installed between the outer and inner annular sections, allowing air to flow between the blades but not above or below.

The NGV and EGV have two holes bored through their bodies near the leading and trailing edges, shown in Figure 38. Nuts attach to 1/8 inch bolts placed through the vanes securing the vanes to the annular housing to ensure a tight fit and remove the possibility of motion.

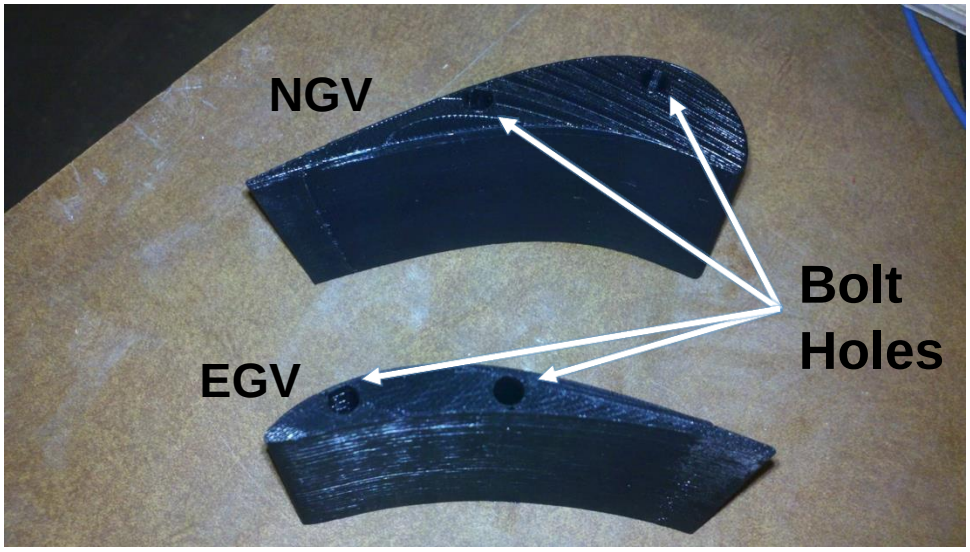

Figure 38 - IGV and EGV with Bolt Holes

A shear stress calculation was executed to ensure that the vanes would not fail due to the load of the passing air. Given the 1/8 inch bolt holes, and analyzing for the worst case of flow normal to its surface; the maximum force on the vane was calculated by Equation 38:

$$F = \rho V^2 A \qquad \text{[Eq. 38]}$$

Here, *F* is the force incurred on the blade, ρ is the density of incoming air, *V* is the inlet velocity, and *A* is the face area of the vane. The force was found to be 2.5 lbs (10.85 N) given a velocity of 74 mph (33 m/s), face area of 12.87 in^2 (0.0083 m^2), and density of air at standard temperature and pressure. The resulting load was assumed

to be shared equally between the bolts, thus the shear stress found was 10.52 psi (72.5 kPa), which is much lower than the shear strength of the ABS material used (1595 psi). The steel bolts used are assumed to be rigid and to have a much higher strength than the ABS material.

3.3.10 Shroud Design and Fabrication

An Aluminum shroud using a pre-defined hole pattern was designed and manufactured (Figure 39). The shroud contains two transparent windows for optical access to the blades by a camera shown in Figure 40. The shroud assembly consists of several components including the shroud, the shroud windows, the shroud plenum, the flanges, and other supporting structures shown in both a 3D model and photograph in Figure 41. The shroud has an inner diameter of 33.725 inches. The shroud was successfully manufactured to within a tolerance of .003 inches. The shroud has 1696 holes, and the hole pattern used in the design is detailed in Figure 6 and Table 2 (page 40) providing shroud hole dimensions along several rows.

Much time was spent searching for a vendor to grow a Zinc Selenide window for IR measurements, but no shop was willing to take the risk of growing a crystal with two curved surfaces and a set of shroud cooling holes. Therefore, the windows were fabricated with an acrylic plastic. As a result, the test parameters were driven to liquid crystal thermography.

Another critical component of the shroud was the leading edge gap. This gap at design conditions was 1 mm wide. Coolant air would be fed through the gap separately, thereby requiring three separate, independent, coolant lines.

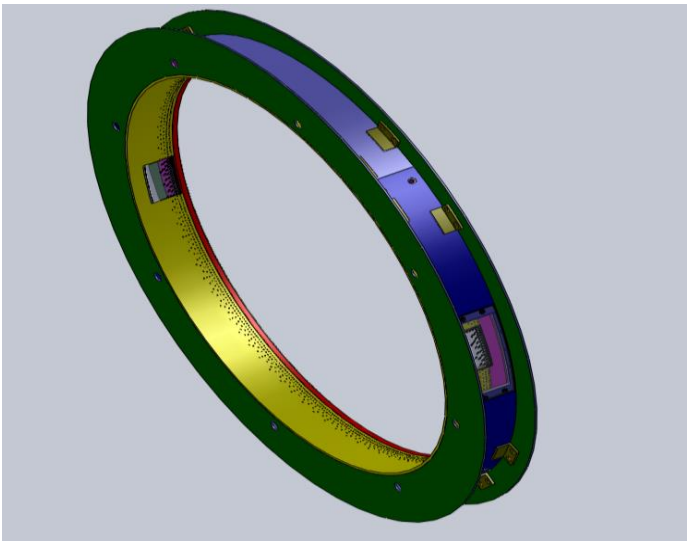

Figure 39 - Shroud Solid Model (Onieluan Tamunobere PHD)

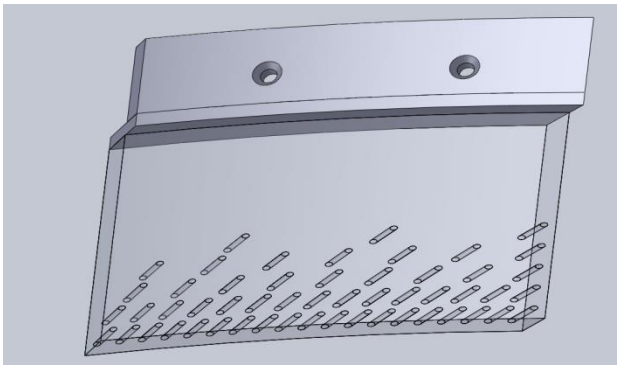

Figure 40 - Shroud Access Window (Onieluan Tamunobere PHD)

The first line feeds the rotor blades through the hub; the second line feeds the shroud holes; and the third line feeds the leading edge gap. The plenum for the shroud holes and leading edge are separated by means of a flange. The assembly is designed to accommodate different leading edge gap dimensions ranging from 0 mm to 9 mm. This was done by fabricating multiple L-shaped flanges of differing thickness that can be switched out to provide the desired leading edge gap. Details of the shroud assembly with the leading edge gap are shown in Fig. 6. The shroud was, by far, the most expensive piece of the test section in terms of both fabrication time and material cost

because of the difficulty in precisely manufacturing a ring with upwards of 1600 holes drilled at a 45 degree angle.

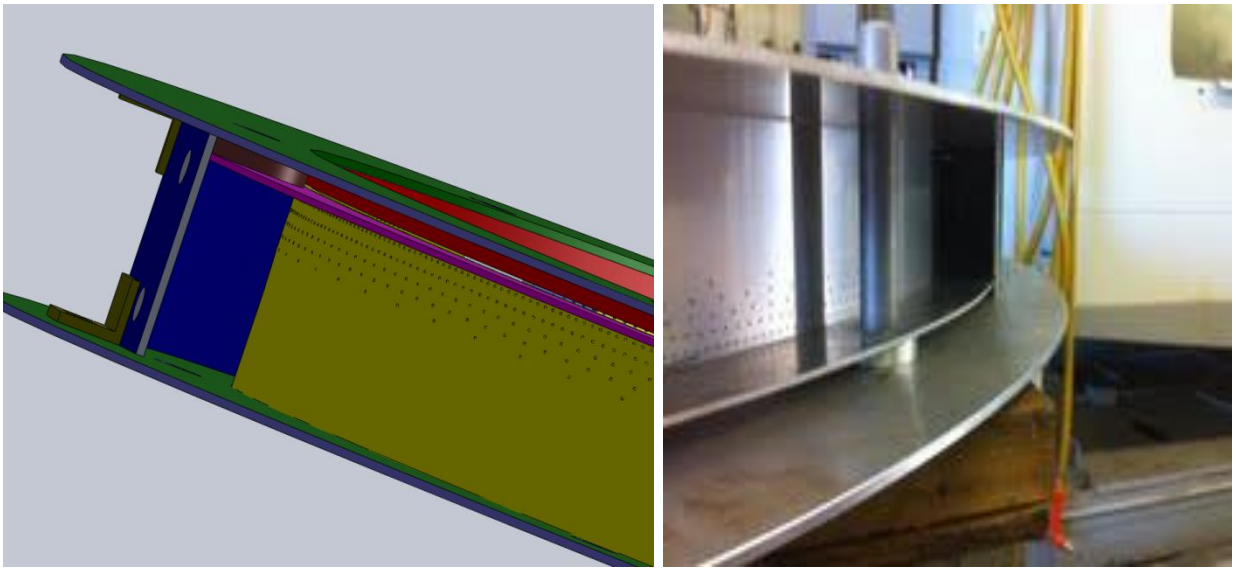

Figure 41 – Shroud Model (left), Actual shroud (right) (Onieluan Tamunobere PHD)

3.3.11 Support Structure

The structure that supports the test section components was manufactured using 3 inch AISI 1040 Steel C channel for the outer frame and legs and 3” x 3” box tubing for the interior struts as shown in figure 42. This C channel and box tubing were purchased from Brecheen Pipe and Steel Company (Port Allen, Louisiana). The basic structure is 7’ in length and 3’ wide. Each C channel piece and box tubing piece were cut to length using an abrasive chop saw with a silicon carbide blade. Once each piece was cut and subsequently ground, the pieces were welded together using the MIG welding machine on-site in the ERAD building room 105a, where the test section is located. The 8.5 inch long legs were welded onto the frame separately at the four corners and at the juncture of the interior box tubing cross-members with the outside frame.

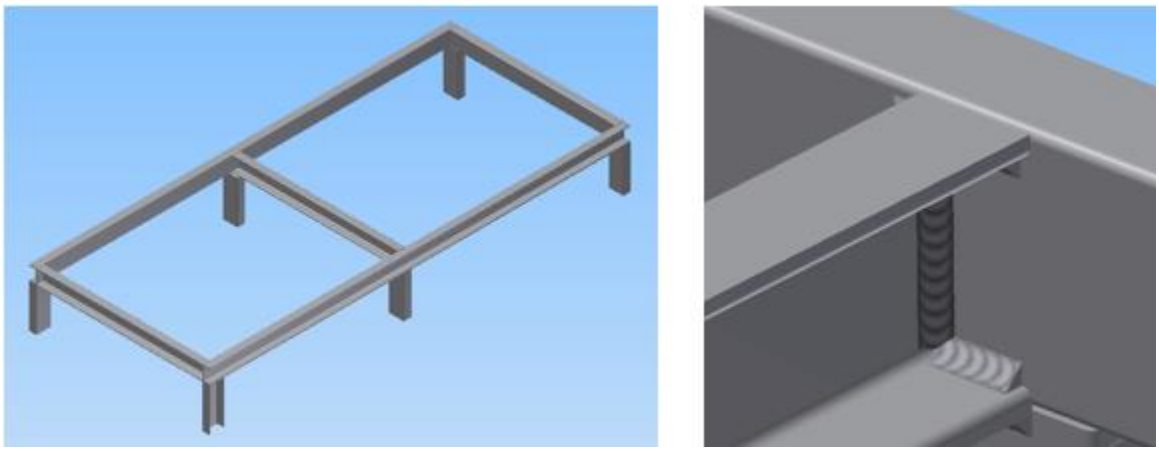

Figure 42 - Support Structure Solid Model (left) with Weld Detail (right)

Each 3 inch x 3 inch box tubing member had two 1 1/32 inch holes drilled to accept a 1 inch threaded rod that would support the test section above. The box tubing supporting the upstream portion of the test section was slotted at the rod holes to offer adjustability when assembling the final components. A photograph of the final support structure assembly can be seen in Figure 43.

Figure 43 - Support Structure as Built

Once the test section location was determined in relation to the adjoining transition duct, L brackets were bolted to the feet and drilled to accept concrete anchors installed in the floor below to provide a rigid, immobile support structure that would help transmit vibrations to the slab of the laboratory building.

3.3.12 Motor and Bearing Supports

Supports were made for each of the bearings and motor as seen in Figure 44. They were cut from ¼ inch steel plate using a waterjet by Louisiana Cutting Baton Rouge, LA. The supports were designed to fit tightly into the inner annular shaft and motor housing with a set screw hole match drilled and tapped to hold the supports in place. Two have a bolt pattern cut to match the bearing and one has a bolt pattern cut to match the motor, in addition to a center hole for the shaft. These supports provide structural rigidity, support for components, and hand access for assembly and disassembly of the shaft and motor housing.

Figure 44 - Bearing Support

Steel L sections were cut and welded to the three inner annular supports with holes cut to accept the 1” threaded rod supports that penetrate the underside of the shaft and motor housing and connect the housing to the support frame below. A finished welded L bracket is shown in Figure 45.

Figure 45 - Welded L Bracket

3.3.13 Annular Test Section

The test section is designed with two annular sections, one inside the other. The inner annular section contains the entire shaft and motor assembly. The inner section was closed off from free stream airflow by two fiberglass domes at each end. These domes were fabricated by inflating a large exercise ball to the size of the inner diameter of the inner shaft and motor housing, then placing mats of woven fiberglass, then painting over the mats with polyester resin. Once the polyester resin set, body filler was applied to smooth the surface of the dome before the domes were sanded to complete the fabrication process. The length of the inner section was comprised of two annular sections of 16 gauge sheet metal. Each section has an outer diameter of 27.9 inches and is 24 inches in length. The two sections were rolled and welded together and are separated by and connected to the rotor blade hub through the bearing supports held up by one inch threaded rod as shown in Figure 46.

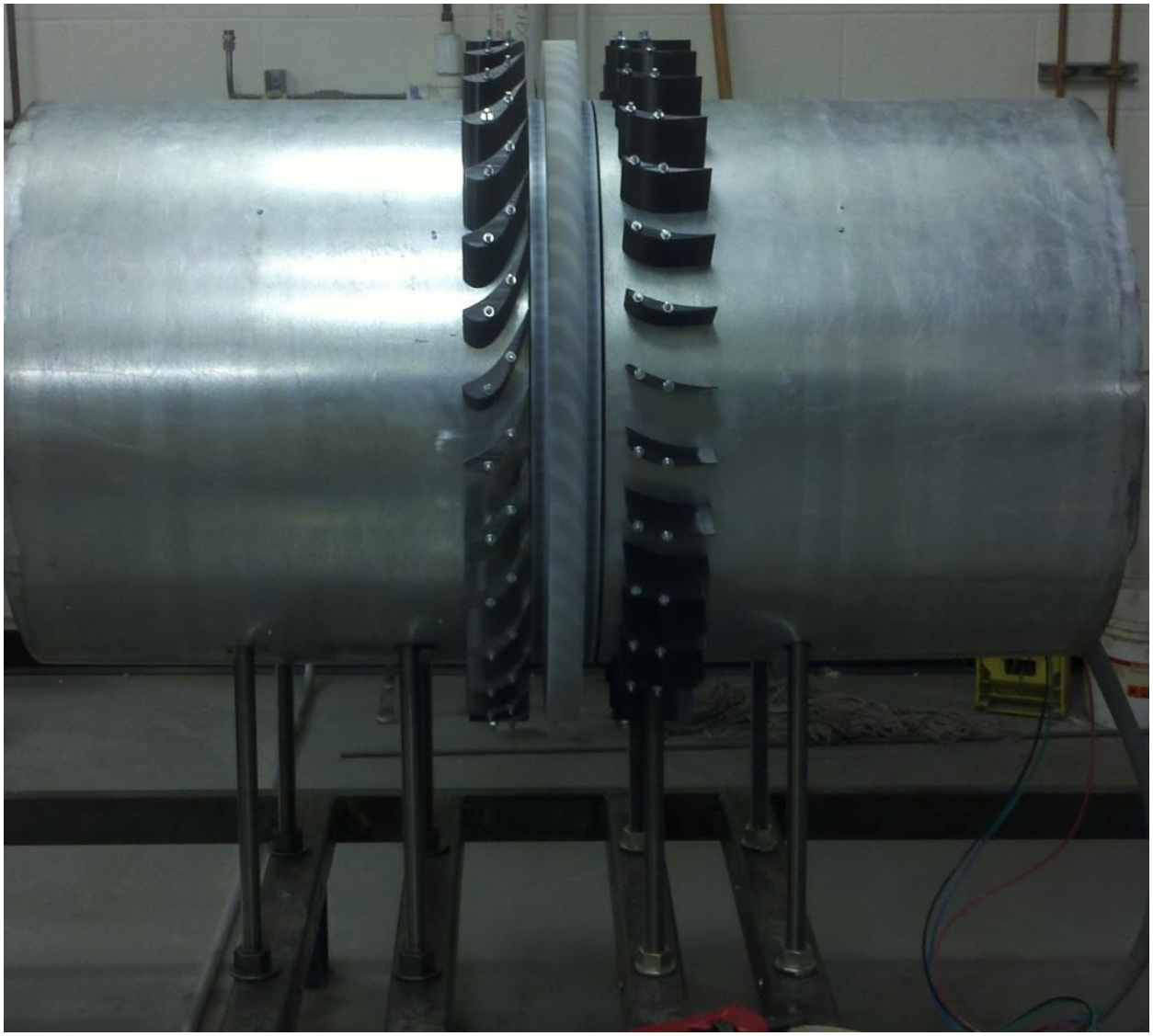

Figure 46 - Inner Annulus and Rotor Setup

3.3.14 Outer Annular Shell Design

The complete inner test section is housed in an outer shell which attaches to the shroud and completes the wind tunnel circuit. The inner test section is supported by one inch threaded rods bolted to a steel frame below, while the outer shells are bolted to the same frame by ¾ inch threaded rods to offer complete adjustability, seen in Figure 47.

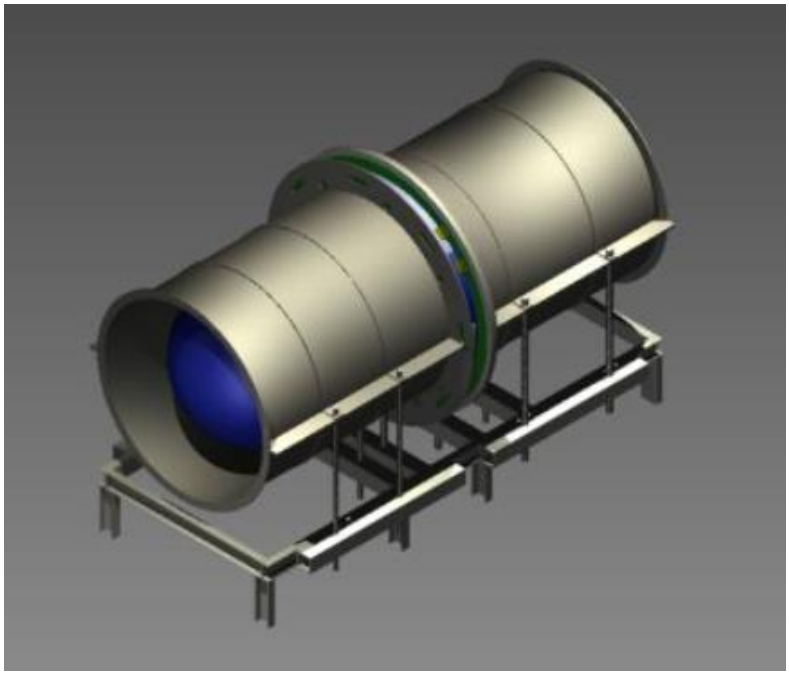

Figure 47 - Test Section Rendered 3D Model

Outer annular shells were designed and fabricated in four half circle segments to form the complete annulus. These four shells were fabricated from rolled 16ga galvanized steel sheet with ¼" thick rolled flat bar stiffeners. The longitudinal and end flanges were ¼" steel, which offered the rigidity needed for assembly. The flanges were laser cut with the end flanges to be placed adjacent to the shroud drilled to match the mating shroud bolt pattern and the end flanges to be placed adjacent to the duct drilled to match the mating duct flange pattern. The two bottom sections adjoining the shroud on either side were fitted with slots to allow for passage of the 1" threaded rods connecting the inner shaft and rotor housing assembly to the support frame below. The longitudinal flanges of the two top and bottom segments were connected by bolts for easy removal and access to the shaft and rotor assembly. Detailed drawings, seen in Figures 48 and 49, were supplied BMR Metal Works of Baton Rouge, LA, for fabrication.

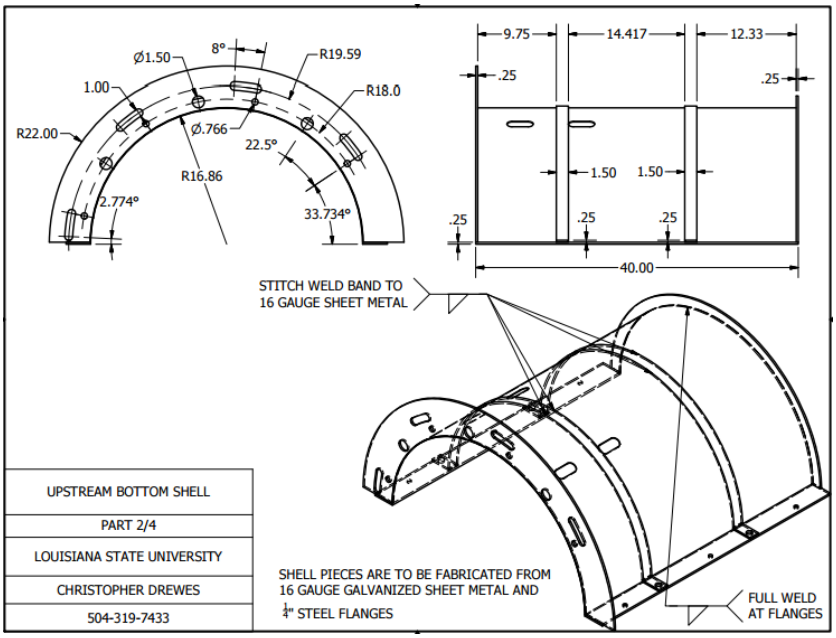

Figure 48 - Outer Annular Shell Production Drawing

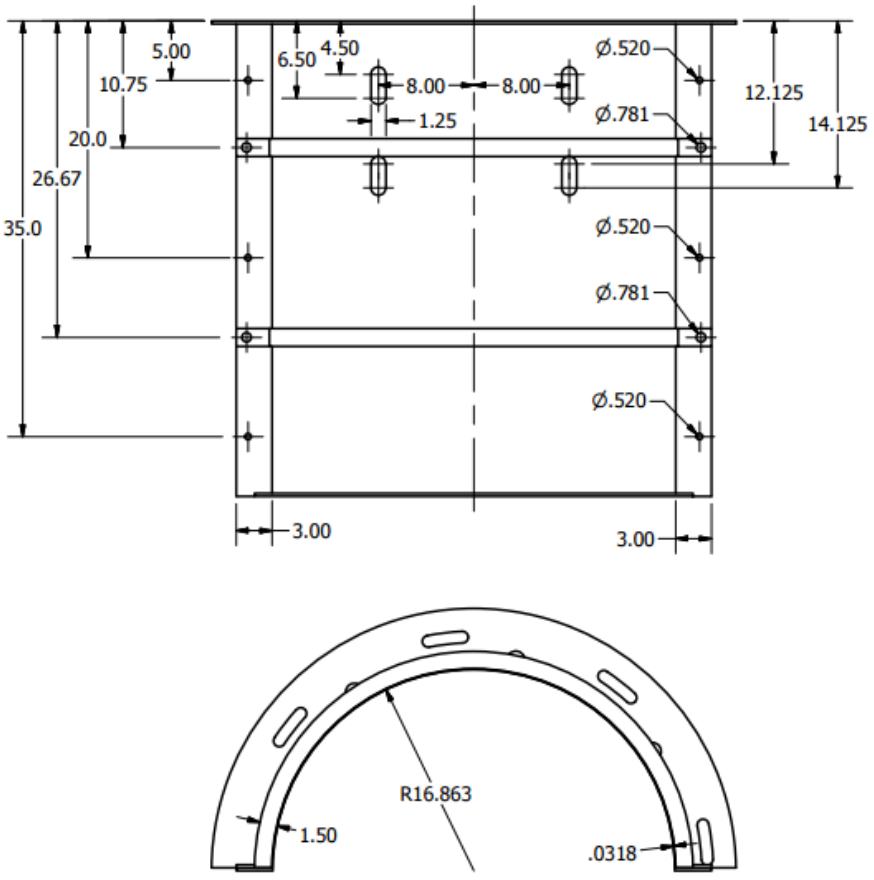

Figure 49 - Outer Annular Shell Production Drawing

3.4 Coolant Line Design and Fabrication

Pressurized coolant air is supplied to the shroud and rotor from two Atlas-Copco G315-150 compressors located outside the ERAD building. These compressors each have a maximum working pressure of 157 psi at 1399 SCFM. Given the pressure rating and a maximum flow rate, coolant lines were designed for both performance, and ease of assembly. A major design consideration was that the shroud and rotor coolant lines had to be completely independent of each other with regards to flowrate, pressure, and temperature. Separate steel pipe air coolant lines were run from the two main supply feed points located in the lab. The simpler rotor cooling line will be discussed first.

3.4.1 Rotor Film Coolant Line Design

Due to the lack of compressor air drying, inline coalescers were needed to sufficiently remove water vapor as well as other particulates from the compressed coolant air. Given the design maximum flow rate of the rotor line of 0.31 kg/s and an operating pressure estimated to be around 30 psi, a 5 micron Wilkerson filter PN F34-06-000 was selected. This off the shelf filter attached with a 3/4” NPT female fitting and offered a pressure drop of less than 1 psi. To reduce installation costs, all pipe and components were connected using NPT fittings with thread sealant or Teflon tape to prevent leaks. It was deemed cost prohibitive to have a certified welder on-site to install the coolant air lines, and joining the pipe nipples with unions allowed for easy removal after the project was completed.

The air filter was the first component in the supply line to protect the following: gate valve, pressure regulator, flow meter, and air heater. During operation, the flow rate needs to be adjusted by operation of a gate valve to maintain the test design flow

which will vary proportionally to the pressure drop across the system. A pressure regulator was used to hold the supply pressure constant. Thermal mass flow meters were selected due to their high accuracy and relatively low length of straight duct required before and after the measurement location. This length of straight duct was a driving factor in the layout of the cooling lines for the shroud, LE Gap, and rotor cooling. Forty diameters upstream and ten diameters downstream of straight length before and after the flow meter were required for proper installation. This determined the design pipe diameters given the length of pipe that could be placed in the lab.

In order to offer the step change in coolant air temperature for the 1-D semi-infinite solid test, a pneumatic 3 way valve with a bypass after the heater was installed in the coolant line. The bypass piping utilized a muffler to keep the noise from the expanding gas within reasonable limits. The complete layout of the rotor supply coolant can be seen in Figure 50 which depicts the piping line transitions to a ½" Hose with ½" NPT fittings to connect to the rotary union, offering the flexibility needed to route the tube into the test section. This coolant line was supported from the bypass wind tunnel ductwork which offered the optimal positioning in the lab space, adjacent to the test section.

When selecting the line sizes, pressure drop and component inlet size were taken into consideration. A system curve was developed using the Crane Technical Paper 410M which is widely accepted in industry.

A simple Bernoulli's calculation was not applicable for the compressed air system. Earlier in this paper, the maximum choked flow conditions were analyzed, whereas the viscous losses were found herein.

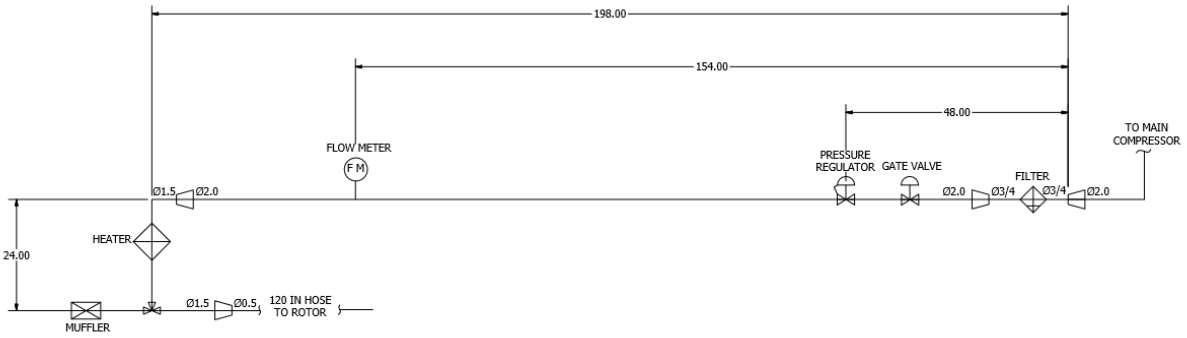

Figure 50 - Rotor Coolant Schematic

Pressure drop along a length of straight pipe for air at the design pressure was described by the Darcy formula:

$$\Delta P_{100} = \frac{62{,}530\, f\, W^2 \bar{V}}{d^5} \quad \text{[Eq. 39]}$$

where ΔP_{100} is the pressure drop across 100m of pipe in Pa, f is the friction factor, W is the mass flow rate in kg/Hr, $\bar{V}$ is the specific volume, and d is the pipe inner diameter. Components purchased from manufacturers such as the heater and coalescer have pressure loss curves that were used in the analysis; otherwise, for standard fittings, equivalent lengths of pipe were added to complete the system analysis. The design flow rate for the rotor was selected by calculating the total coolant flow from a given blowing ratio of 5 based on the design rotor mainstream air velocity, which is the maximum blowing ratio that was tested. This flow rate was calculated as 115 SCFM and thus, the system analysis revealed a probable pressure loss of almost 30 psi. The majority of the system pressure loss occurs at the flexible hose where the diameter needed to be reduced to ease integration into the test section rotor assembly. Still, this loss is only 20% of the maximum compressor operating pressure and offers a wide margin for system performance and the complete system curve can be found in Figure 51.

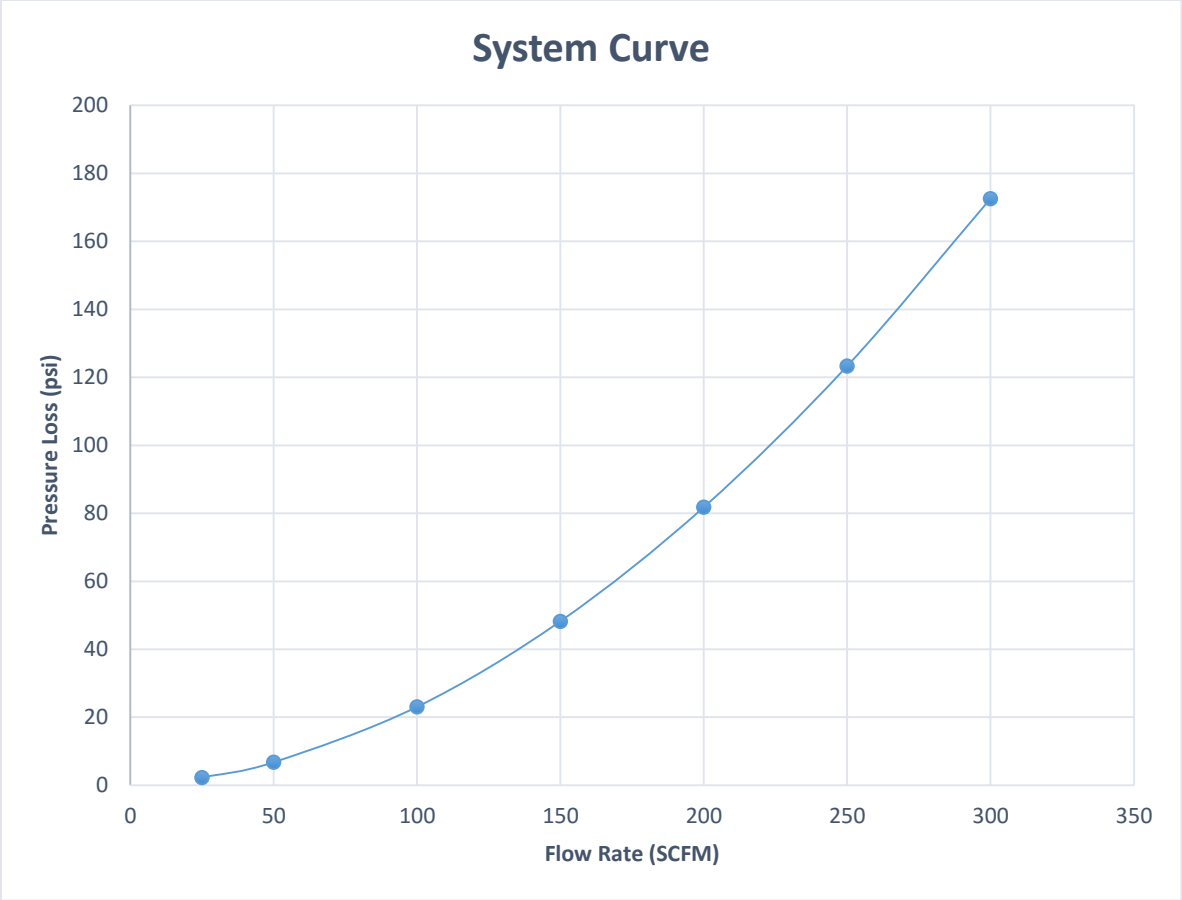

Figure 51 - Rotor Coolant System Curve

3.4.2 Leading Edge Gap and Shroud Film Coolant Line

A similar analysis was performed for the LE Gap and Shroud Coolant lines. These two coolant assemblies branch off from a common line coming from the main supply. The design flow rate for the LE Gap and Shroud were 805 SCFM and 230 SCFM respectively. These flow rates were also calculated from a maximum blowing ratio of 5 based on the design rotor mainstream air velocity. The Darcy formula was also used to compute the pressure drop in the system. This system was similar to the rotor line in that it had similar components, but in larger sizes to accommodate the higher flow rate. The resulting schematic and system curve can be seen in Figure 52.

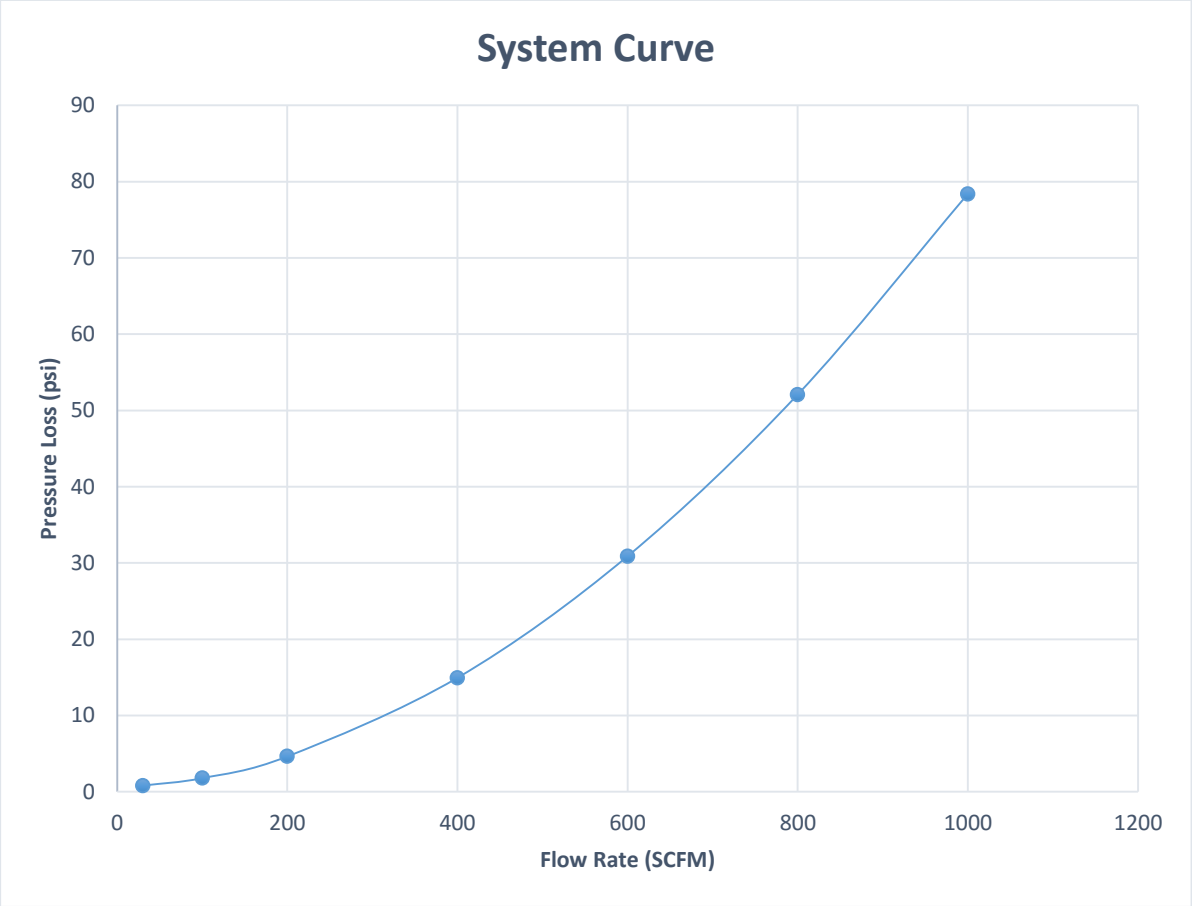

Figure 52 - Shroud and LE Gap Coolant System Curve

The design pressure drop was calculated to be nearly 53 psi for the LE Gap coolant line which was found to be the driving line in the design. It was determined that 83% of the pressure loss was due to the coolant manifold at the end of the LE Gap system. Here, 16 ¼" tubes were split to integrate with the small area of the LE Gap plenum. Although this reduction is 35% of the maximum compressor operating pressure, a wide margin for system performance is still maintained. The overall schematic for both coolant lines can be seen in Figure 53 and in the drawings package provided in the appendix. Photographs of the final rotor and shroud can be seen in Figure 54, while a photo of the completed Wind Tunnel Assembly can be seen in Figure 55.

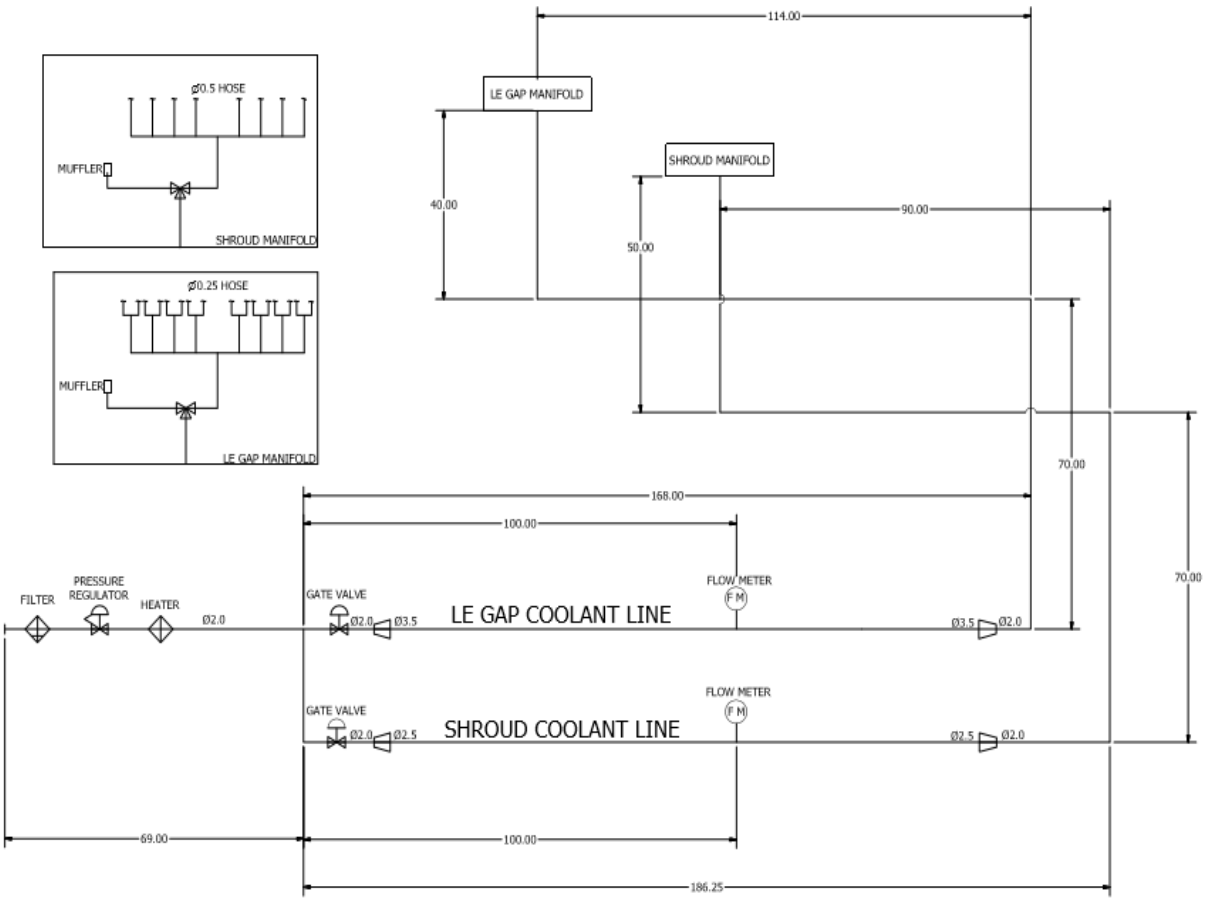

Figure 53 - LE Gap and Shroud Coolant Schematic

Figure 54 - Rotor and Shroud

Figure 55 - Wind tunnel facility

3.5 Wind Tunnel Flow Testing

3.5.1 Test Section Velocity Measurements

Without the vanes and the rotor in place, a liquid water manometer and pitot-static probe were inserted near the test section and used to measure the total and static pressure for varying fan speeds from which the velocity of the free-stream air was determined and shown in Table 8 and Figure 56. The wind velocities will differ when the added pressure drops of the rotor and guide vanes are introduced.

Table 8 - Wind Tunnel Velocity Measurements

Fan Setting (Hz)	Velocity (m/s)	Mass Flow (kg/s)
20	19.21	4.17
25	24.18	5.24
30	29.08	6.31
35	34.20	7.42

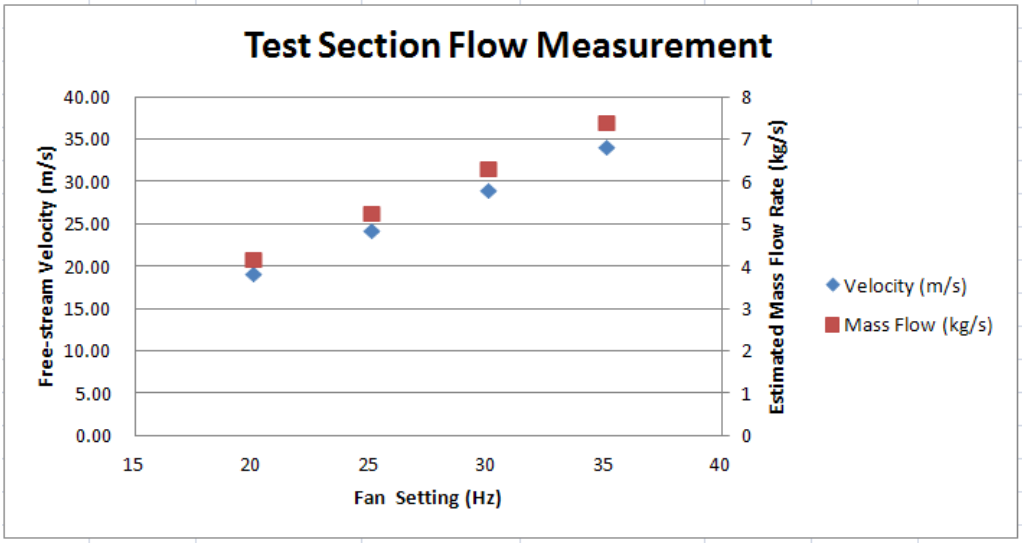

Figure 56 - Fan Speed and Velocity

The fan setting will go as high as 60 Hz, but the manometer used has a full scale differential pressure of 3" H_2O, thereby limiting the useful range of data to a fan speed slightly above 35 Hz. However, extrapolating this data, a maximum velocity and flow rate of approximately 59 m/s and 12.5 kg/s, respectively, should be attainable. Note again that this will be lower when the rotor and guide vanes are introduced. The linear trend in the measured data follows the fan affinity laws which state that the flow rate is directly proportional to the rotor speed for a given impeller diameter.

$$\frac{Q_1}{Q_2} = \left(\frac{N_1}{N_2}\right)\left(\frac{d_1}{d_2}\right)^3 \quad \text{[Eq. 40]}$$

3.5.2 Wind Tunnel Pressure Drop Measurements

The pressure drop through the test section loop of the wind tunnel without the rotor and guide vanes has been recorded for varying fan speeds in Table 9. Pressure was measured at the fan exit and inlet using the recently acquired DSA3217 eight channel pressure transducer array with a full scale resolution of 10 inWg. The difference between the two is the total pressure drop through the tunnel and can be seen graphically in Figure 57.

Table 9- Pressure Loss across the Wind Tunnel

Fan Setting (Hz)	P_exit ("H2O)	P_inlet ("H2O)	ΔP ("H2O)	ΔP (Pa)
25	1.25	0.00	1.25	311.25
30	1.63	0.00	1.63	404.63
35	2.13	0.00	2.13	529.13
40	2.88	0.00	2.88	715.88
45	3.50	0.00	3.50	871.50
50	4.25	0.00	4.25	1058.25
55	5.13	0.00	5.13	1276.13
60	6.00	0.06	5.94	1478.44

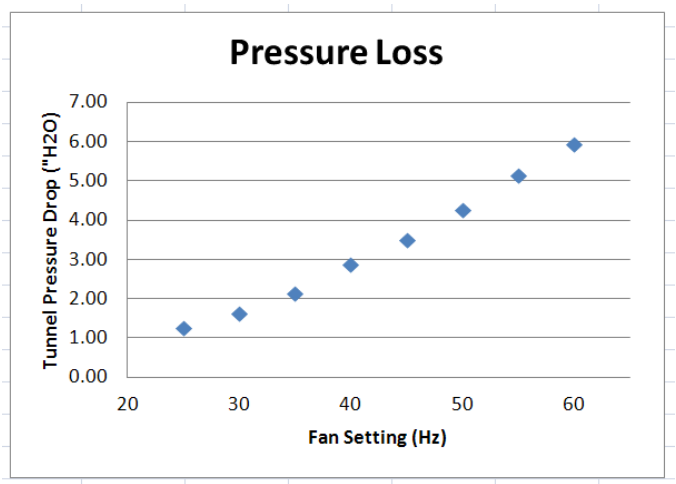

Figure 57 - Pressure Drop with Respect to Fan Speed

Previously, it was shown that the velocity and flow rate vary linearly with the fan setting. Also, basic fluid mechanics and the fan affinity laws show that pressure head is proportional to the square of the velocity.

$$\frac{\Delta P_1}{\Delta P_2} = \left(\frac{N_1}{N_2}\right)^2 \left(\frac{d_1}{d_2}\right)^2 \quad \text{[Eq. 41]}$$

Thus, as detailed above, the pressure drop variation versus fan setting data obtained by the testing is quadratic. Similarly, as detailed below, the tested pressure loss versus the subsequently calculated flow rate is also quadratic.

Once the tunnel was tested under these conditions, the measured results could be compared to the predicted system curve as detailed below in Figure 58.

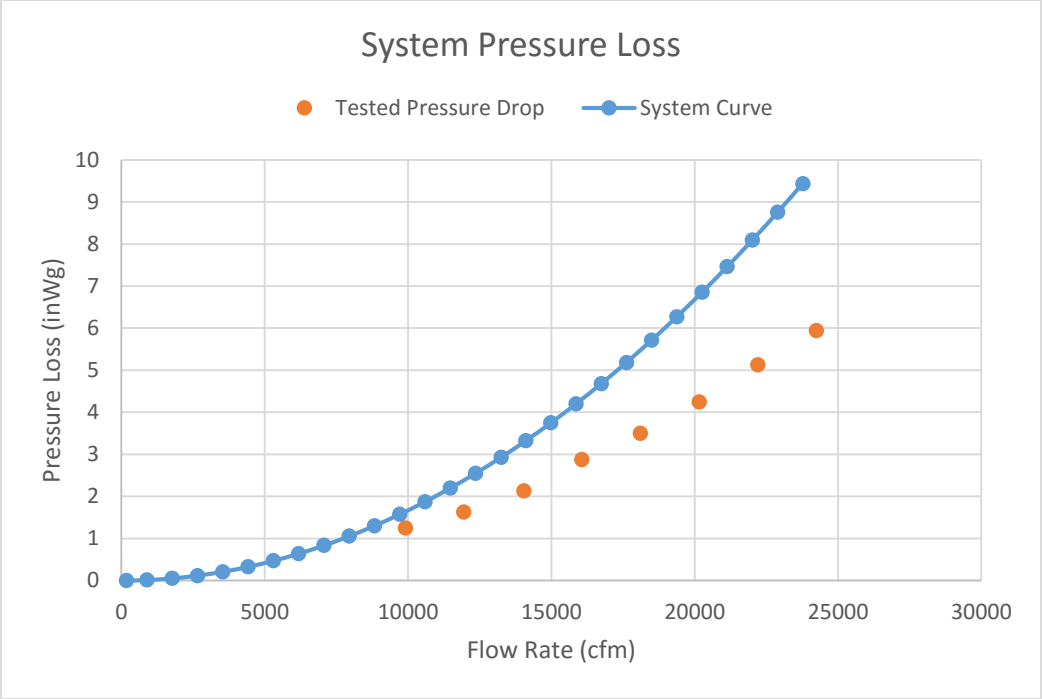

Figure 58 - Wind Tunnel System Pressure Drop

Predicted pressure loss in the system is higher than that measured confirming that the design assumptions for the test system are conservative. Predicted system loss included 1.1 inWg of pressure loss for the test section at the design flow rate which was not completely manifested during the testing as per the recorded measurements. This test data gave the designers high confidence in the wind tunnel performance leading to a decision that heat transfer testing could begin.

Chapter 4: Experimental Procedure and Results

After the detailed design and fabrication of the rotating turbine cascade and wind tunnel facility, it was necessary to validate the flow field at the test section. In order to obtain aerodynamic measurements which could offer insight into the incoming mainstream flow, a calibration and data reduction scheme was created for a 5-hole probe to obtain velocity vectors and static pressure.

To begin, the flow and rotor conditions would have to be set in order to scale the prescribed design conditions. The prescribed design velocity triangles are shown in Figure 59.

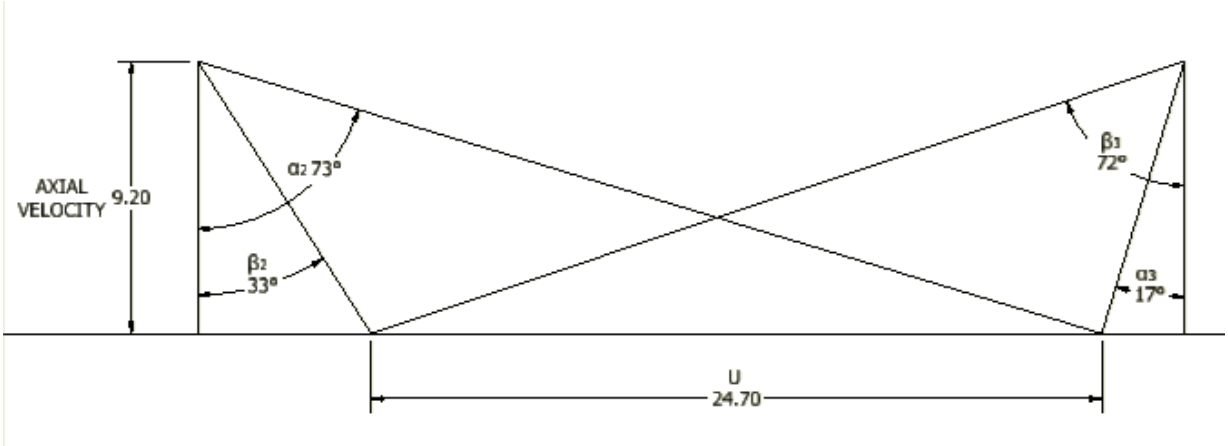

Figure 59 - Design Velocity Triangles (Units: m/s)

Running the test to a scaled rotor condition allowed for more accurate and reliable measurements to be taken. At a lower speed, the reliability of the test section increased due to reduced down time from shaft misalignment caused by high vibration at higher rotational speeds. The velocity triangles, scaled down, are shown in Figure 60, and they describe the inlet conditions for the testing found in the following sections.

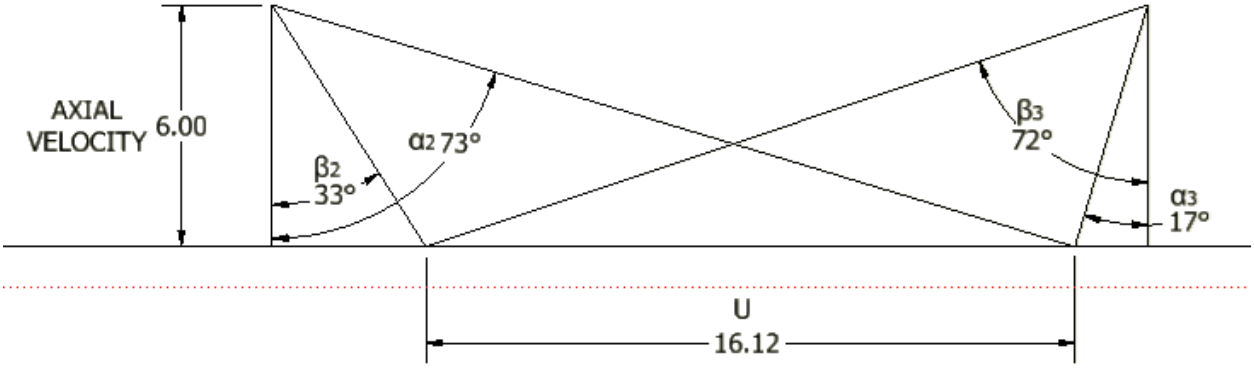

Figure 60 - Test Design Conditions (Scale: 1.53:1) (Units: m/s)

The design condition called for a rotational speed of 1667 RPM where frequent maintenance was required to continue testing. With a rotor speed scaled down to by 1.53, the resulting rotor speed was 355 RPM and the inlet flow was 6.0 m/s. The fan speed was set through trial and error to obtain a mainstream flow of 6.0 m/s measured by a pitot static probe upstream of the nozzle guide vanes. Measurements were taken radially and averaged at multiple locations to develop confidence in the test conditions. In order to scale the velocity triangles, the geometric angles were held constant, while the incoming flow and rotor speed were allowed to vary. That is, the exit angle from the Nozzle guide vanes, and the exit relative velocity angle were held constant given their geometry does not change.

4.1 Uncertainty Analysis

Now that the experimental results have been presented, a look into the uncertainty of the velocity and total pressure coefficient results is needed. The primary instrumentation used in the experimental analysis is the Scanivalve DSA3217 eight channel pressure transducer array, calibrated by the manufacturer with a maximum error of 0.02% of the full scale 2488.4 Pa (10 in H2O). The Kline McClintock method

was used to estimate the uncertainty in the velocity and pressure coefficient calculations.

For a particular measured variable, Xi:

$$X_i = X_i \pm \delta X_i \quad \text{[Eq. 42]}$$

where δX_i is the uncertainty in the measurement. Given a function F that is a result of multiple independent measurements or variables:

$$F = F(X_1, X_2, X_3 \ \ldots \ X_N) \text{ [Eq. 43]}$$

For a single measurement, the effect of the uncertainty on the final result would be:

$$\delta F_{X_i} = \frac{\partial F}{\partial X_i}\delta X_i \quad \text{[Eq. 44]}$$

where $\frac{\partial F}{\partial X_i}$, the partial deriviative with respect to the measured variable Xi, is the sensitivity coefficient for the function F [37]. In order to combine the effects of multiple independent measurements with uncertainty, the root-sum-square combination method described by Moffat was used where,

$$\delta F = \left\{\sum_{i=1}^{N}\left(\frac{\partial F}{\partial X_i}\delta X_i\right)^2\right\}^{\frac{1}{2}} \quad \text{[Eq. 45]}$$

To describe the uncertainty in the calculation of the velocity magnitude shown in equation 44

$$\left\{\left(\frac{\partial V}{\partial P_1}\delta P_1\right)^2 + \left(\frac{\partial V}{\partial \bar{P}}\delta \bar{P}\right)^2 + \left(\frac{\partial V}{\partial C_{pt}}\delta C_{pt}\right)^2 + \left(\frac{\partial V}{\partial C_{ps}}\delta C_{ps}\right)^2 + \left(\frac{\partial V}{\partial \rho}\delta \rho\right)^2\right\}^{\frac{1}{2}} \quad \text{[Eq. 46]}$$

Similarly, the uncertainty in $\bar{P}$, C_{pt}, C_{ps} are:

$$\delta \bar{P} = \left\{\left(\frac{\partial \bar{P}}{\partial P_2}\delta P_2\right)^2 + \left(\frac{\partial \bar{P}}{\partial P_3}\delta P_3\right)^2 + \left(\frac{\partial \bar{P}}{\partial P_4}\delta P_4\right)^2 + \left(\frac{\partial \bar{P}}{\partial P_5}\delta P_5\right)^2\right\}^{\frac{1}{2}} \quad \text{[Eq. 47]}$$

$$\delta C_{pt} = \left\{\left(\frac{\partial C_{pt}}{\partial P_t}\delta P_t\right)^2 + \left(\frac{\partial C_{pt}}{\partial \bar{P}}\delta \bar{P}\right)^2 + \left(\frac{\partial C_{pt}}{\partial P_1}\delta P_1\right)^2\right\}^{\frac{1}{2}} \quad \text{[Eq. 48]}$$

$$\delta C_{ps} = \left\{ \left(\frac{\partial C_{ps}}{\partial P_s} \delta P_s \right)^2 + \left(\frac{\partial C_{ps}}{\partial \bar{P}} \delta \bar{P} \right)^2 + \left(\frac{\partial C_{ps}}{\partial P_1} \delta P_1 \right)^2 \right\}^{\frac{1}{2}} \quad \text{[Eq. 49]}$$

$$\delta C_{ps} = \left\{ \left(\frac{\partial C_{ps}}{\partial P_s} \delta P_s \right)^2 + \left(\frac{\partial C_{ps}}{\partial \bar{P}} \delta \bar{P} \right)^2 + \left(\frac{\partial C_{ps}}{\partial P_1} \delta P_1 \right)^2 \right\}^{\frac{1}{2}} \quad \text{[Eq. 50]}$$

An uncertainty analysis was also performed on the total pressure coefficient shown in equation 47 and the uncertainty can be defined by the RSS combination method as,

$$\delta C_p = \left\{ \left(\frac{\partial C_p}{\partial P_O} \delta P_O \right)^2 + \left(\frac{\partial C_p}{\partial \rho} \delta \rho \right)^2 + \left(\frac{\partial C_p}{\partial V} \delta V \right)^2 \right\}^{\frac{1}{2}} \quad \text{[Eq. 51]}$$

The uncertainty results for the independent variables can be seen in table 10.

Table 10 - Uncertainty Values

Variable	Uncertainty
$\delta\rho$	3.00%
δP_1	0.34%
$\delta\bar{P}$	0.18%
δC_{pt}	6.62%
δC_{ps}	4.76%
δP_O	0.02%
δC_p	8.82%
δV	4.65%

The uncertainty was shown in the table as a percentage of the measured value except in the case of density, where 3.0% of the tabulated value based on temperature and pressure was assumed. A combined uncertainty of 4.65% in the velocity calulation and a combined uncertainty of 8.82% in the total pressure coefficient were estimated. This shows that the experiments were performed with enough confidence to validate the incoming and exiting wind tunnel flow properties.

4.2 Five-Hole Probe Analysis

A 5-hole probe consists of a central pressure tap with two opposing holes in the yaw (β) plane and two opposing holes in the pitch (α) plane. The direction of the flow is found by comparing the measured pressure difference between the pitch holes and the

difference between the yaw holes, while the velocity magnitude is found by determining the dynamic head based on the pressure measured at the center hole compared to the remaining holes [34]. The pitch, yaw, and total pressure holes can be seen below in Figure 61.

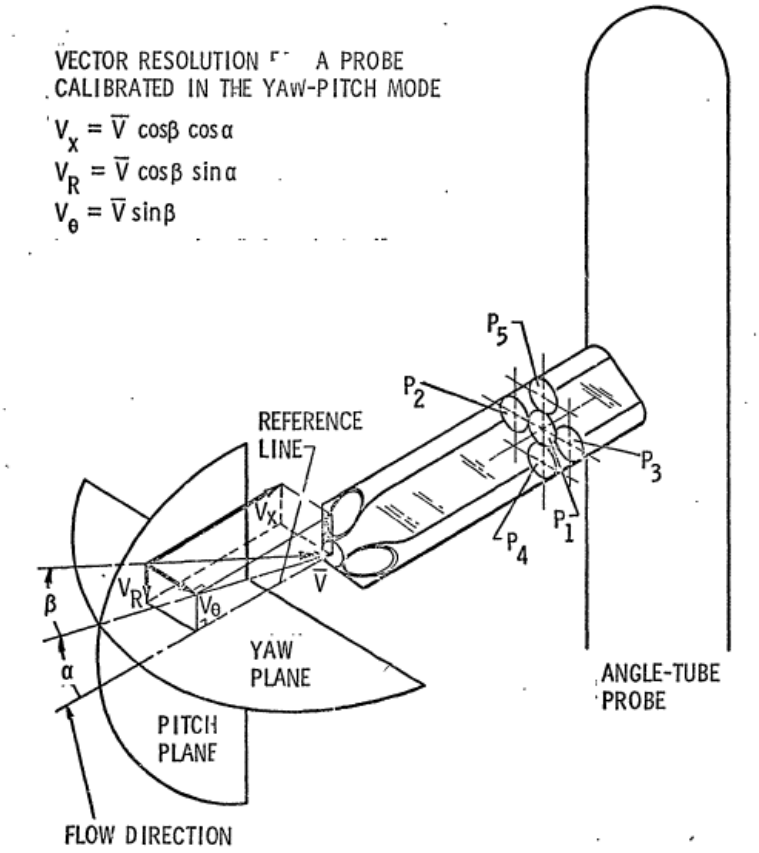

Figure 61 - Five-hole Probe Velocity Resolution [34]

Due to the spacial constraints driven by the rotating cascade design, the 5-hole probe was used in a non-nulling analysis. Nulling a 5-hole probe consists of actively reading the pitch and yaw ports and adjusting the probe using a three dimensional traverse until the pitch ports and the yaw ports are equal to obtain the incoming flow angle. Given the difficulty in manufacturing such a traverse system as well as allowing test section access, it was deemed cost prohibitive to pursue a 5-hole probe nulling

technique. The non-nulling technique offers unique challenges in that even commercially bought probes do not come with a set of calibration data, and each probe has a unique calibration that must be determined by the end user.

Before performing the probe calibration, a calibration scheme was determined using the method outlined by Lee and Wood [34]. The measured pressure values would have to be normalized to reduce fluctuations in the data set and allow for easier interpolation of the directional vectors. The pressure coefficients used can be seen below where P_1 to P_5 are the pressures at the taps described in the above figure, P_t and P_s are the total and static pressure respectively, and the subscript y and p denote yaw and pitch respectively.

$$C_{Py} = \frac{(P_2 - P_3)}{(P_1 - \bar{P})} \quad C_{Pp} = \frac{(P_4 - P_5)}{(P_1 - \bar{P})} \quad C_{Pt} = \frac{(P_t - \bar{P})}{(P_1 - \bar{P})} \quad C_{Ps} = \frac{(P_1 - P_s)}{(P_1 - \bar{P})} \quad \bar{P} = \frac{P_2 + P_3 + P_4 + P_5}{4}$$

[Eq. 52] [Eq. 53] [Eq. 54] [Eq. 55] [Eq. 56]

Typically when normalizing pressure measurements, the free stream dynamic head is used. For the 5-hole probe, the dynamic head is a constant value and is independent of the probe orientation, thus the difference between the pressure at the central hole and the average of the surrounding holes is used to remove plot scatter. The total and static pressures are values that can only be measured in the calibration phase since they cannot be measured using the 5-hole probe alone [35].

4.2.1 Calibration Technique

A calibration of the 5-hole probe was performed at a location 8 diameters from the first set of turning vanes in the straight section of duct in the rotating turbine cascade wind tunnel. This location was selected because it had the longest stretch of straight duct to allow for the flow to develop and was the sole location that would allow traverse

installation and access to utilize and mount the probe. A Scanivalve DSA3217 eight channel pressure transducer array, calibrated by the manufacturer with a maximum error of 0.02% of the full scale 2488.4 Pa was connected to the probe. The first five pressure taps measured the 5-hole probe pressures, while ports six and seven measured the total and static pressure of a pitot tube located in the flow. This array allowed for the recording of not only the five pressure measurements, but also the total and static pressure used later to back out the velocity magnitude in the experiments.

Pressure measurements were recorded at each combination of pitch and yaw from +25º to -25º in increments of 5º. This robust data set was the maximum of the traverse itself, and it encompassed the useful range of the probe before separation would occur and the measurements would lose their accuracy. For each of the 121 pitch/yaw combinations, an individual .csv file was created by recording the pressure with the Scanivalve system for 120 seconds at 6Hz to offer more than enough data points to be averaged for the analysis. Each .csv was named according to its pitch and yaw angle.

When developing the calibration code in MatLab, first, a code was written to compile a list of the calibration file names in a text file to later be used by the calibration code. The initial step in the calibration code, which can be seen in the appendix, was to extract the pitch and yaw from their respective file names and to couple them with their associated data. The code was written to take an average for each of the pressure readings and to create a matrix of pressure coefficients along with their corresponding angle.

4.2.2 Calibration Results

Three dimensional plots of the pitch, yaw, static pressure, and total pressure coefficient calibration data can be seen in Figure 62, Figure 63, Figure 64, and Figure 65 respectively. These plots were later used to interpolate measurements taken just upstream of the nozzle guide vanes in a test case for wind tunnel validation. These plots were created using the Matlab “meshgrid” function in order to stitch the calibration points together and allow for a three dimensional interpolation scheme to be used.

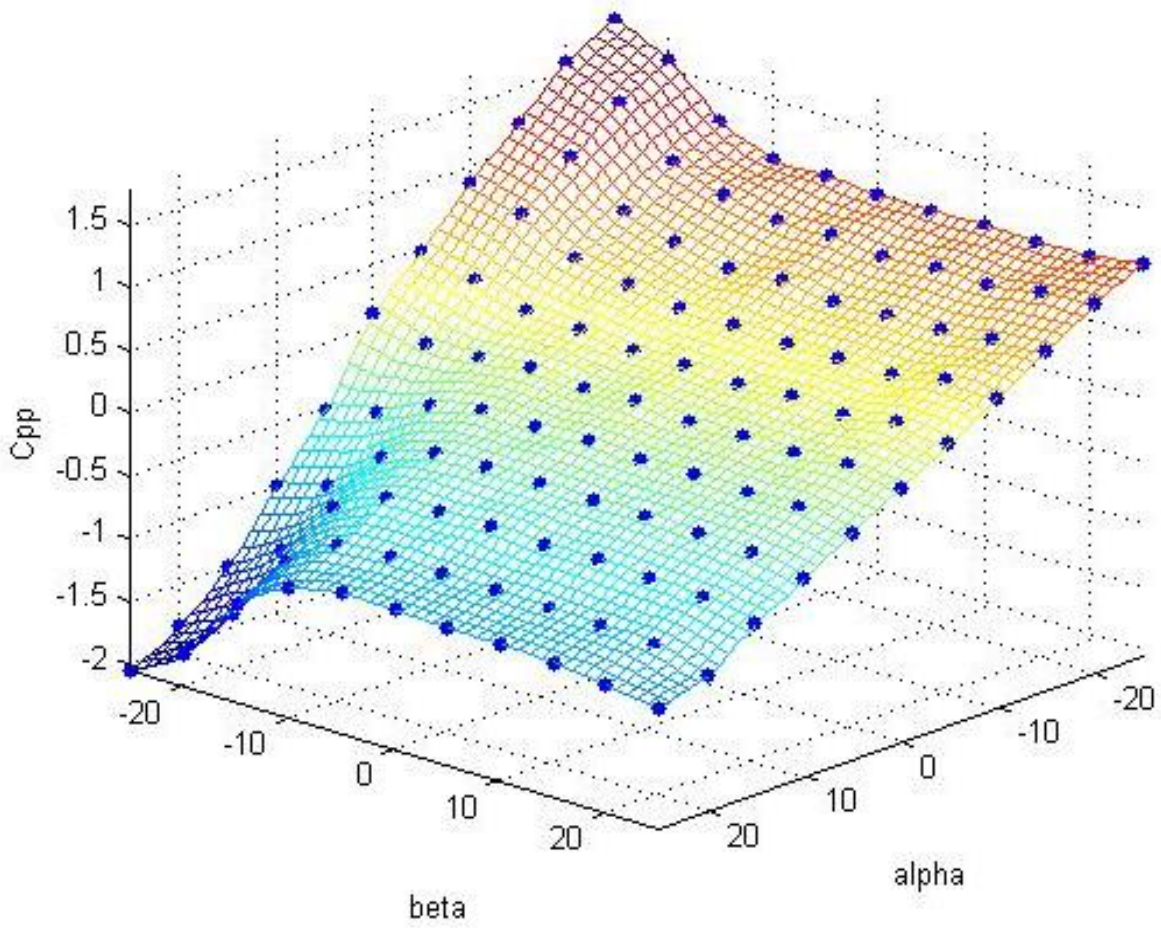

Figure 62 - Pitch Coefficient Calibration Curve

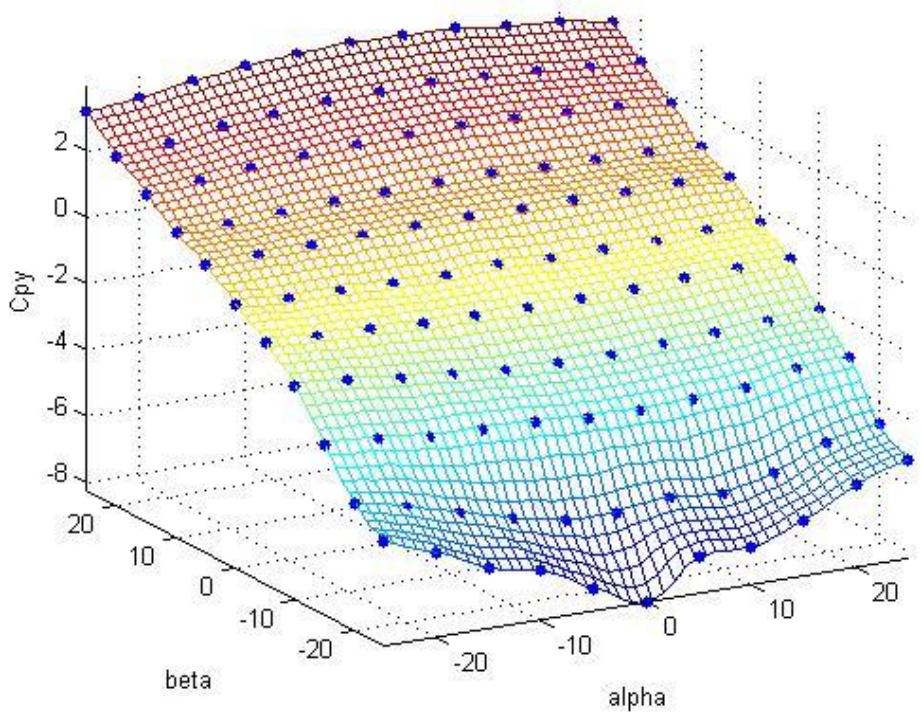

Figure 63 - Yaw Coefficient Calibration Curve

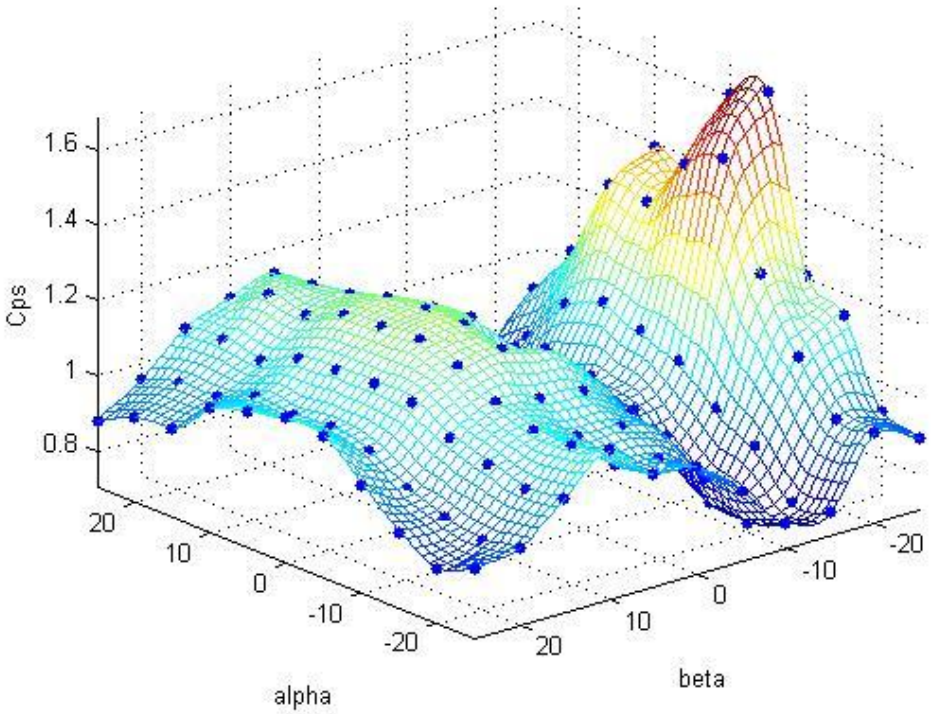

Figure 64 - Static Pressure Coefficient Calibration Curve

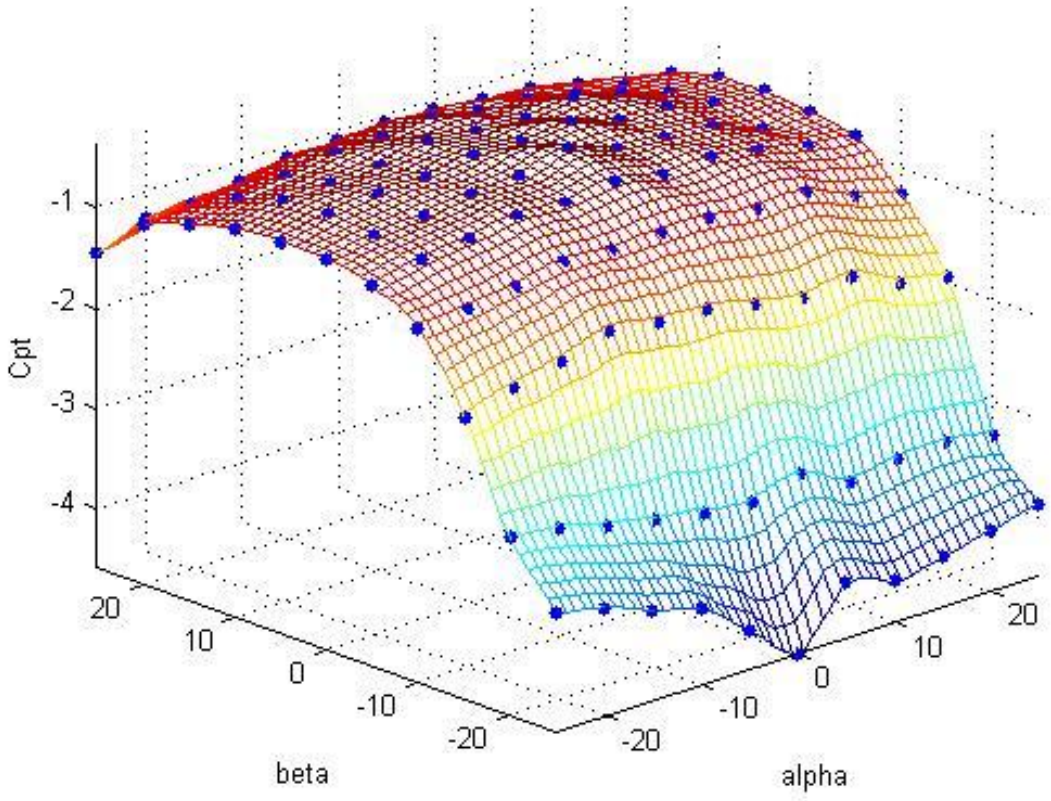

Figure 65 - Total Pressure Coefficient Calibration Curve

4.2.3 Five Hole Probe Analysis Technique

Once the calibration was complete, testing began at the inlet of the cascade, at the leading edge of a nozzle guide vane. A grid of 231 points was created by positioning the probe using a manual traverse where 11 radial points were taken on 21 circumferential columns. Similar to the calibration scheme, the measurement points' file names were denoted with their radial and circumferential position so that this information could be extracted later using the code. Initially, a text file was created cataloging the measurement file names to be used in the analysis code. The analysis code takes the pressure information, calculates the pressure coefficients, and interpolates the results using a 3D "Griddata, Cubic" interpolation function.

First, the pitch angle was determined by interpolation using the calibration yaw coefficient, pitch coefficient, and pitch angle, along with the newly found measured pitch and yaw coefficients. Similarly, the yaw angle was found through interpolation using the calibration yaw coefficient, pitch coefficient, and yaw angle, along with the newly found measured pitch and yaw coefficients. Once the angle of the incoming flow was known, the total and static pressure coefficients could be interpolated by using the calibration data from which the velocity magnitude could be resolved. Thus, the total pressure coefficient was found using the three dimensional interpolation scheme inputting the calibration data pitch angle, yaw angle, total pressure coefficient, and the interpolated pitch and yaw angle. A similar scheme was used for the static pressure coefficient. The following equation was then used to calculate the velocity magnitude (V) given all of the variables previously found.

$$V = \sqrt{\frac{2}{\rho}(P_1 - \bar{P})(1 - C_{Pt} + C_{Ps})} \quad \text{[Eq. 57]}$$

Now that both the magnitude and direction of the incoming flow have been determined from probe measurements, a coordinate transform must be completed and the data converted into a useful form for graphical representation. Again, code was written to compile the results files which held the pitch and yaw angle information for each point. The final code grabbed these results files and indexed them into each specific location and evaluated the corresponding mean angle and velocity magnitude. A final coordinate transform was completed in which the velocity vectors were resolved from the pitch-yaw mode with the following equations.

$$V_X = V\cos\alpha\ \cos\beta \quad \text{[Eq. 58]} \qquad V_R = V\sin\alpha \quad \text{[Eq. 59]} \qquad V_\theta = V\cos\alpha\ \sin\beta \quad \text{[Eq. 60]}$$

$$V_Y = V_R\sin\theta + V_\theta\cos\theta \quad \text{[Eq. 61]} \qquad V_Z = V_R\cos\theta - V_\theta\sin\theta \quad \text{[Eq. 62]}$$

Now that the velocity components were resolved, the velocity vectors could be plotted on a quiver plot and the magnitude of each component could be produced graphically to offer insight into the flow field.

4.2.4 Five-Hole Probe Results Upstream of the Nozzle Guide Vanes

The first case run was done at an operating condition that mimicked the heat transfer testing performed in the Turbine Innovation and Energy Research (TIER) Laboratory at LSU. The rotational velocity of the rotor was 550 RPM and the average inlet mainstream velocity was 6.0 m/s resulting in a Reynolds Number of 15,155 based on the axial chord length. The measurements were taken upstream of the nozzle guide vanes, detailed in Figure 66 and Figure 67, from one passageway center to the next to encompass the flow on the suction and pressure side of the nozzle guide vane. The measurement grid, shown in Figure 68, consisted of 231 points taken 5 mm apart in the radial and circumferential directions forming a grid for 20s each at 6 Hz. Each of the pressure measurements taken were averaged to remove the time dependency of the measurements taken. The source code for the calibration and analysis can be found in the appendix.

The results can be seen in figures 69 through 75 and correlate to a typical airfoil velocity distribution where the air speed is higher on the suction side and lower on the pressure side, developing lift. In this first case, the nozzle guide vane is used to turn the flow, rather than extract energy from it, yet the streamlines should be representative of an airfoil with a large amount of camber.

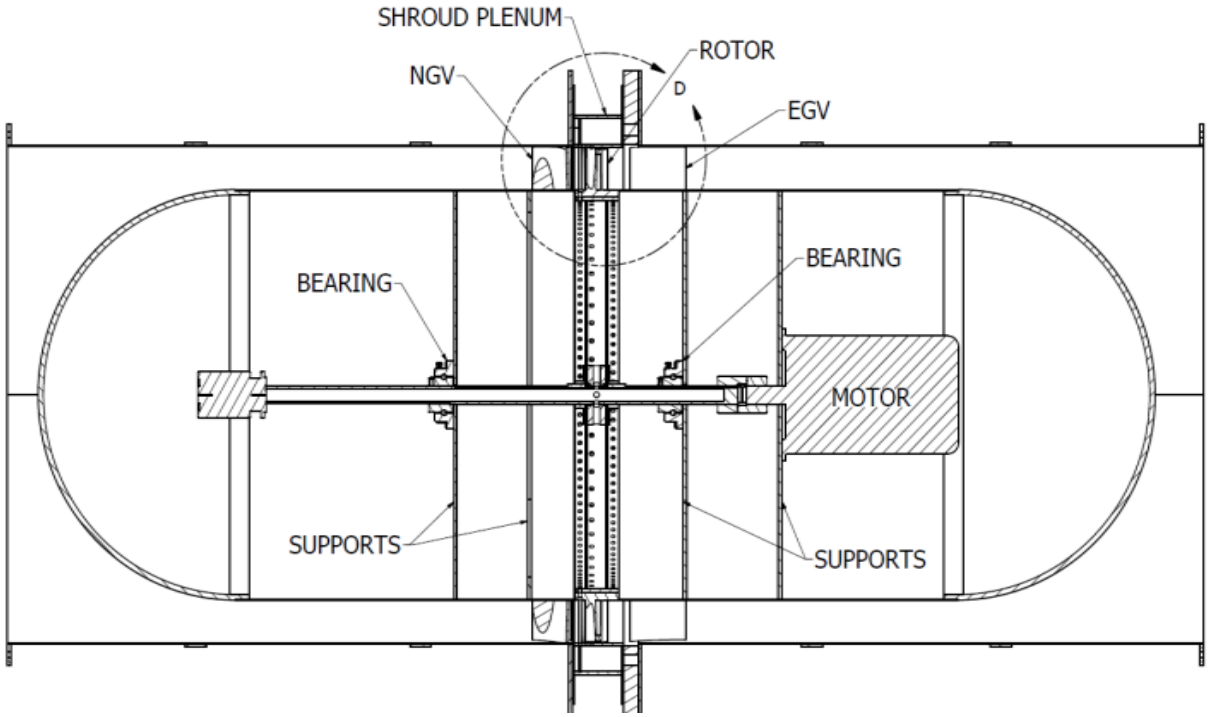

Figure 66 - Cascade Section View (Scale: None)

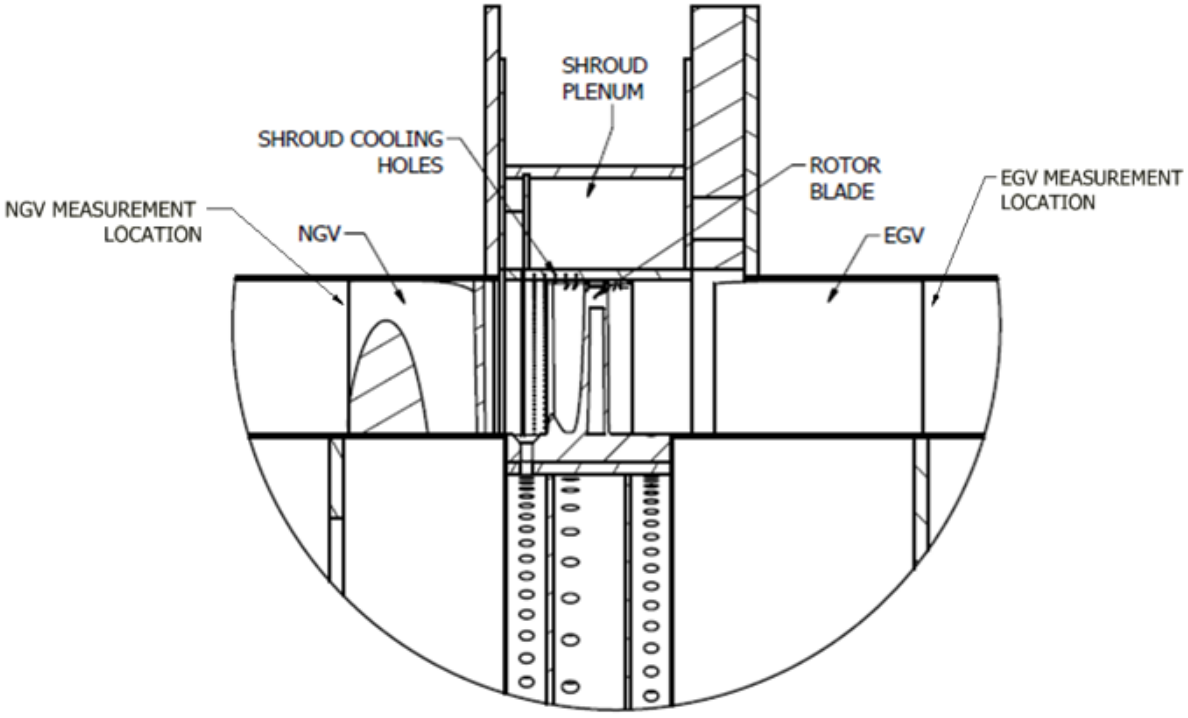

Figure 67 - Section D with Measurement Locations (Scale: None)

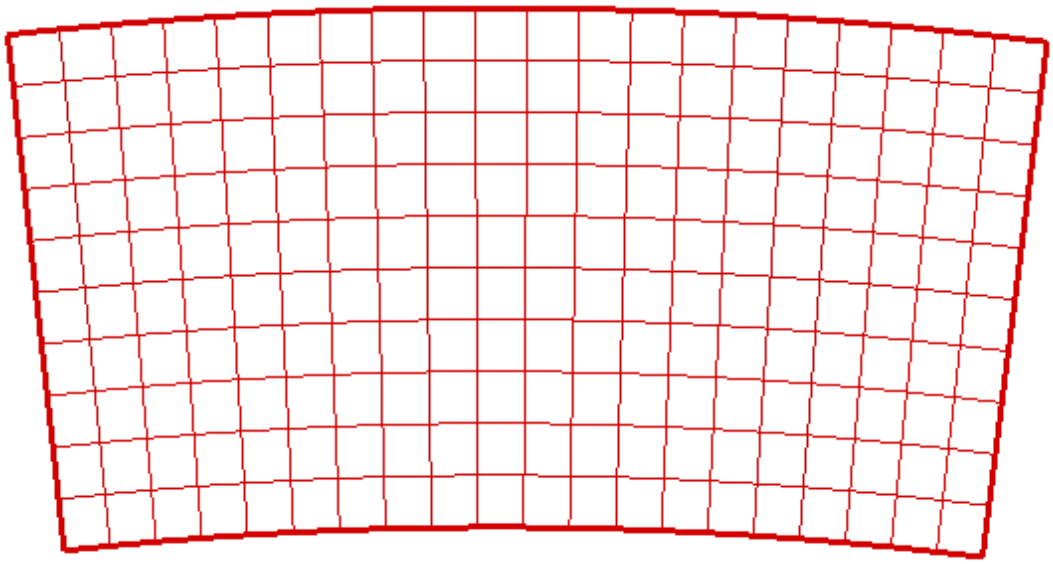

Figure 68 - Measurement Grid

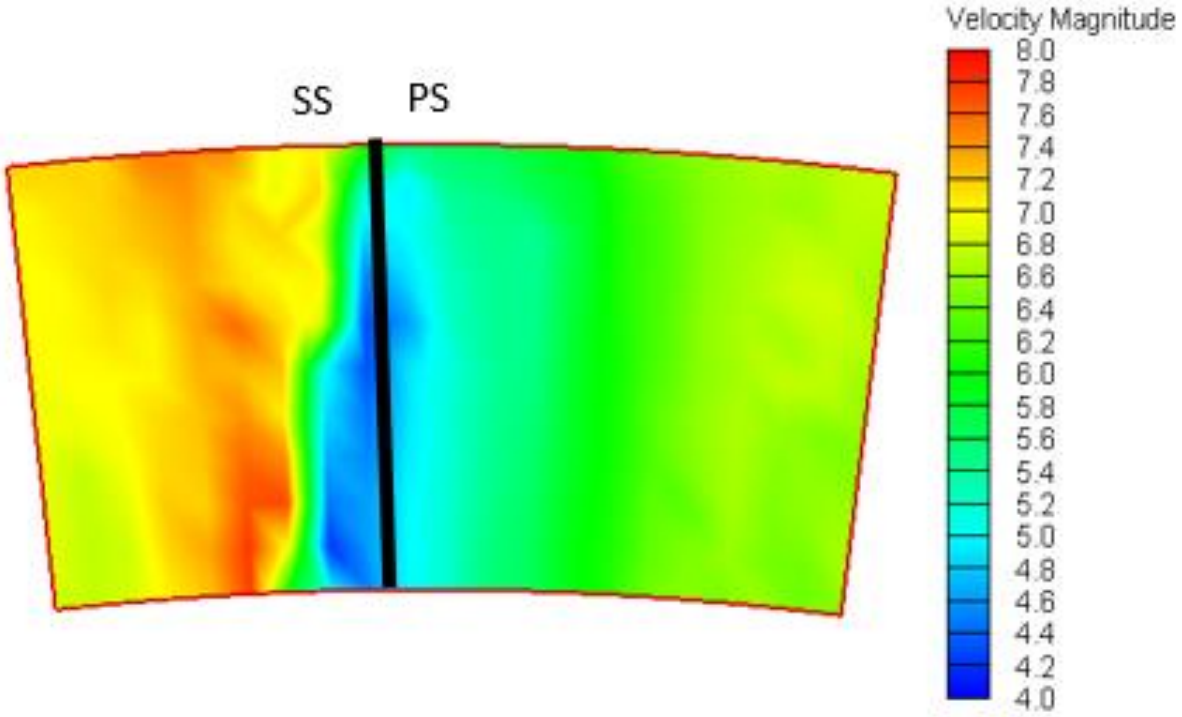

Figure 69 - Velocity Magnitude (m/s)

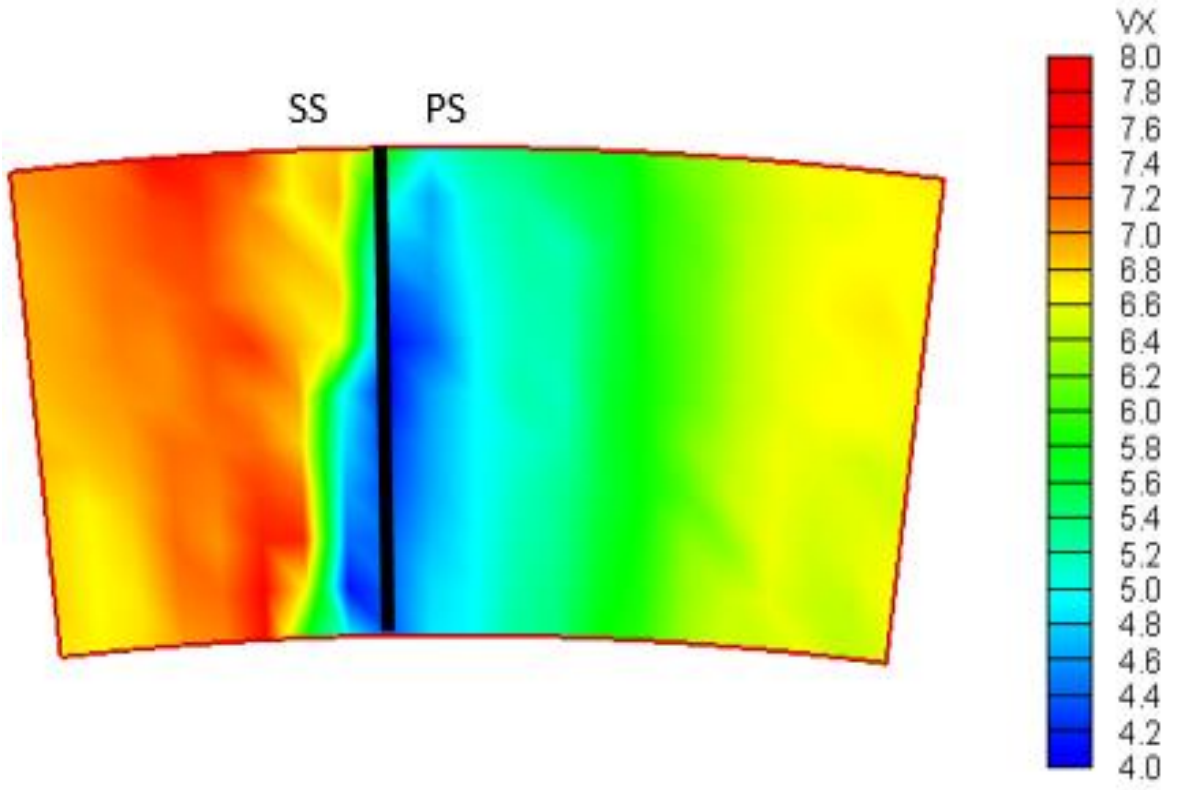

Figure 70 - Axial Velocity (m/s)

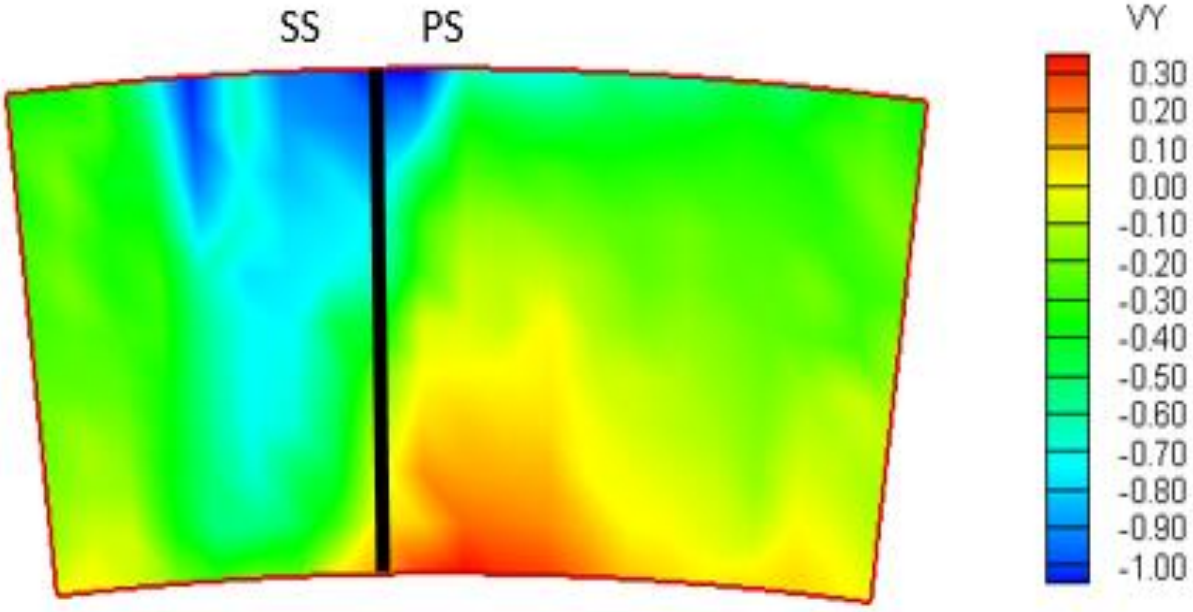

Figure 71 - Radial Velocity (m/s)

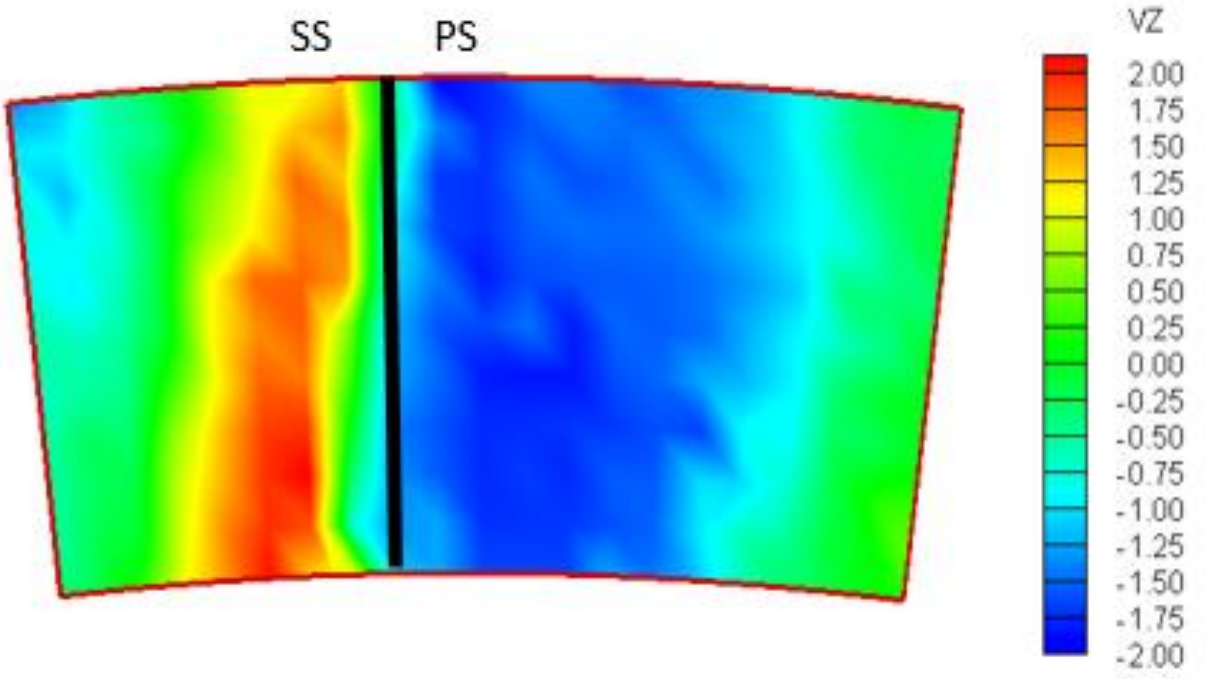

Figure 72 - Azimuthal Velocity (m/s) Positive is Counter-Clockwise

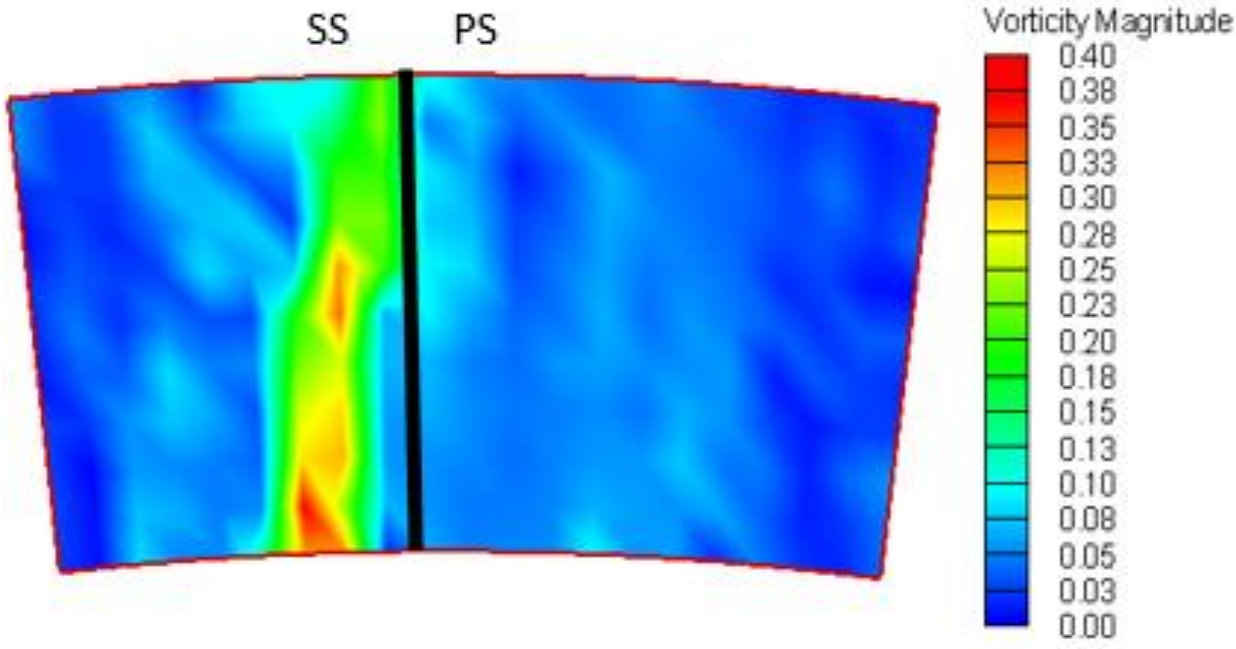

Figure 73 - Vorticity Magnitude (1/s)

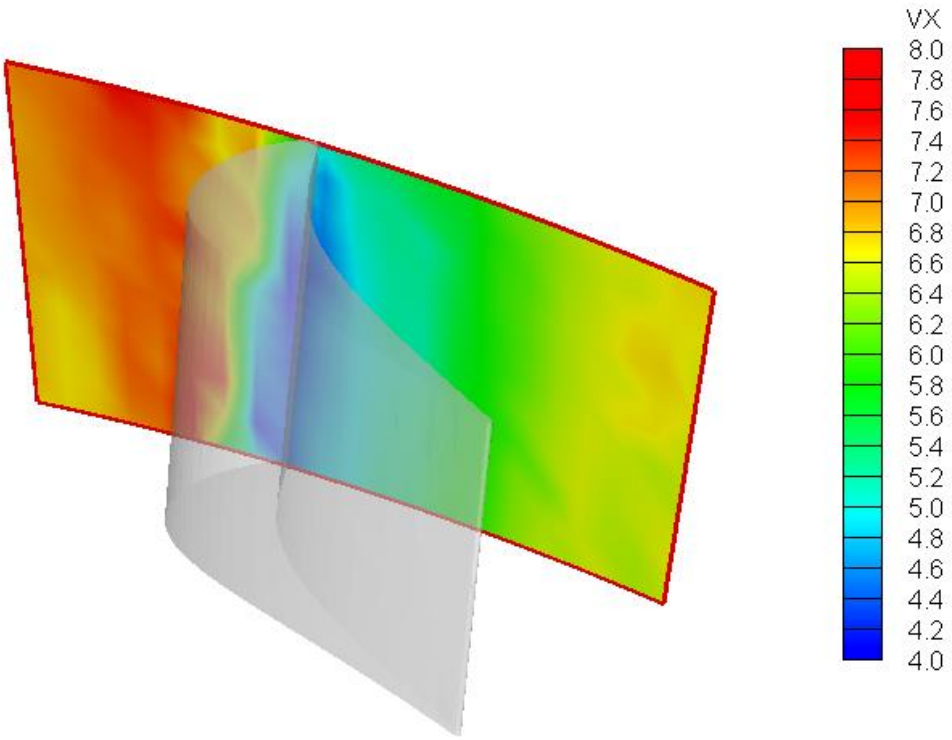

Figure 74 - Axial Velocity Showing the Nozzle Guide Vane (m/s)

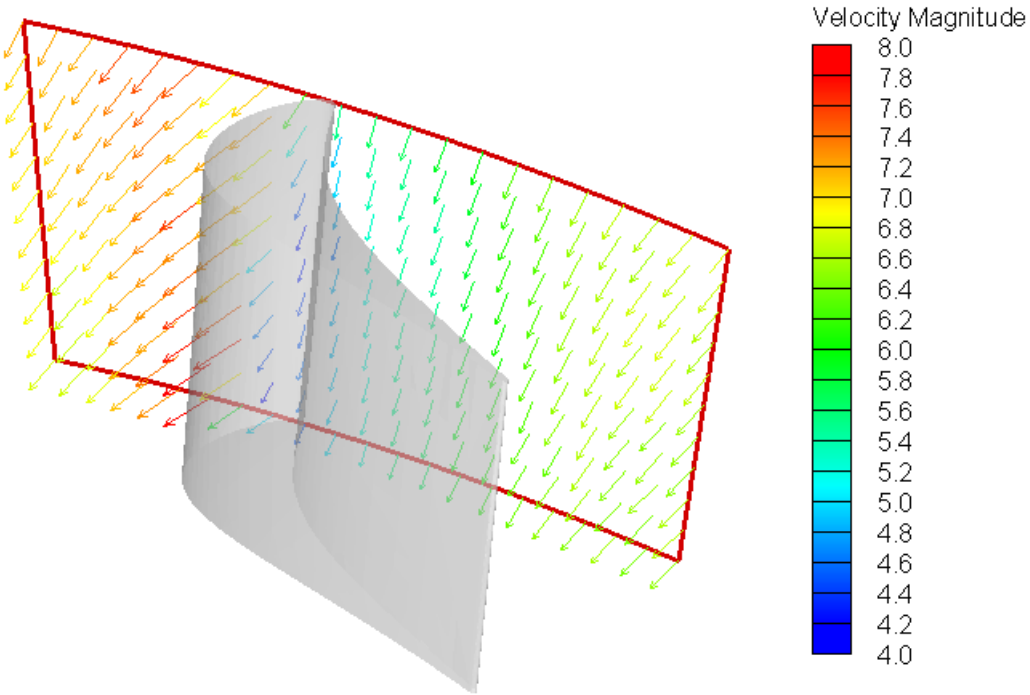

Figure 75 - Velocity Vectors Colored by the Magnitude (m/s)

The above figures show the flow accelerating near the suction side of the blade where the contour of the airfoil reduces the local cross sectional area; likewise, the air decelerates near the pressure side, where the cross sectional area is restored, causing an increase in static pressure. The nozzle guide vanes are used to accelerate and direct the flow, but their contoured shape optimizes the flow and reduces form drag in the mainstream flow. The mainstream and axial velocity contours show the impingement region where the flow dead heads on the leading edge of the airfoil. A 3D iges file was imported into the contour and vector plots to show the location of the measurement grid and offer insight into the location of the corresponding increased and decreased velocities.

4.3 Kiel Probe Total Pressure Analysis

Once the incoming flow was analyzed, the flow leaving the exit guide vanes was explored. Given the turbulent nature of the flow, measurements using the 5-hole probe resulted in various points falling off the calibration curve in both the pitch and yaw directions. Thus, the total pressure was observed using a kiel probe, shown in Figure 76, which is relatively insensitive to pitch and yaw variations. The kiel probe chosen for this application was the United Sensor KCC-12-F-8-C probe with a pitch range of ±49º and a yaw range of ±54º. This probe offered the smallest probe head with the lowest sensitivity to pitch and yaw variation.

Kiel probe measurements were taken downstream of the exit guide vanes in a similar way that the 5-hole probe measurements were taken. A similar grid of 231 points was taken to create a total pressure contour to observe the flow characteristics at the exit of the one and half stages of the rotating turbine cascade.

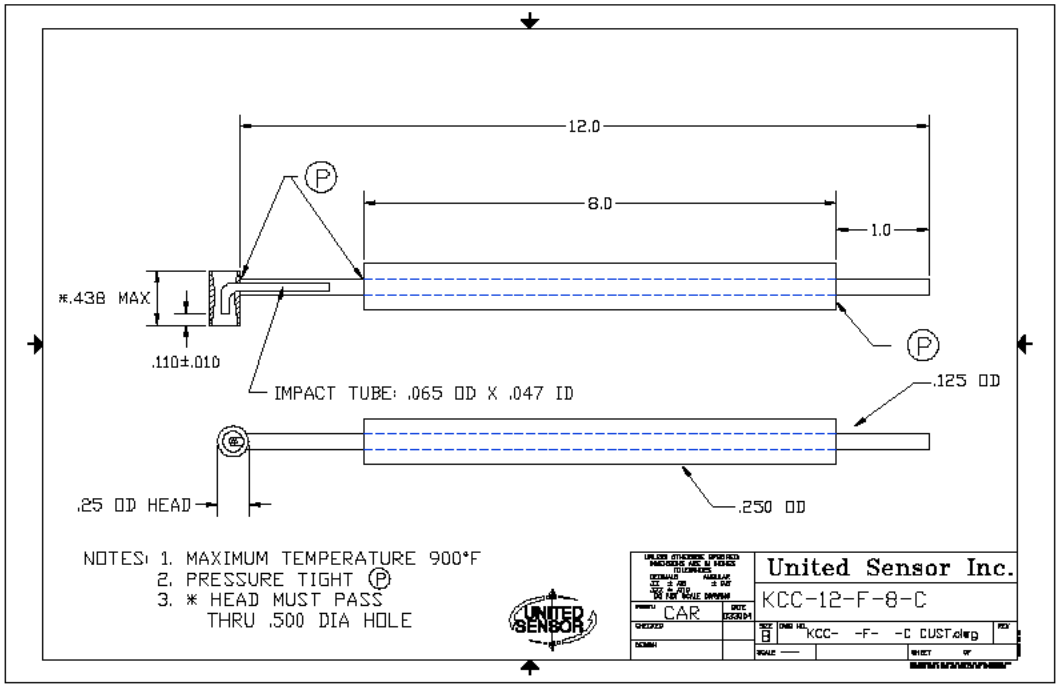

Figure 76 - Kiel Probe Drawing (United Sensor Inc.)

Of particular interest was locating loss structures developed in the flow from the introduction of coolant air and the relative motion of the rotor. Various blowing ratios tests at the design rotor speed were performed to analyze the total pressure loss; then, various rotor speed tests at a constant blowing ratio were conducted to determine the effects of rotor speed on pressure loss.

A total pressure contour was created for two blowing ratios to explore the differences in the flow properties due to the introduction of coolant air at the shroud. A detailed description of the shroud cooling holes was given in the experimental apparatus portion of this report. The total pressure is normalized with the dynamic head to create the pressure coefficient, C_p. Figures 77 and 78 display a consistent location of the shed vortex located at the casing on the suction side of the exit guide vane. This region of low total pressure is consistent regardless of the presence of coolant air. Gaetani et al [38] show a similar shed vortex on the suction side near the casing as well

as the tip leakage vortex spread over the casing near the pressure side. They also show a loss region associated with the shed vortex at the root of the vane. In the test performed in the Tier lab at a blowing ratio of 4, this shed vortex can be seen more clearly.

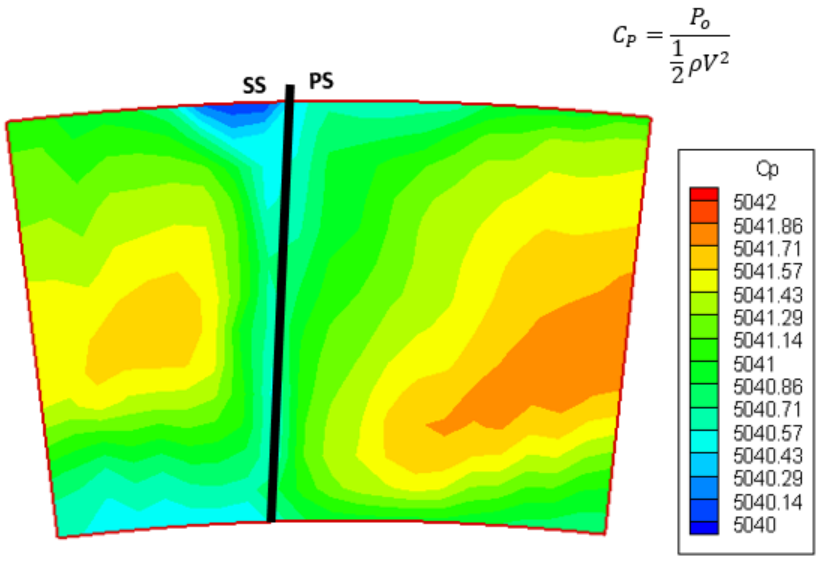

Figure 77 - Pressure Coefficient Contour (BR=2)

Lakshminarayana et al. [39] used Laser Doppler Velocimetry (LDV) to obtain high resolution aerodynamic measurements downstream of a guide vane in an axial flow turbine. They showed the same vortex structure at the casing on the pressure side of the vane. They attribute this to the tip leakage vortex which hugs the suction side of the vane. Test measurements show good periodicity in the flow field at this point and display that the highest total pressure or the region of highest energy is located in the passage and reduces monotonically toward the walls. Another result of interest is that the pressure only varies by 0.03% showing that the flow is highly uniform in terms of total pressure.

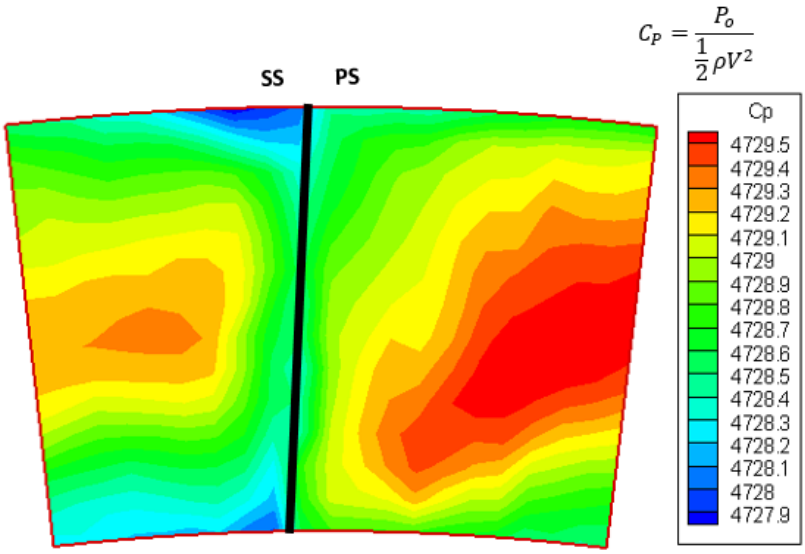

Figure 78 - Pressure Coefficient Contour (BR=4)

4.4 Pressure Loss across the Turbine Stage at Varying Blowing Ratios

Additional testing was performed to observe total pressure losses across the turbine stage at various conditions. First a set of tests were run varying the blowing ratio to observe the effects of introducing the coolant flow at the outer casing. Total pressure measurements were taken one hydraulic diameter upstream of the nozzle guide vanes. These measurements were taken radially from the inner annulus to the outer annulus; and likewise, measurements were taken one hydraulic diameter downstream of the exit guide vanes. In order to normalize the total pressure loss across the one and a half stages, the pressure difference from upstream to downstream of the section was normalized by the dynamic head of the exiting mainstream flow, accounting for the additional mass flow of coolant air, and represented by the pressure loss coefficient below, where P_{o1} is the upstream total pressure and P_{o2} is the downstream total pressure.

$$C_P = \frac{P_{o1} - P_{o2}}{\frac{1}{2}\rho V^2} \quad \text{[Eq. 63]}$$

All of the measurements were taken at the prescribed scaled down design conditions described by the velocity triangles previously detailed in this report, and are compiled in Figure 79 below..

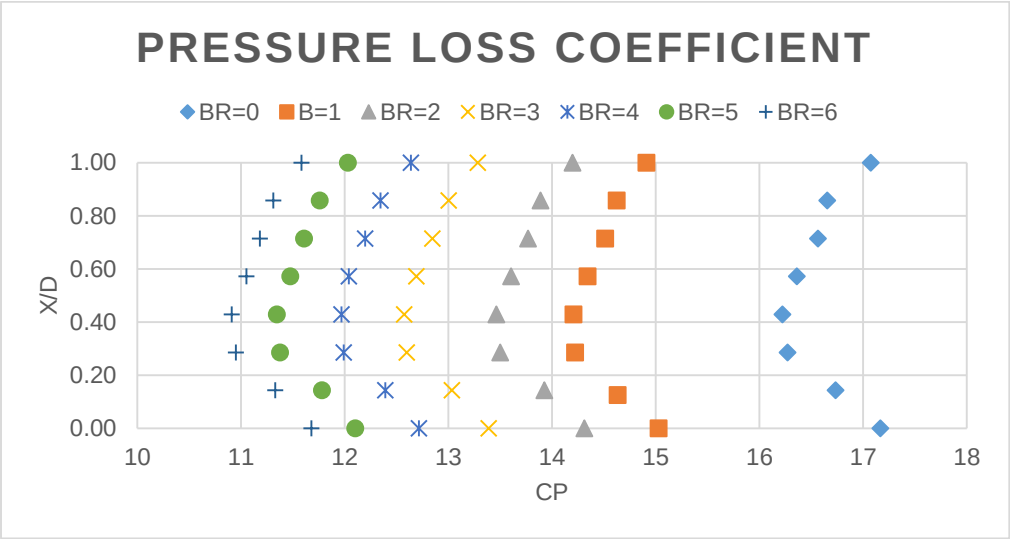

Figure 79 - Pressure Loss at Varying Blowing Ratios

In turbine design, the introduction of additional coolant air results in a reduction in aerodynamic and thermal efficiency. In the measured case described by the plot above, the normalized total pressure loss decreases as the coolant mass flux increases. This is due to the introduction of additional mass flow, which increases the total energy in the flow resulting in a decrease of total pressure loss.

4.5 Pressure Loss across the Turbine Stage at Varying Rotor Speeds

Another point of interest in the performance of the turbine test section was to characterize the losses at off design conditions with no coolant flow. Pressure measurements were taken similarly to the coolant flow analysis. Here, the rotational speed was varied from 55-655 RPM in steps of 100 RPM bracketing the design condition. The inlet velocity was held constant and the fan speed was adjusted to maintain constant inlet flow conditions for this analysis. The total pressure loss

coefficient is shown with respect to the rotor speed in Figure 80 and with respect to the measurement location in Figure 81.

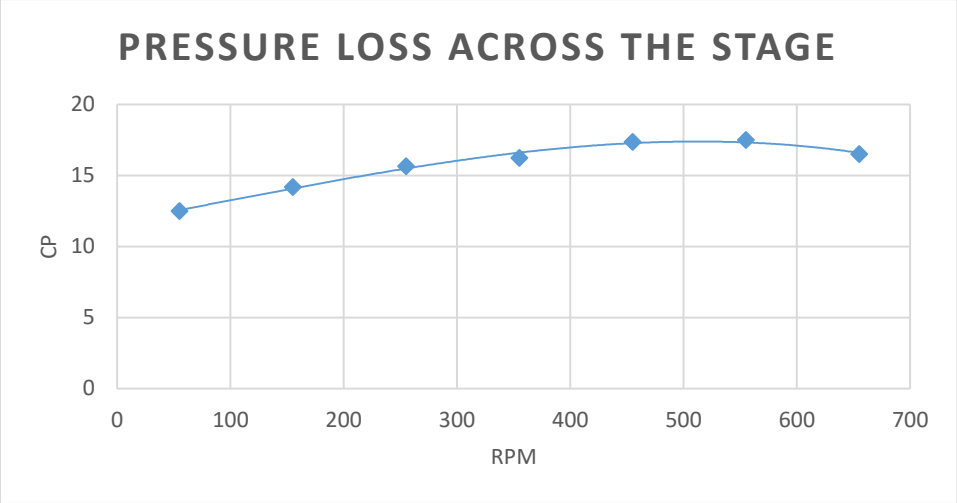

Figure 80 - Total Pressure Loss at Varying Rotor Speed

The pressure loss analysis shows that the pressure loss across the stage increases as the rotor speed increases, peaks at 550 RPM, then begins to reduce at higher speeds. The turbine is designed to extract energy through expanding the flow and extracting shaft work through the rotor.

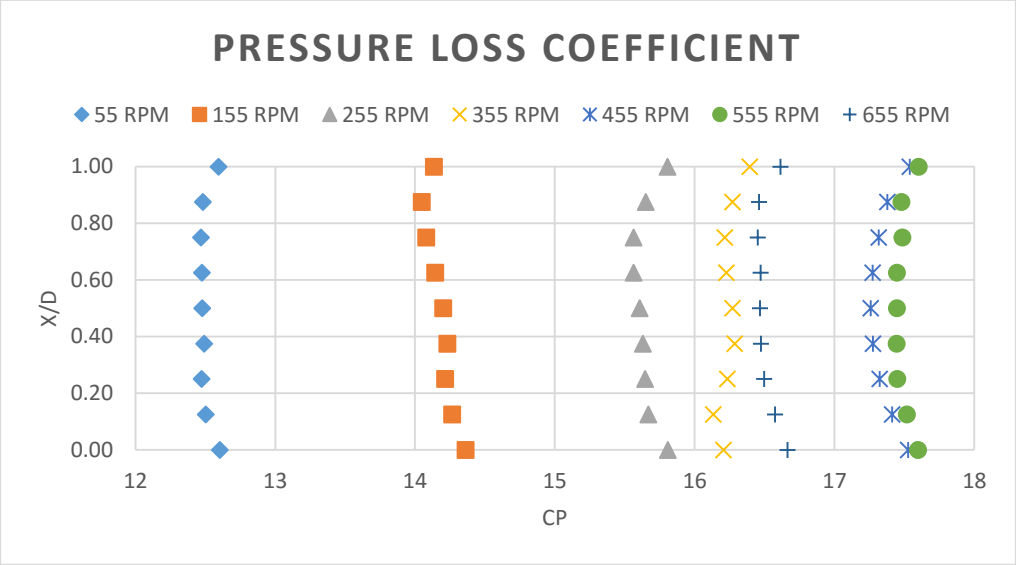

Figure 81 - Total Pressure Loss at Varying Rotor Speed

In order to help explain the phenomena shown above, the velocity triangles can offer insight into the bulk flow pattern through the test section. Figures 82-88 show the velocity triangles consistent with the measured cases, while Figure 89 displays the total pressure loss coefficient plotted against the rotor incidence angle.

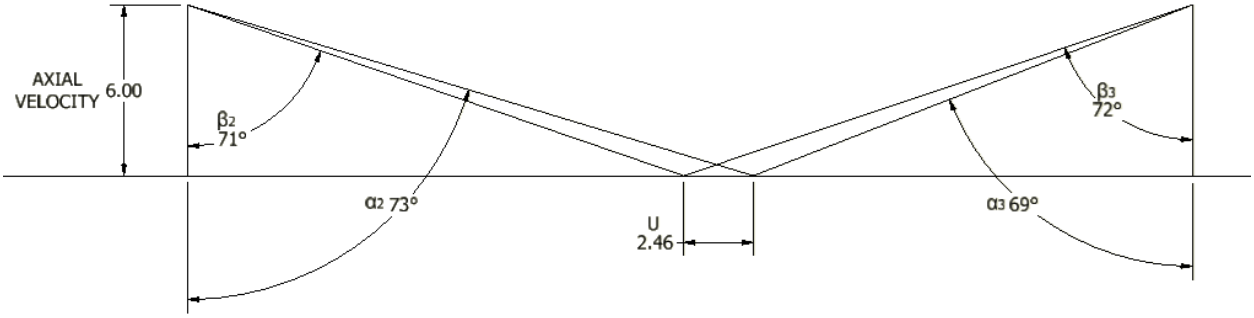

Figure 82 - Rotor Speed 55 RPM

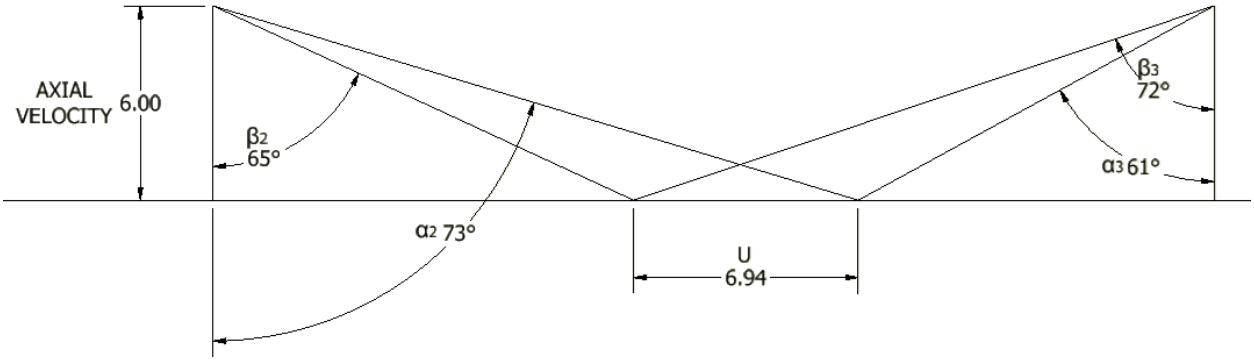

Figure 83 - Rotor Speed 155 RPM

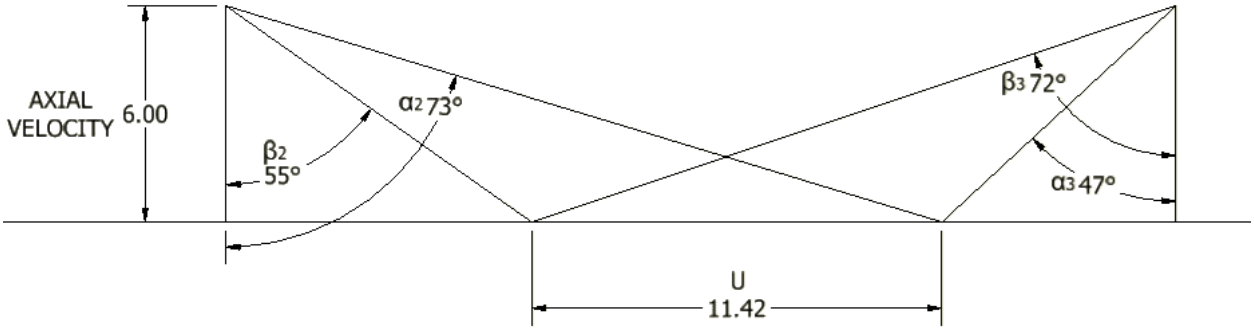

Figure 84 - Rotor Speed 255 RPM

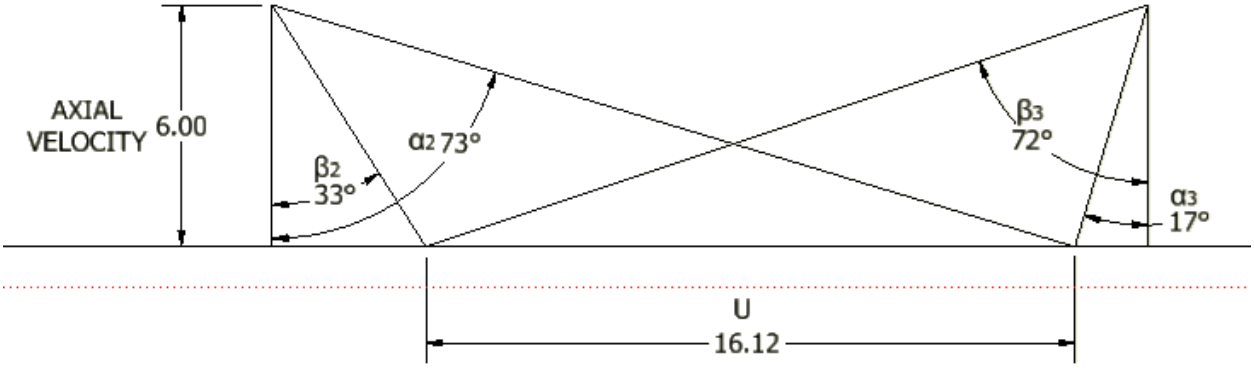

Figure 85 - Rotor Speed 355 RPM (Shown Again for Clarity)

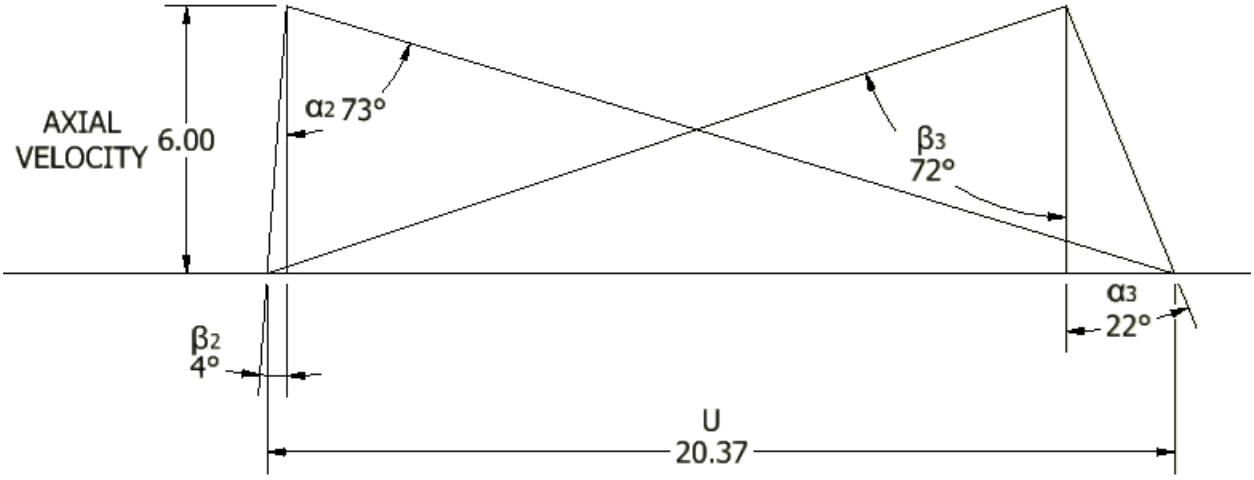

Figure 86 - Rotor Speed 455 RPM

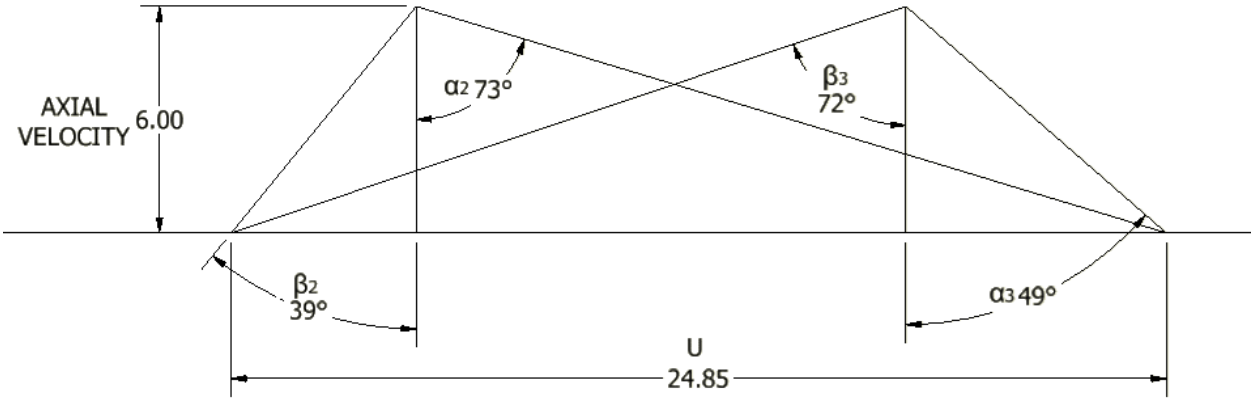

Figure 87 - Rotor Speed 555 RPM

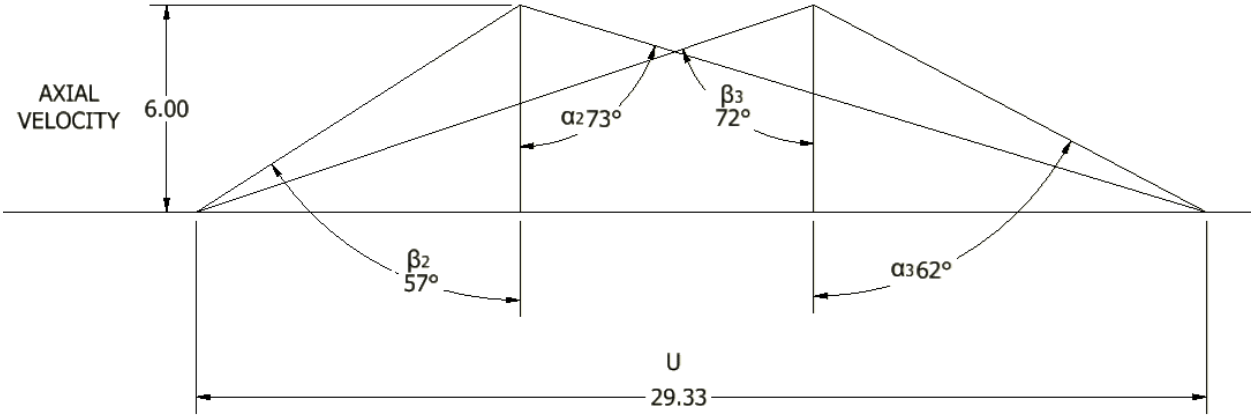

Figure 88 - Rotor Speed 655 RPM

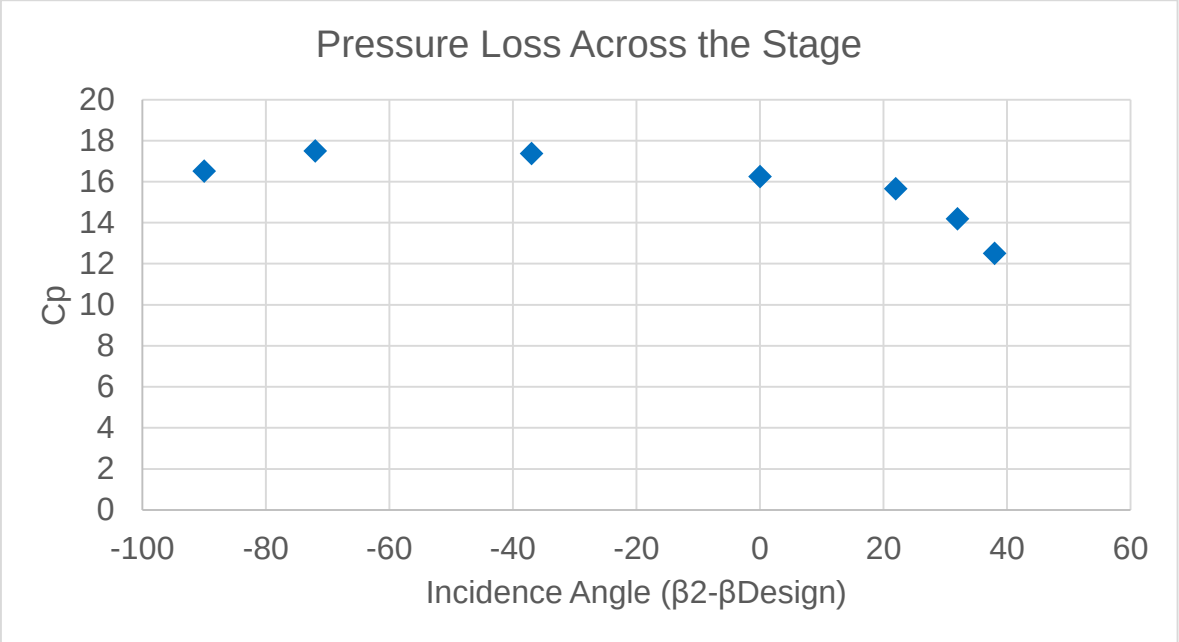

Figure 89 - Pressure Loss with Respect to Incidence Angle

The figure above shows the relationship between the incidence angle and the total pressure loss coefficient. The results are at odds with findings by McVetta et al. [40] who studied the effects of incidence angle on total pressure loss across a turbine stage using a stationary cascade modified to vary the incidence angle. They found that as the incidence angle approaches the design angle, the losses are at a minimum, while as the incidence angle becomes highly positive, the losses increase. Welch et al. [41]

found similar results to McVetta et al in their study when comparing their CFD results to the experimental results performed in the linear cascade. The results in literature are opposite of what was found as a result of testing in the rotating rig. At the TIER Center, the total pressure loss is affected by not only flow losses, but by energy being extracted or added to the flow through the shaft and motor.

Once the rotor speed increases past the design speed, the airflow is no longer impinging the rotor or the exit guide vanes at a positive angle of attack. At low speeds, the pressure drop is lower because the rotor speed is lower causing less viscous losses through the stage. The peak of viscous losses occurs just past the design speed until the total pressure loss begins to decrease again. This decrease in total pressure loss is due to the addition of energy that is greater than the viscous losses in the system. At this point, the rotor is acting as a fan or compressor, and one would expect the curve to continue to a stall point where the viscous losses would again overcome the energy added. These tests show that the test section does not extract energy like a true turbine. During testing, the VFD is used to brake the motor and apply a torque load to slow the rotor down.

Conclusions

In order to find heat transfer coefficients for a unique turbine blade tip and casing design, a film cooled rotating turbine cascade with an actively cooled shroud in a closed loop wind tunnel was designed, built, and validated. This design was unique and offered investigators the ability to fully map out heat transfer coefficients and film cooling effectiveness on a turbine blade tip and shroud whereas most other researchers could only obtain similar information at instrumented locations. Testing had previously been performed in a stationary cascade using IR Thermography, and the effects of rotation on heat transfer and film cooling were desired.

Liquid crystal thermography and transient heat transfer testing were chosen as the means for obtaining heat transfer and film cooling effectiveness due to complications associated with the rotating test pieces. The wind tunnel fan and heater were selected after pressure loss and heat transfer calculations were performed. A unique system was designed to deliver coolant air to the rotating turbine blades through a hollow shaft and hub connected to a rotary union. A requirement of transient testing was the use of non-conductive materials for the test pieces including the shroud and turbine blade. As a result, the blade was fabricated using a selective laser sintering 3D printing technique with a material of ABS plastic while the shroud was formed from Acrylic. The blade, highly loaded at the design speed, required exhaustive analysis. A classical structural analysis as well as a computational FEA model were performed to fully define the stress levels in the blade and ensure proper structure to avoid catastrophic blade loss.

In order to validate the wind tunnel and test rig design, a 5-hole probe analysis was performed. In order to obtain velocity vectors in the flow field, a commercially produced 5-hole probe was purchased. A calibration curve was created for this probe using the straight portion of duct in the closed loop wind tunnel. A unique code was written to extract the locations of the measurements taken, and to convert the pressure readings into velocity visualizations. By analyzing the 5-hole probe measurements, it was concluded that the test section would perform correctly at the design condition at which heat transfer testing was to be performed. The airflow entering the first stage of the test section is uniform and has minimal radial or azimuthal velocity components which is desired for accurate heat transfer testing of the shroud and blade tip region. Measurements revealed the location of the flow turning around the pressure side and suction side of the nozzle guide vane and the flow velocities were observed to be at the desired levels for testing. The performance of the duct, fan, coolant air, and rotor system outperform the requirements for heat transfer testing prescribed by the project sponsor.

In addition to the 5-hole probe measurements taken at the inlet of the turbine stage, a kiel probe was used to extract total pressures at the trailing edge of the exit guide vanes to offer insight into the loss structures from shroud film cooling. A shed vortex near the tip of the exit guide vane was found as well as a weaker loss structure near the root of the vane. These findings were corroborated by results from other studies of vane-blade aerodynamic measurements.

As a supplement to heat transfer testing performed on the test rig, total pressure readings were taken both upstream and downstream of the one and half stage rotating

turbine cascade to explore the overall losses in the system at varying blowing ratio and rotor speed. It was found that as the blowing ratio was increased, the total pressure loss decreased. This was due to the addition of energy into the system via the film cooling flow. When the rotor speed was varied, it was observed that the total pressure loss was lowest at the lowest speed, increased as it approached the design speed, then decreased near the highest test speed of 655 RPM, nearly twice the design speed. When flow losses were compared to the incidence angle, contrary to results published from experiments in a stationary cascade, it was observed that as the incidence angle approaches the design angle the losses increase, while as the incidence angle becomes highly positive or negative, the losses decrease. This could be attributed to extraction or addition of energy into or out of the flow through shaft work. The rotating nature of the test involves a more complex system than that of a stationary cascade which only accounts for the aerodynamic losses.

Future testing could offer more detailed insight into the effects of rotation on the leakage flow. Particle image velocimetry would be an optimal method to investigate this flow if a suitable seeding apparatus and optical access were incorporated into the test section design. Additionally miniaturized flow probes and an electro-mechanical traverse could be designed and implemented to increase the efficiency of aerodynamic measurements taken at various locations in the test section. Additional coding could be applied to automate the traversing system and build on the analysis and visualization coding that can be found in the appendix. Additional heat transfer testing could be performed at various blowing ratios and speed ranges on new vane and blade profiles

given the wide performance parameters of the closed loop wind tunnel and rotating test section.

References

[1] Çengel, Yunus A., and Michael A. Boles. Thermodynamics: An Engineering Approach. Boston: McGraw-Hill Higher Education, 2008. Print.

[2] Hill, Philip Graham, and Carl R. . Peterson. Mechanics and Thermodynamics of Propulsion. Reading, MA: Addison-Wesley, 2010. Print.

[3] Ekkad, S., and J. C. Han. "A Transient Liquid Crystal Thermography Technique for Gas Turbine Heat Transfer Measurements." *Measurement Science and Technology* 11.7 (2000). Web.

[4] Newton, Paul J., Youyou Yan, Nia E. Stevens, Simon T. Evatt, Gary D. Lock, and J.michael Owen. "Transient Heat Transfer Measurements Using Thermochromic Liquid Crystal. Part 1: An Improved Technique. *International Journal of Heat and Fluid Flow* 24.1 (2003): 14-22. Web.

[5] Kwak, Jae Su, and Je-Chin Han, 2003, "Heat Transfer Coefficients and Film Cooling Effectiveness on the Squealer Tip of a Gas Turbine Blade." *Journal of Turbomachinery*. 125: 648-657.

[6] O'Dowd, Devin, Quiang Zheng, Phil Ligrani, Li He, and Stefan Friedrichs. "Gas Turbine." Comparison of Heat Transfer Measurement Techniques on a Transonic Turbine Blade Tip. Proc. of ASME Turbo Expo 2009, Orlando, Florida, USA. ASME, 2009. Print.

[7] Nasir, Hasan, Srinath V. Ekkad, and Ronald S. Bunker. "Effect of Tip and Pressure Side Coolant Injection on Heat Transfer Distributions for a Plane and Recessed Tip." *Journal of Turbomachinery* 129.1 (2007): 151. Print.

[8] Srinivasan, V., and R. J. Goldstein. "Effect of Endwall Motion on Blade Tip Heat Transfer." Journal of Turbomachinery 125.2 (2003): 267. Print.

[9] Cho, Hyung Hee, Dong Ho Rhee, and R. J. Goldstein. "Effects of Hole Arrangements on Local Heat/Mass Transfer for Impingement/Effusion Cooling With Small Hole Spacing." *J. Turbomach. Journal of Turbomachinery* 130.4 (2008): 041003. Web.

[10] Newton, P. J., G. D. Lock, S. K. Krishnababu, H. P. Hodson, W. N. Dawes, J. Hannis, and C. Whitney. "Aerothermal Investigations of Tip Leakage Flow in Axial Flow Turbines—Part III: TIP Cooling." *J. Turbomach. Journal of Turbomachinery* 131.1 (2009): 011008. Web.

[11] Christophel, J. R., K. A. Thole, and F. J. Cunha. "Cooling the Tip of a Turbine Blade Using Pressure Side Holes—Part II: Heat Transfer Measurements." *J. Turbomach. Journal of Turbomachinery* 127.2 (2005): 278. Web.

[12] Kwak, Jae Su, Jaeyong Ahn, Je-Chin Han, C. Pang Lee, Ronald S. Bunker, Robert Boyle, and Raymond Gaugler. "Heat Transfer Coefficients on the Squealer Tip and Near-Tip Regions of a Gas Turbine Blade With Single or Double Squealer." *J. Turbomach. Journal of Turbomachinery* 125.4 (2003): 778. Web.

[13] Azad, Gm Salam, Je-Chin Han, Ronald S. Bunker, and C. Pang Lee. "Effect of Squealer Geometry Arrangement on a Gas Turbine Blade Tip Heat Transfer." *J. Heat Transfer Journal of Heat Transfer* 124.3 (2002): 452. Web.

[14] Saxena, Vikrant, and Srinath V. Ekkad. "Effect of Squealer Geometry on Tip Flow and Heat Transfer for a Turbine Blade in a Low Speed Cascade."J. *Heat Transfer Journal of Heat Transfer* 126.4 (2004): 546. Web.

[15] Srinivasan, V., and R. J. Goldstein. "Effect of Endwall Motion on Blade Tip Heat Transfer." *J. Turbomach. Journal of Turbomachinery* 125.2 (2003): 267. Web.

[16] Palafox, P., M. L. G. Oldfield, P. T. Ireland, T. V. Jones, and J. E. Lagraff. "Blade Tip Heat Transfer and Aerodynamics in a Large Scale Turbine Cascade With Moving Endwall." *J. Turbomach. Journal of Turbomachinery* 134.2 (2012): 021020. Web.

[17] Zhang, Q., O. O'Dowd, L. He, M. L. G. Oldfield, and P. M. Ligrani. "Transonic Turbine Blade Tip Aero-Thermal Performance with Different Tip Gaps: Part I - Tip Heat Transfer." Gas Turbine. Proc. of ASME Turbo Expo, Glasgow, UK. Rolls Royce, 2010. Print.

[18] Jackson, Adam J., Andrew P.s. Wheeler, and Roger W. Ainsworth. "An Experimental and Computational Study of Tip Clearance Effects on a Transonic Turbine Stage." *International Journal of Heat and Fluid Flow* 56 (2015): 335-43. Web.

[19] Acharya, S., Kramer, G. Moreaux, L., Nakamata, C., 2010, “Squealer Tip Heat Transfer with Film Cooling,” ASME GT2010-23688.

[20] Mhetras, Shantanu, Diganta Narzary, Zhihong Gao, and Je-Chin Han. "Effect of a Cutback Squealer and Cavity Depth on Film-Cooling Effectiveness on a Gas Turbine Blade Tip." *Journal of Turbomachinery* 130.2 (2008): 021002. Print.

[21] Wang, Jianhua, Yalin Lui, Xiaochun Wang, and Zhineng Yang. "Characteristics of Tip Leakage Flow of the Turbine Blade with Cutback Squealer and Coolant Injection." ASME Turbo Expo (2010). Print.

[22] Tamunobere, Onieluan, and Sumanta Acharya. "Turbine Blade Tip Film Cooling With Blade Rotation Part I: Tip And Pressure Side Coolant Injection." *J. Turbomach Journal of Turbomachinery* (2016): n. pag. Web.

[23] Pietrzyk, J., Bogard, D., & Crawford, M. 1990. “Effects of Density Ratio on the Hydrodynamics of Film Cooling” *ASME J. TurboMachinery*, 112, 437-443.

[24] Kanjirakkad, V., Thomas, R., Hodson, H., Janke, E., Haselbach, F., & Whitney, C. (n.d). “Passive shroud cooling concepts for HP turbines: Experimental investigations*.” Journal of Turbomachinery-Transactions of the ASME*, 130(1).

[25] Michel, Brice, Pierre Gajan, Alain Strzelecki, Nicolas Savary, Azeddine Kourta, and Henri-Claude Boisson. 2009 "Full Coverage Film Cooling Using Compound Angle." *C.R. Mecanique* 337: 562-72.

[26] Rahman, M. H., Kim, S.I., Hassan, I. “Tip Leakage Flow and Heat Transfer on Turbine Blade Tip and Casing, Part 1: Effect of Tip Clearance Height and Rotation Speed.” *International Journal for Computational Methods in Engineering Science and Mechanics*. 14:4, 290-303.

[27] Yaras, M.I., Sjolander, S.A., Kind, R.J., 1992. Effects of simulated rotation on tip leakage in a planar cascade of turbine blades: Part II-Downstream flow field and blade loading. *J. Turbomach*. 114, 660–667.

[28] Tallman J., Lakshminarayana, B., “Numerical Simulation of Tip Leakage Flows in Axial Flow Turbines, with Emphasis on Flow Physics: Part II-Effect of Outer Casing Relative Motion, *J. Turbomach*., vol. 123, pp. 324-333, 2001.

[29] Thorpe, S.J., S. Yoshino, R.W. Ainsworth, and N.W. Harvey, 2004, "An Investigation Of The Heat Transfer And Static Pressure On The Over-tip Casing Wall Of An Axial Turbine Operating At Engine Representative Flow Conditions. (I). Time-mean Results." *International Journal of Heat and Fluid Flow* 25: 933-944.

[30] Thorpe, S.J., S. Yoshino, R.W. Ainsworth, and N.W. Harvey, 2004, "An Investigation Of The Heat Transfer And Static Pressure On The Over-tip Casing Wall Of An Axial Turbine Operating At Engine Representative Flow Conditions. (II). Time-Resolved Results." *International Journal of Heat and Fluid Flow* 25: 945-960.

[31] Tamunobere, Onieluan, Christopher Drewes, Sumanta Acharya, and Chiyuki Nakamata. "Heat Transfer to an Actively Cooled Shroud with Blade Rotation." *Journal of Thermal Science and Engineering Applications J. Thermal Sci. Eng. Appl* (2015): n. pag. Web.

[32] Ostanek, Jason K., J. Prausa, A. Van Suetendael, and Karen A. Thole. "Establishing a Methodology for Resolving Convective Heat Transfer from Complex Geometries." *Journal of Turbomachinery* 031014th ser. 132.3 (2010). ASME Digital Library. Web.

[33] Incropera, Frank P., and David P. DeWitt. Fundamentals of Heat and Mass Transfer. New York: J. Wiley, 2002. Print.

[34] Lee, C. S., and N. J. Wood. Calibration and Data Reduction for a Five-Hole Probe. Stanford, CA: Stanford University, 1986. JIAA TR-73.

[35] United States. Department of the Navy. Naval Sea Systems Command. The Calibration and Application of Five-Hole Probes. By A. L. Treaster and A. M. Yocum. Technical Memorandum File No. TM 78-10.

[36] "ASM Material Data Sheet." ASM Material Data Sheet. N.p., n.d. Web. 29 Dec. 2014.

[37] Moffat, Robert J. "Describing the Uncertainties in Experimental Results." *Experimental Thermal and Fluid* Science 1.1 (1988): 3-17. Web.

[38] Gaetani, P., G. Persico, V. Dossena, and C. Osnaghi. "Investigation of the Flow Field in a High-Pressure Turbine Stage for Two Stator-Rotor Axial Gaps—Part I: Three-Dimensional Time-Averaged Flow Field." *J. Turbomach. Journal of Turbomachinery* 129.3 (2007): 572. Web.

[39] Lakshminarayana, B., D. Ristic, and S. Chu. The Three Dimensional Flow Field at the Exit of an Axial-Flow Turbine Rotor. Tech. no. E-11092. Cleveland, Ohio: National Aeronautics and Space Administration, 1998. Print.

[40] Mcvetta, Ashlie B., Paul W. Giel, and Gerard E. Welch. "Aerodynamic Measurements of a Variable-Speed Power-Turbine Blade Section in a Transonic Turbine Cascade at Low Inlet Turbulence." Tech. no. E-18745. Cleveland, Ohio: National Aeronautics and Space Administration 2013. Web.

[41] Welch, Gerard E., Ashlie B. Mcvetta, Mark A. Stevens, Samuel A. Howard, Paul W. Giel, Ali A. Ameri, Waiming To, Gary J. Skoch, and Douglas R. Thurman. "Variable-Speed Power-Turbine Research at Glenn Research Center." Tech. no. E-18186. Cleveland, Ohio: National Aeronautics and Space Administration 2012. Web.

[42] Budynas, Richard G., J. Keith. Nisbett, and Joseph Edward. Shigley.Shigley's Mechanical Engineering Design. New York: McGraw-Hill, 2011. Print.

Appendix 1: Five-Hole and Kiel Probe MatLab Code

Appendix 1.1 Generate Calibration Input List

This code was used to generate the input list for measurements taken for the 5-hole probe calibration. Each measurement was denoted with its pitch and yaw angle which will be extracted in a later code.

```
clear all
clc
close all
% % % INPUT PARAMETERS
 input_dir = 'C:\Users\cdrewe1\Desktop\5_Hole_Probe\Calibration';
input_file = 'input.txt';
 % % % END INPUT PARAMETERS
 % Filter CSV files
files = dir(strcat(input_dir,'\*.csv'));
 % Open file for writing
out_path = strcat(input_dir,'\',input_file);
fout = fopen(out_path, 'w');

for i=1: length(files)
    fname = files(i).name;
    s1 = regexp(fname, '.csv', 'split');
    s1 = s1{1};
    s2 = regexp(s1, '_b', 'split');
    sb1 = s2{2};
    if sb1(1) == '_'
        sb2 = regexp(sb1, '_', 'split');
        sb = -1 * str2num(sb2{2});
    else
        sb = str2num(sb1);
    end
    s3 = regexp(s2{1}, '_a', 'split');
    sa1 = s3{2};
    if sa1(1) == '_'
        sa2 = regexp(sa1, '_', 'split');
        sa = -1 * str2num(sa2{2});
    else
        sa = str2num(sa1);
    end
    fprintf(fout, '%s\t%f\t%f\n', fname, sa, sb);
end

fclose(fout);
```

Appendix 1.2 Create Calibration Matrix

This code was used to create the calibration matrix used to extract the velocity vectors from the 5-hole probe measurements. The pitch and yaw angles are extracted from the file names and the pressure coefficients are taken from the measurement files themselves, averaged, and stored in a matrix.

```
clear all
clc
close all

% % % INPUT PARAMETERS

input_dir = 'C:\Users\cdrewe1\Desktop\5_Hole_Probe\Calibration';
input_file = 'input.txt';
output_file = 'calibration.csv';
stats_file = 'stats.txt';

% % % END INPUT PARAMETERS

in_path = strcat(input_dir, '/', input_file);
out_path = strcat(input_dir, '/', output_file);
stats_path = strcat(input_dir, '/', stats_file);

input_data = importdata(in_path, '\t');
in_files = input_data.rowheaders;
alphas = input_data.data(:,1);
betas = input_data.data(:,2);

fout = fopen(out_path, 'w');
fstats = fopen(stats_path, 'w');
fprintf(fout,
'Alpha,Beta,P_bar,C_py,C_pp,C_pt,C_ps,P1,P2,P3,P4,P5,Pstatic,Ptotal\n');
N = length(in_files);
P_bar = zeros(N,1);
C_py = zeros(N,1);
C_pp = zeros(N,1);
C_pt = zeros(N,1);
C_ps = zeros(N,1);

for fn=1:length(in_files),
    fname = in_files{fn};
    fpath = strcat(input_dir, '/', fname);
    alpha = alphas(fn);
    beta = betas(fn);
    data = importdata(fpath, '\t');
%     t = data(:,1);
    p1s = data(:,3);
    p2s = data(:,4);
```

```
    p3s = data(:,5);
    p4s = data(:,6);
    p5s = data(:,7);
    pss = data(:,9);
    pts = data(:,10);
    p1 = mean(p1s);
    p2 = mean(p2s);
    p3 = mean(p3s);
    p4 = mean(p4s);
    p5 = mean(p5s);
    ps = mean(pss);
    pt = mean(pts);

    p_bar = mean([p2, p3, p4, p5]);
    c_py = (p2 - p3) / (p1 - p_bar);
    c_pp = (p4 - p5) / (p1 - p_bar);
    c_pt = (p1 - pt) / (p1 - p_bar);
    c_ps = (p_bar - ps) / (p1 - p_bar);

    fprintf('%s\tstd: %.2f, %.2f, %.2f, %.2f, %.2f, %.2f, %.2f\n', fname,
std(p1s), std(p2s), std(p3s), std(p4s), std(p5s), std(pss), std(pts));
    fprintf(fstats, '%s\tstd: %.2f, %.2f, %.2f, %.2f, %.2f, %.2f, %.2f\n',
fname, std(p1s), std(p2s), std(p3s), std(p4s), std(p5s), std(pss), std(pts));

    P_bar(fn) = p_bar;
    C_py(fn) = c_py;
    C_pp(fn) = c_pp;
    C_pt(fn) = c_pt;
    C_ps(fn) = c_ps;


    fprintf(fout, '%f,%f,%f,%f,%f,%f,%f,%f,%f,%f,%f,%f,%f,%f,%f\n', alpha, beta,
p_bar, c_py, c_pp, c_pt, c_ps, p1, p2, p3, p4, p5, ps, pt);
end

fclose(fout);
fclose(fstats);
```

Appendix 1.2.1 Calibration Matrix Result

Alpha	Beta	P_bar	C_py	C_pp	C_pt	C_ps	P1	P2	P3	P4	P5	Pstatic	Ptotal
0	0	12.57	-0.37	0.04	-0.38	1.03	21.72	3.82	7.21	19.79	19.45	3.18	25.16
0	10	12.44	1.13	0.00	-0.52	1.19	20.95	10.98	1.35	18.73	18.69	2.26	25.37
0	15	12.11	2.11	0.00	-0.55	1.11	20.74	14.83	-3.35	18.47	18.49	2.54	25.49
0	20	10.74	2.94	0.03	-0.76	1.03	18.97	16.81	-7.38	16.91	16.63	2.27	25.20
0	25	9.55	3.96	-0.02	-1.26	1.09	16.59	18.75	-9.17	14.23	14.40	1.89	25.48
0	5	12.56	0.56	0.00	-0.48	1.20	21.20	8.66	3.79	18.88	18.91	2.20	25.34
0	-10	10.52	-2.44	0.04	-0.89	0.93	18.47	-5.29	14.10	16.81	16.45	3.12	25.52
0	-15	9.97	-3.61	0.00	-1.49	1.05	16.13	-5.58	16.71	14.36	14.37	3.49	25.31
0	-20	8.81	-6.01	-0.02	-3.24	1.46	12.71	-5.33	18.14	11.18	11.26	3.12	25.35
0	-5	11.58	-1.23	0.01	-0.53	1.04	20.37	-0.46	10.37	18.24	18.17	2.46	25.01
10	0	12.28	-0.48	-0.34	-0.57	1.13	20.77	4.15	8.20	16.92	19.85	2.66	25.60
10	10	12.16	1.04	-0.35	-0.51	1.18	20.67	10.61	1.78	16.64	19.62	2.11	25.04
10	15	11.87	2.07	-0.37	-0.67	1.10	20.17	14.64	-2.51	16.14	19.20	2.76	25.69
10	20	10.55	2.88	-0.39	-0.84	1.03	18.56	16.45	-6.61	14.61	17.73	2.28	25.33
10	25	9.61	3.85	-0.48	-1.24	1.03	16.67	18.71	-8.46	12.42	15.79	2.33	25.41
10	5	12.29	0.53	-0.36	-0.56	1.19	20.70	8.69	4.26	16.61	19.60	2.27	25.38
10	-10	10.24	-2.37	-0.36	-0.96	0.89	18.14	-4.96	13.79	14.67	17.47	3.22	25.70
10	-15	8.95	-3.60	-0.52	-1.69	1.04	15.01	-6.16	15.66	11.58	14.70	2.63	25.25
10	-20	8.55	-5.97	-0.87	-3.34	1.33	12.45	-5.40	17.88	9.17	12.55	3.39	25.48
10	-25	7.92	-7.09	-1.00	-4.17	1.39	11.30	-5.69	18.23	7.89	11.27	3.24	25.36
10	-5	11.47	-1.21	-0.33	-0.62	1.02	20.20	-0.07	10.46	16.29	19.21	2.59	25.57
15	0	11.87	-0.48	-0.54	-0.63	1.10	20.26	4.23	8.27	15.21	19.75	2.66	25.52
15	10	11.79	1.01	-0.56	-0.62	1.14	20.20	10.60	2.14	14.84	19.59	2.22	25.43
15	15	10.60	1.99	-0.59	-0.77	1.05	18.85	13.49	-2.90	13.46	18.36	1.92	25.24
15	20	10.23	2.76	-0.62	-0.88	0.99	18.30	16.11	-6.18	13.01	17.98	2.24	25.42
15	25	8.92	3.64	-0.70	-1.27	0.94	16.19	17.87	-8.60	10.68	15.74	2.08	25.45
15	5	11.87	0.52	-0.58	-0.59	1.16	20.19	8.70	4.40	14.79	19.59	2.20	25.10
15	-10	9.89	-2.34	-0.58	-0.95	0.83	17.87	-4.91	13.72	13.09	17.68	3.30	25.44
15	-15	8.70	-3.50	-0.78	-1.62	0.92	14.96	-6.23	15.71	10.21	15.09	2.96	25.12
15	-20	7.69	-5.63	-1.24	-3.27	1.11	11.81	-6.09	17.13	7.30	12.41	3.13	25.30
15	-25	7.20	-6.55	-1.49	-4.08	1.08	10.76	-6.04	17.32	6.09	11.42	3.34	25.32
15	-5	10.85	-1.15	-0.56	-0.69	0.99	19.28	0.41	10.11	14.08	18.81	2.54	25.11
20	0	11.17	-0.42	-0.79	-0.79	1.08	19.28	4.68	8.12	12.72	19.16	2.43	25.65
20	10	11.33	0.96	-0.81	-0.76	1.15	19.34	10.60	2.91	12.64	19.16	2.08	25.41
20	15	10.39	1.90	-0.82	-0.86	1.07	18.40	13.40	-1.82	11.70	18.28	1.84	25.27
20	20	10.36	2.62	-0.84	-0.99	0.99	18.12	16.06	-4.33	11.58	18.11	2.68	25.81
20	25	8.21	3.54	-0.97	-1.44	0.93	15.11	16.86	-7.54	8.43	15.11	1.79	25.07
20	5	11.23	0.51	-0.80	-0.70	1.15	19.38	8.70	4.58	12.59	19.07	1.91	25.10
20	-10	8.67	-2.21	-0.81	-1.15	0.78	16.36	-4.66	12.31	10.41	16.62	2.70	25.19

20	-15	7.97	-3.20	-1.07	-1.83	0.84	14.04	-5.11	14.35	8.08	14.55	2.84	25.18
20	-20	7.60	-4.98	-1.61	-3.26	0.97	11.80	-4.71	16.18	6.09	12.84	3.54	25.46
20	-25	6.95	-5.74	-1.84	-3.97	0.87	10.69	-5.09	16.36	4.85	11.71	3.70	25.52
20	-5	10.61	-1.08	-0.78	-0.80	0.97	18.83	1.30	10.22	12.26	18.65	2.61	25.37
25	0	11.18	-0.44	-0.94	-0.78	1.04	19.21	5.11	8.65	11.69	19.26	2.85	25.47
25	10	11.21	0.87	-0.96	-0.75	1.11	19.23	10.67	3.67	11.40	19.11	2.35	25.28
25	15	10.39	1.74	-0.98	-0.88	1.06	18.31	13.17	-0.58	10.60	18.36	1.99	25.26
25	20	9.36	2.50	-1.04	-1.12	0.96	16.97	14.98	-4.08	9.33	17.22	2.08	25.51
25	25	8.33	3.25	-1.09	-1.39	0.88	15.48	16.61	-6.65	7.80	15.56	2.03	25.44
25	5	11.33	0.41	-0.96	-0.73	1.14	19.21	8.95	5.72	11.55	19.10	2.36	24.98
25	-10	8.30	-2.16	-1.02	-1.27	0.74	15.73	-3.95	12.11	8.73	16.32	2.84	25.18
25	-15	7.74	-3.12	-1.27	-1.93	0.76	13.83	-4.80	14.18	6.93	14.67	3.14	25.59
25	-20	6.21	-4.67	-1.80	-3.33	0.77	10.60	-5.83	14.68	4.04	11.95	2.83	25.25
25	-25	5.83	-5.25	-2.05	-3.86	0.70	9.79	-5.70	15.04	2.95	11.04	3.06	25.07
25	-5	10.00	-1.07	-0.93	-0.86	0.94	18.17	1.21	9.91	10.64	18.25	2.29	25.20
5	0	12.19	-0.48	-0.14	-0.52	1.14	20.86	3.62	7.77	18.07	19.29	2.27	25.36
5	10	12.23	1.13	-0.17	-0.56	1.19	20.64	10.88	1.35	17.65	19.04	2.25	25.32
5	15	11.41	2.13	-0.18	-0.65	1.11	19.80	14.20	-3.67	16.80	18.31	2.11	25.27
5	20	10.52	2.93	-0.17	-0.79	1.02	18.79	16.61	-7.58	15.83	17.24	2.09	25.31
5	25	9.89	3.92	-0.25	-1.17	1.07	17.10	19.19	-9.06	13.82	15.61	2.21	25.54
5	5	12.72	0.54	-0.17	-0.43	1.20	21.35	8.78	4.15	18.24	19.69	2.33	25.11
5	-10	10.24	-2.44	-0.15	-0.90	0.91	18.18	-5.52	13.86	15.73	16.90	3.05	25.33
5	-15	9.66	-3.66	-0.24	-1.59	1.09	15.69	-5.70	16.35	13.26	14.73	3.11	25.27
5	-20	8.68	-5.82	-0.42	-3.12	1.32	12.77	-5.60	18.20	10.20	11.92	3.30	25.51
5	-25	8.03	-7.13	-0.52	-4.04	1.36	11.46	-6.01	18.44	8.95	10.73	3.36	25.29
5	-5	11.25	-1.23	-0.16	-0.63	1.03	19.96	-0.62	10.09	17.07	18.44	2.25	25.48
0	-25	8.22	-8.25	0.10	-4.59	1.61	11.23	-5.89	18.92	10.08	9.78	3.38	25.02
-10	0	12.05	-0.45	0.36	-0.51	1.07	20.89	3.93	7.89	19.78	16.59	2.61	25.41
-10	10	11.69	1.08	0.36	-0.56	1.11	20.45	10.45	1.01	19.22	16.10	1.99	25.32
-10	15	11.16	2.00	0.35	-0.59	1.05	19.94	13.89	-3.70	18.76	15.70	1.97	25.15
-10	20	10.99	2.79	0.43	-0.79	0.94	19.32	17.08	-6.18	18.32	14.75	3.14	25.93
-10	25	9.49	3.78	0.41	-1.22	0.99	16.75	18.59	-8.87	15.61	12.62	2.31	25.58
-10	5	12.23	0.54	0.34	-0.52	1.08	21.08	8.65	3.85	19.71	16.71	2.64	25.65
-10	-10	9.94	-2.23	0.44	-0.87	0.81	18.17	-5.04	13.32	17.56	13.92	3.27	25.34
-10	-15	9.83	-3.41	0.53	-1.39	0.92	16.37	-5.81	16.52	16.03	12.59	3.80	25.47
-10	-20	8.06	-5.66	0.76	-3.11	1.24	12.22	-6.17	17.35	12.11	8.97	2.89	25.14
-10	-25	7.90	-6.75	0.87	-3.82	1.20	11.48	-6.08	18.03	11.38	8.29	3.60	25.14
-10	-5	11.39	-1.16	0.37	-0.56	0.98	20.38	-0.16	10.27	19.38	16.06	2.62	25.45
-15	0	11.51	-0.37	0.59	-0.58	1.02	20.35	4.35	7.60	19.66	14.41	2.52	25.50
-15	10	11.49	1.03	0.57	-0.58	1.07	20.23	10.58	1.59	19.36	14.41	2.12	25.29
-15	15	10.70	1.92	0.56	-0.67	1.02	19.26	13.56	-2.91	18.49	13.67	2.01	25.01
-15	20	9.59	2.68	0.61	-0.89	0.91	17.95	15.75	-6.67	17.20	12.07	1.99	25.37

-15	25	8.74	3.60	0.65	-1.27	0.90	16.15	17.82	-8.89	15.44	10.59	2.04	25.53
-15	5	11.84	0.51	0.54	-0.52	1.02	20.79	8.69	4.17	19.65	14.84	2.70	25.41
-15	-10	9.10	-2.09	0.64	-0.96	0.74	17.53	-5.03	12.62	17.10	11.69	2.84	25.64
-15	-15	8.67	-3.37	0.77	-1.53	0.86	15.24	-6.69	15.43	15.49	10.47	3.04	25.28
-15	-20	7.89	-5.21	1.07	-3.01	1.07	12.20	-5.81	16.67	12.67	8.03	3.29	25.18
-15	-25	7.61	-6.40	1.21	-3.69	1.14	11.34	-6.34	17.52	11.89	7.38	3.35	25.10
-15	-5	10.75	-1.08	0.55	-0.65	0.95	19.54	0.33	9.79	18.86	14.00	2.35	25.25
-20	0	11.02	-0.35	0.80	-0.62	0.97	19.85	4.92	7.97	19.14	12.04	2.46	25.37
-20	10	11.11	0.94	0.80	-0.61	1.07	19.65	10.67	2.64	19.00	12.13	1.98	24.83
-20	15	10.36	1.76	0.79	-0.74	0.99	18.85	13.26	-1.71	18.31	11.60	1.98	25.09
-20	20	9.11	2.44	0.85	-0.96	0.89	17.31	15.06	-4.98	16.68	9.69	1.83	25.17
-20	25	8.61	3.36	0.89	-1.26	0.84	16.07	17.36	-7.70	15.71	9.08	2.31	25.46
-20	5	11.14	0.47	0.77	-0.57	0.98	20.08	8.68	4.45	19.15	12.26	2.33	25.22
-20	-10	9.18	-1.89	0.88	-1.03	0.73	17.20	-2.81	12.36	17.12	10.05	3.32	25.47
-20	-15	8.36	-3.19	1.02	-1.64	0.75	14.82	-5.76	14.80	15.50	8.91	3.53	25.39
-20	-20	7.60	-4.75	1.37	-2.88	0.94	12.18	-5.65	16.11	13.10	6.83	3.31	25.36
-20	-25	7.46	-5.66	1.56	-3.51	0.92	11.46	-5.79	16.82	12.52	6.30	3.78	25.47
-20	-5	10.49	-1.01	0.80	-0.70	0.88	19.21	1.22	10.04	18.83	11.86	2.78	25.34
-25	0	11.08	-0.24	0.99	-0.70	0.99	19.57	6.48	8.48	18.86	10.50	2.70	25.54
-25	10	11.78	0.96	1.00	-0.72	1.10	19.91	12.16	4.35	19.38	11.24	2.85	25.75
-25	15	10.34	1.67	1.00	-0.84	1.00	18.47	13.49	-0.12	18.05	9.96	2.20	25.33
-25	20	9.11	2.35	1.01	-1.01	0.91	17.11	15.07	-3.74	16.61	8.51	1.86	25.21
-25	25	8.19	3.24	1.07	-1.46	0.89	15.24	16.52	-6.28	15.05	7.49	1.94	25.52
-25	5	11.27	0.47	0.99	-0.69	1.00	19.72	9.77	5.84	18.94	10.53	2.83	25.54
-25	-10	9.03	-1.79	1.02	-1.07	0.77	16.85	-1.86	12.12	16.93	8.93	3.03	25.26
-25	-15	8.16	-3.07	1.20	-1.79	0.76	14.45	-4.92	14.41	15.36	7.78	3.36	25.73
-25	-20	8.35	-4.39	1.56	-2.82	0.94	12.92	-3.85	16.21	14.09	6.93	4.05	25.82
-25	-25	6.91	-5.08	1.77	-3.41	0.89	10.97	-5.13	15.51	12.21	5.03	3.27	24.83
-25	-5	10.11	-0.92	1.02	-0.81	0.89	18.45	2.43	10.10	18.22	9.71	2.70	25.19
-5	0	12.22	-0.46	0.18	-0.51	1.14	20.94	3.78	7.83	19.42	17.85	2.28	25.36
-5	10	12.84	1.09	0.19	-0.48	1.16	21.48	11.36	1.92	19.83	18.23	2.78	25.62
-5	15	11.41	2.10	0.17	-0.60	1.10	19.89	14.17	-3.60	18.27	16.81	2.06	24.96
-5	20	10.79	2.92	0.23	-0.79	1.01	19.05	16.99	-7.09	17.60	15.66	2.48	25.56
-5	25	10.02	3.90	0.18	-1.21	1.08	17.06	19.06	-8.44	15.37	14.08	2.41	25.58
-5	5	12.32	0.56	0.16	-0.44	1.17	21.13	8.46	3.57	19.32	17.94	1.99	25.01
-5	-10	10.22	-2.38	0.22	-0.90	0.91	18.31	-5.55	13.71	17.26	15.45	2.84	25.64
-5	-15	9.71	-3.48	0.24	-1.46	1.01	16.05	-5.70	16.37	14.86	13.32	3.34	25.28
-5	-20	8.91	-6.00	0.36	-3.19	1.51	12.83	-5.27	18.24	12.04	10.62	2.98	25.31
-5	-25	8.89	-7.54	0.47	-4.19	1.65	12.09	-5.10	19.08	11.54	10.04	3.58	25.54
-5	-5	11.35	-1.19	0.18	-0.59	1.04	20.02	-0.22	10.13	18.53	16.97	2.36	25.14

Appendix 1.3 Create Surface Plot of Calibration Parameters

This file was used to generate 3-D plots of various calibration parameters to compare them with similar plots generated in literature.

```
clear all
clc
close all

 % % % INPUT PARAMETERS
 cal_file = 'C:\Users\Christopher\Google Drive\Grad School\5-Hole Probe
Calculator\Programs\calibrate\calibration.csv';
 % % % END INPUT PARAMETERS
cal_path = cal_file;
cal_data = importdata(cal_path, ',');
cal_alphas = cal_data.data(:,1);
cal_betas = cal_data.data(:,2);
cal_Pbars = cal_data.data(:,3);
cal_Cpys = cal_data.data(:,4);
cal_Cpps = cal_data.data(:,5);
cal_Cpts = cal_data.data(:,6);
cal_Cpss = cal_data.data(:,7);

x = cal_Cpps;
y = cal_Cpys;
z = cal_betas;

xmin = min(x);
xmax = max(x);
ymin = min(y);
ymax = max(y);
% zmin = min(z);
% zmax = max(z);

N = 50;
X = linspace(xmin, xmax, N);
Y = linspace(ymin, ymax, N);

[X, Y] = meshgrid(X, Y);
Z = griddata(x, y, z, X, Y, 'cubic');

mesh(X,Y,Z);
axis tight;
hold on;

plot3(x,y,z,'.','MarkerSize',15);
xlabel('cpp');
ylabel('cpy');
zlabel('beta');
```

Appendix 1.4 Generate Input List

This code was used to generate the input list for both the 5-hole probe measurements as well as the kiel probe measurements.

```
clear all
clc
close all


% % % INPUT PARAMETERS

%input_dir = 'C:\Users\cdrewe1\Desktop\550 RPM 5.8 m_s';
input_dir = 'C:\Users\Christopher\Google Drive\Grad School\EGV BR4 355 PRESS
9_27';
input_file = 'input_ptot.txt';

% % % END INPUT PARAMETERS


% Filter CSV files
files = dir(strcat(input_dir,'\*.csv'));

% Open file for writing
out_path = strcat(input_dir,'\',input_file);
fout = fopen(out_path, 'w');

for i=1: length(files)
    fname = files(i).name;
    fprintf(fout, '%s\n', fname);
end

fclose(fout);

fprintf('Done\n');
```

Appendix 1.5 Find the Velocity Vectors

This code was used to find the velocity vectors by taking the measurements and interpolating their values over the calibration curves using the “griddata” function.

```
clear all
clc
close all

% % % INPUT PARAMETERS
 %cal_file =
'C:\Users\cdrewe1\Desktop\5_Hole_Probe\Calibration\calibration.csv';
cal_file = 'C:\Users\Christopher\Google Drive\Grad School\5-Hole Probe
Calculator\Programs\calibrate\calibration.csv';
%input_dir = 'C:\Users\cdrewe1\Desktop\550 RPM 5.8 m_s';
input_dir = 'C:\Users\Christopher\Google Drive\Grad School\EGV BR 5 355 RPM
PRESS\EGV BR 5 355 RPM PRESS';
input_file = 'input_aoa.txt';
% output_file = 'results.csv';
 kiel_ptot = true;
kiel_path = 'C:\Users\Christopher\Google Drive\Grad School\EGV 355 RPM Kiel
BR 5';
  den = 1.225;

% % % END INPUT PARAMETERS
cal_path = cal_file;
in_path = strcat(input_dir, '\', input_file);
% out_path = strcat(input_dir, '\', output_file);
in_files = importdata(in_path, '\t');
% fout = fopen(out_path, 'w');
N = length(in_files);
cal_data = importdata(cal_path, ',');
cal_alphas = cal_data.data(:,1);
cal_betas = cal_data.data(:,2);
cal_Pbars = cal_data.data(:,3);
cal_Cpys = cal_data.data(:,4);
cal_Cpps = cal_data.data(:,5);
cal_Cpts = cal_data.data(:,6);
cal_Cpss = cal_data.data(:,7);

for fn=1:length(in_files),
    fname = in_files{fn};
    basename = regexp(fname, '.csv', 'split');
    basename = basename{1};
    fpath = strcat(input_dir, '\', fname);
    opath = strcat(input_dir, '\', strcat(basename, '_results.csv'));

    if exist(opath, 'file')
        fprintf('File %s already exists.\n', opath)
    else

        data = importdata(fpath, ',');
```

```
        ts = data(:,3);
        p1s = data(:,5);
        p2s = data(:,6);
        p3s = data(:,7);
        p4s = data(:,8);
        p5s = data(:,9);
    %     pss = data(:,9);
    %     pts = data(:,10);
         rout = fopen(opath, 'w');
        fprintf(rout, 't,i,alpha,beta,velocity, P_tot, P_static\n');
        for i=1:length(ts)

            t = ts(i);
            p1 = p1s(i);
            p_bar = mean([p2s(i), p3s(i), p4s(i), p5s(i)]);
            c_py = (p2s(i) - p3s(i)) / (p1s(i) - p_bar);
            c_pp = (p4s(i) - p5s(i)) / (p1s(i) - p_bar);
    %         c_pt = (p1s(i) - pts(i)) / (p1s(i) - p_bar);
    %         c_ps = (p_bar - pss(i)) / (p1s(i) - p_bar);
            alpha = griddata(cal_Cpys, cal_Cpps, cal_alphas, c_py, c_pp,
'cubic');
            if isnan(alpha)
                slkdfjsldf = 1;
            end
            beta = griddata(cal_Cpys, cal_Cpps, cal_betas, c_py, c_pp,
'cubic');
            if (kiel_ptot == true)
                ptot_path = strcat(kiel_path, '\', strrep(fname, '_results',
''));
                p_tot = get_ptot(ptot_path);
                c_pt = (p1s(i) - p_tot) / (p1s(i) - p_bar);
            else
                c_pt = griddata(cal_alphas, cal_betas, cal_Cpts, alpha, beta,
'cubic');
                p_tot = p1 - c_pt * (p1 - p_bar);
            end

            c_ps = griddata(cal_alphas, cal_betas, cal_Cpss, alpha, beta,
'cubic');
            p_s = p_bar - c_ps * (p1 - p_bar);
            vel = sqrt(2/den * (p1 - p_bar) * (1 - c_pt + c_ps));

            fprintf(rout, '%f,%d,%f,%f,%f,%f,%f\n', t, i, alpha, beta, vel,
p_tot, p_s);
            fprintf('%s\t%f,%d,%f,%f,%f,%f,%f\n', basename, t, i, alpha,
beta, vel, p_tot, p_s);
        end
        fclose(rout);
    end
end


fprintf('Done\n');
```

Appendix 1.6 Generate Input File List for Visualization

Similar to the other input list generation codes, this one is used to generate the input list for velocity and pressure contour plot creation using Tecplot.

```
clear all
clc
close all


% % % INPUT PARAMETERS

%input_dir = 'C:\Users\cdrewe1\Desktop\550 RPM 5.8 m_s';
input_dir = 'C:\Users\Christopher\Google Drive\Grad School\EGV BR4 355 PRESS
9_27';
input_file = 'input_tecplot_aoa.txt';

% % % END INPUT PARAMETERS


% Filter CSV files
files = dir(strcat(input_dir,'\*_results.csv'));

% Open file for writing
out_path = strcat(input_dir,'\',input_file);
fout = fopen(out_path, 'w');

for i=1: length(files)
    fname = files(i).name;
    fprintf(fout, '%s\n', fname);
end

fclose(fout);

fprintf('Done\n');
```

Appendix 1.7 Generate Measurement Contour Plots

This code was written to generate a file that is usable in Tecplot that has location information coupled with velocity and/or pressure data.

```
clear all
clc
close all

% % % INPUT PARAMETERS

%input_dir = 'C:\Users\cdrewe1\Desktop\550 RPM 5.8 m_s';
input_dir = 'C:\Users\Christopher\Google Drive\Grad School\EGV BR 5 355 RPM
PRESS\EGV BR 5 355 RPM PRESS';
input_file_aoa = 'input_tecplot_aoa.txt';
output_file = 'vectors.plt';
Ro = 428.3;          % Outer radius
ds_o = 10.0;         % Arc length between measurements at outer radius
dr = 10.0;           % Radial distance between measurements
N_angular = 21.0;  % Number of evenly spaced measurements in theta direction
N_radial = 11.0;

 % % % END INPUT PARAMETERS

Ri = Ro - (N_radial - 1) * dr;
dth = ds_o / Ro;    % angle between measurements in angular direction (DUH!)
tot_angle = ds_o * (N_angular - 1) / Ro;  % total angle across all
measurements
th_datum = pi/2 + tot_angle / 2; % in radians
r_datum = Ri;

in_path_aoa = strcat(input_dir, '\', input_file_aoa);
out_path = strcat(input_dir, '\', output_file);

in_files_aoa = sort_nat(importdata(in_path_aoa, '\t'));

fout = fopen(strcat(input_dir, '\', output_file), 'w');
N = length(in_files_aoa);

hold on
axis equal

X = zeros(length(in_files_aoa),1);
R = zeros(size(X));
Th = zeros(size(X));
Vx = zeros(size(X));
Vr = zeros(size(X));
Vth = zeros(size(X));
Y = zeros(size(X));
Z = zeros(size(X));
Vy = zeros(size(X));
Vz = zeros(size(X));
Vmag = zeros(size(X));
```

```
Ptot = zeros(size(X));
Ps = zeros(size(X));

for fn=1:length(in_files_aoa),

    %%%% Get circumferential and radial indices

    fname = in_files_aoa{fn};
    s1 = regexp(fname, '_results.csv', 'split');
    s1 = s1{1};
    s2 = regexp(s1, '_', 'split');
    s2 = s2{1};
    c_index = regexp(s2, 'c', 'split');
    c_index = str2num(c_index{2});
    s3 = regexp(s1, '_', 'split');
    s3 = s3{2};
    r_index = regexp(s3, 'r', 'split');
    r_index = str2num(r_index{2});

    %fprintf('r_index = %f,\t c_index = %f,\t ', r_index, c_index)

    r = r_datum + dr * (r_index);
    th = th_datum - dth * (c_index);
    z = r * cos(th);
    y = r * sin(th);
    fprintf('%s,\t r = %f,\t th = %f\n', fname, r, th-pi/2);

       %%%%% Get alpha and beta from results file
    fpath = strcat(input_dir, '\', fname);
    dataObj = importdata(fpath, ',');
    data = dataObj.data;
    ts = data(:,1);
    is = data(:,2);
    alphas = data(:,3);
    betas = data(:,4);
    vel_magss = data(:,5);
    Ptots = data(:,6);
    Pss = data(:,7);
    alpha = mean(alphas);
    beta = mean(betas);
    alpha_rad = degtorad(alpha);
    beta_rad = degtorad(beta);
    vel_mag = mean(vel_magss);
    P_tot = mean(Ptots);
    P_s = mean(Pss);


    %%%%% Convert alpha, beta, and magnitude to velocity components

    % '_p' signifies prime coordinate system (local to probe)
    vx = vel_mag * cos(alpha_rad) * cos(beta_rad);
    vr = vel_mag * sin(alpha_rad);
    vth = vel_mag * cos(alpha_rad) * sin(beta_rad);
    vz = vr * cos(th) - vth * sin(th);
    vy = vr * sin(th) + vth * cos(th);
```

```
    X(fn) = 0;
    R(fn) = r;
    Th(fn) = th;
    Vx(fn) = vx;
    Vr(fn) = vr;
    Vth(fn) = vth;
    Vmag(fn) = vel_mag;
    Ptot(fn) = P_tot;
    Ps(fn) = P_s;

    Z(fn) = z;
    Y(fn) = y;
    Vz(fn) = vz;
    Vy(fn) = vy;
end

% polar(0, 0, 'r*')
% polar(pi/2,Ro, 'g*')

quiver3(X,Y,Z,Vx,Vy,Vz)

%%%%% Write Tecplot data file
fprintf(fout, 'VARIABLES = "X", "Y", "Z", "VX", "VY", "VZ", "Ptot", "Ps"\n');
fprintf(fout, 'ZONE I=%d, J=%d, K=%d, DATAPACKING=POINT\n', 1, N_radial,
N_angular);
for i=1:length(X),
    fprintf(fout, '%f, %f, %f, %f, %f, %f, %f, %f\n', X(i), Y(i), Z(i),
Vx(i), Vy(i), Vz(i), Ptot(i), Ps(i));
end
fclose(fout);

contour_var = Ps;
Z1 = zeros(N_angular, N_radial);
Y1 = zeros(N_angular, N_radial);
C1 = zeros(N_angular, N_radial);

count = 0;
for i=1:N_angular,
    for j = 1:N_radial,
        count = count + 1;
        Z1(i, j) = Z(count);
        Y1(i, j) = Y(count);
        C1(i, j) = contour_var(count);
    end
end

figure(2)
contourf(Z1, Y1, C1);


fprintf('Done\n');
```

Appendix 2: Equipment Specifications

Appendix 2.1 Fan Specifications

SUBMITTAL

Customer: W/A

Job Name: LSU Wind Tunnel

Job ID: 09720

Date: September 28, 2010

Submitted By:

Dennis Maranto
P.O. Box 66730
Baton Rouge, LA 70806
Phone: 225-926-2590
Fax: 225-926-2593

Fan Tag:

Job Name:	LSU Wind Tunnel
Job ID:	09720
Date:	September 28, 2010
Page:	Page 2 of 3

BAV - Airfoil Utility Set

CONSTRUCTION FEATURES

Housing is rugged, all-welded construction, rotatable to eight standard discharge positions.
Shaft is AISI 1045 steel, turned, ground and polished for accuracy.
Heavy-duty, grease lubricated pillow block bearings selected for minimum average L-50 life of at least 200,000 hours.
Deep spun inlet cone, aerodynamically designed for smooth air entry into the wheel. Available with an *See Attached Drawing* **FAN DESCRIPTION**

Qty	Type	Size	Width	Wt (lb.)
1	BAV	365	SWSI	1,544

Approximate weight each, includes fan, motor and accessories.

FAN CONFIGURATION

Class	Rotation	Arr.	Disch
II	CW	10	THD

FAN PERFORMANCE

CFM	SP (in.wg)	RPM	Oper. BHP
25,000	5.0	1246	26.65

Temperature: 70°F, Altitude: 0ft

MOTOR DATA

HP	RPM	Volt/Ph/Hz	Encl
30	1800	230/460/3/60	ODP

Efficiency: Standard/EPACT

SOUND DATA

Octave Bands	1	2	3	4	5	6	7	8	LwA	dBA	Sones
Level at Inlet	94	99	97	88	87	84	78	73	94	80	39

LwA: The overall (single value) fan sound power level in dB re. 10^{-12} Watts, 'A' weighted.

dBA: Estimated sound pressure level (re:0.0002 microbar) based on a single ducted installation at 5 ft., using a directivity factor of 1.

ACCESSORIES INCLUDED

Access Door - Bolted
Drain W/ Plug
Flange - Inlet, Punched
Flange - Outlet, Unpunched
Weather Cover - Std Type
Shutter - Gravity, Heavy Duty
Vibration Isolators - RIS
Mount TCF Motor

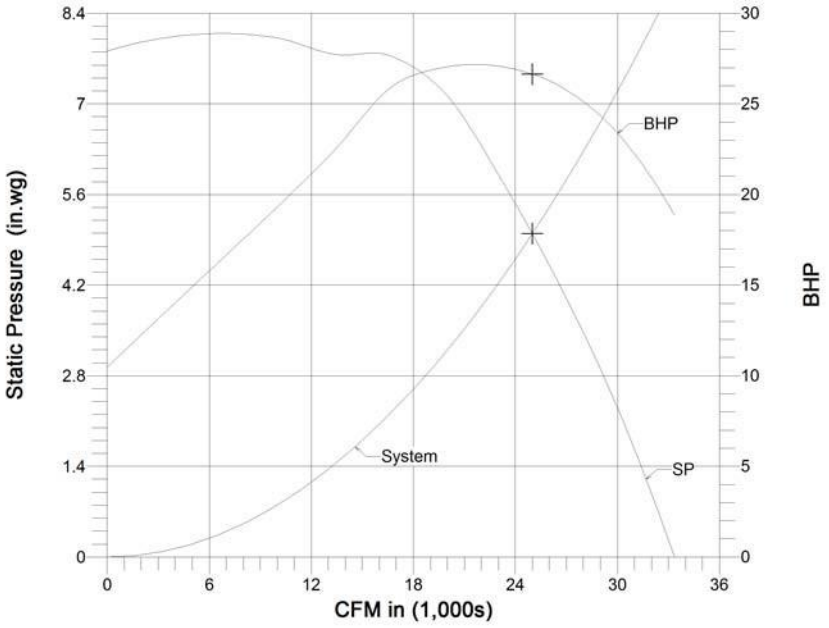

Fan Tag:

Job Name: LSU Wind Tunnel
Job ID: 09720
Date: September 28, 2010
Page: Page 3 of 3

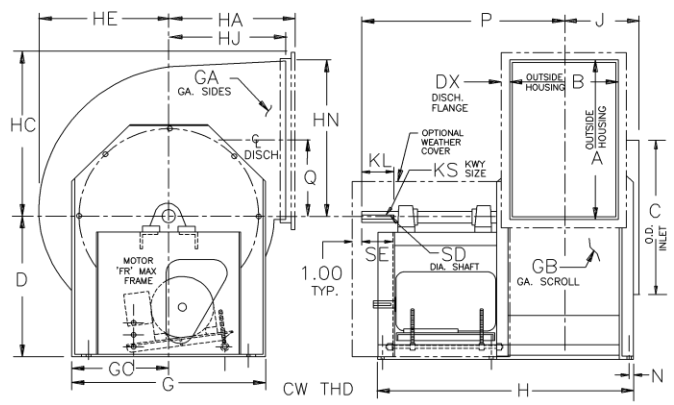

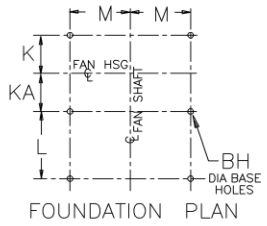

FOUNDATION PLAN

NOTES:
01 FLANGED OUTLET IS OPTIONAL ON SIZES 122–200 FLANGED OUTLET IS STANDARD ON SIZES 222 THRU 365 (EXCEPT ON TAD & DBD).
02 'CW' ROTATION IS SHOWN. 'CCW' ROTATION IS SIMILAR BUT OPPOSITE.
03 ALL UNITS ARE ROTATABLE TO ALL POSITIONS (EXCEPT SIZES 300–365 WITH "D" CENTER LINE HEIGHT ARE NOT ROTATABLE TO BHD).

'BCV', 'BAV', & 'FCV' ARR. 10 CLASS II VENT SETS

TWIN CITY FAN & BLOWER
5959 TRENTON LANE MINNEAPOLIS, MN. 55442
MEMBER OF AIR MOVEMENT AND CONTROL ASSOC.

DRAWN 8/8/91
REVISED 7/15/05
DWG NO AC14301E

JOB:
LOC.
ENG./ARCH.
CERT BY.
S.O. NO.

SIZE	CLASS	DISCH	ROT.	UNIT NO.	
CFM	SP	RPM	BHP	OV	TS

ACCESSORIES REQ'D

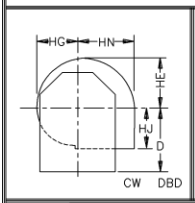

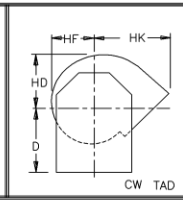

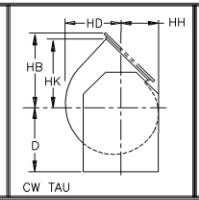

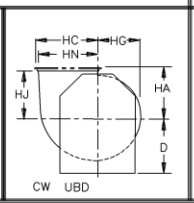

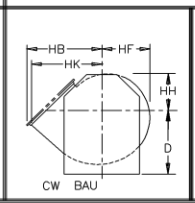

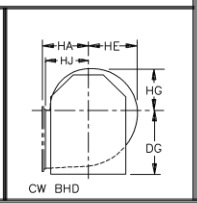

FAN SIZE	A	B	BH	C	D	DG	DX	FR	G	GA	GB	GC	H	HA	HB	HC	FAN SIZE
122	13.00	9.75	0.44	13.25	17.63	17.63	1.00	184T	16.00	14	14	8.00	32.00	9.75	16.75	13.94	122
135	14.31	10.81	0.44	14.56	19.13	19.13	1.00	215T	17.50	14	14	8.75	34.81	10.75	18.38	15.25	135
150	15.88	11.94	0.44	16.19	19.38	19.38	1.00	215T	19.00	14	14	9.50	36.00	11.94	20.31	16.81	150
165	17.44	13.19	0.44	17.75	19.38	19.38	1.00	215T	20.50	14	14	10.25	37.31	13.13	22.25	18.38	165
182	19.38	14.56	0.44	19.50	21.88	21.88	1.25	256T	25.00	12	14	12.50	43.44	14.50	24.81	20.56	182
200	21.19	15.94	0.56	21.38	22.75	22.75	1.25	256T	25.00	12	14	12.50	44.81	15.81	27.00	22.38	200
222	23.56	17.69	0.56	23.75	25.50	25.50	1.25	256T	27.25	12	14	13.63	47.13	17.69	30.00	24.75	222
245	25.94	19.44	0.56	26.06	28.00	28.00	1.25	256T	29.75	12	14	14.88	48.81	19.50	33.00	27.13	245
270	28.63	21.38	0.56	28.50	30.50	30.50	1.50	286T	33.00	12	14	16.50	53.00	21.44	36.44	30.06	270
300	31.81	23.81	0.56	31.63	27.50	34.25	1.50	286T	36.13	10	12	18.06	56.00	23.81	40.31	33.25	300
330	35.13	26.06	0.56	34.75	30.00	37.25	1.50	326T	38.88	10	12	19.44	61.75	26.25	44.44	36.56	330
365	38.75	28.88	0.56	38.50	33.50	41.00	1.50	326T	43.75	10	12	21.88	64.56	29.00	48.88	40.13	365

FAN SIZE	HD	HE	HF	HG	HH	HJ	HK	HN	J	K	KA	KL	KS	L	M	N	P	Q	SD	SE	FAN SIZE
122	11.19	10.56	9.94	9.31	8.69	9.25	15.69	12.94	7.44	5.75	6.75	2.00	.25x.13	18.50	7.31	0.50	26.50	6.44	1.187	2.75	122
135	12.31	11.63	10.94	10.25	9.56	10.25	17.31	14.25	8.00	6.31	7.25	2.63	.25x.13	20.25	8.06	0.50	29.56	7.13	1.187	3.38	135
150	13.75	12.88	12.13	11.38	10.63	11.44	19.25	15.81	9.06	6.88	7.88	2.63	.25x.13	20.25	8.81	0.50	30.13	7.88	1.187	3.38	150
165	15.06	14.13	13.31	12.50	11.69	12.63	21.19	17.38	9.69	7.50	8.56	2.63	.25x.13	20.00	9.25	0.63	30.75	8.69	1.187	3.38	165
182	16.69	15.69	14.75	13.81	12.88	14.00	23.56	19.31	10.88	8.19	9.25	3.25	.38x.19	24.75	10.88	0.63	36.81	9.63	1.437	4.00	182
200	18.38	17.31	16.25	15.19	14.13	15.31	25.75	21.13	11.56	8.88	10.06	3.25	.38x.19	24.63	10.88	0.63	37.50	10.56	1.437	4.00	200
222	20.44	19.06	17.94	16.81	15.69	17.19	28.75	23.50	12.44	10.00	11.50	3.25	.38x.19	23.88	11.13	0.88	38.38	11.75	1.437	4.00	222
245	22.38	21.00	19.75	18.50	17.25	19.00	31.75	25.88	13.31	10.88	12.31	3.25	.38x.19	23.88	11.63	0.88	39.25	12.94	1.687	4.00	245
270	24.69	23.19	21.81	20.44	19.06	20.94	35.00	28.56	14.25	11.81	13.31	3.63	.38x.19	26.13	12.13	0.88	43.13	14.25	1.687	4.63	270
300	27.44	25.75	24.25	22.75	21.25	23.31	38.94	31.75	15.50	13.31	15.06	3.63	.50x.25	25.38	12.38	1.13	44.44	15.81	1.937	4.63	300
330	30.13	28.38	26.69	25.00	23.31	25.75	43.00	35.06	16.63	14.44	16.19	4.50	.50x.25	28.88	14.13	1.13	49.69	17.50	2.187	5.25	330
365	33.50	31.50	29.63	27.75	25.88	28.50	47.44	39.63	18.00	15.81	17.63	4.50	.63x.31	28.88	14.13	1.13	51.06	19.25	2.437	5.25	365

DWG NO AC14301E

Appendix 2.2 Inline Air Dryer Specifications ¾”

Catalog 9EM-TK-190-2 Basic 3/4" Body

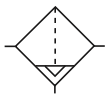

Specifications

F34

Flow Capacity*	1/2	190 SCFM (90.4 dm^3/s)
	3/4	285 SCFM (134.4 dm^3/s)
	1	362 SCFM (171.0 dm^3/s)

Maximum Supply Pressure	Plastic Bowl	150 PSIG (10.3 bar)
	Metal Bowl	200 PSIG (13.8 bar)
Operating Temperature	Plastic Bowl	32° to 125°F (0° to 52°C)
	Metal Bowl	32° to 150°F (0° to 65.5°C)
Port Size	NPT / BSPP-G	1/2, 3/4, 1
Standard Filtration		5 Micron
Weight		6.4 lb. (2.9 kg)

Auto Drain

* Inlet pressure 150 PSIG (10.3 bar). Pressure drop 5 PSID (0.3 bar).

“F” Series Filters, Type “A” 5 micron elements: All Wilkerson Type “A” 5 micron elements **meet or exceed ISO** Class 3 for maximum particle size and concentration of solid contaminants.

Particulate Filter

= "Most Popular"

F34-06-000

B

Features

Standard Auto. Drain

Standard 5 Micron Rated Element

Quick-disconnect Clamp Ring for Easy Bowl Removal • Bowl Guard

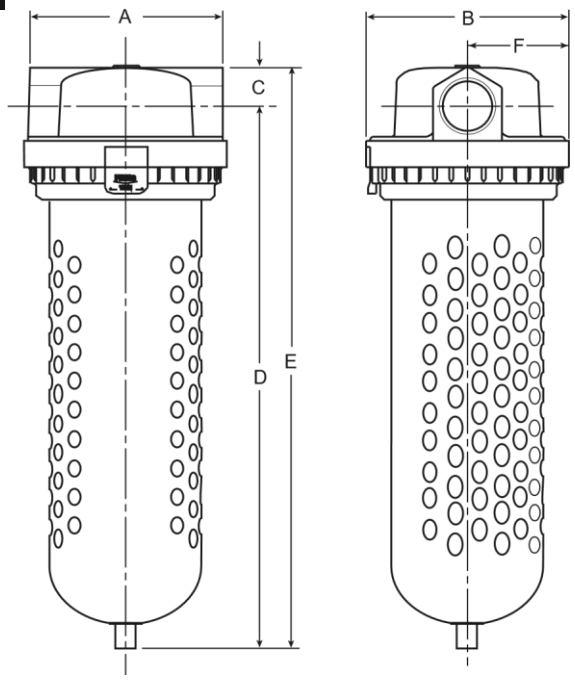

Materials of Construction

Baffle		Acetal
Body		Zinc
Bowls	Plastic Bowl	Polycarbonate
	Metal Bowl	Aluminum
Deflector		Aluminum
Element Retainer		Steel Stud
Filter Element		Polyethylene
Seals	Plastic Bowl	Nitrile
	Metal Bowl	Fluorocarbon

Dimensions

Models (Inches (mm))	A	B	C	D	E	F
Standard Unit (Automatic Drain Standard) F34-XX-000	4.61 (117)	4.80 (122)	.94 (24)	12.96 (329)	13.90 (353)	2.40 (61)
Metal Bowl	4.61 (117)	4.80 (122)	.94 (24)	12.44 (315.9)	13.38 (340)	2.40 (61)

Hi-Flow Particulate Filter F34 = "Most Popular"

Replacement Bowl Kits

Plastic Bowl –
Bowl Guard, Manual Drain GRP-95-902

Replacement Element Kits

Type "A", 5 Micron FRP-95-209

Accessories

Float Drain Assembly FRP-15-487-000

F34-04-000

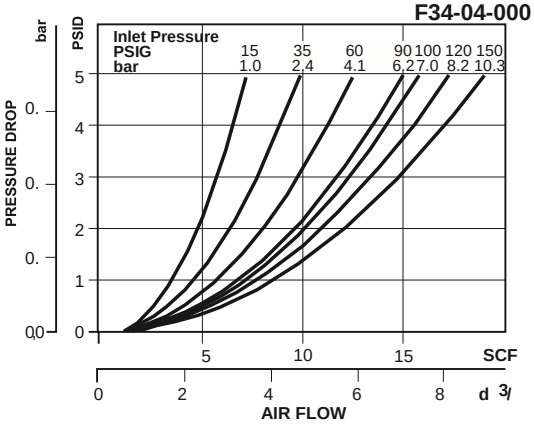

Model Type	Port Size	Polycarbonate Bowl / Bowl Guard	Metal Bowl
Automatic Drain	1/2	F34-04-000	F34-04-M00
	3/4	F34-06-000	F34-06-M00
	1	F34-08-000	F34-08-M00

F34-06-000

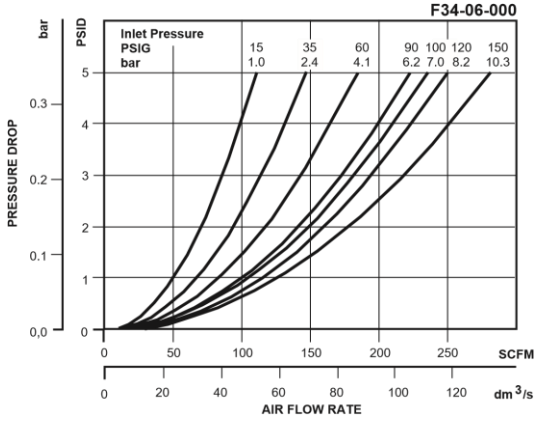

F34-08-000

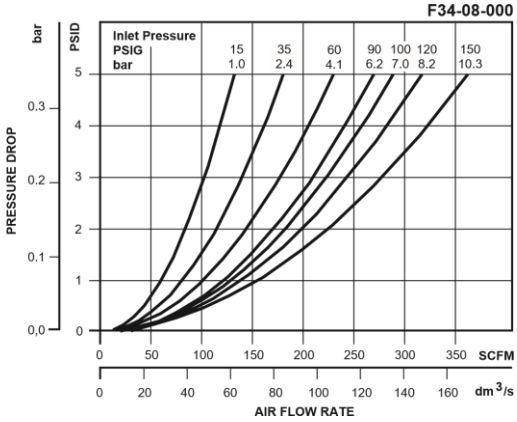

Appendix 2.3 Inline Air Dryer Specifications 2”

Particulate Filter

F35

Auto Drain

B

F35-0B-000

= "Most Popular"

Specifications

Flow Capacity*	1-1/4	970 SCFM (458 dm³/s)
	1-1/2	1280 SCFM (604 dm³/s)
	2	1400 SCFM (660 dm³/s)
Maximum Supply Pressure	without DP2	300 PSIG (20.7 bar)**
	with DP2	150 PSIG (10.3 bar)
Operating Temperature		32° to 150°F (0° to 65.5°C)
Port Size	NPT / BSPP-G	1-1/4, 1-1/2, 2
Standard Filtration		5 Micron
Weight		19.3 lb. (8.7 kg)

* Inlet pressure 150 PSIG (10.3 bar). Pressure drop of 5 PSID (0.3 bar).

** Without pressure indicator – Max. supply pressure is 300 PSIG (20.7 bar).

"F" Series Filters, Type "A" 5 micron elements: All Wilkerson Type "A" 5 micron elements **meet or exceed ISO** Class 3 for maximum particle size and concentration of solid contaminants.

Features

- Heavy-duty Cast Aluminum Housings to Withstand Operating Pressures Up to 300 PSIG*
- Differential Pressure Indicator to Eliminate the Guesswork of Element Replacement
- Unique Drain Mounting Plate Design Offers a Trouble-free Method for Interchanging and Installing External Drains

Materials of Construction

Baffle	Plated Steel
Body	Aluminum
Bowls	Aluminum
Deflector	Plated Steel
Element Retainer	Plated Steel
Filter Element	Polyethylene
Seals	Fluorocarbon
Stud	Plated Steel

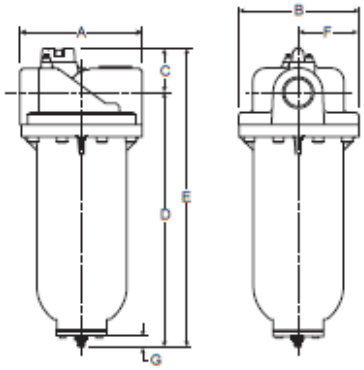

NOTE: Automatic internal float drain shown is included on F35 filters with F00 suffix only.
Models with 000 suffix include drain plate with tapped 1/2 NPT / BSPP-G drain port.

Dimensions

Models (Inches (mm))	A	B	C	D	E	F	G
Standard Unit F35-XX-000	7.80 (198)	7.76 (197)	2.83 (72)	16.24 (412.5)	19.07 (484)	3.88 (98.6)	.55 (14)
Automatic Drain F35-XX-F00	7.80 (198)	7.76 (197)	2.83 (72)	15.69 (398.5)	18.52 470	3.88 (98.6)	.55 (14)

= "Most Popular"

Replacement Element Kit

Element, F35, 5 Micron, Fluorocarbon O-rings.....FRP-95-505

Accessories

Cap, Differential Pressure Indicator –
For pressures over 150 PSIG.....GRP-95-022

Drain, Automatic, Internal, Fluorocarbon,
1/8 NPT.....GRP-95-981

Drain Plate Kit (.56 Dia.) –
For use with internal auto float drain.....GRP-95-391

Drain Plate Kit –
1/4 NPT tapped drain port.....GRP-95-392
1/2 NPT tapped drain port.....GRP-95-393

Gauge, Differential Pressure.....DP3-01-000

Indicator, Differential Pressure.....DP2-01-001

Manual Override for Auto Float Drain –
GRP-95-981 required.....GRP-96-000

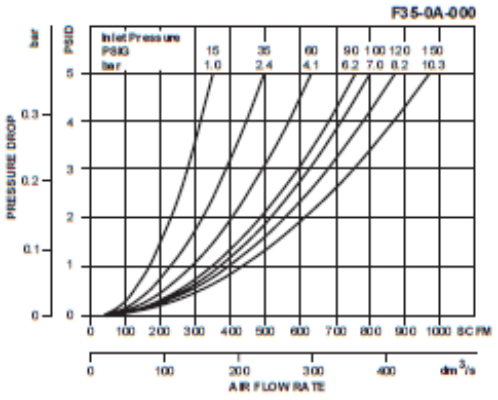

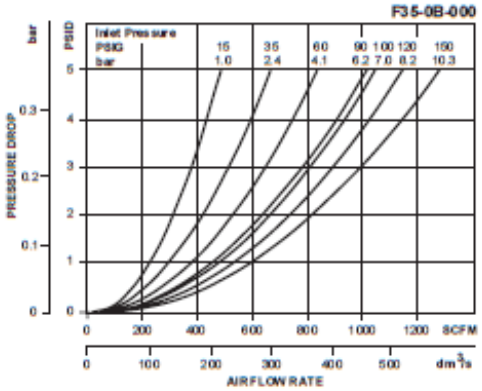

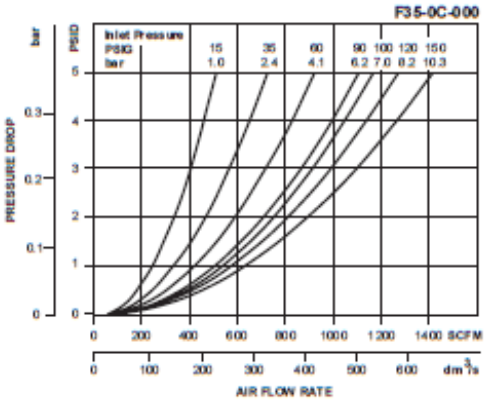

Ordering Information

Model Type	Port Size	Metal Bowl	
Manual Drain	1-1/4	F35-0A-000	(Includes 1/2 NPT / BSPP-G Drain Plate)
	1-1/2	F35-0B-000	
	2	F35-0C-000	
Automatic Drain	1-1/4	F35-0A-F00	
	1-1/2	F35-0B-F00	
	2	F35-0C-F00	

Options - To order an option supplied with the unit model, add the appropriate coded suffix letter in the designated position of the model number.

Appendix 2.4 Thermal Mass Flow Meter Installation Specifications

Unobstructed Flow Requirements

Select an installation site that will minimize possible distortion in the flow profile. Valves, elbows, control valves and other piping components may cause flow disturbances. Check your specific piping condition against the examples shown below. In order to achieve accurate and repeatable performance install the flow meter using the recommended number of straight run pipe diameters upstream and downstream of the sensor.

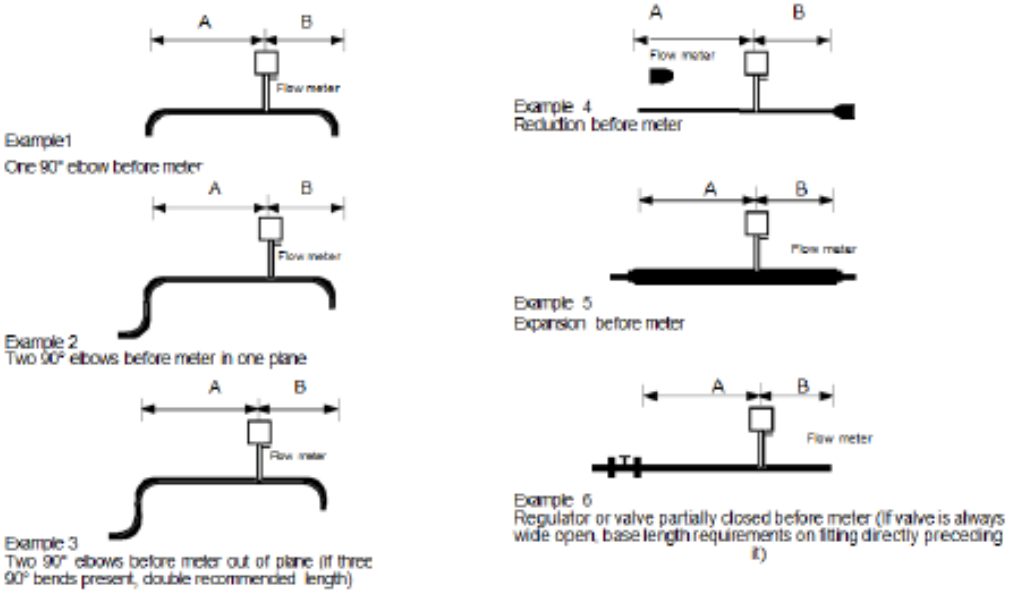

Example	A – Upstream, Requirements	B – Downstream(2) Requirements
1	15 D	5 D
2	20 D	5 D
3	40 D	10 D
4	15 D	5 D
5	30 D	10 D
6	40 D	5 D

(1) Number of diameters (D) of straight pipe required between upstream disturbance and the flow meter.
(2) Number of diameters (D) of straight pipe required downstream of the flow meter.

Figure 2-1. Recommended Pipe Length Requirements for Installation

Appendix 2.5 Inline Air Heater Wiring Diagram

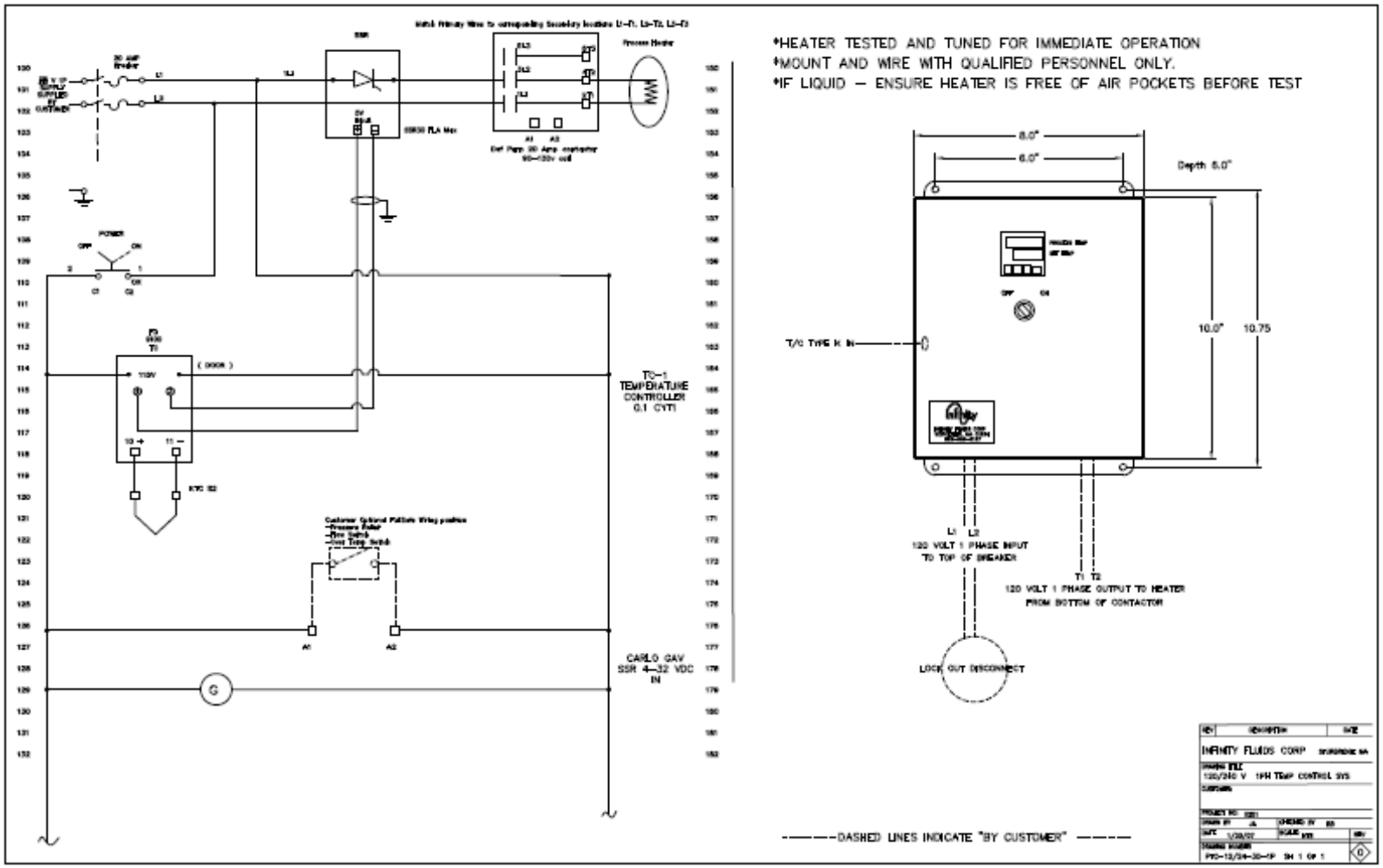

Appendix 2.6 Inline Air heater Drawing

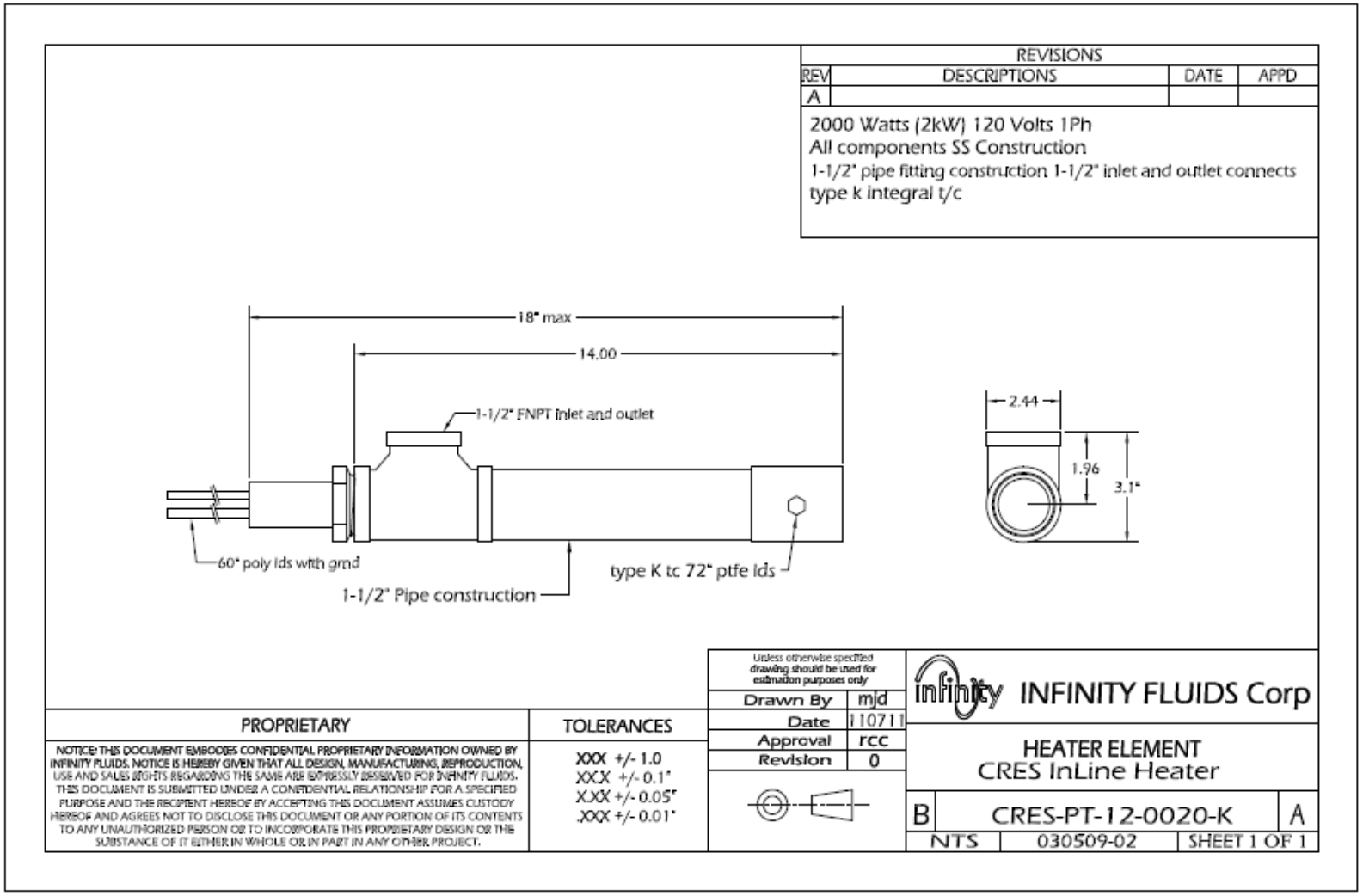

Appendix 2.7 air duct damper specifications

GREENHECK
Building Value in Air.

Printed Date: 2/10/2011
Job: LSU - WIND TUNNEL
Product Type: Damper
Mark: MOTORIZED DAMPERS

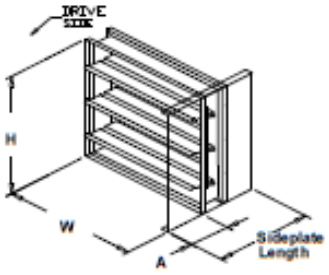

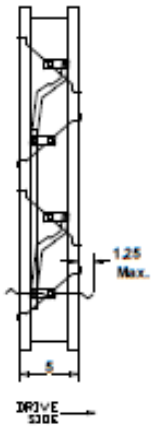

VCD-23

Low Leakage Control Damper

Application & Design

The model VCD-23 is a ruggedly built low leakage control damper for application as an automatic control or manual balancing damper. A wide range of electric and pneumatic actuators are available. Non-jackshafted dampers will be supplied with a blade drive lever for internal actuator mounting unless external actuator mounting is specified in which case an extension pin with clip kit will be provided. Note: The extension pin with clip kit includes the extension pin and clip. The VCD-23 is intended for applications in low to medium pressure and velocity systems.

- FRAME: Galvanized, 5 in x 1 in hat channel, reinforced corners, low profile head and sill on dampers 17 in high and smaller. (When 304 SS material is selected the frame, blades and all damper components will be provided in 304 SS except: the actuator, mounting hardware and jackshaft)
- BLADES: Galvanized, reinforced with 3 longitudinal structurally designed Vs.
- LINKAGE: Side linkage out of air stream.
- AXLES: 0.5 in dia.

Notes: All dimensions shown are in units of inches.

W & H furnished approximately 0.25 in undersized and only refer to damper dimensions (sleeve thickness is not included).

Electrical accessory wiring terminates at the accessory. Field wiring is required to individual components.

CONSTRUCTION FEATURES

Blade Action:	Opposed	**Sizing:**	Nominal
Frame Type:	Channel	**Frame Thickness (ga):**	16
Material:	Galvanized	**Actuator Type:**	120 VAC
Axle Material:	Steel	**Actuator Mount:**	Ext Sideplate
Axle Bearings:	Synthetic	**Actuator Location:**	Left Side
Linkage Material:	Steel	**Fail Position:**	Closed
Blade Seal:	TPE	**Cycle:**	60 Cycle
Jamb Seal Mat.:	304 SS		

amca CERTIFIED RATINGS AIR

ID #	Tag	Qty	W (in)	H (in)	Drive Arr.	Actuator	Act. Qty.	Sideplate Length...	A-Dim. (in)
1-1		4	30.500	30.500	11-1FEL-0	ML4302F1008	1	8	1.5
Tags:									

Pressure Drop Data

VCD-23

This pressure drop testing was conducted in accordance with AMCA Standard 500 using the three configurations shown. All data has been corrected to represent standard air at a density of 0.075 lb/ft3.
Actual pressure drop found in any HVAC system is a combination of many factors. This pressure drop information along with an analysis of other system influences should be used to estimate actual pressure losses for a damper installed in a given HVAC system.

AMCA Test Figures

Figure 5.3 Illustrates a fully ducted damper. This configuration has the lowest pressure drop of the three test configurations because entrance and exit losses are minimized by straight duct runs upstream and downstream of the damper.

Figure 5.2 Illustrates a ducted damper exhausting air into an open area. This configuration has a lower pressure drop than Figure 5.5 because entrance losses are minimized by a straight duct run upstream of the damper.

Figure 5.5 Illustrates a plenum mounted damper. This configuration has the highest pressure drop because of extremely high
entrance and exit losses due to the sudden changes of area in the system.

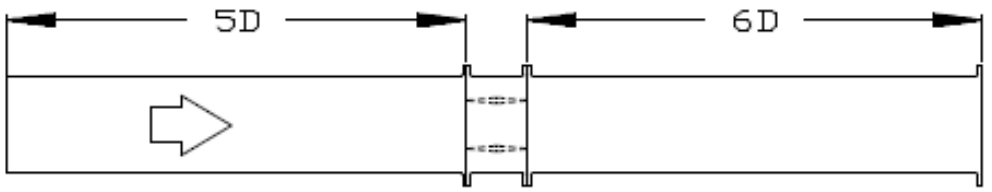

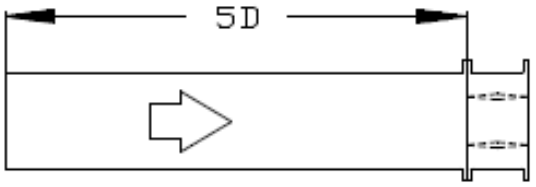

$$D = \sqrt{\frac{4(W)(H)}{3.14}}$$

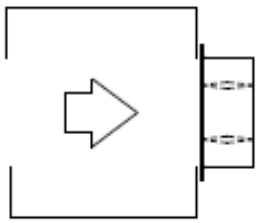

AMCA 5.3 Pressure Drop

VCD-23

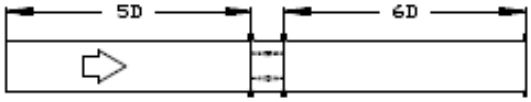

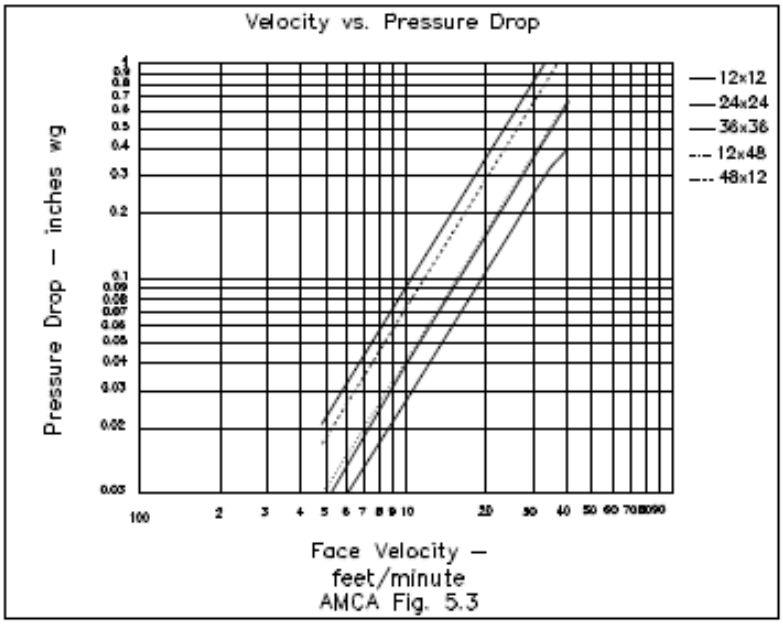

12 x 12 (305mm x 305mm)	
Velocity (fpm)	Pressure Drop (in. wg)
500	0.02
1000	0.09
1500	0.20
2000	0.36
2500	0.56
3000	0.81
3500	1.10
4000	1.44

24 x 24 (610mm x 610mm)	
Velocity (fpm)	Pressure Drop (in. wg)
500	0.01
1000	0.04
1500	0.09
2000	0.16
2500	0.25
3000	0.35
3500	0.48
4000	0.63

36 x 36 (914mm x 914mm)	
Velocity (fpm)	Pressure Drop (in. wg)
500	0.01
1000	0.03
1500	0.06
2000	0.11
2500	0.17
3000	0.24
3500	0.33
4000	0.42

12 x 48 (305mm x 1219mm)	
Velocity (fpm)	Pressure Drop (in. wg)
500	0.01
1000	0.04
1500	0.10
2000	0.17
2500	0.27
3000	0.39
3500	0.53
4000	0.70

48 x 12 (1219mm x 305mm)	
Velocity (fpm)	Pressure Drop (in. wg)
500	0.02
1000	0.07
1500	0.16
2000	0.29
2500	0.45
3000	0.64
3500	0.88
4000	1.14

Greenheck certifies that the model VCD-23 shown herein is licensed to bear the AMCA seal.

The ratings shown are based on tests and procedures performed in accordance with AMCA Publication 511 and comply with the requirements of the AMCA Certified Ratings Programs.

Appendix 2.8 Rotor Motor VFD Specifications

VS1MX NEMA 4X/12 AC DRIVES

VS1 MX Catalog Number Definition

VS1	MX	2	OP5	-	4	TDF

Options	
T	Transistor Output
D	Disconnect Switch
F	EMC Filter

Enclosure	
2	NEMA 12
4	NEMA 4X

HP/kW (1, 2 or 3 Characters)	
OP5	1/2 hp
1	1 hp
2	2 hp
3	3 hp
5	5 hp
7	7.5 hp
10	10 hp

Voltage	
1	115V 1-Phase
2	230V 3-Phase
4	460V 3-Phase
8	230V 1-Phase

Series	
MX	MicroDrive

Agency Certifications / Listings:

- UL
- cUL
- CE

Optional Equipment and Accessories*

• Remote Keypad	VS1ST-RKEY3
• CopyCat Loader	VS1ST-CCL
• 2nd Relay Output Card	VS1ST-2ROUT
• HVAC Output Card (Fault & Drive Run)	VS1ST-HVAC
• 100 or 230V Control Input Card	VS1ST-LOGHV-11 or 23
• DB Resistor Kit	VS1MX-R50W200
• Serial Network Cables:	
Splitter Cable	VS1ST-J45SP
0.5, 1 or 3M Cable	VS1ST-CBLOP3, CBL1 or CBL3
• Communication Network Gateway Interface:	
Profibus Gateway	VS1ST-PBUS
DeviceNet Gateway	VS1ST-DNET
Ethernet Gateway	VS1ST-ENET

Note: The VS1MX shares many of the same option kits as the VS1ST.

VS1 MX Connections

Control Terminal	Signal	Description
1	+24 Volts	+24V, 100mA
2	Digital Input 1	0 = 0-4 VDC; 1 = 8-30 VDC
3	Digital Input 2	0 = 0-4 VDC; 1 = 8-30 VDC
4	Digital Input 3	0 = 0-4 VDC; 1 = 8-30 VDC
	Analog Input 2	Analog: 0 to 10V, 0 to 20mA or 4 to 0mA
5	+10 Volts	10mA, (1kOhm min) potentiometer
6	Analog Input 1	Analog: 0 to 10V, 0 to 20 or 4 to 20mA
	Digital Input 4	0 = 0-4 VDC; 1 = 8-30 VDC
7	0 Volts	User ground, connected to terminal 9
8	Analog Output	Analog: 0 to 10V, 20mA maximum
	Digital Output	Digital: 0 to 24V
9	0 Volts	User ground, connected to terminal 7
10	Relay Common	
11	Relay N/O	250V AC 6A / 30V DC 5A
Power Terminal	**Signal**	**Description**
L1/L, L2/N, L3	AC Line Input	Input power to drive
U, V, W	Drive output	Output terminals to motor (3-Phase)
+DC, BR	Brake control	DB Resistor Connection only available for B and C frames
⏚	Ground	Chassis Ground

Terminal Description Chart

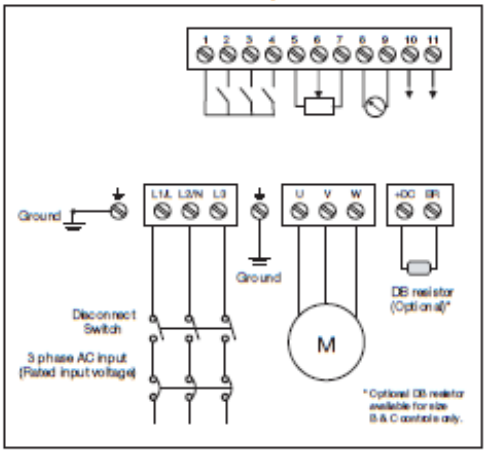

BALDOR

BALDOR · DODGE · RELIANCE

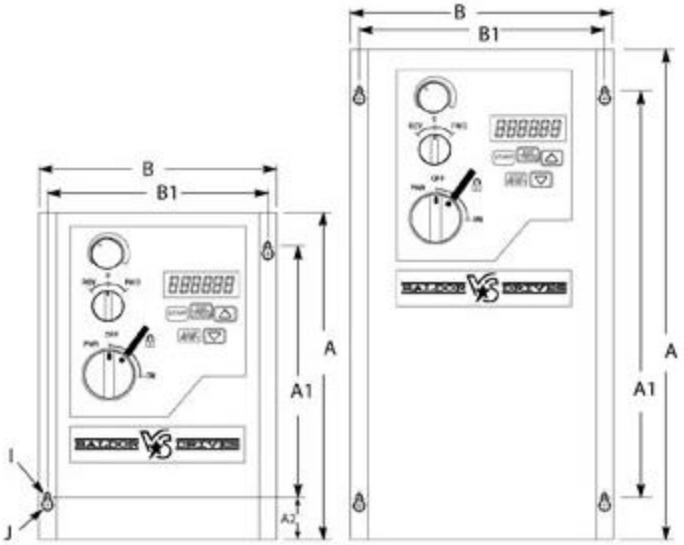

Frame	A		A1		A2		B		B1		I Φ		J Φ		C (Depth)		Weight	
	in	mm	in	mm	in	mm	in	mm	in	mm	in	mm	in	mm	in	mm	lb	kg
A	7.87	200	5.55	141	1.30	33	5.51	140	5.04	128	0.17	4.2	0.33	8.4	6.54	166	5.07	2.3
B	12.20	310	9.88	251	1.30	33	6.46	164	6.02	153	0.17	4.2	0.33	8.4	7.09	180	9.92	4.5

Appendix 3: Experimental Results

Non Dimensional Temperature for BR=4

- V_= 6 m/s (measured with Pitot Static Probe)
- Rotor Speed = 355 RPM (Measured with VFD)
- **BR = 4**
- Average Mainstream Temperature was 32.9°C
- Average Shroud Coolant Air Temperature was 63.9 °C
- Average Probe Temperature was 33.9°C

T1=MAINSTREAM TEMP
T7=COOLANT TEMP
T10=PROBE TEMP

THETA = (T1-T10)/(T1-T7)

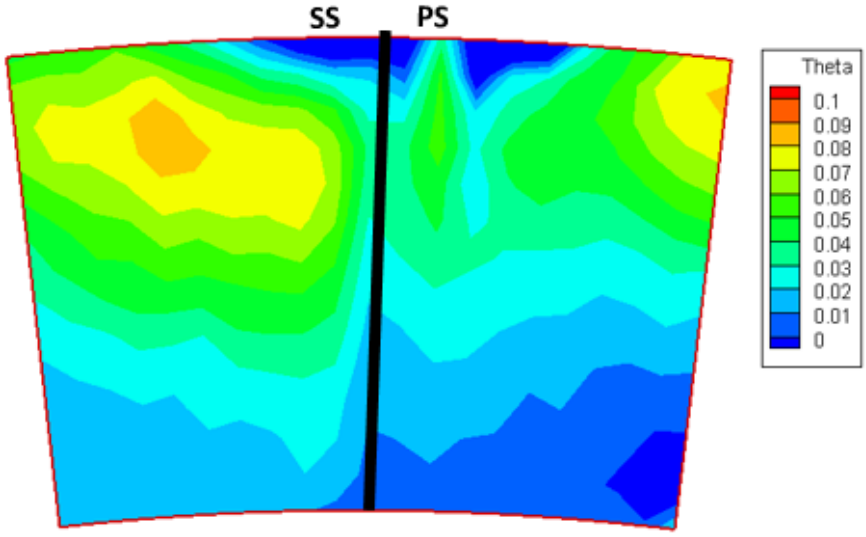

Appendix 4: Wind Tunnel Drawings Package

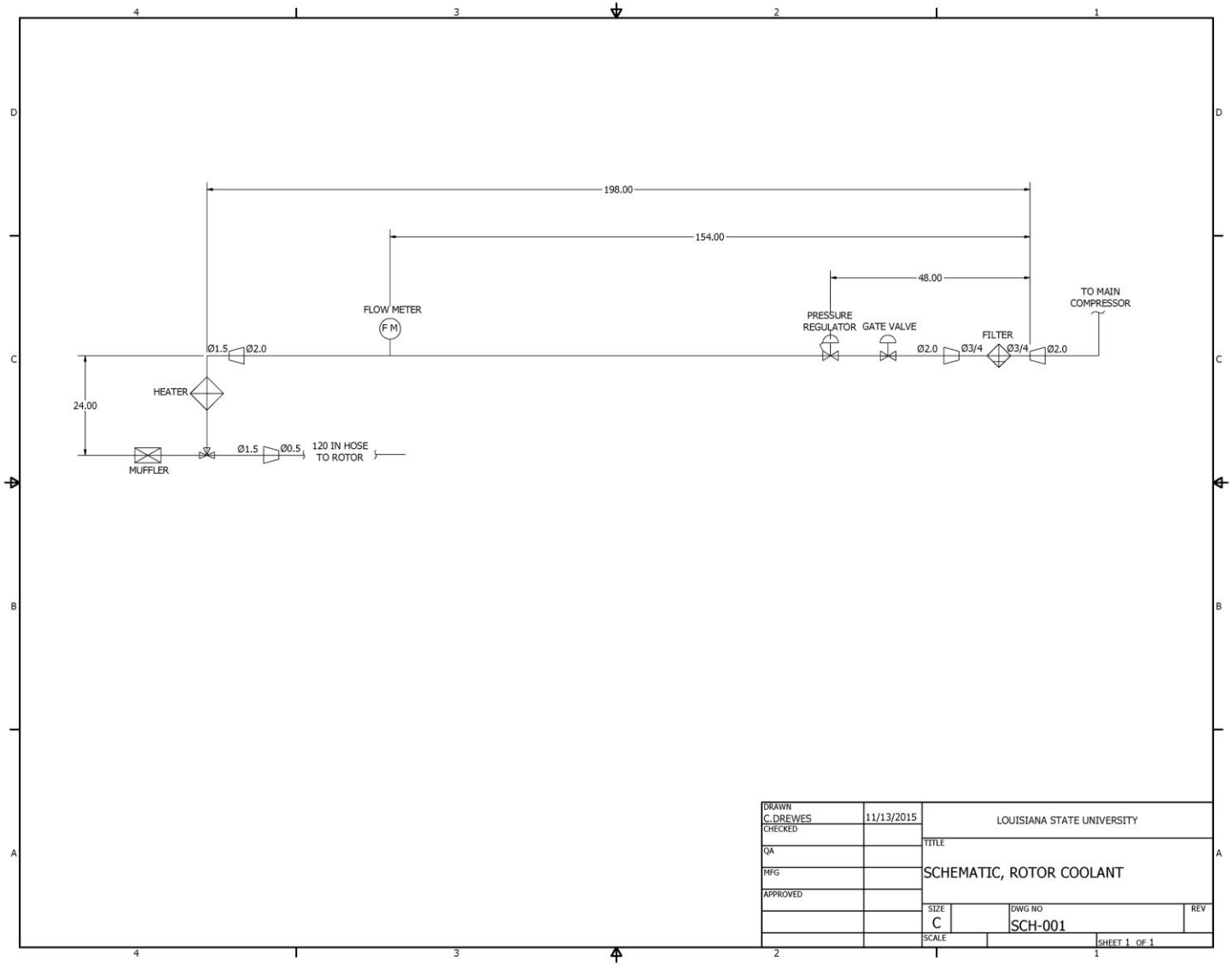

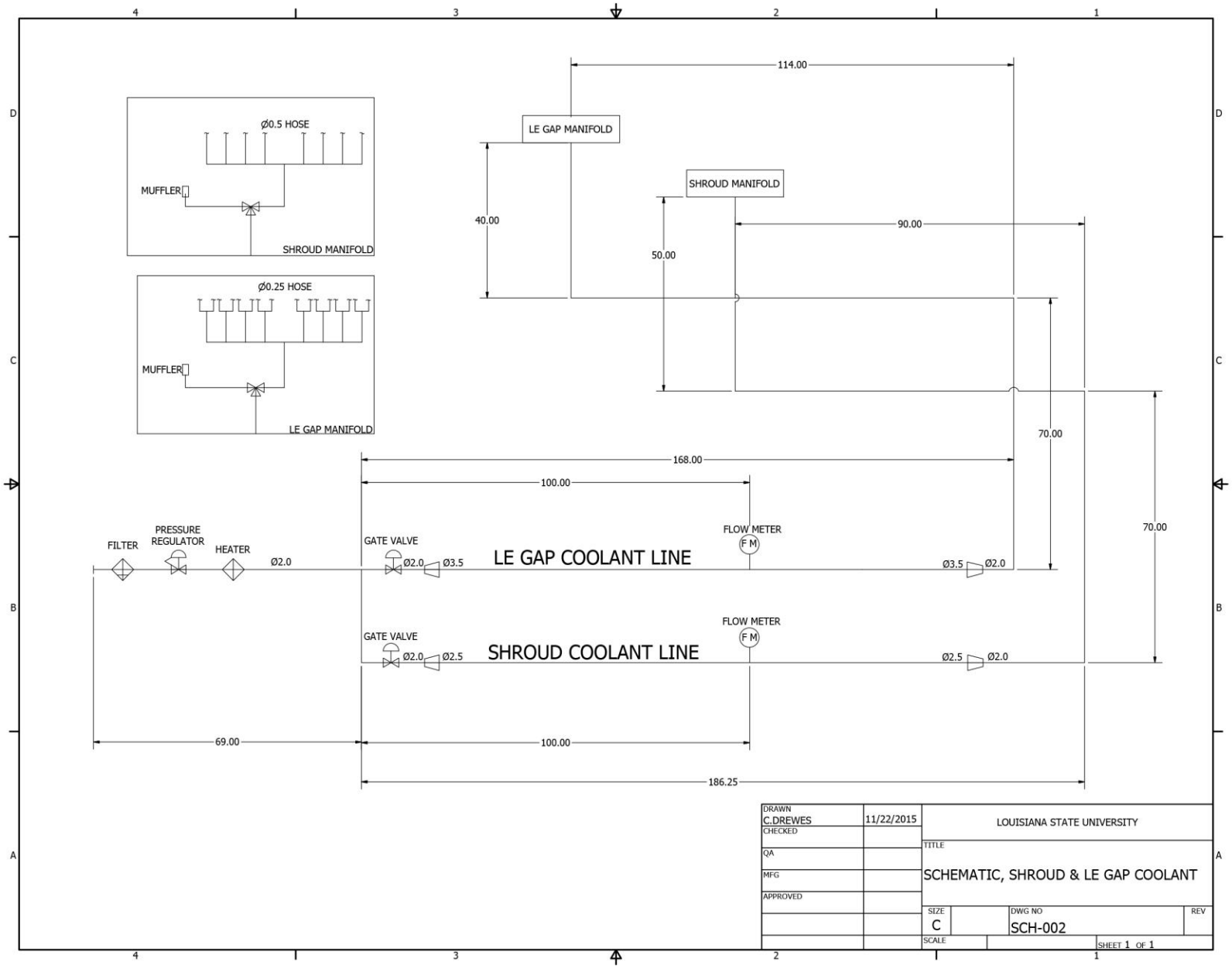
Ø0.5 HOSE
MUFFLER
SHROUD MANIFOLD
Ø0.25 HOSE
MUFFLER
LE GAP MANIFOLD
114.00
LE GAP MANIFOLD
SHROUD MANIFOLD
40.00
50.00
90.00
70.00
168.00
100.00
70.00
FILTER
PRESSURE REGULATOR
HEATER
Ø2.0
GATE VALVE
Ø2.0
Ø3.5
LE GAP COOLANT LINE
FLOW METER
F M
Ø3.5
Ø2.0
GATE VALVE
Ø2.0
Ø2.5
SHROUD COOLANT LINE
FLOW METER
F M
Ø2.5
Ø2.0
69.00
100.00
186.25
DRAWN
C.DREWES
11/22/2015
CHECKED
QA
MFG
APPROVED
LOUISIANA STATE UNIVERSITY
TITLE
SCHEMATIC, SHROUD & LE GAP COOLANT
SIZE
C
DWG NO
SCH-002
REV
SCALE
SHEET 1 OF 1

GENERAL NOTES:

1. SEAL ALL FAYING SURFACES WITH SILICONE CAULK
2. ALL SHEET METAL WELDS PER AWS/ANSI D9.1
3. GALVANIZED STEEL SHEET PER AISI A526
4. DUCT HANGERS AND HARDWARE NOT SHOWN FOR CLARITY

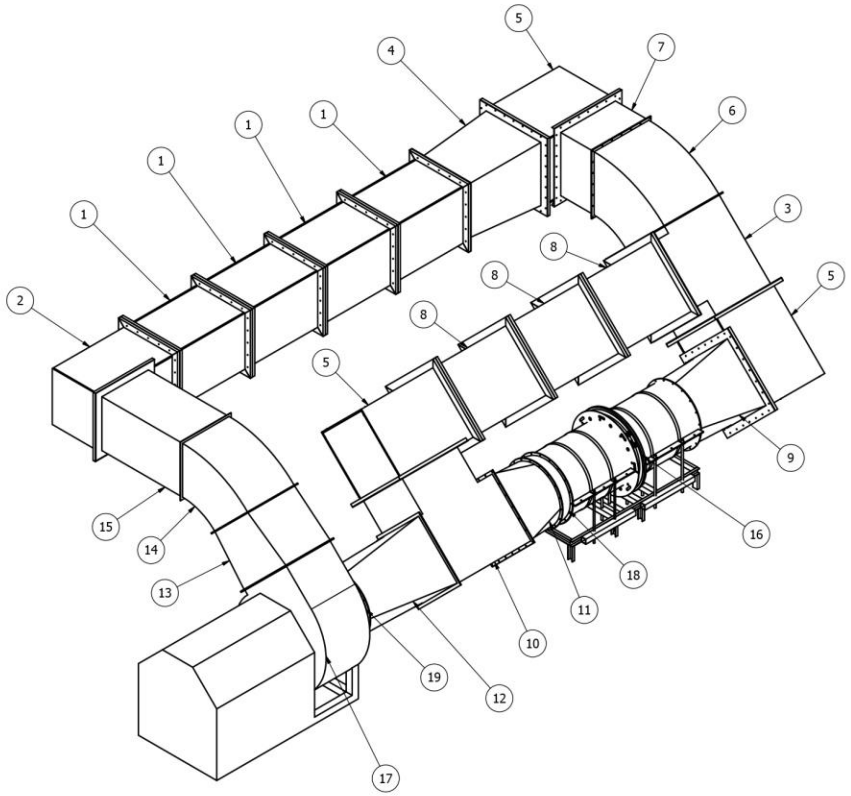

PARTS LIST

ITEM	QTY	PART NUMBER	DESCRIPTION	VENDOR	ZONE	NOTES
1	4	100	ASSY, DUCT			
2	1	200	ASSY, DUCT, ELBOW			
3	1	300	DUCT, BYPASS TEE	SPIRAL METALS		
4	1	500	DUCT, DIFFUSER	SPIRAL METALS		
5	3	600	DUCT, ELBOW			
6	1	700	DUCT, ELBOW 45	SPIRAL METALS		
7	1	800	ASSY, DUCT	SPIRAL METALS		
8	3	900	ASSY, DUCT			
9	1	1000	DUCT, TRANSITION	SPIRAL METALS		
10	1	1100	ASSY, DUCT	SPIRAL METALS		
11	1	1200	ASSY, DUCT	SPIRAL METALS		
12	1	1300	ASSY, DUCT	LSU FACILITY SERVICES		
13	1	1400	ASSY, DUCT	SPIRAL METALS		
14	1	1500	ASSY, DUCT	SPIRAL METALS		
15	1	1600	ASSY, DUCT	SPIRAL METALS		
16	1	TS-001	ASSY, TEST SECTION			
17	1	BAV-365-SWSI-CLASSII-CW-10-THD	FAN - AIRFOIL UTILITY SET	TWIN CITY FAN & BLOWER		
18	1	CQM25659	BELLOWS	CQM INC.		
19	1	Q436458	BELLOWS	A&A MANUFACTURING		

DRAWN	C.DREWES	3/6/2015
CHECKED		
QA		
MFG		
APPROVED		

LOUISIANA STATE UNIVERSITY

TITLE

ROTATING TURBINE CASCADE WIND TUNNEL ASSEMBLY AND DETAILS

SIZE		DWG NO	REV
C		WIND TUNNEL -001	

SCALE

SHEET 1 OF 33

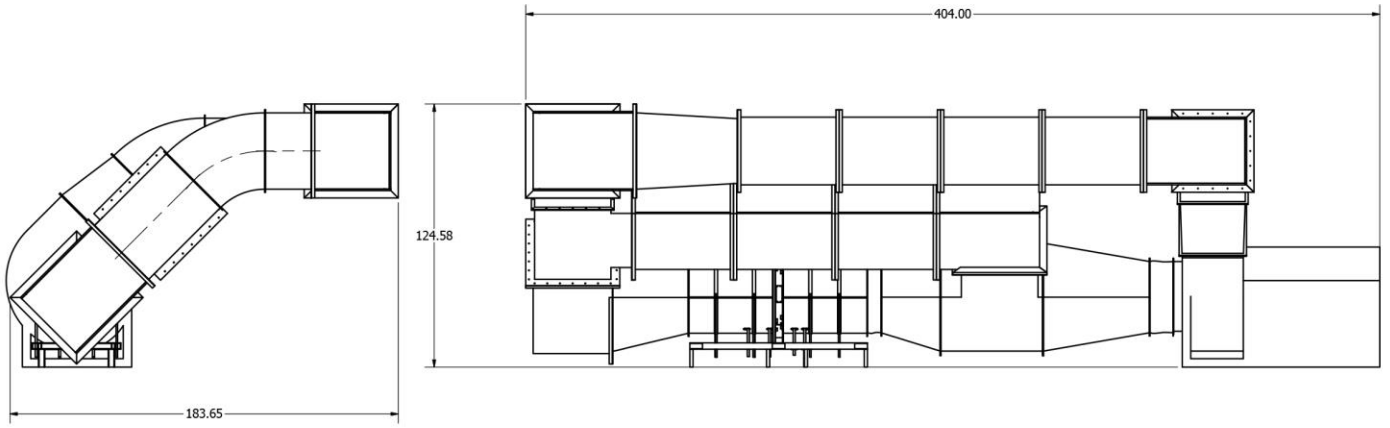

WIND TUNNEL -001

DRAWN C.DREWES	3/6/2015	LOUISIANA STATE UNIVERSITY	
CHECKED		TITLE	
QA		ROTATING TURBINE CASCADE WIND TUNNEL ASSEMBLY AND DETAILS	
MFG			
APPROVED		SIZE C	DWG NO WIND TUNNEL -001 REV
		SCALE	SHEET 2 OF 33

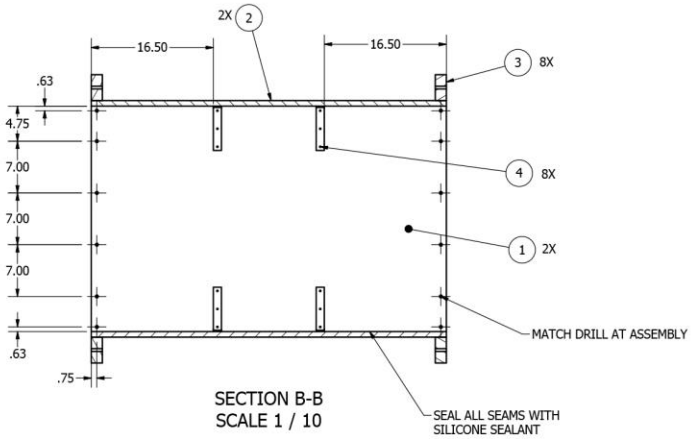

SECTION B-B
SCALE 1 / 10

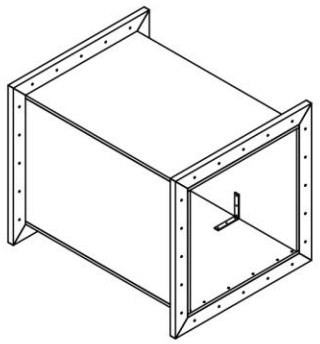

ISOMETRIC VIEW
(REFERENCE ONLY)
SCALE: NONE

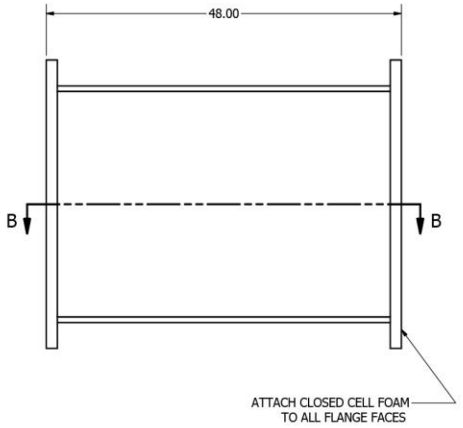

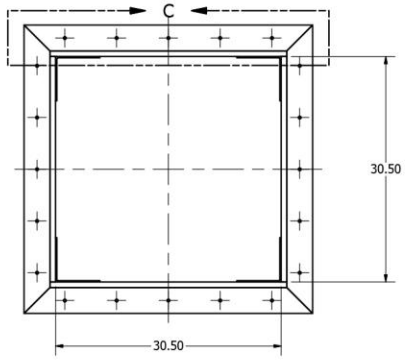

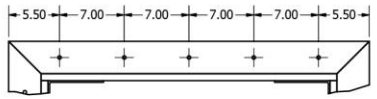

DETAIL C
SCALE 1 / 8

100

PARTS LIST				
ITEM	QTY	PART NUMBER	DESCRIPTION	VENDOR
1	2	101	PANEL, DUCT	
2	2	102	PANEL, DUCT	
3	8	103	FLANGE, DUCT	
4	8	104	BRACKET, DUCT	McMASTER CARR

DRAWN	C.DREWES	3/6/2015
CHECKED		
QA		
MFG		
APPROVED		

LOUISIANA STATE UNIVERSITY

TITLE
ROTATING TURBINE CASCADE WIND TUNNEL ASSEMBLY AND DETAILS

SIZE	DWG NO	REV
C	WIND TUNNEL -001	

SCALE

SHEET 3 OF 33

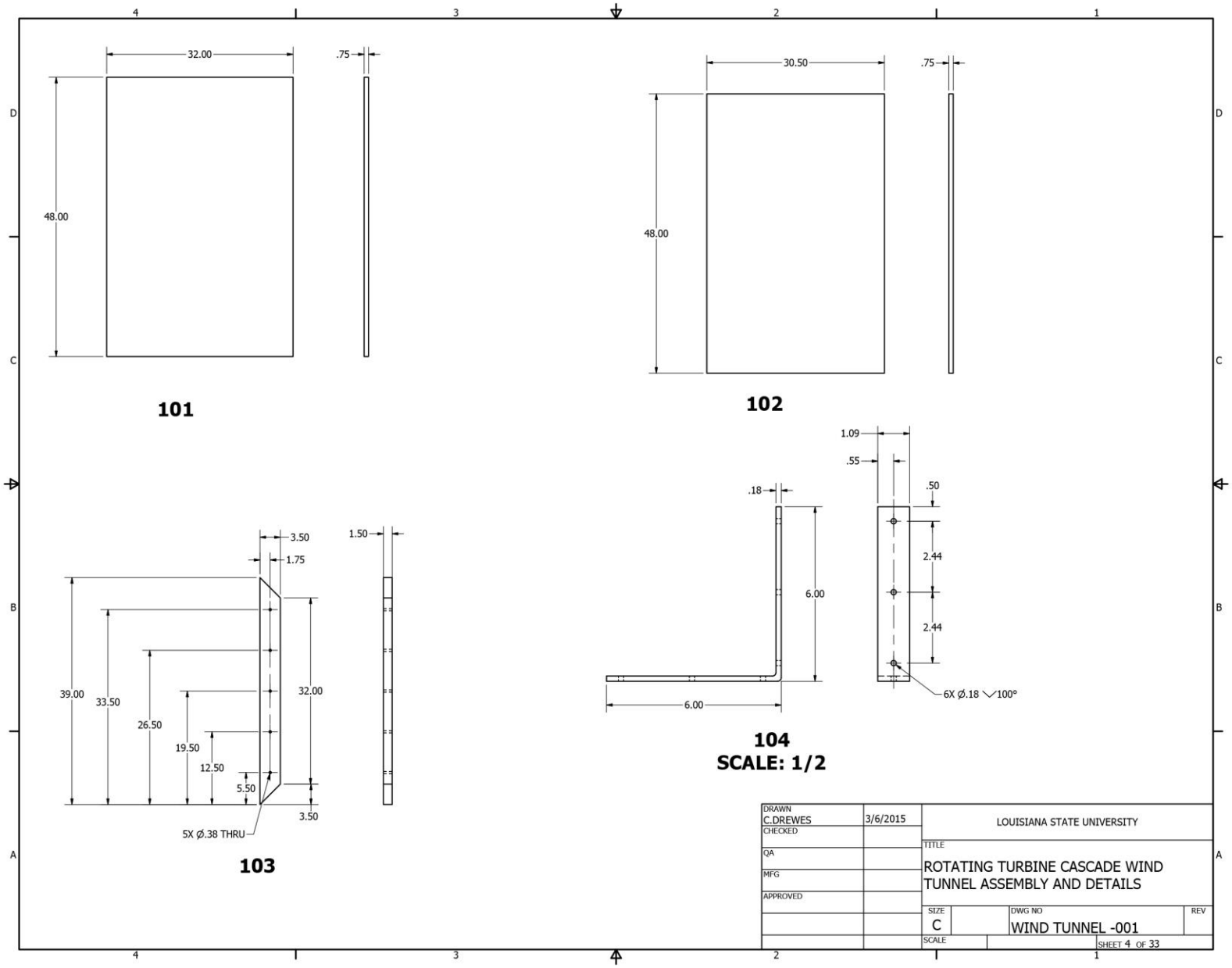
32.00
.75
48.00
101
30.50
.75
48.00
102
1.09
.55
.50
.18
2.44
2.44
6.00
6.00
6X Ø.18 100°
104
SCALE: 1/2
3.50
1.75
1.50
39.00
33.50
26.50
19.50
12.50
5.50
32.00
3.50
5X Ø.38 THRU
103
DRAWN
C.DREWES
3/6/2015
CHECKED
QA
MFG
APPROVED
LOUISIANA STATE UNIVERSITY
TITLE
ROTATING TURBINE CASCADE WIND TUNNEL ASSEMBLY AND DETAILS
SIZE
C
DWG NO
WIND TUNNEL -001
REV
SCALE
SHEET 4 OF 33

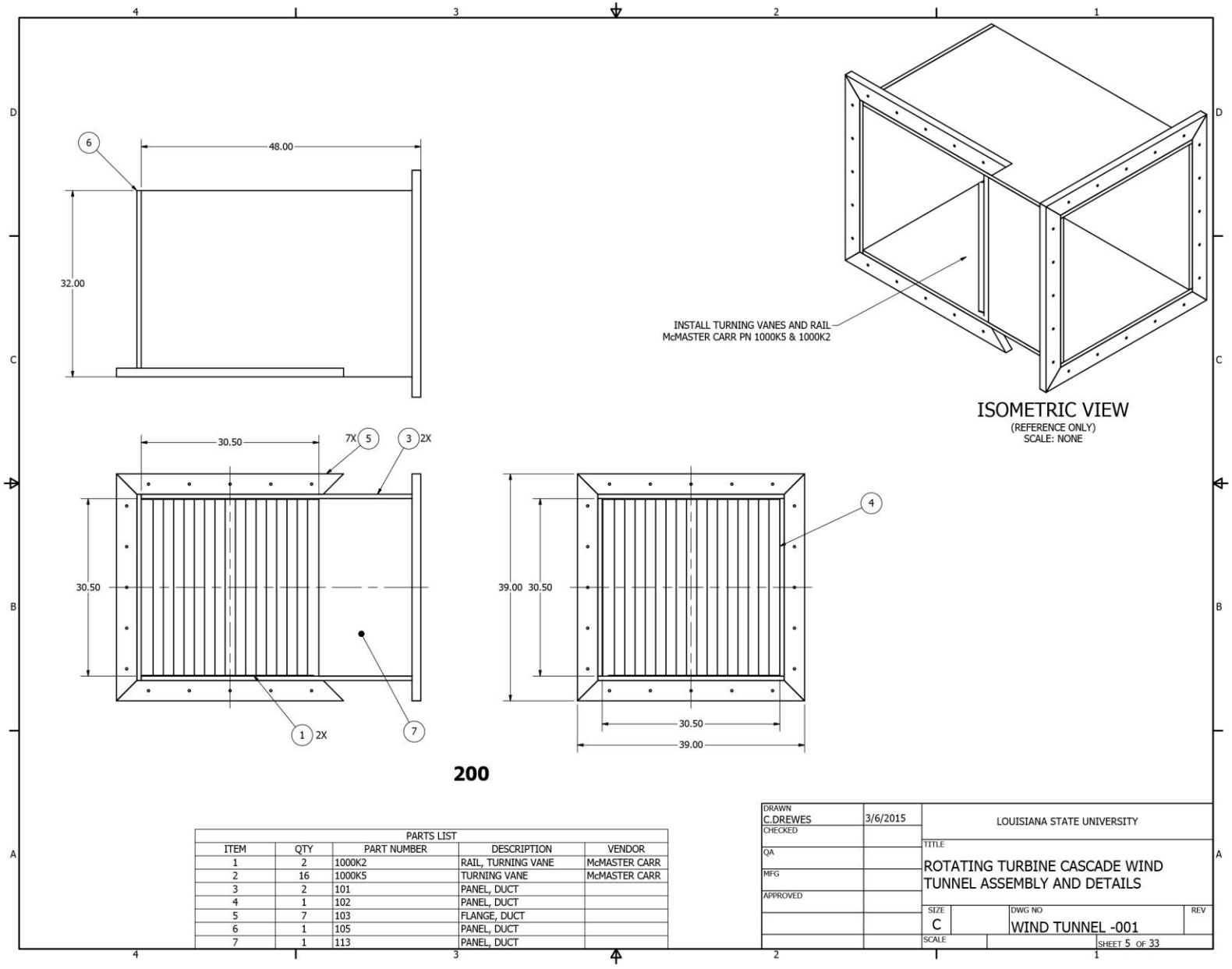

PARTS LIST				
ITEM	QTY	PART NUMBER	DESCRIPTION	VENDOR
1	2	1000K2	RAIL, TURNING VANE	McMASTER CARR
2	16	1000K5	TURNING VANE	McMASTER CARR
3	2	101	PANEL, DUCT	
4	1	102	PANEL, DUCT	
5	7	103	FLANGE, DUCT	
6	1	105	PANEL, DUCT	
7	1	113	PANEL, DUCT	

DRAWN C.DREWES	3/6/2015	LOUISIANA STATE UNIVERSITY
CHECKED		TITLE: ROTATING TURBINE CASCADE WIND TUNNEL ASSEMBLY AND DETAILS
QA		
MFG		
APPROVED		SIZE C | DWG NO WIND TUNNEL -001 | REV
		SCALE | SHEET 5 OF 33

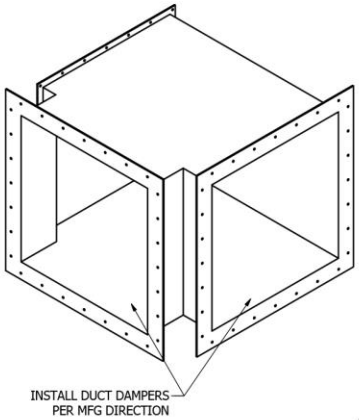

ISOMETRIC VIEW
(REFERENCE ONLY)
SCALE: NONE

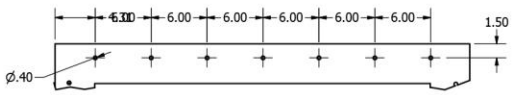

DETAIL E
SCALE 1 / 8

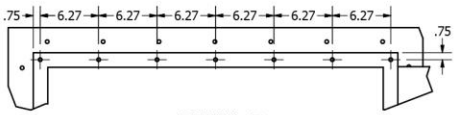

DETAIL F
SCALE 1 /8

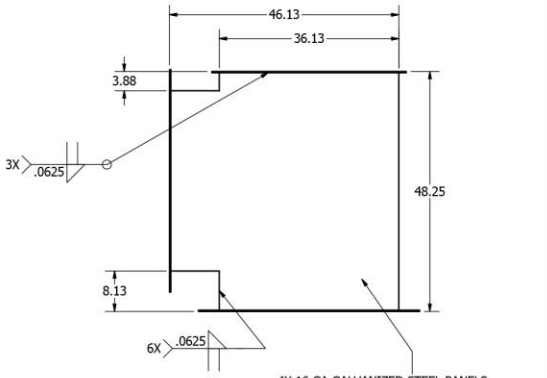

4X 16 GA GALVANIZED STEEL PANELS
COLD GALVANIZE WELDS AFTER FABRICATION

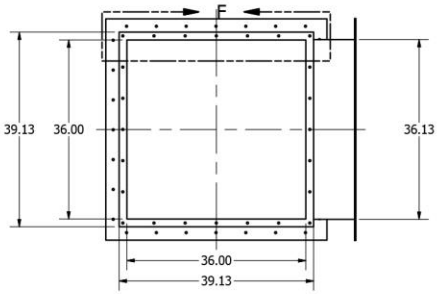

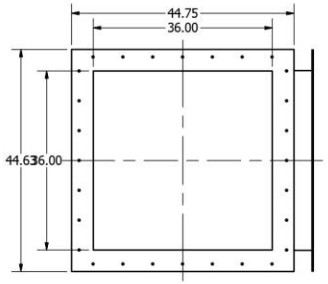

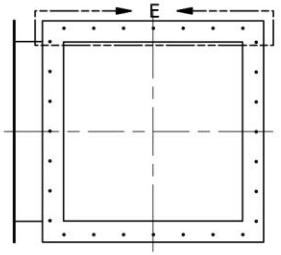

300

PARTS LIST				
ITEM	QTY	PART NUMBER	DESCRIPTION	VENDOR
1	1	300	DUCT, BYPASS TEE	SPIRAL METALS

DRAWN C.DREWES	3/6/2015	LOUISIANA STATE UNIVERSITY
CHECKED		TITLE: ROTATING TURBINE CASCADE WIND TUNNEL ASSEMBLY AND DETAILS
QA		
MFG		
APPROVED		SIZE C · DWG NO WIND TUNNEL -001 · REV
		SCALE · SHEET 6 OF 33

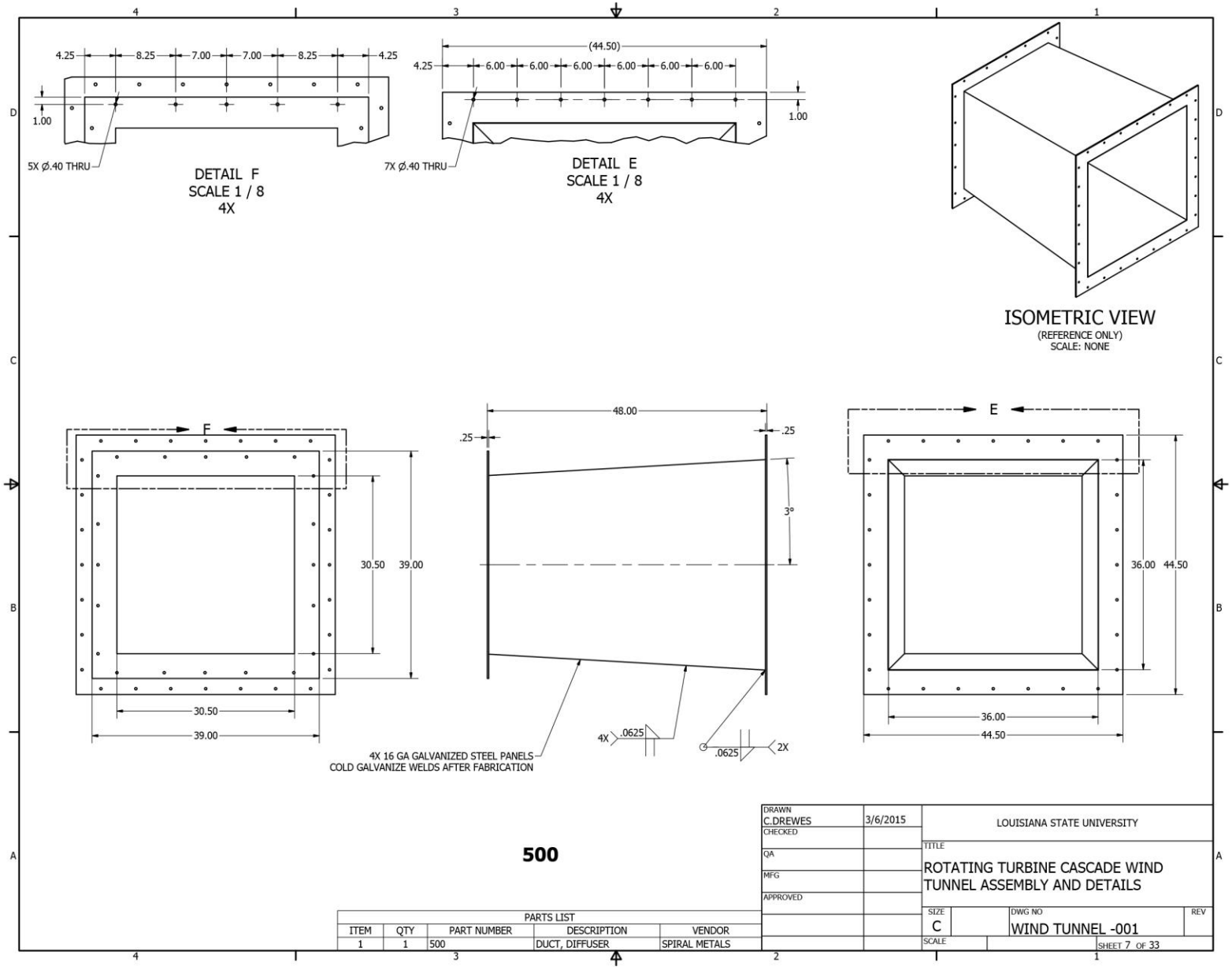
4.25
8.25
7.00
7.00
8.25
4.25
1.00
5X Ø.40 THRU
DETAIL F
SCALE 1 / 8
4X
(44.50)
4.25
6.00
6.00
6.00
6.00
6.00
6.00
1.00
7X Ø.40 THRU
DETAIL E
SCALE 1 / 8
4X
ISOMETRIC VIEW
(REFERENCE ONLY)
SCALE: NONE
F
30.50
39.00
30.50
39.00
48.00
.25
.25
3°
4X .0625
.0625
2X
4X 16 GA GALVANIZED STEEL PANELS
COLD GALVANIZE WELDS AFTER FABRICATION
E
36.00
44.50
36.00
44.50
500
PARTS LIST
ITEM
QTY
PART NUMBER
DESCRIPTION
VENDOR
1
1
500
DUCT, DIFFUSER
SPIRAL METALS
DRAWN
C.DREWES
3/6/2015
CHECKED
QA
MFG
APPROVED
LOUISIANA STATE UNIVERSITY
TITLE
ROTATING TURBINE CASCADE WIND TUNNEL ASSEMBLY AND DETAILS
SIZE
C
DWG NO
WIND TUNNEL -001
REV
SCALE
SHEET 7 OF 33

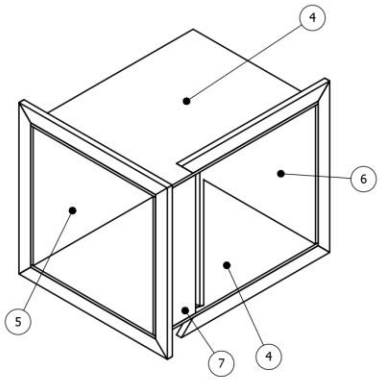

ISOMETRIC VIEW
(REFERENCE ONLY)
SCALE: NONE

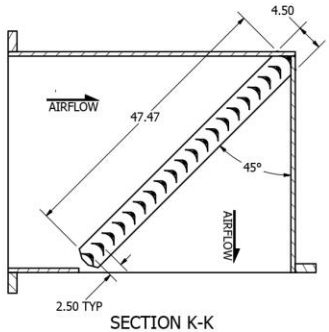

SECTION K-K
SCALE 1 / 12

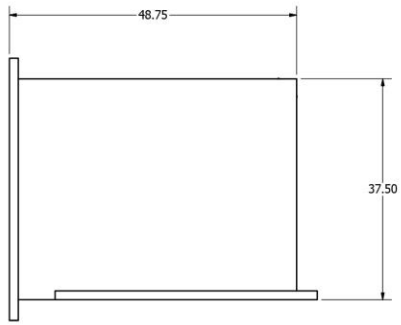

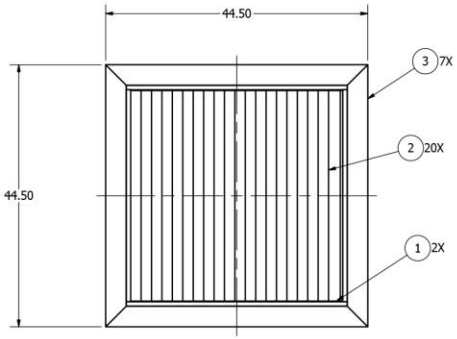

600

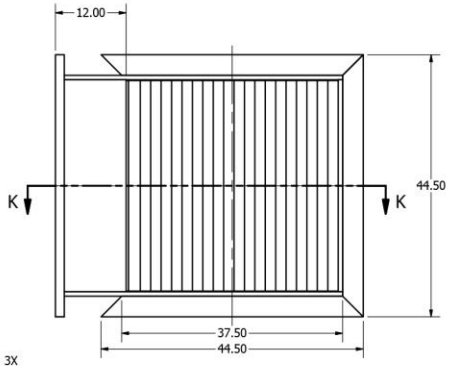

PARTS LIST				
ITEM	QTY	PART NUMBER	DESCRIPTION	VENDOR
1	2	1000K2	RAIL, TURNING VANE	McMASTER CARR
2	20	1000K5	TURNING VANE	McMASTER CARR
3	7	106	FLANGE, DUCT	
4	2	107	PANEL, DUCT	
5	1	108	PANEL, DUCT	
6	1	109	PANEL, DUCT	
7	1	110	PANEL, DUCT	

DRAWN C.DREWES	3/6/2015	LOUISIANA STATE UNIVERSITY
CHECKED		TITLE: ROTATING TURBINE CASCADE WIND TUNNEL ASSEMBLY AND DETAILS
QA		
MFG		
APPROVED		SIZE C · DWG NO WIND TUNNEL -001 · REV
		SCALE · SHEET 8 OF 33

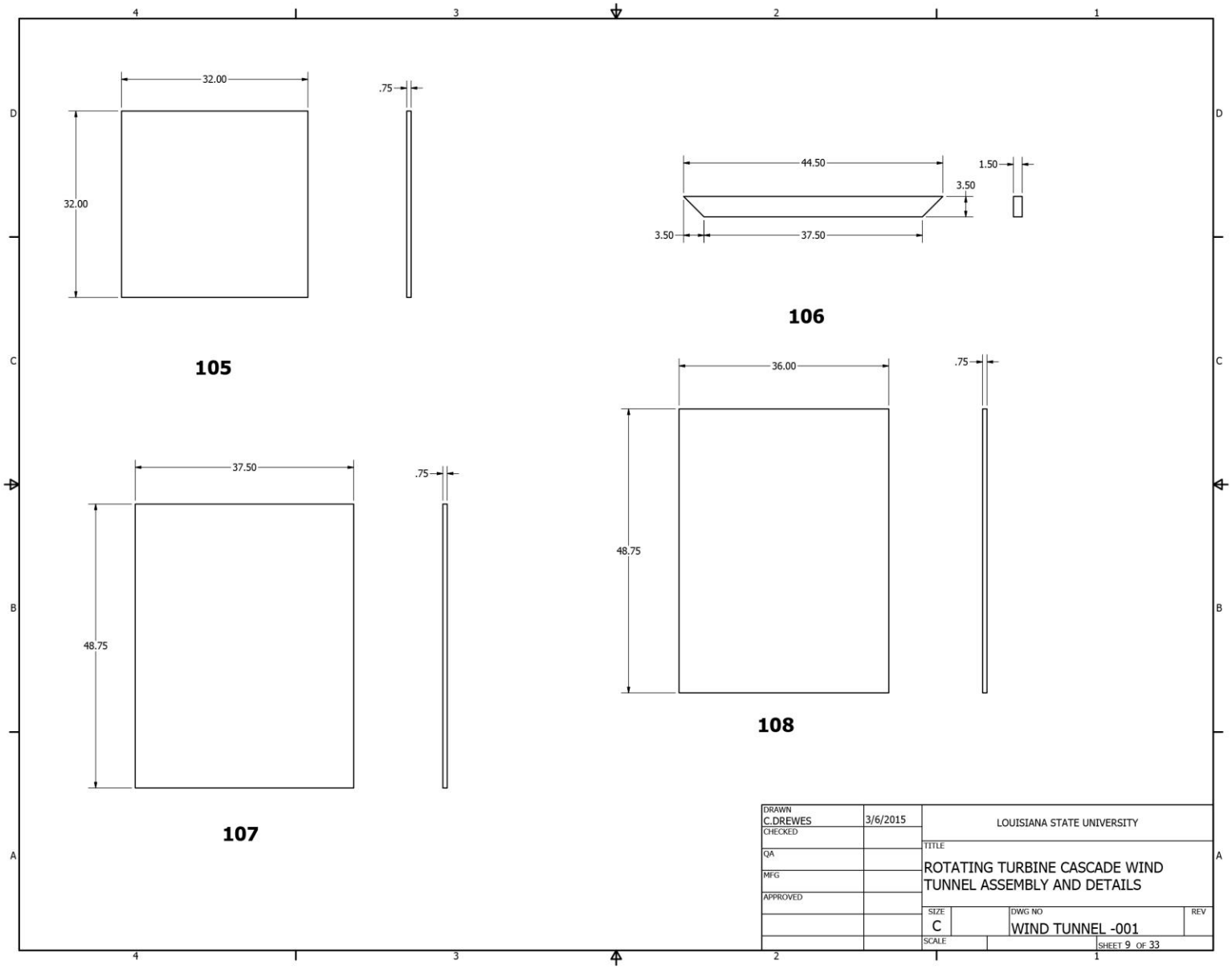
32.00
32.00
.75
105
44.50
1.50
3.50
3.50
37.50
106
36.00
.75
48.75
108
37.50
.75
48.75
107
DRAWN
C.DREWES
3/6/2015
CHECKED
QA
MFG
APPROVED
LOUISIANA STATE UNIVERSITY
TITLE
ROTATING TURBINE CASCADE WIND TUNNEL ASSEMBLY AND DETAILS
SIZE
C
DWG NO
WIND TUNNEL -001
REV
SCALE
SHEET 9 OF 33

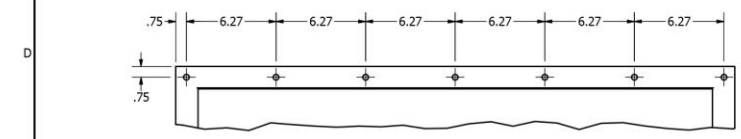

DETAIL L
SCALE 1 / 5

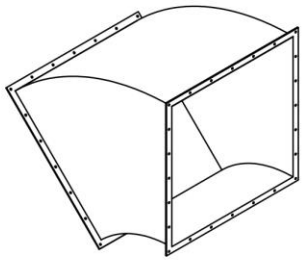

ISOMETRIC VIEW
(REFERENCE ONLY)
SCALE: NONE

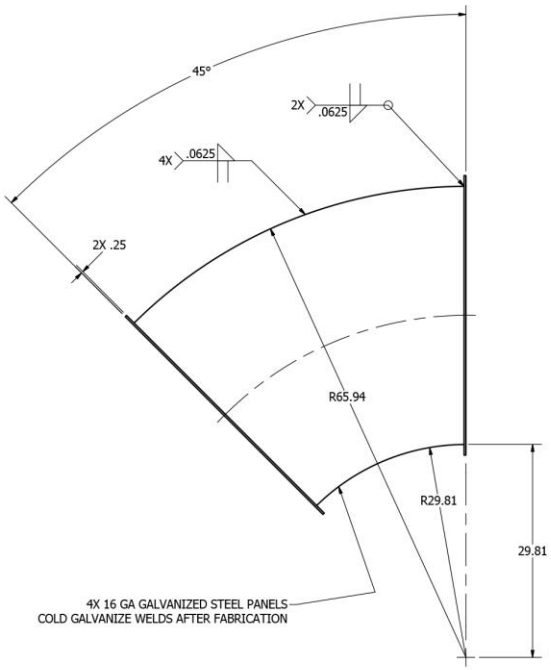

4X 16 GA GALVANIZED STEEL PANELS
COLD GALVANIZE WELDS AFTER FABRICATION

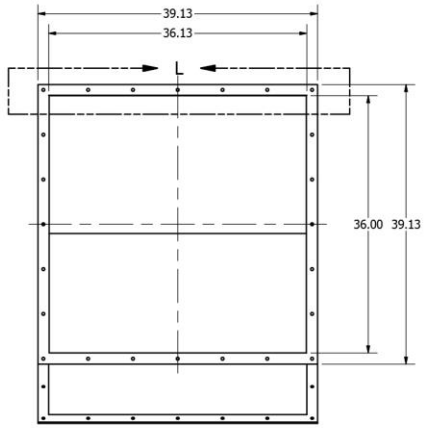

700

PARTS LIST				
ITEM	QTY	PART NUMBER	DESCRIPTION	VENDOR
1	1	700	DUCT, ELBOW 45	SPIRAL METALS

DRAWN	C.DREWES	3/6/2015
CHECKED		
QA		
MFG		
APPROVED		

LOUISIANA STATE UNIVERSITY

TITLE
ROTATING TURBINE CASCADE WIND TUNNEL ASSEMBLY AND DETAILS

SIZE	DWG NO	REV
C	WIND TUNNEL -001	

SCALE

SHEET 10 OF 33

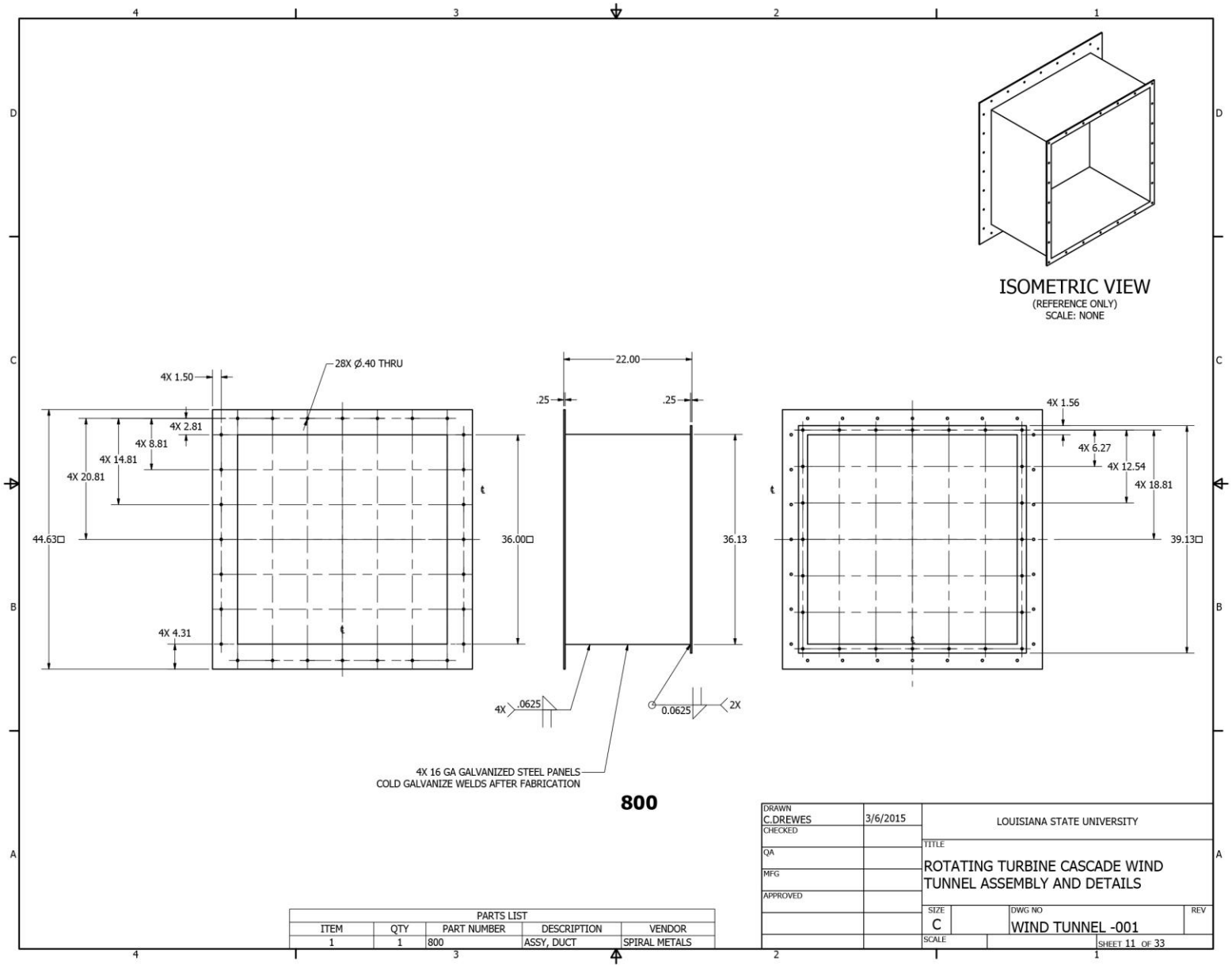
ISOMETRIC VIEW
(REFERENCE ONLY)
SCALE: NONE
4X 1.50
28X Ø.40 THRU
4X 2.81
4X 8.81
4X 14.81
4X 20.81
44.63□
4X 4.31
36.00□
22.00
.25
.25
36.13
4X .0625
0.0625
2X
4X 16 GA GALVANIZED STEEL PANELS
COLD GALVANIZE WELDS AFTER FABRICATION
4X 1.56
4X 6.27
4X 12.54
4X 18.81
39.13□
800
PARTS LIST
ITEM | QTY | PART NUMBER | DESCRIPTION | VENDOR
1 | 1 | 800 | ASSY, DUCT | SPIRAL METALS
DRAWN C.DREWES 3/6/2015
CHECKED
QA
MFG
APPROVED
LOUISIANA STATE UNIVERSITY
TITLE
ROTATING TURBINE CASCADE WIND TUNNEL ASSEMBLY AND DETAILS
SIZE C
DWG NO WIND TUNNEL -001
REV
SCALE
SHEET 11 OF 33

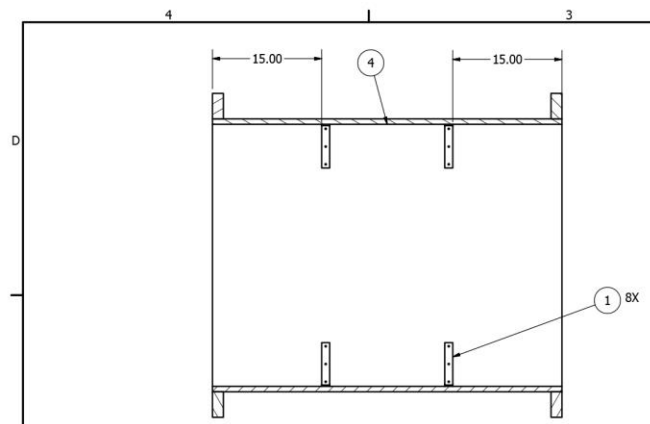

SECTION M-M
SCALE 1 / 10

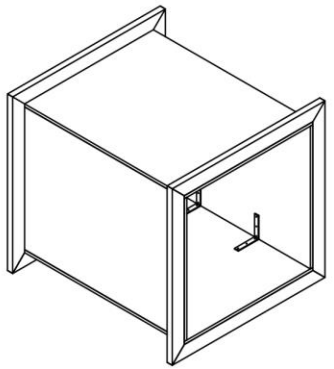

ISOMETRIC VIEW
(REFERENCE ONLY)
SCALE: NONE

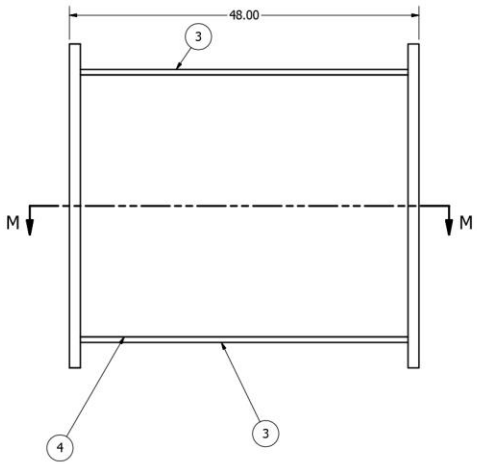

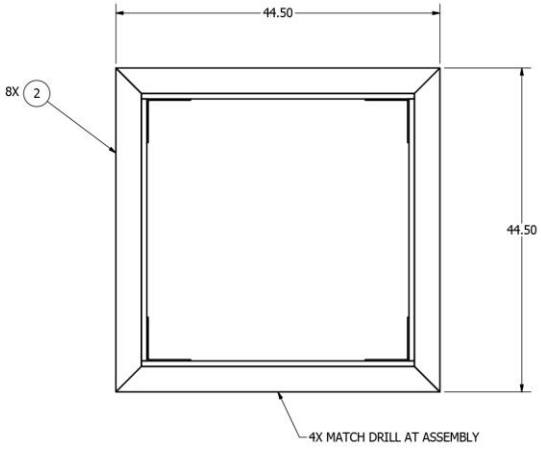

900

PARTS LIST			
ITEM	QTY	PART NUMBER	DESCRIPTION
1	8	104	BRACKET, DUCT
2	8	106	FLANGE, DUCT
3	2	111	PANEL, DUCT
4	2	112	PANEL, DUCT

DRAWN C.DREWES	3/6/2015	LOUISIANA STATE UNIVERSITY
CHECKED		TITLE: ROTATING TURBINE CASCADE WIND TUNNEL ASSEMBLY AND DETAILS
QA		
MFG		
APPROVED		SIZE: C; DWG NO: WIND TUNNEL -001; REV
		SCALE; SHEET 12 OF 33

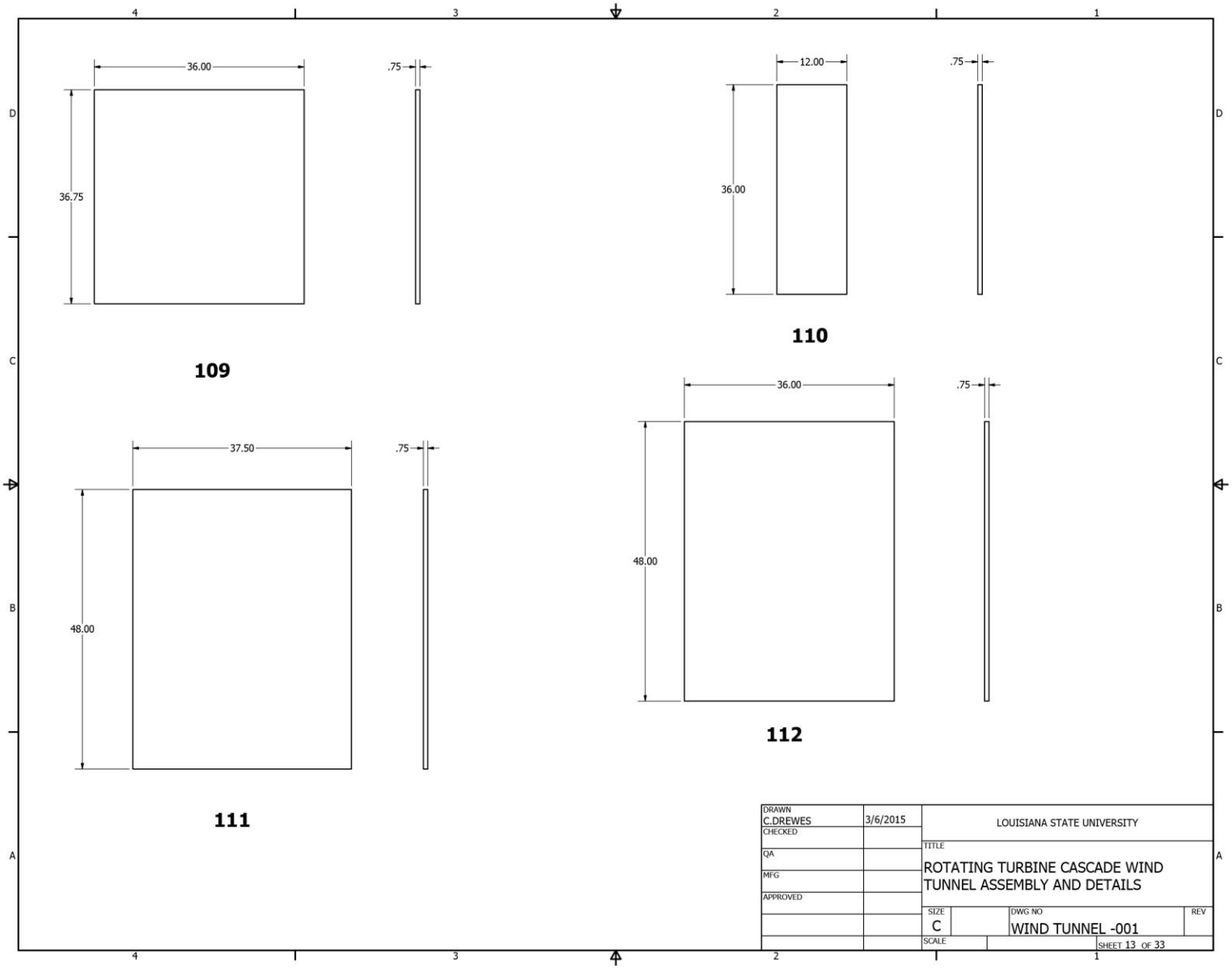
36.00
.75
36.75
109
12.00
.75
36.00
110
37.50
.75
48.00
111
36.00
.75
48.00
112
DRAWN
C.DREWES
3/6/2015
CHECKED
QA
MFG
APPROVED
LOUISIANA STATE UNIVERSITY
TITLE
ROTATING TURBINE CASCADE WIND TUNNEL ASSEMBLY AND DETAILS
SIZE
C
DWG NO
WIND TUNNEL -001
REV
SCALE
SHEET 13 OF 33

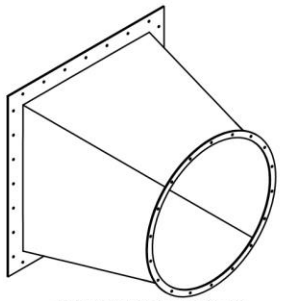

ISOMETRIC VIEW
(REFERENCE ONLY)
SCALE: NONE

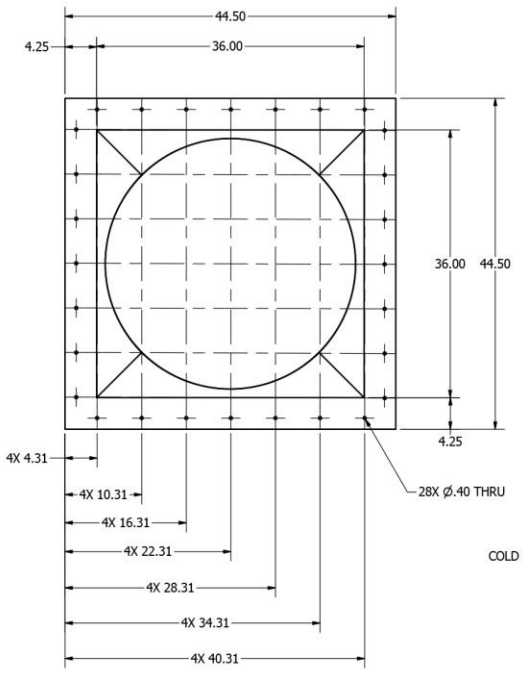

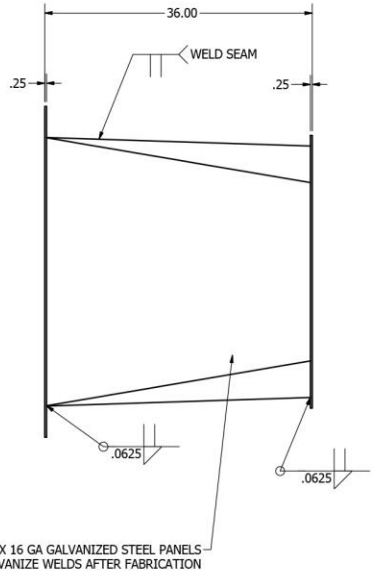

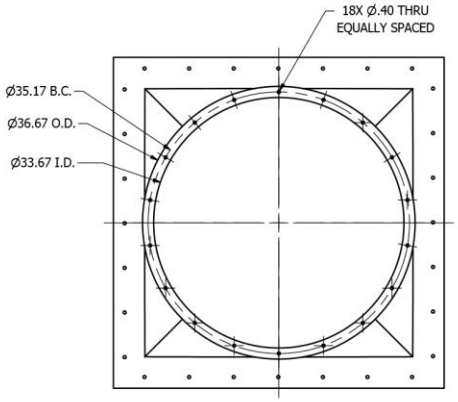

1000

PARTS LIST				
ITEM	QTY	PART NUMBER	DESCRIPTION	VENDOR
1	1	1000	DUCT, TRANSITION	SPIRAL METALS

DRAWN C.DREWES	3/6/2015	LOUISIANA STATE UNIVERSITY
CHECKED		TITLE: ROTATING TURBINE CASCADE WIND TUNNEL ASSEMBLY AND DETAILS
QA		
MFG		
APPROVED		SIZE C | DWG NO WIND TUNNEL -001 | REV
		SCALE | SHEET 14 OF 33

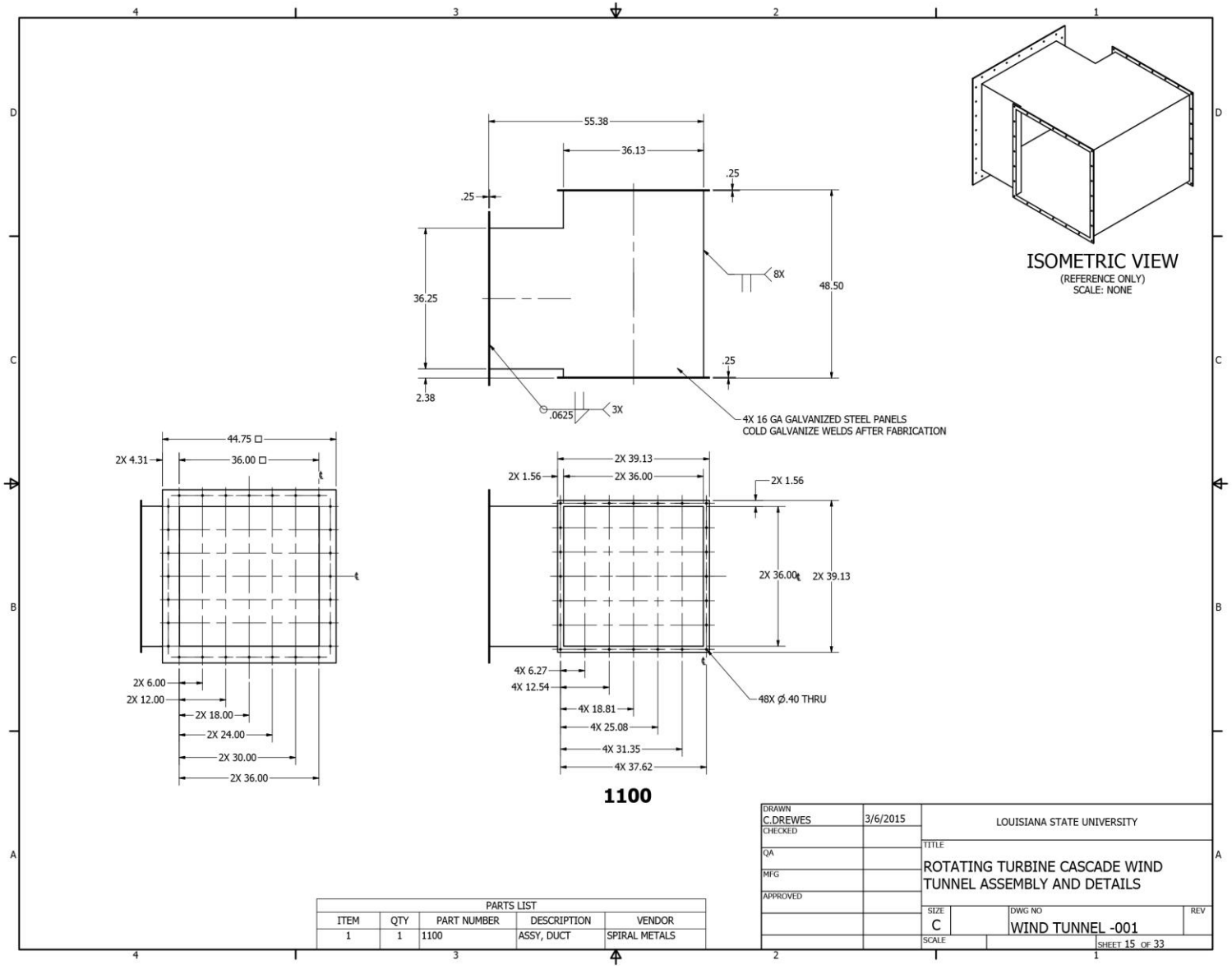
ISOMETRIC VIEW
(REFERENCE ONLY)
SCALE: NONE
55.38
36.13
.25
.25
8X
36.25
48.50
.25
2.38
.0625
3X
4X 16 GA GALVANIZED STEEL PANELS
COLD GALVANIZE WELDS AFTER FABRICATION
44.75
2X 4.31
36.00
2X 6.00
2X 12.00
2X 18.00
2X 24.00
2X 30.00
2X 36.00
2X 39.13
2X 1.56
2X 36.00
2X 1.56
2X 36.00
2X 39.13
4X 6.27
4X 12.54
4X 18.81
4X 25.08
4X 31.35
4X 37.62
48X Ø.40 THRU
1100
PARTS LIST
ITEM | QTY | PART NUMBER | DESCRIPTION | VENDOR
1 | 1 | 1100 | ASSY, DUCT | SPIRAL METALS
DRAWN C.DREWES 3/6/2015
CHECKED
QA
MFG
APPROVED
LOUISIANA STATE UNIVERSITY
TITLE
ROTATING TURBINE CASCADE WIND TUNNEL ASSEMBLY AND DETAILS
SIZE C
DWG NO WIND TUNNEL -001
REV
SCALE
SHEET 15 OF 33

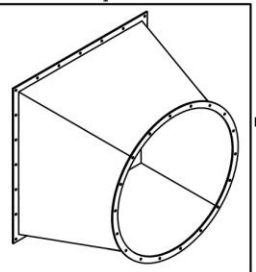

ISOMETRIC VIEW
(REFERENCE ONLY)
SCALE: NONE

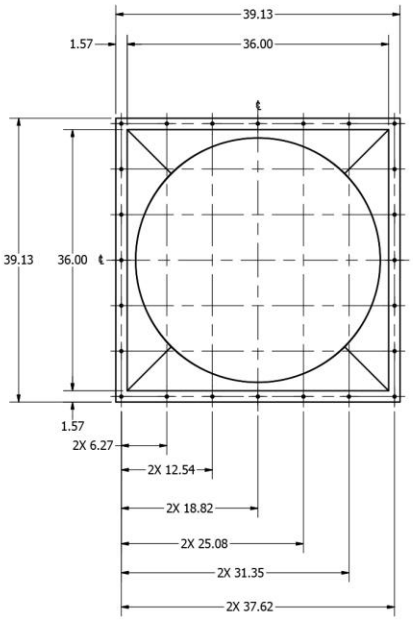

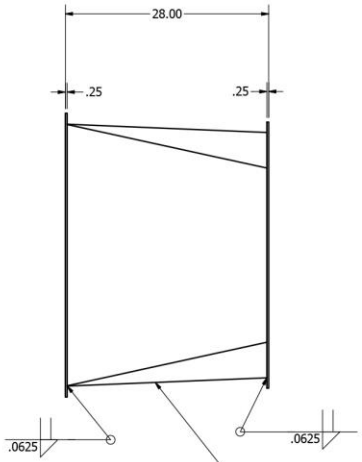

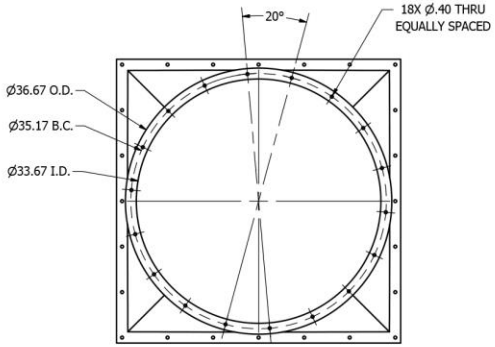

1200

PARTS LIST				
ITEM	QTY	PART NUMBER	DESCRIPTION	VENDOR
1	1	1200	ASSY, DUCT	SPIRAL METALS

DRAWN C.DREWES	3/6/2015	LOUISIANA STATE UNIVERSITY
CHECKED		TITLE: ROTATING TURBINE CASCADE WIND TUNNEL ASSEMBLY AND DETAILS
QA		
MFG		
APPROVED		SIZE: C; DWG NO: WIND TUNNEL -001; REV
		SCALE; SHEET 16 OF 33

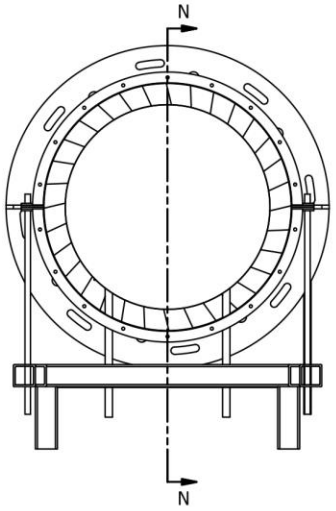

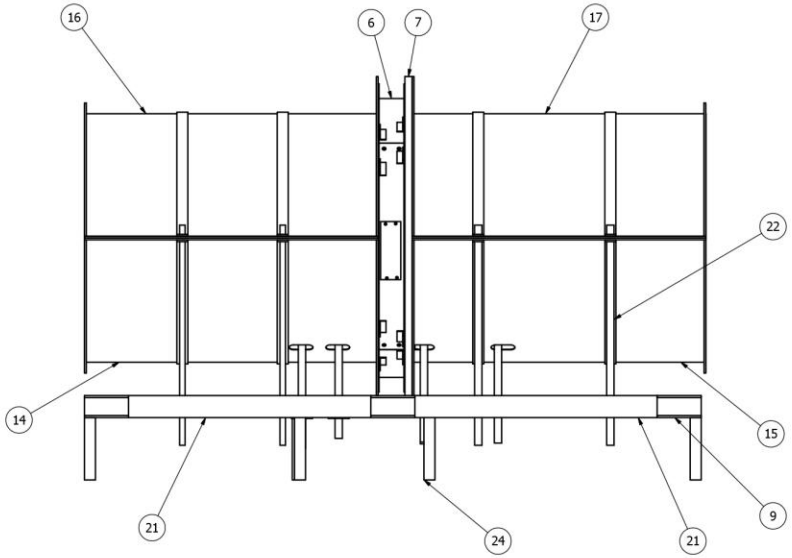

PARTS LIST

ITEM	QTY	PART NUMBER	DESCRIPTION	VENDOR	MATERIAL
1	1	1205-000-003	ROTARY UNION	DEUBLIN	
2	1	3PH 3HP 230V 3400 RPM	ELECTRIC MOTOR	BALDOR	
3	2	6494K35	BEARING, FLANGE MOUNTED BALL	McMASTER CARR	
4	1	HUB-001	ASSY, HUB		AL 6061-T6
5	1	L-095	SPIDER INSERT COUPLING	LOVE JOY	
6	1	SH-001	ASSY, SHROUD	BOSCO MACHINE	
7	1	SH-101	PLATE, SHROUD SUPPORT	BOSCO MACHINE	STEEL
8	1	TS-002	ASSY, TURNING VANE		
9	1	TS-003	ASSY, STRUCTURE		STEEL
10	2	TS-101	BEARING SUPPORT		STEEL
11	1	TS-102	MOTOR SUPPORT		STEEL
12	2	TS-103	ANNULUS, INNER	LSU FACILITY SERVICES	STEEL
13	2	TS-104	TRANSITION DOME		GLASS FIBER REINFORCED RESIN
14	1	TS-105	ASSY, OUTER ANNULUS	BMR METAL WORKS	STEEL
15	1	TS-106	ASSY, OUTER ANNULUS	BMR METAL WORKS	STEEL
16	1	TS-107	ASSY, OUTER ANNULUS	BMR METAL WORKS	STEEL
17	1	TS-108	ASSY, OUTER ANNULUS	BMR METAL WORKS	STEEL
18	1	TS-109	INNER SUPPORT		STEEL
19	8	TS-110	SUPPORT, ANGLE		STEEL
20	4	TS-111	CHANNEL, SQUARE SUPPORT		STEEL
21	4	TS-112	CHANNEL, SQUARE SUPPORT		STEEL
22	10	TS-113	THREADED ROD, 1IN SUPPORT		STEEL
23	6	TS-114	THREADED ROD, 0.75IN SUPPORT		STEEL
24	4	TS-115	C3 x 5 x 8in		STEEL

DRAWN	C.DREWES	3/6/2015
CHECKED		
QA		
MFG		
APPROVED		

LOUISIANA STATE UNIVERSITY

TITLE: ROTATING TURBINE CASCADE WIND TUNNEL ASSEMBLY AND DETAILS

SIZE: C | DWG NO: WIND TUNNEL -001 | REV:

SCALE: | SHEET 17 OF 33

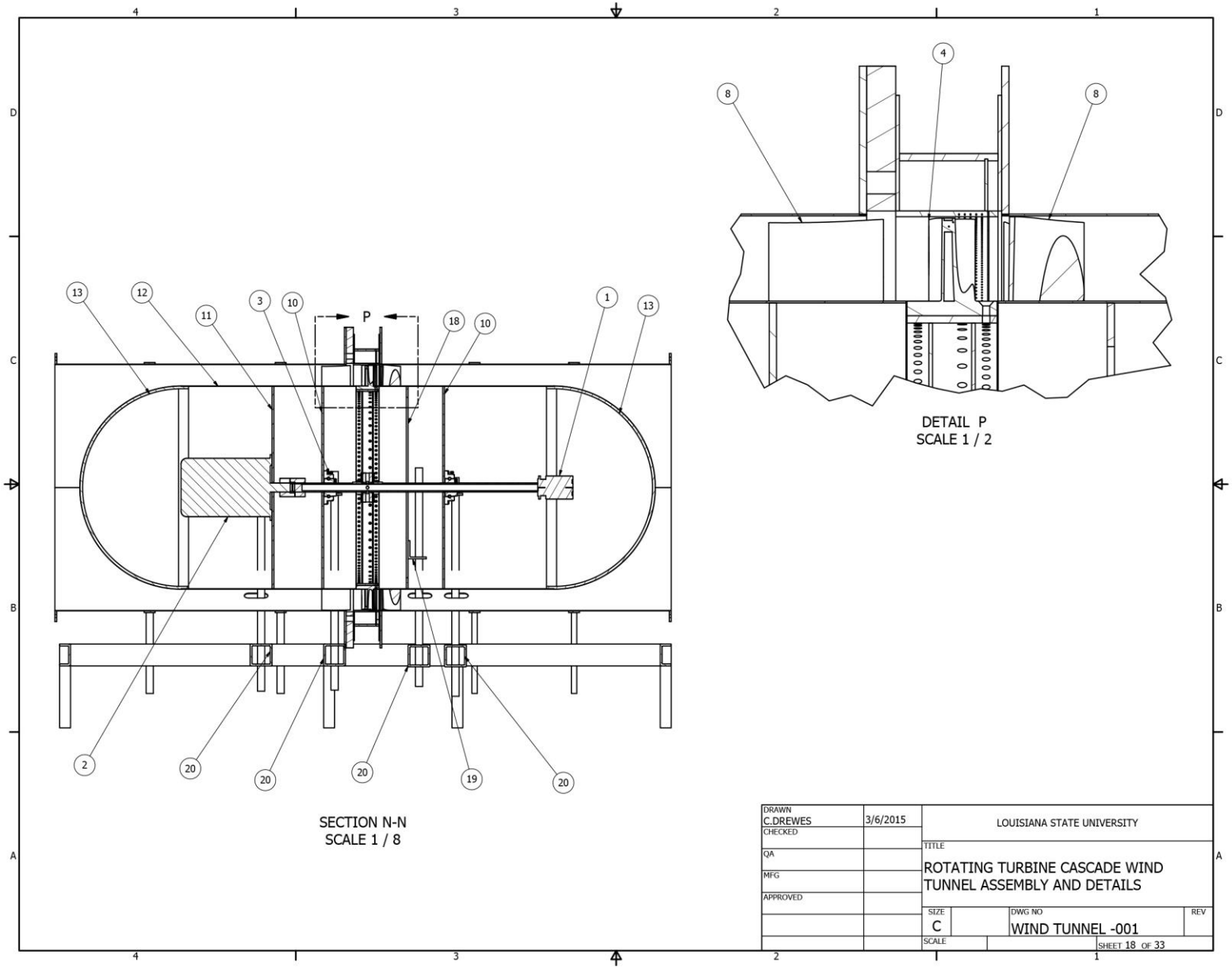
4
3
2
1
D
C
B
A
13
12
11
3
10
P
18
10
1
13
2
20
20
20
19
20
SECTION N-N
SCALE 1 / 8
8
4
8
DETAIL P
SCALE 1 / 2
DRAWN
C.DREWES
3/6/2015
CHECKED
QA
MFG
APPROVED
LOUISIANA STATE UNIVERSITY
TITLE
ROTATING TURBINE CASCADE WIND TUNNEL ASSEMBLY AND DETAILS
SIZE
C
DWG NO
WIND TUNNEL -001
REV
SCALE
SHEET 18 OF 33

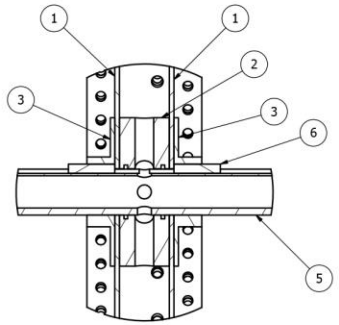

DETAIL U
SCALE 1/2

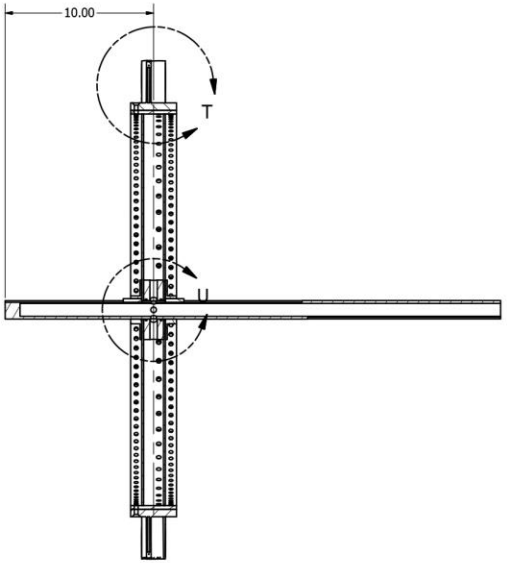

SECTION R-R
SCALE 1/5

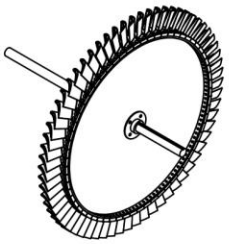

ISOMETRIC VIEW
(REFERENCE ONLY)
SCALE: NONE

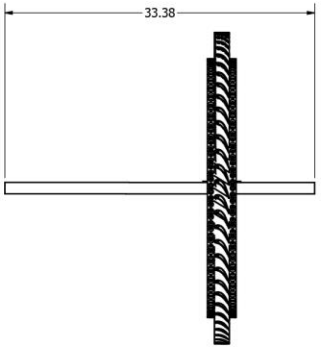

HUB-001

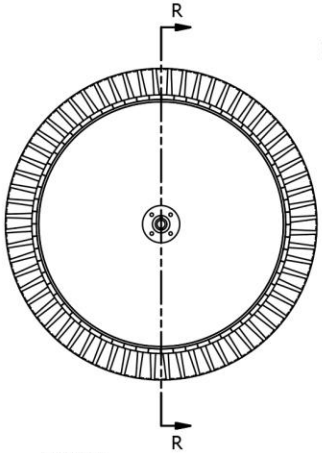

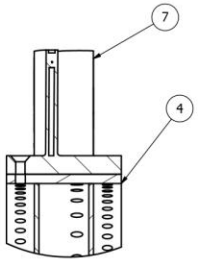

DETAIL T
SCALE 1/2

PARTS LIST				
ITEM	QTY	PART NUMBER	DESCRIPTION	VENDOR
1	2	HUB-101	DISK, SUPPORT	PLANT MACHINE WORKS
2	1	HUB-102	CENTER, PORT	PLANT MACHINE WORKS
3	2	HUB-103	HUB, RETAINER	GOCART GALAXY
4	1	HUB-104	MOUNTING PLATE	PLANT MACHINE WORKS
5	1	HUB-105	SHAFT	GOCART GALAXY
6	2	HUB-106	KEY	McMASTER CARR
7	64	TEST BLADE	BLADE, HPT	IHI

DRAWN C.DREWES	3/6/2015	LOUISIANA STATE UNIVERSITY
CHECKED		TITLE: ROTATING TURBINE CASCADE WIND TUNNEL ASSEMBLY AND DETAILS
QA		
MFG		
APPROVED		
		SIZE C; DWG NO WIND TUNNEL -001; REV
		SCALE; SHEET 19 OF 33

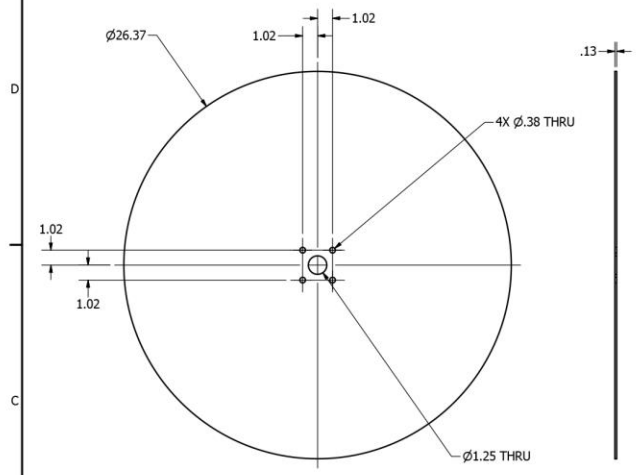

HUB-101

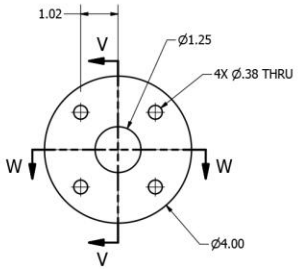

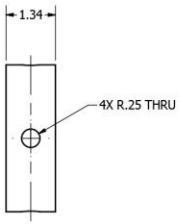

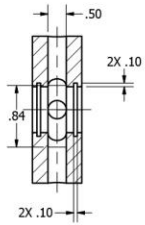

SECTION V-V
SCALE 1/2

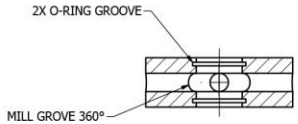

SECTION W-W
SCALE 1/2

HUB-102

DRAWN C.DREWES	3/6/2015	LOUISIANA STATE UNIVERSITY
CHECKED		TITLE: ROTATING TURBINE CASCADE WIND TUNNEL ASSEMBLY AND DETAILS
QA		
MFG		
APPROVED		SIZE C | DWG NO WIND TUNNEL -001 | REV
		SCALE | SHEET 20 OF 33

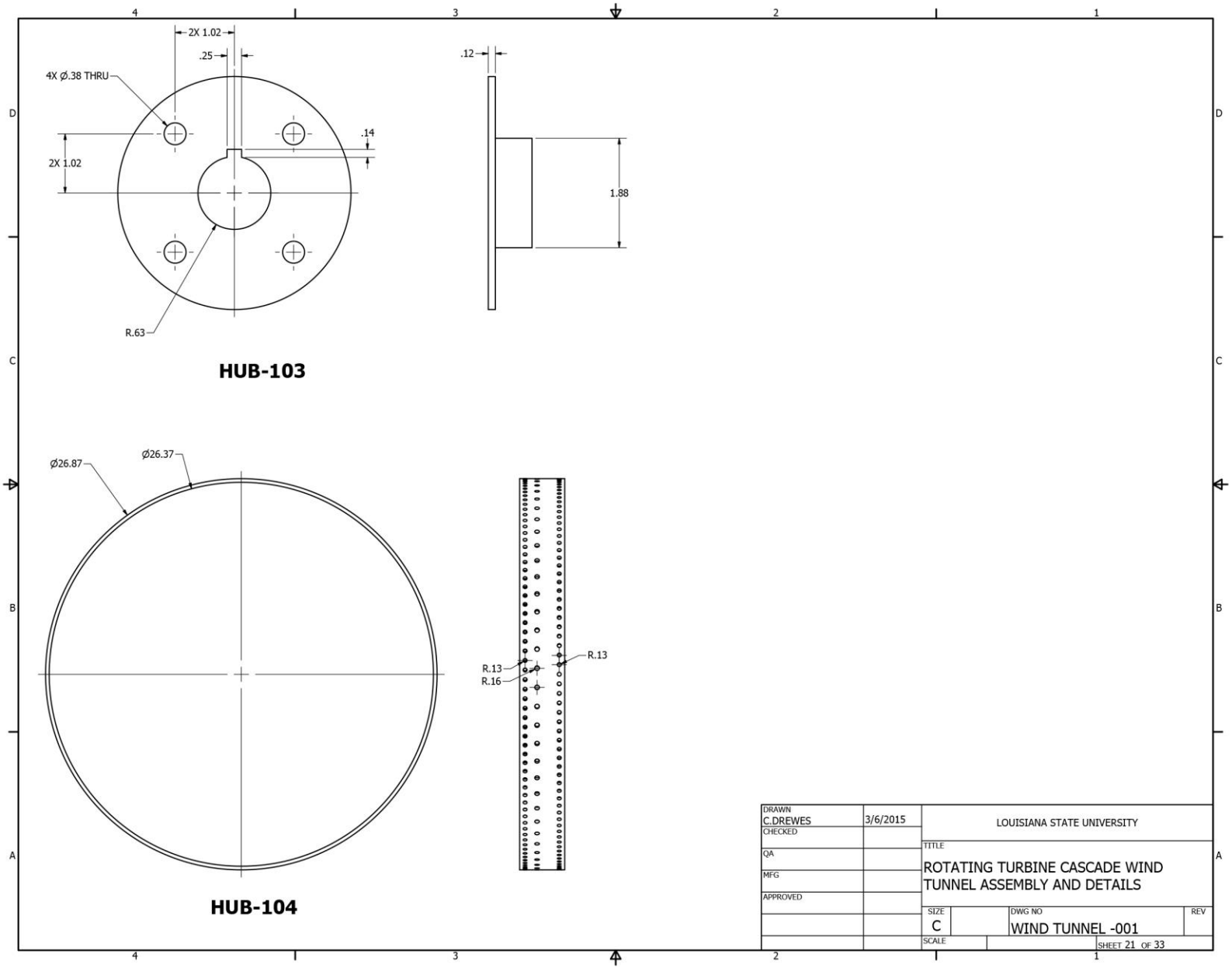
2X 1.02
.25
4X Ø.38 THRU
.14
2X 1.02
R.63
.12
1.88
HUB-103
Ø26.87
Ø26.37
R.13
R.13
R.16
HUB-104
DRAWN
C.DREWES
3/6/2015
CHECKED
QA
MFG
APPROVED
LOUISIANA STATE UNIVERSITY
TITLE
ROTATING TURBINE CASCADE WIND TUNNEL ASSEMBLY AND DETAILS
SIZE
C
DWG NO
WIND TUNNEL -001
REV
SCALE
SHEET 21 OF 33

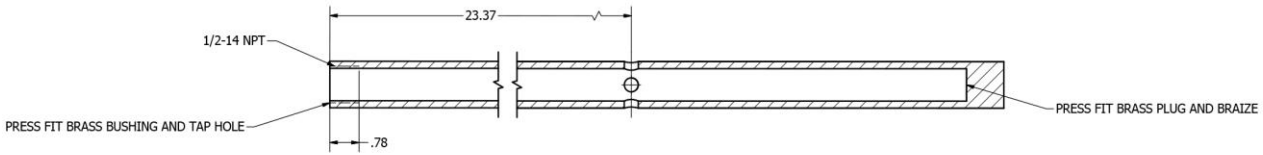

SECTION AB-AB
SCALE 1/2

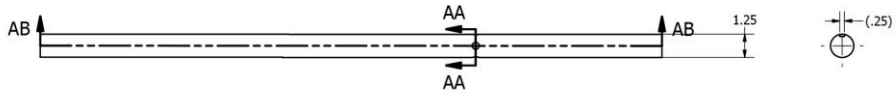

HUB-105

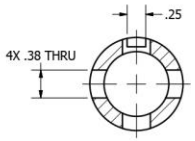

SECTION AA-AA
SCALE 1/1

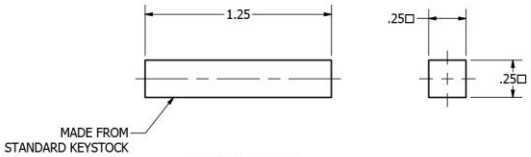

HUB-106

DRAWN C.DREWES	3/6/2015	LOUISIANA STATE UNIVERSITY
CHECKED		TITLE: ROTATING TURBINE CASCADE WIND TUNNEL ASSEMBLY AND DETAILS
QA		
MFG		
APPROVED		SIZE C; DWG NO WIND TUNNEL -001; REV
		SCALE; SHEET 22 OF 33

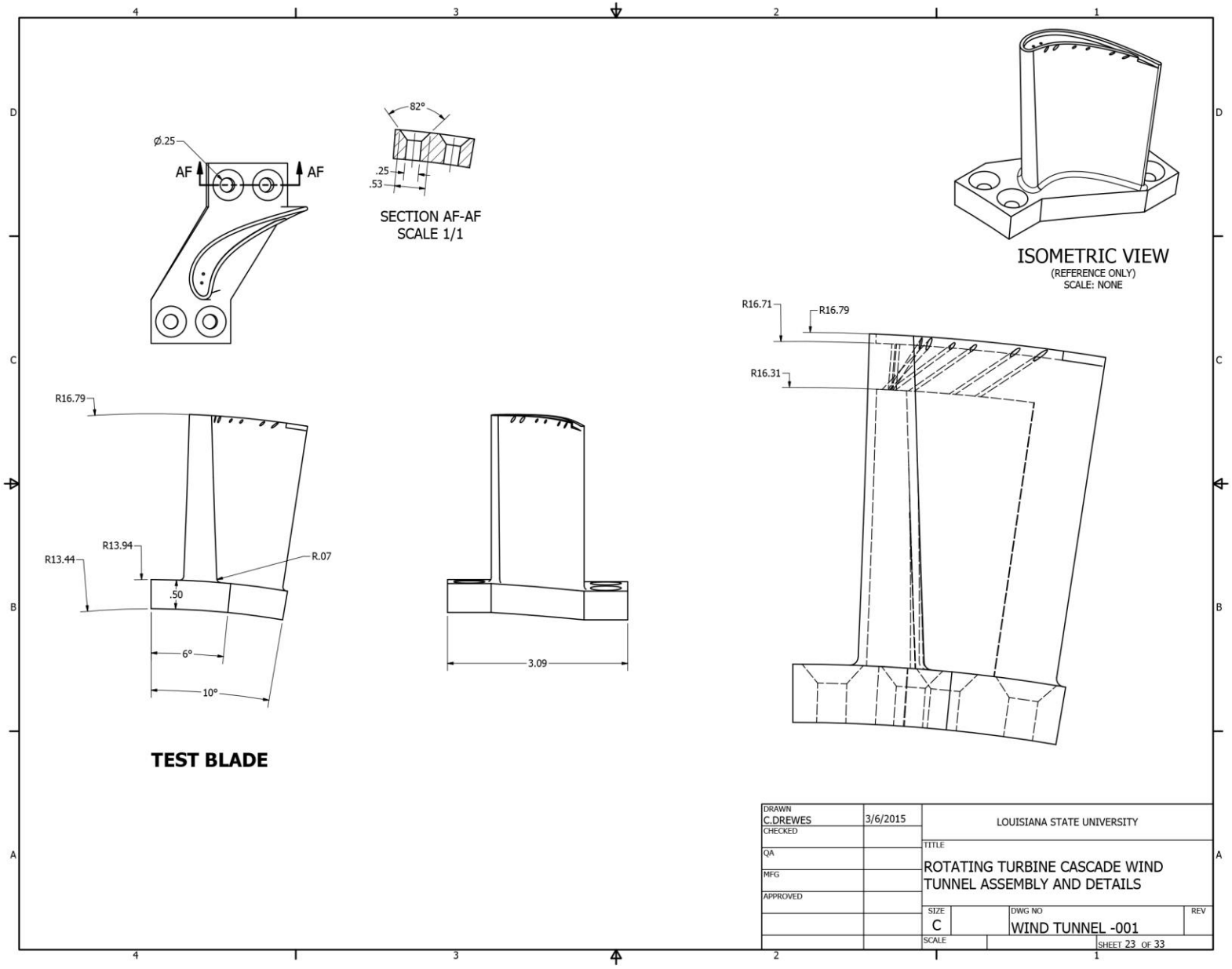
Ø.25
AF
AF
82°
.25
.53
SECTION AF-AF
SCALE 1/1
ISOMETRIC VIEW
(REFERENCE ONLY)
SCALE: NONE
R16.79
R13.94
R13.44
R.07
.50
6°
10°
3.09
R16.71
R16.79
R16.31
TEST BLADE
DRAWN
C.DREWES
3/6/2015
CHECKED
QA
MFG
APPROVED
LOUISIANA STATE UNIVERSITY
TITLE
ROTATING TURBINE CASCADE WIND TUNNEL ASSEMBLY AND DETAILS
SIZE
C
DWG NO
WIND TUNNEL -001
REV
SCALE
SHEET 23 OF 33

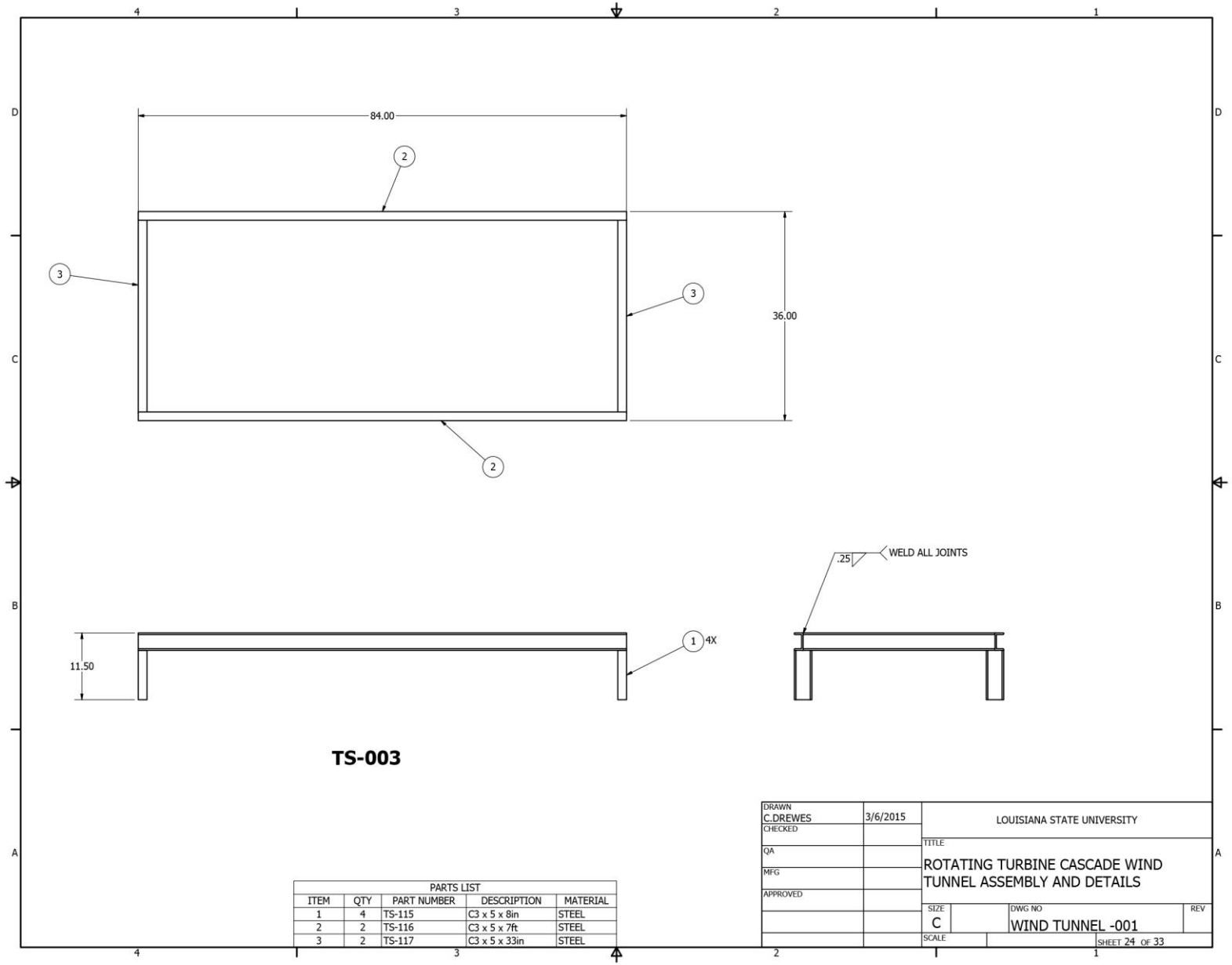

TS-003

PARTS LIST				
ITEM	QTY	PART NUMBER	DESCRIPTION	MATERIAL
1	4	TS-115	C3 x 5 x 8in	STEEL
2	2	TS-116	C3 x 5 x 7ft	STEEL
3	2	TS-117	C3 x 5 x 33in	STEEL

DRAWN C.DREWES	3/6/2015	LOUISIANA STATE UNIVERSITY
CHECKED		TITLE: ROTATING TURBINE CASCADE WIND TUNNEL ASSEMBLY AND DETAILS
QA		
MFG		
APPROVED		SIZE C; DWG NO WIND TUNNEL -001; REV
		SCALE; SHEET 24 OF 33

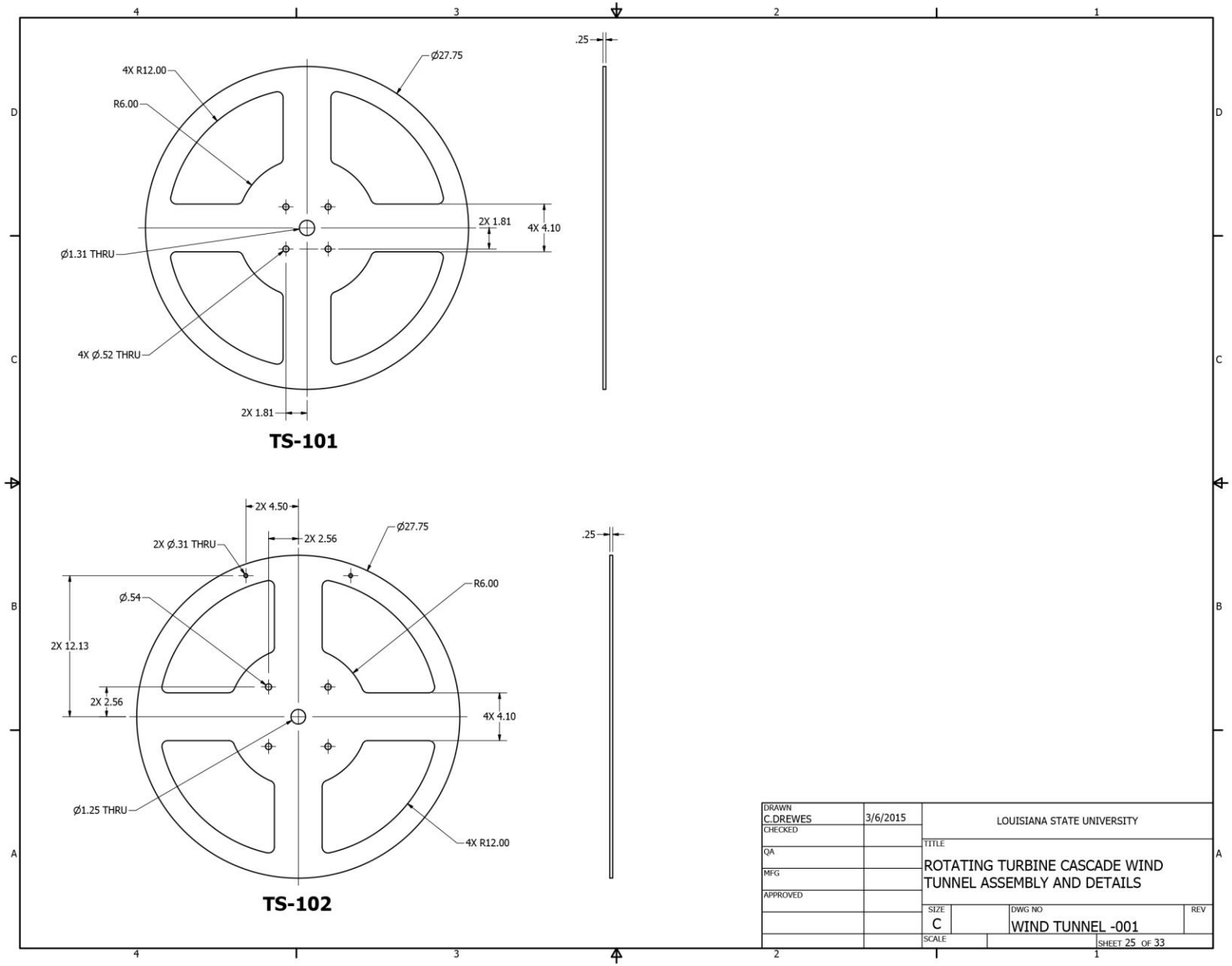
4X R12.00
R6.00
Ø27.75
.25
2X 1.81
4X 4.10
Ø1.31 THRU
4X Ø.52 THRU
2X 1.81
TS-101
2X 4.50
2X Ø.31 THRU
2X 2.56
Ø27.75
.25
R6.00
Ø.54
2X 12.13
2X 2.56
4X 4.10
Ø1.25 THRU
4X R12.00
TS-102
DRAWN
C.DREWES
3/6/2015
CHECKED
QA
MFG
APPROVED
LOUISIANA STATE UNIVERSITY
TITLE
ROTATING TURBINE CASCADE WIND TUNNEL ASSEMBLY AND DETAILS
SIZE
C
DWG NO
WIND TUNNEL -001
REV
SCALE
SHEET 25 OF 33

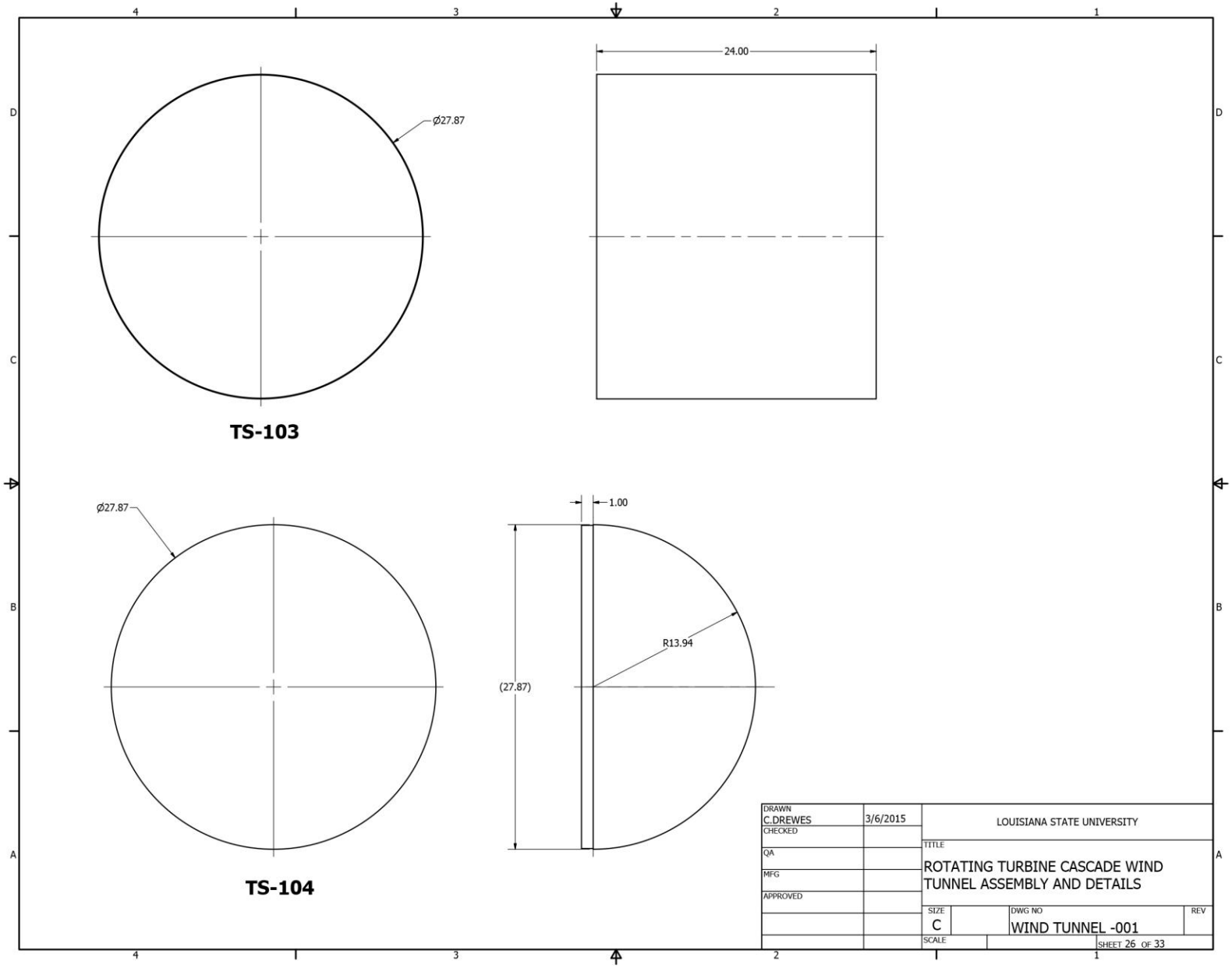
24.00
Ø27.87
TS-103
Ø27.87
1.00
R13.94
(27.87)
TS-104
DRAWN
C.DREWES
3/6/2015
CHECKED
QA
MFG
APPROVED
LOUISIANA STATE UNIVERSITY
TITLE
ROTATING TURBINE CASCADE WIND TUNNEL ASSEMBLY AND DETAILS
SIZE
C
DWG NO
WIND TUNNEL -001
REV
SCALE
SHEET 26 OF 33

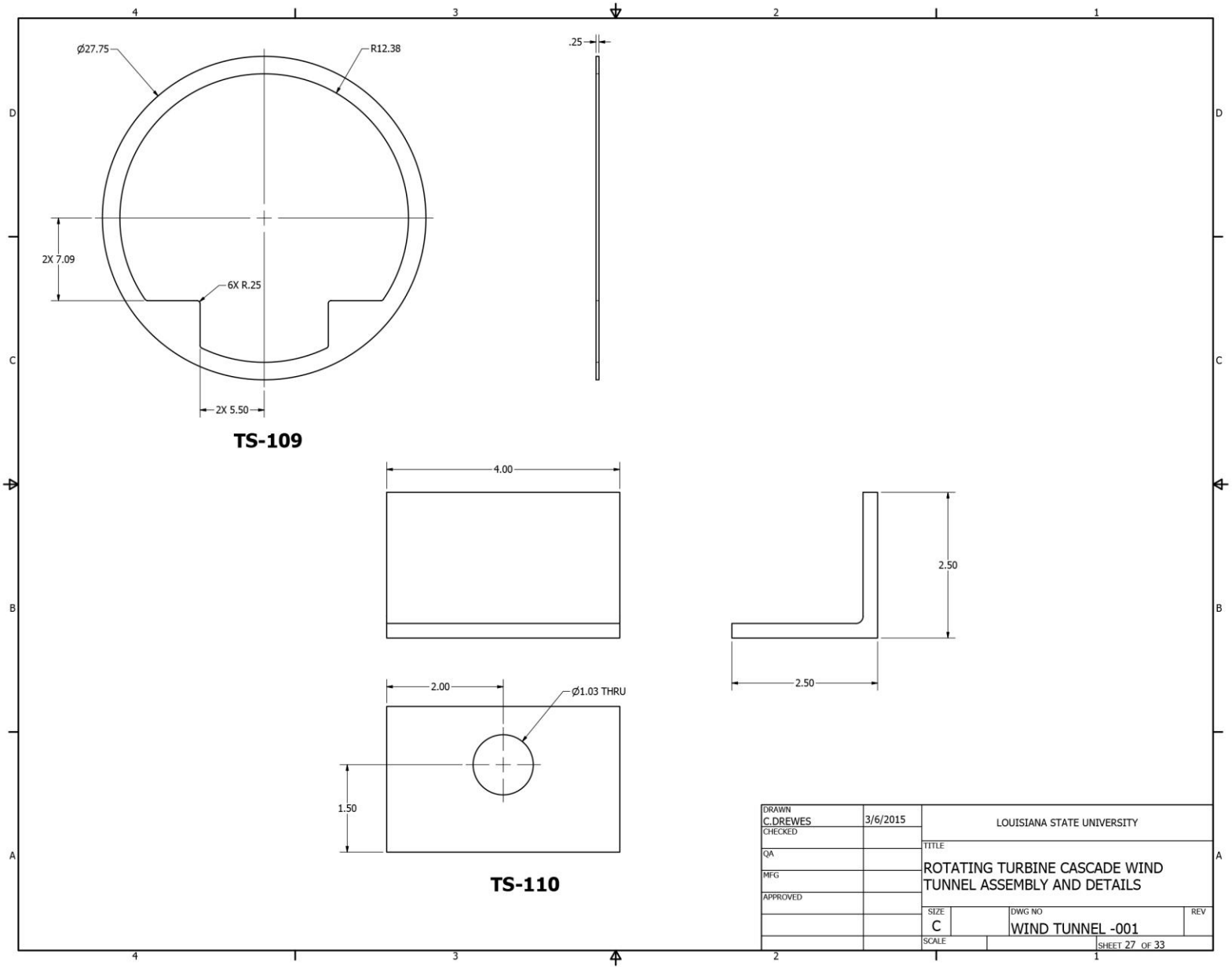
Ø27.75
R12.38
.25
2X 7.09
6X R.25
2X 5.50
TS-109
4.00
2.50
2.50
2.00
Ø1.03 THRU
1.50
TS-110
DRAWN
C.DREWES
3/6/2015
CHECKED
QA
MFG
APPROVED
LOUISIANA STATE UNIVERSITY
TITLE
ROTATING TURBINE CASCADE WIND TUNNEL ASSEMBLY AND DETAILS
SIZE
C
DWG NO
WIND TUNNEL -001
REV
SCALE
SHEET 27 OF 33

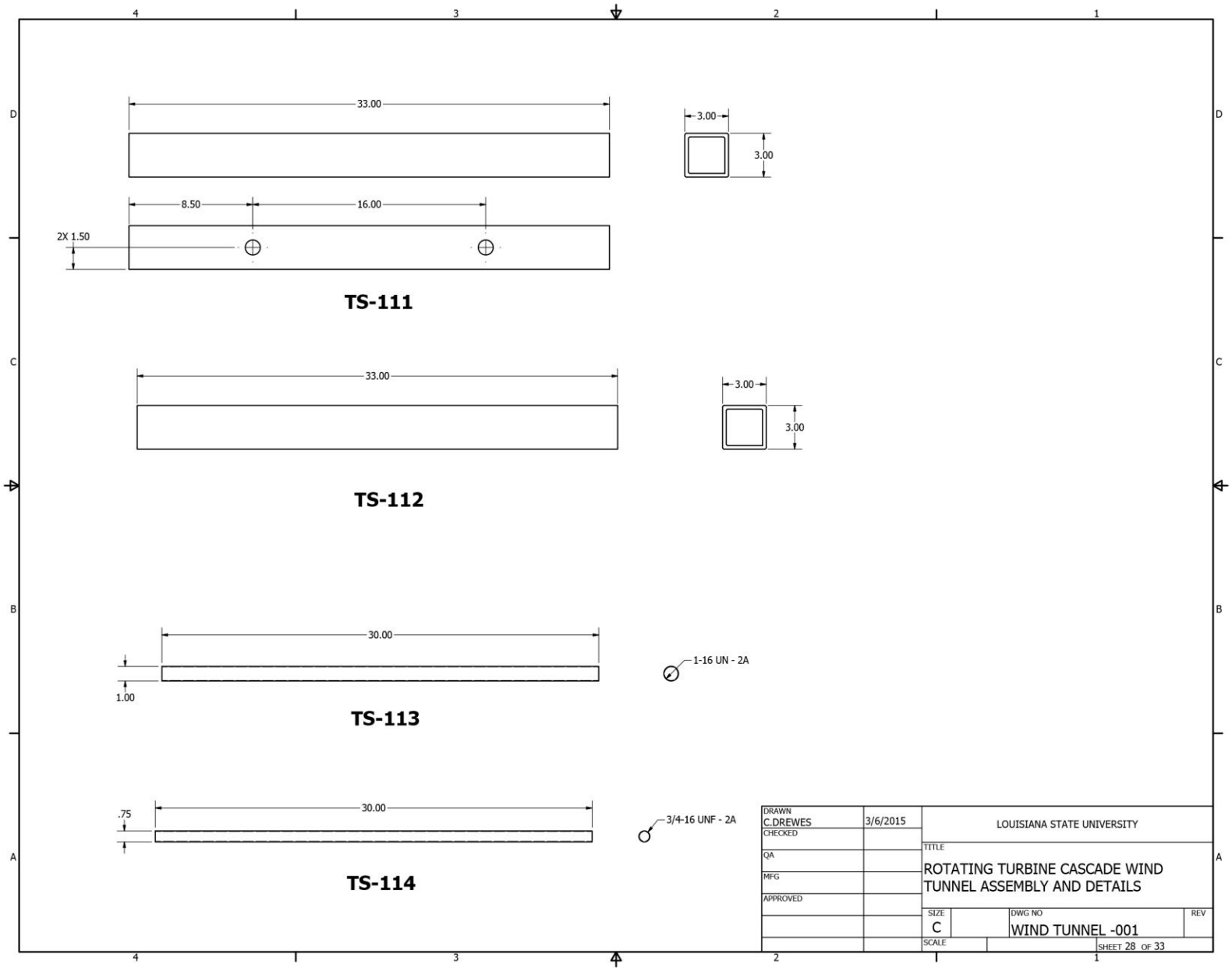
33.00
3.00
3.00
8.50
16.00
2X 1.50
TS-111
33.00
3.00
3.00
TS-112
30.00
1.00
1-16 UN - 2A
TS-113
.75
30.00
3/4-16 UNF - 2A
TS-114
DRAWN
C.DREWES
3/6/2015
CHECKED
QA
MFG
APPROVED
LOUISIANA STATE UNIVERSITY
TITLE
ROTATING TURBINE CASCADE WIND TUNNEL ASSEMBLY AND DETAILS
SIZE
C
DWG NO
WIND TUNNEL -001
REV
SCALE
SHEET 28 OF 33

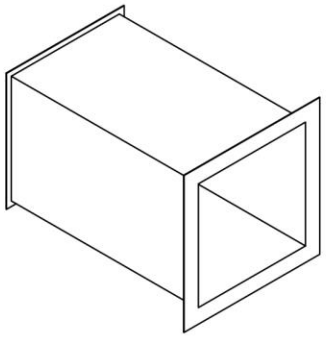

ISOMETRIC VIEW
(REFERENCE ONLY)
SCALE: NONE

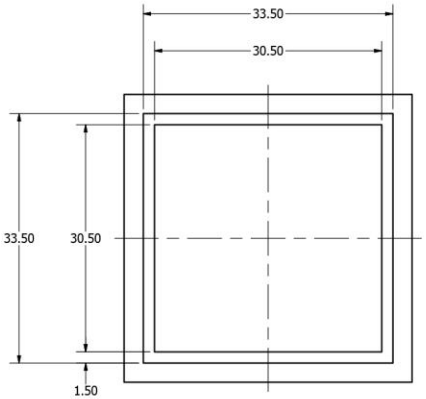

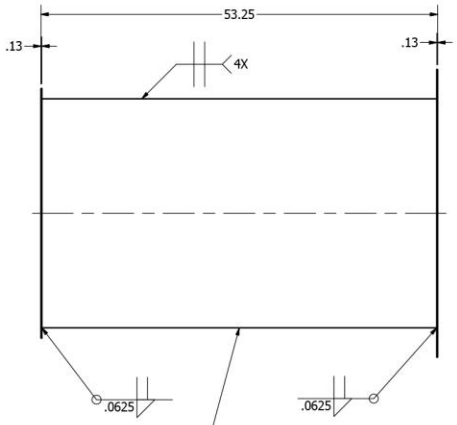

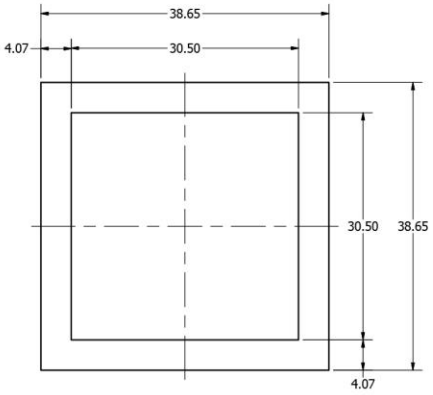

4X 16 GA GALVANIZED STEEL PANELS
COLD GALVANIZE WELDS AFTER FABRICATION

1600

PARTS LIST				
ITEM	QTY	PART NUMBER	DESCRIPTION	VENDOR
1	1	1600	ASSY, DUCT	SPIRAL METALS

DRAWN C.DREWES	3/6/2015	LOUISIANA STATE UNIVERSITY
CHECKED		TITLE: ROTATING TURBINE CASCADE WIND TUNNEL ASSEMBLY AND DETAILS
QA		
MFG		
APPROVED		SIZE C | DWG NO WIND TUNNEL -001 | REV
		SCALE | SHEET 29 OF 33

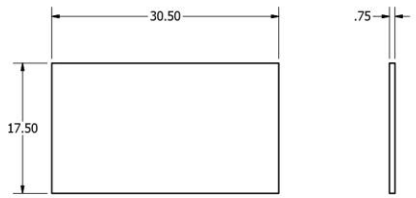

113

DRAWN C.DREWES	3/6/2015	LOUISIANA STATE UNIVERSITY
CHECKED		TITLE: ROTATING TURBINE CASCADE WIND TUNNEL ASSEMBLY AND DETAILS
QA		
MFG		
APPROVED		SIZE: C; DWG NO: WIND TUNNEL -001; REV
		SCALE; SHEET 30 OF 33

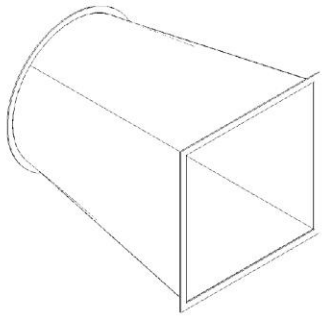

ISOMETRIC VIEW
(REFERENCE ONLY)
SCALE: NONE

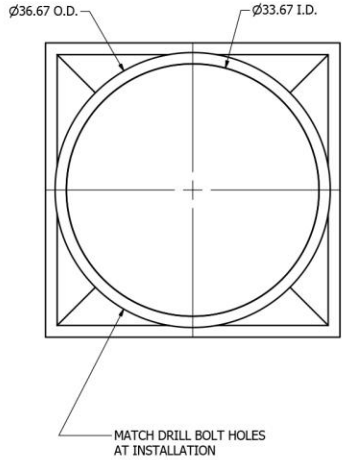

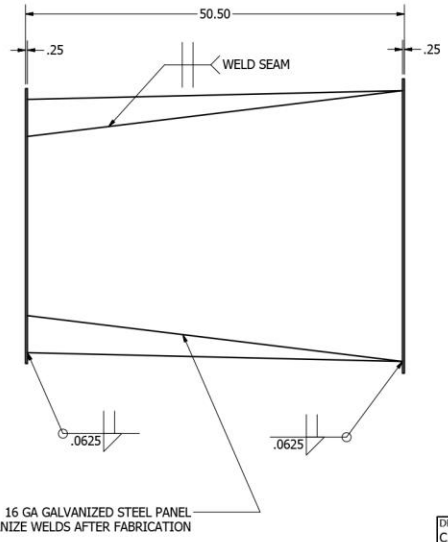

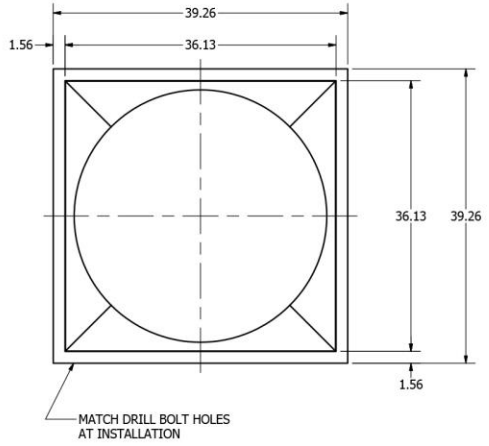

1300

PARTS LIST				
ITEM	QTY	PART NUMBER	DESCRIPTION	VENDOR
1	1	1300	ASSY, DUCT	LSU FACILITY SERVICES

DRAWN C.DREWES	3/6/2015	LOUISIANA STATE UNIVERSITY
CHECKED		TITLE: ROTATING TURBINE CASCADE WIND TUNNEL ASSEMBLY AND DETAILS
QA		
MFG		
APPROVED		SIZE C · DWG NO WIND TUNNEL -001 · REV
		SCALE · SHEET 31 OF 33

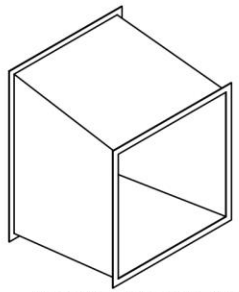

ISOMETRIC VIEW
(REFERENCE ONLY)
SCALE: NONE

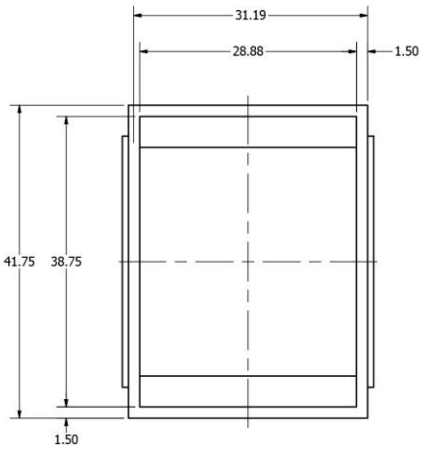

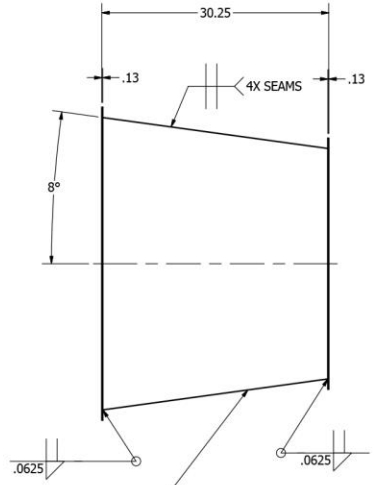

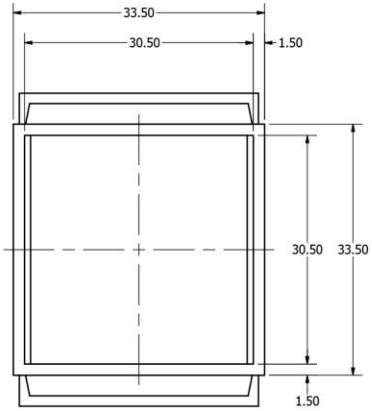

4X 16 GA GALVANIZED STEEL PANELS
COLD GALVANIZE WELDS AFTER FABRICATION

1400

PARTS LIST				
ITEM	QTY	PART NUMBER	DESCRIPTION	VENDOR
1	1	1400	ASSY, DUCT	SPIRAL METALS

DRAWN C.DREWES	3/6/2015	LOUISIANA STATE UNIVERSITY
CHECKED		TITLE: ROTATING TURBINE CASCADE WIND TUNNEL ASSEMBLY AND DETAILS
QA		
MFG		
APPROVED		SIZE C · DWG NO WIND TUNNEL -001 · REV
		SCALE · SHEET 32 OF 33

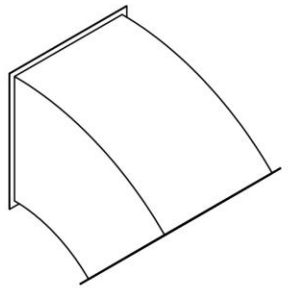

ISOMETRIC VIEW
(REFERENCE ONLY)
SCALE: NONE

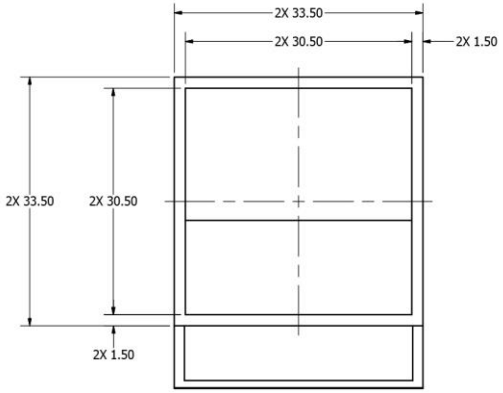

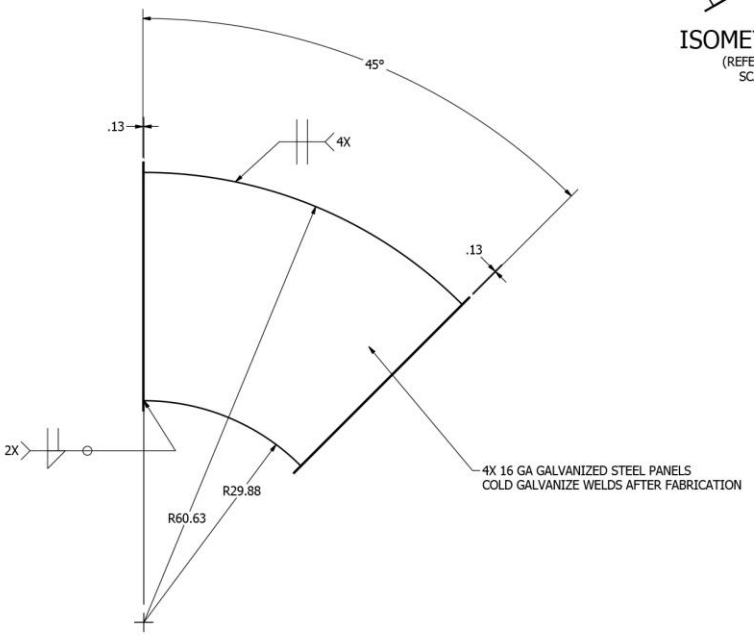

1500

PARTS LIST				
ITEM	QTY	PART NUMBER	DESCRIPTION	VENDOR
1	1	1500	ASSY, DUCT	SPIRAL METALS

DRAWN C.DREWES	3/6/2015	LOUISIANA STATE UNIVERSITY
CHECKED		TITLE: ROTATING TURBINE CASCADE WIND TUNNEL ASSEMBLY AND DETAILS
QA		
MFG		
APPROVED		SIZE C | DWG NO WIND TUNNEL -001 | REV
		SCALE | SHEET 33 OF 33

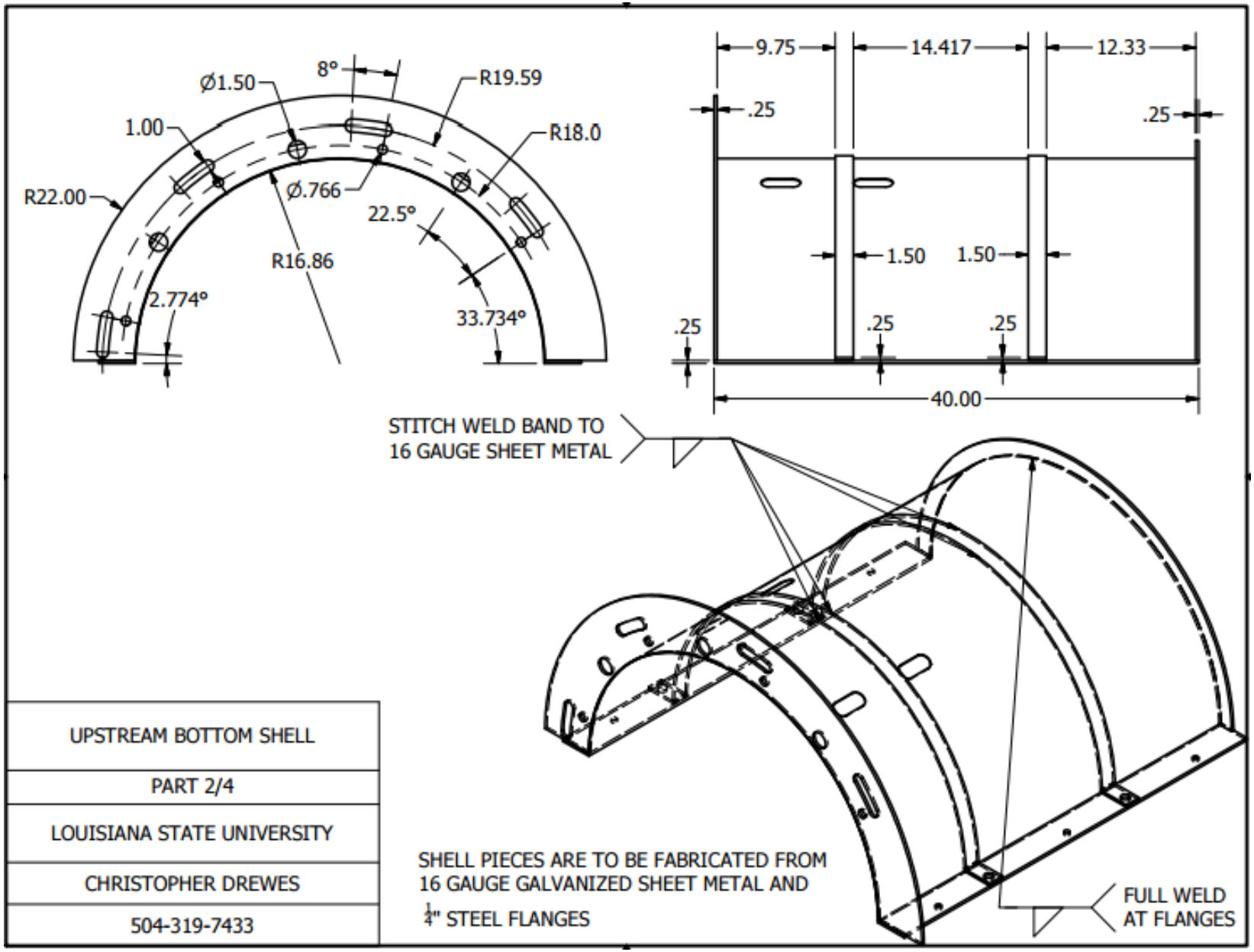
Ø1.50
8°
R19.59
1.00
R18.0
R22.00
Ø.766
22.5°
R16.86
2.774°
33.734°
9.75
14.417
12.33
.25
.25
1.50
1.50
.25
.25
.25
40.00
STITCH WELD BAND TO
16 GAUGE SHEET METAL
UPSTREAM BOTTOM SHELL
PART 2/4
LOUISIANA STATE UNIVERSITY
CHRISTOPHER DREWES
504-319-7433
SHELL PIECES ARE TO BE FABRICATED FROM
16 GAUGE GALVANIZED SHEET METAL AND
¼" STEEL FLANGES
FULL WELD
AT FLANGES

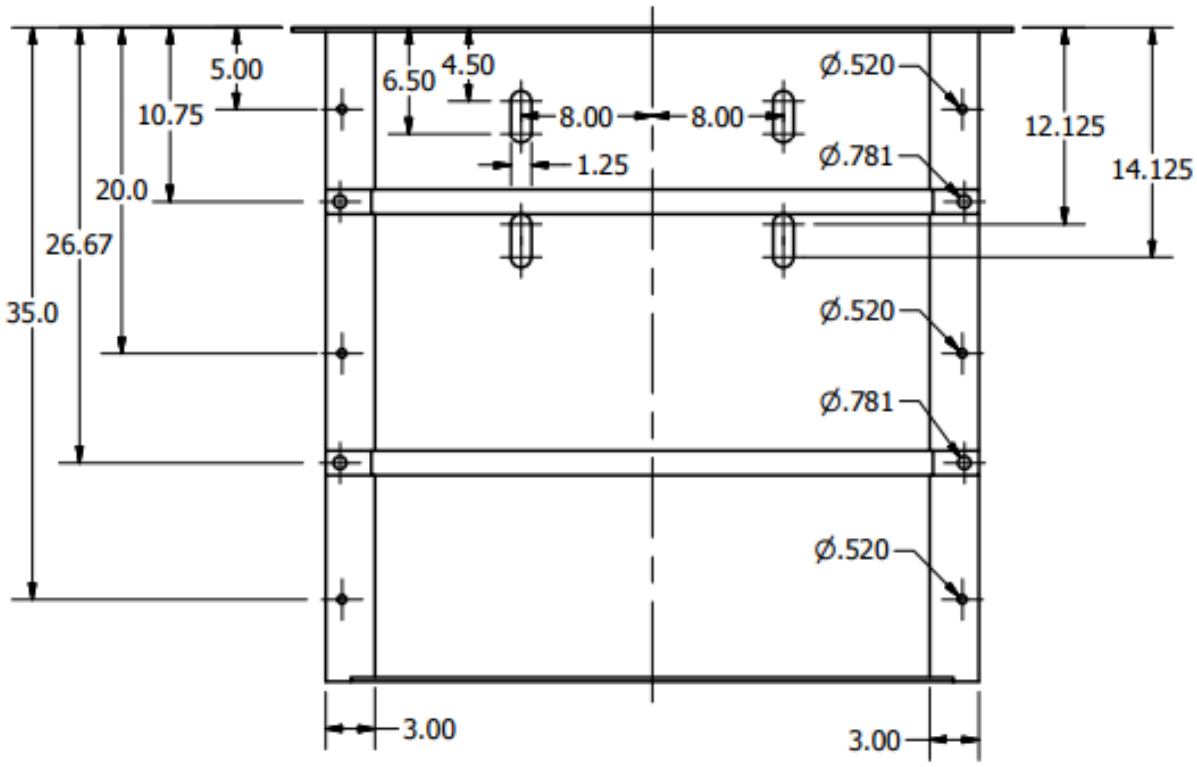
5.00
10.75
20.0
26.67
35.0
6.50
4.50
8.00
8.00
1.25
Ø.520
Ø.781
Ø.520
Ø.781
Ø.520
12.125
14.125
3.00
3.00

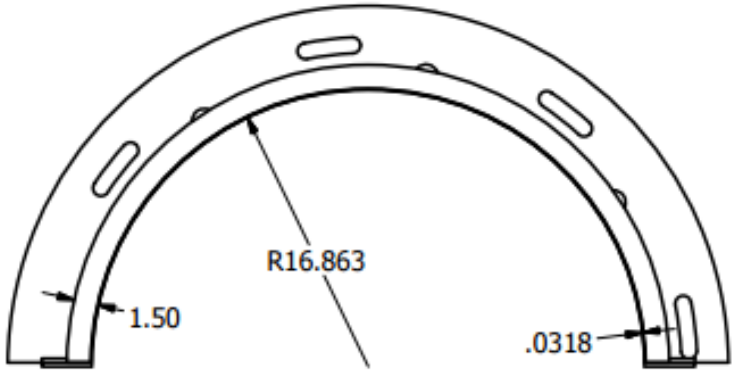
R16.863
1.50
.0318

Vita

Christopher Drewes was born in New Orleans, LA, to Mark and Robin Drewes. He grew up in Metairie and attended Jesuit High School. He graduated cum laude with a BS in Mechanical Engineering from LSU in 2011. He began pursuing his Masters of Science in Mechanical Engineering in the summer of 2010 as a part of the Accelerated Masters program. In October of 2012 he took a Mechanical Engineering position at Textron Systems, Marine & Land Systems where he currently works on the development of the Ship to Shore Connector for the United States Navy.